BEFORE-CLOSURE ANALYSIS OF FRACTURE CALIBRATION TEST

A Dissertation

by

GUOQING LIU

Submitted to the Office of Graduate and Professional Studies of
Texas A&M University
in partial fulfillment of the requirements for the degree of

DOCTOR OF PHILOSOPHY

Chair of Committee,	Christine Ehlig-Economides
Co-Chair of Committee,	Peter Valkó
Committee Members,	Benchun Duan
	George J. Moridis
Head of Department,	Daniel Hill

August 2015

Major Subject: Petroleum Engineering

ABSTRACT

Since injection falloff fracture calibration test is generally accepted as a reliable way to obtain several key formation parameters, it is one of the essential parts of hydraulic fracturing design. While several abnormal behaviors have been described qualitatively and are frequently observed in an injection falloff fracture calibration test, the only quantitative model for before-closure behavior accounts only for normal leakoff which usually seldom happens in practice. This paper describes several new analytical and semi-analytical models to simulate and quantify abnormal leakoff behaviors such as tip extension, pressure dependent leakoff (PDL), multiple apparent closures and transverse storage.

Based on material balance, we model pressure change with time considering the fracture geometry and leakoff volume under various leakoff mechanisms. Then, we show that the appearance of the modeled mechanisms both on the standard Nolte plot and on the log-log diagnostic Bourdet derivative presentation qualitatively matches behavior seen in previously published field data examples.

Results suggest that the early ½-slope occasionally observed on the log-log diagnostic plot is probably fracture linear flow. When present it can mask all or part of a wellbore storage effect. Natural fractures have a significant impact on the pressure falloff behavior when they are opened during treatment. Depending on the properties of the natural fracture system, the pressure response can behave as pressure-dependent leakoff (PDL), transverse storage, multiple closures or even normal leakoff in some

cases. In addition, if tip extension or PDL behavior are observed, propagation pressure or natural fissures opening pressure can be estimated respectively.

The flow regime models are combined to provide a global model for the closure behavior. When shown on the log-log diagnostic plot, the various model features can be identified and used to estimate parameters to which each model is sensitive. Sensitivity analyses with the new model show relative importance with time of the various model features. This work promotes a complete understanding of the pressure response from various leakoff physics and provides a method to quantify parameters needed for more effective hydraulic fracture design.

DEDICATION

To my family

ACKNOWLEDGEMENTS

Before anything else, I would first like to thank my committee chair, Dr. Christine Ehlig-Economides for her perseverant guidance, patience and support throughout the course of the research. Without her great help, this research would not have been possible.

Also, thanks to Dr. Peter Valkó, Dr. George J. Moridis and Dr. Benchun Duan for their availability and patience as my committee members, and for their valuable and insightful advices on the research.

Thanks also to Apache Canada, Ltd. for providing the Horn River Shale data for the case study in this research.

Thanks also to all friends, colleagues, the department faculty and staff for making my time at Texas A&M University an invaluable experience.

Finally, thanks to my father, mother, and all my family for their love and encouragement.

NOMENCLATURE

AC	After Closure
A_f	Fracture surface area, ft^2
A_{fo}	Fracture surface area at end of pumping, ft^2
A_{f1}	Fracture surface area at end of fracture tip-extension, ft^2
A_{fm}	Surface area of main fracture, ft^2
A_{fn}	Surface area of natural fracture, ft^2
A_{fr}	Ratio of main fracture surface area over natural fracture surface area, dimensionless
BC	Before Closure
C	wellbore storage coefficient, ft^3/psi
c_f	Fracture compliance, ft/psi
c_{fm}	Compliance of main fracture, ft/psi
c_{fn}	Compliance of natural fracture, ft/psi
c_{fn0}	Compliance of natural fracture at end of pumping, ft/psi
c_w	Water compressibility, psi^{-1}
C_{fbc}	Before-closure fracture storage, bbl/psi
c_t	Total compressibility, psi^{-1}
C_L	Leakoff coefficient, $ft/min^{0.5}$
C_{Lm}	Leakoff coefficient from main fracture into matrix, $ft/min^{0.5}$
C_{Ln}	Leakoff coefficient from natural fracture into matrix, $ft/min^{0.5}$

C_{Ln1}	Leakoff coefficient from natural fracture into matrix before shut-in, ft/min$^{0.5}$
C_{Ln2}	Leakoff coefficient from natural fracture into matrix after its closure, ft/min$^{0.5}$
erfc	Error-function, dimensionless
E’	Plane-strain modulus, psi
f	f-function, dimensionless
g	g-function, dimensionless
G	g-function, dimensionless
h_f	Fracture height, ft
h	Formation height, ft
k_{fil}	Relative permeability to the filtrate of frac fluid, md
k or k_r	Formation permeability, md
L_w	Wellbore length, ft
p	Pressure, psi
p_c	Final closure pressure, psi
p_{ci}	Start pressure of normal closure behavior ending with the final closure, psi
p_{fo}	Opening pressure of natural fissures, psi
p_i	Initial formation pressure, psi
p_{net}	Net Pressure on fracture face, psi
p_w	Hydraulic pressure in the fracture or at bottomhole, psi

p_{ws}	Bottomhole pressure at end of injection, psi
PDL	Pressure Dependent Leakoff
R_f	Fracture radius in radial fracture model, ft
r_p	Ratio of permeable fracture surface area to the gross fracture area, dimensionless
r_w	Wellbore radius, ft.
S_f	Fracture stiffness, psi/ft
t	Time, s
t_{fc}	Time when natural fissures closes, s
t_{er}	Equivalent time function in radial flow, dimensionless
t_p	Pumping time, s
t_{p1}	Fracture propagation time, s
x_f	Fracture half-length, ft
v	Leakoff rate, ft/s
V_{AF}	After-flow volume, bbl
V_{frac}	Fracture volume, ft^3
V_l	Total leakoff volume into formation through fracture face, ft^3
Vp	Total pumping volume into fracture before shut-in, ft^3
Vw	Wellbore volume, ft^3
w	Fracture width, in
WBS	Wellbore storage effect, bbl

Subscript

D	Dimensionless
f	Fracture
face	Fracture face
j	time step
mf	Main fracture
nf	Natural fracture
r	Formation
te	Tip extension
v	Filtrate zone from fracture into formation

Greek

α	Area exponent, dimensionless
α_0	Area exponent before shut-in, dimensionless
α_{cp}	Power law coefficient for pressure dependent leakoff (PDL) into matrix, dimensionless
ϕ	Formation porosity, dimensionless
Δ	Difference, dimensionless
μ_{fil}	Viscosity of filtrate of frac fluid, cp
μ or μ_r	Formation fluid viscosity, cp
τ	Superposition time, dimensionless
$\sigma_{resistant}$	Confining stress on the fracture face, psi

σ_{min}	Minimum horizontal stress, psi
θ	Fluid-loss exponent, dimensionless
ξ	Variable, dimensionless
η	Fluid efficiency, %

TABLE OF CONTENTS

Page

Page

LIST OF FIGURES

Page

Page

Page

Page

Page

Page

Page

Page

LIST OF TABLES

Page

Page

CHAPTER I

INTRODUCTION AND LITERATURE REVIEW

The fracture calibration test (FCT), also known as mini-frac, injection/falloff test and diagnostic fracture injection test (DFIT), is widely used to extract several essential input parameters for the following main fracturing treatment design. These parameters usually include leakoff coefficient, fracture closure pressure, fluid efficiency, formation permeability, etc.

Due to distinct fluid flow mechanisms, FCT analysis can be divided into two sections: before- and after-closure analysis. This work is mainly on before-closure analysis. In normal leakoff condition, which will be discussed later in detail, three factors can be quantified from before-closure analysis: fracture closure pressure, fluid efficiency, and leakoff coefficient.

Several models currently available for FCT analysis are based on the normal leakoff, which in practice seldom happens (Craig et al. 2000; Craig et al. 2000). This thesis tends to expand the application of FCT analysis to several commonly observed abnormal leakoff behavior, tip-extension, pressure-dependent leakoff (PDL), transverse storage, etc.

1.1 Introduction to the Fracture Calibration Test

A typical fracture-injection and falloff test is graphed in Figure 1-1. To obtain representative pressure decline data, it is recommended to inject same type of fluid with

that in following main treatment, but without proppant. The injection volume for tight formation usually is very limited (Marongiu-Porcu 2014; Nguyen and Cramer 2013), in the range of 1-12 bbl in some cases. Although the volume could be more than 20 bbl (Bachman et al. 2012; Barree et al. 2014; Xue and Ehlig-Economides 2013), it is still much less than that of a main fracturing job. After the breakdown of formation, fracture continues propagating at a stable pressure level until the pump is shut in. Then the pressure falloff can be recorded at the bottomhole, which is recommended, or at the surface. To calculate the pressure change along elapsed time, instantaneous shut-in pressure (ISIP) is usually picked as the pressure reference to get rid of the friction in the string and near wellbore. When the fracture pressure decreases to a level less than the confining pressure, the fracture is supposed to freely close on its face. The closure event is required to be identified to calculate the closure pressure. Besides closure pressure, leakoff coefficient and fluid efficiency can also be quantified if the closure can be picked out from the before-closure analysis. After-closure section is typically used to extract formation permeability and initial pressure if corresponding flow regime is observed.

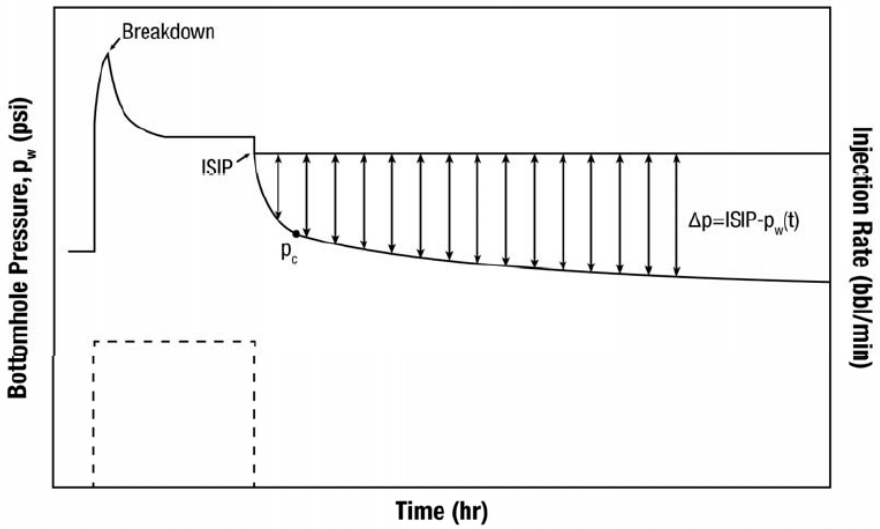

Figure 1-1 **Schematic sequence of events in fracture calibration test (Marongiu-Porcu et al. 2011)**

1.2 Overview of Current Before-Closure analysis models

Since the publication of pioneered work by Nolte (Gulrajani and Nolte 2000; Nolte 1979, 1990; Nolte et al. 1993; Nolte et al. 1997), several analytical models has been developed and are available now for the before-closure analysis.

1.2.1 Nolte G time function (NGTF) method

In last few decades before the kickoff of unconventional, hydraulic fracturing was mainly used in conventional reservoir typically with relatively high permeability. To reduce leakoff and create an efficient fracture with high conductivity, crosslinked gel is the primary choice as the treatment fluid with high load of proppant. For most of these treatments with crosslinked fluid, filter cake will deposit in the fracture face shortly after the start of leakoff, and then, the leakoff rate will be greatly reduced. The dominant

leakoff factor in these cases is the filter cake, which can be expressed by the Carter leakoff model (Carter 1957).

$$v = \frac{C_{\mathrm{L}}}{\sqrt{t}} \tag{1.1}$$

where, v is the leakoff rate through unit area of fracture face from hydraulic fracture into formation; C_{L} is the leakoff coefficient controlled by filter cake, which is usually believed to be constant and independent of pressure change; t is the length of time since the point of fracture has been exposed to the fracturing fluid.

Based on Carter leakoff model, G-function was derived by Nolte in his pioneered work (Nolte 1979), and it has been one of the most commonly used model for hydraulic design and post-frac analysis, including FCTs analysis. Widely application of G-function demonstrates the valid of Nolte G-function technique, and also Carter leakoff model. Nolte original model is based on the following assumptions,

1) material balance between leakoff fluid volume and fracture volume;
2) Carter leakoff model where leakoff coefficient is independent of pressure change;
3) constant fracture surface area after shut-in;
4) constant fracture compliance or stiffness, which guarantees the linear relationship between the change of fracture width and that of fracture pressure;
5) constant fracture height;
6) constant closure pressure;

With above assumptions, Nolte G time function (NGTF) model is developed as follows.

Fracture compliance is the key parameter to connect the pressure behavior with the fracture geometry, and it is defined as Eq.(1.2).

$$c_f = \frac{\overline{w}}{p_{net}} \tag{1.2}$$

where, c_f is the fracture compliance, and it can be calculated for different types of fractures, as listed in Table 1-1; E' and $\overline{w}$ in the table are the plane strain modulus and the average fracture width; p_{net} is the net pressure on fracture face, and it can be calculated with Eq. (1.3).

Table 1-1 Fracture compliance for 2D fracture geometry models

	PKN	KGD	Radial
c_f	$\frac{\pi h_f}{2E'}$	$\frac{\pi x_f}{E'}$	$\frac{16R_f}{3\pi E'}$

$$p_{net} = p_{frac}(t) - \sigma_{resistant} = p_w(t) - \sigma_{resistant} \tag{1.3}$$

where, $p_w(t)$ is the fluid pressure in the fracture, and it is usually assumed to be same as recorded or calibrated bottom hole pressure. $\sigma_{resistant}$ is the confining stress on the fracture face, and can be assumed to be minimum horizontal principal stress (σ_{min}) if the fracture propagates in the direction perpendicular to it. Besides, the fracture is supposed to close when $p_{frac}(t) < \sigma_{resistant}$. For FCT analysis, Δp_w is defined as Eq.(1.4).

$$\Delta p_w = p_{ws} - p_w(t) \tag{1.4}$$

where, p_{ws} is the pressure at end of injection (EOJ), or the instantaneous shut-in pressure (ISIP) if no friction pressure loss at very early time after shut-in.

Average fracture width is,

$$\overline{w} = \frac{V_{frac}}{A_f} \tag{1.5}$$

where, V_{frac} is fracture volume, and A_f is the area of one-side fracture surface.

Differentiating Eq.(1.3) with respect to time and substituting Eq. (1.4) and (1.5) into it, we can get,

$$\frac{d\Delta p_w}{dt} = -\frac{dp_w(t)}{dt} = -\frac{dp_{net}(t)}{dt} = -\frac{d}{dt}\left(\frac{\overline{w}}{c_f}\right) = -\frac{d}{dt}\left(\frac{V_{frac}}{c_f A_f}\right) \tag{1.6}$$

According to material balance theory that the total fluid volume pumped into the fracture is the summation of fracture volume, which is filled by frac fluid, and the leakoff volume, the following governing equation can be derived.

$$V_p = V_{frac} + V_l \tag{1.7}$$

where, V_p is the total pumping volume, and V_l is the leakoff volume.

If there is no additional fluid flow into fracture after shut-in, which is the common assumption for almost all current FCT models, V_p is a constant. After differentiation with respect to time, we can get,

$$\frac{dV_{frac}}{dt} = -\frac{dV_l}{dt} \tag{1.8}$$

And then, substitute Eq.(1.8) into Eq.(1.6), and assume that c_f and A_f are constant. Eq.(1.6) can be derived as,

$$\frac{d\Delta p_w}{dt} = -\frac{1}{c_f A_f}\frac{dV_{frac}}{dt} = \frac{1}{c_f A_f}\frac{dV_l}{dt} \tag{1.9}$$

The leakoff volume for Carter leakoff model has been derived by Nolte(Gulrajani and Nolte 2000; Nolte et al. 1993), which is given as,

$$V_l = 2r_p C_L t_p^{\theta} A_f g(\Delta t_D, \alpha, \theta) \tag{1.10}$$

where, r_p is the ratio of permeable fracture surface area to the gross fracture area; C_L is the leakoff coefficient, and it is assumed to be constant during the derivation of Eq.(1.10); t_p is the pumping time. $g(\Delta t_D, \alpha, \theta)$ is the g-function formulated by Nolte, and it is given as,

$$g(\Delta t_D, \alpha, \theta) = \frac{1}{\theta}\int_0^1 \left(1 + \Delta t_D - \xi^{1/\alpha}\right)^{\theta} d\xi \qquad \Delta t_D \geq 0 \tag{1.11}$$

where, θ is referred to as the fluid-loss exponent, and for Newtonian filtrate, $\theta = 1/2$. α is defined as the area exponent; it has a value between ½ and 1 for typical treatments. The value of α for PKN, KGD and Radial fracture model during injection is listed in Table 1-2. Δt_D is defined as Eq.(1.12).

Table 1-2 Area exponents factor (α) for PKN, KGD and Radial model

Model	PKN	KGD	Radial
α	4/5	2/3	8/9

$$\Delta t_D = \frac{t - t_p}{t_p} \tag{1.12}$$

It should be noted that the cumulative leakoff volume for Newtonian filtrate before shut-in is,

$$V_{l,p} = 2r_p C_L \sqrt{t_p} A_f g(0,\alpha) \tag{1.13}$$

By substituting Eq. (1.10) into (1.9), we can get the material balance in the differentiation form,

$$\frac{d\Delta p_w}{dt} = \frac{2r_p C_L}{c_f \sqrt{t_p}} f(\Delta t_D, \alpha) \tag{1.14}$$

where, $f(\Delta t_D, \alpha)$ is the derivative of g-function with respect to Δt_D and expressed as following with $\theta = 1/2$.

$$f(\Delta t_D, \alpha) = \frac{dg(\Delta t_D, \alpha)}{d\Delta t_D} = \int_0^1 \frac{d\xi}{\sqrt{1 + \Delta t_D - \xi^{1/\alpha}}} \qquad \Delta t_D \geq 0 \tag{1.15}$$

and,

$$g(\Delta t_D, \alpha) = \int f(\Delta t_D, \alpha)\, d\Delta t_D \tag{1.16}$$

Both g-function and $f(\Delta t_D, \alpha)$ can be approximated with following analytical solutions for the bounding values of α,

$$f(\Delta t_D) = \begin{cases} \sin^{-1}(1 + \Delta t_D)^{-1/2} & \alpha = 1/2 \\ 2\left((1 + \Delta t_D)^{1/2} - {\Delta t_D}^{1/2}\right) & \alpha = 1 \end{cases} \tag{1.17}$$

$$g(\Delta t_D) = \begin{cases} (1 + \Delta t_D) \sin^{-1}(1 + \Delta t_D)^{-1/2} + {\Delta t_D}^{1/2} & \alpha = 1/2 \\ \frac{4}{3}\left((1 + \Delta t_D)^{3/2} - {\Delta t_D}^{3/2}\right) & \alpha = 1 \end{cases} \tag{1.18}$$

Another significant fact is that Eq.(1.14) is still valid even when the leakoff coefficient, C_L, is not constant (Meyer and Jacot 2000), which greatly facilitates the modeling of Pressure Dependent Leakoff (PDL) behavior.

By integration both sides of Eq.(1.14), the pressure solution can be obtained,

$$p_{ws} - p_w(\Delta t_D) = p^* G(\Delta t_D) \tag{1.19}$$

where,

$$p^* = \frac{\pi r_p C_L \sqrt{t_p}}{2c_f} \tag{1.20}$$

$$G(\Delta t_D) = \frac{4}{\pi}[g(\Delta t_D) - g_0] \tag{1.21}$$

$$g_0 = g(\Delta t_D = 0) \tag{1.22}$$

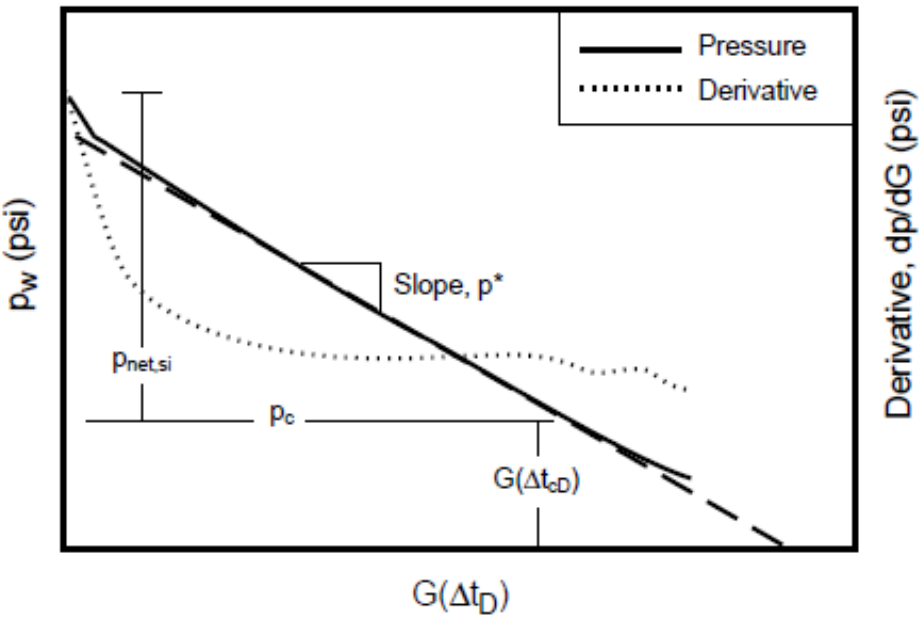

Figure 1-2 Linear relation between pressure drop and G-function time (Gulrajani and Nolte 2000)

It can be figured out from Eq.(1.19) that the pressure difference has a linear relationship with the G-function, which is given in Eq.(1.21). According to Nolte, for

normal leakoff, the deviation point from the straight line between pressure difference and the G-function time can be picked as fracture closure event, and the pressure at this point thus is the closure pressure, as shown in Figure 1-2.

Then fluid efficiency, fracture geometry and the leakoff coefficient can be calculated out with the following equations.

$$\eta = \frac{G_c}{G_c + 4g_0/\pi} \tag{1.23}$$

where, G_c is the G-function at closure, or $G_c = G(\Delta t_D = \Delta t_{cD})$.

$$\left.\begin{matrix} L \\ L^2 \\ R^3 \end{matrix}\right\} = \frac{(1-\eta)V_p E'}{2g_0 p^*} \begin{cases} 1/\left(2h_f^2\right) & \text{PKN} \\ 1/\left(4h_f\right) & \text{KGD} \\ 3\pi/32 & \text{Radial} \end{cases} \tag{1.24}$$

$$C_L = \frac{p^*}{r_p\sqrt{t_p}E'} \begin{cases} h_f & \text{PKN} \\ 2L & \text{KGD} \\ 32R_f/(3\pi^2) & \text{Radial} \end{cases} \tag{1.25}$$

In the following text, two most commonly used diagnostic methods will be covered. Based on Nolte G-function model as shown above, (Barree 1998; Barree et al. 2009) proposed a diagnostic approach to help identify closure event. Instead of using linear relation between pressure drop and G-function time (Gulrajani and Nolte 2000), as shown in Figure 1-2 Linear relation between pressure drop and G-function time (Gulrajani and Nolte 2000) (Barree 1998; Barree et al. 2009) introduced the composite derivative of G-function, Gdp/dG, to make the pressure change more obvious. As shown in top-left plot of Figure 1-3, for normal leakoff, there is a straight line through the origin between Gdp/dG with G-function. The deviation point in Gdp/dG curve from the straight line is taken as the closure point. Furthermore, distinct abnormal leakoff

behavior can be identified qualitatively from the curve, as shown in the other three plots in Figure 1-3. In the real practice, normal leakoff seldom happens, and the commonly observed abnormal leakoff includes tip extension, pressure dependent leakoff (PDL), height recession or transverse storage, multiple closure, etc. These phenomenon and their associated leakoff mechanisms will be discussed later in detail.

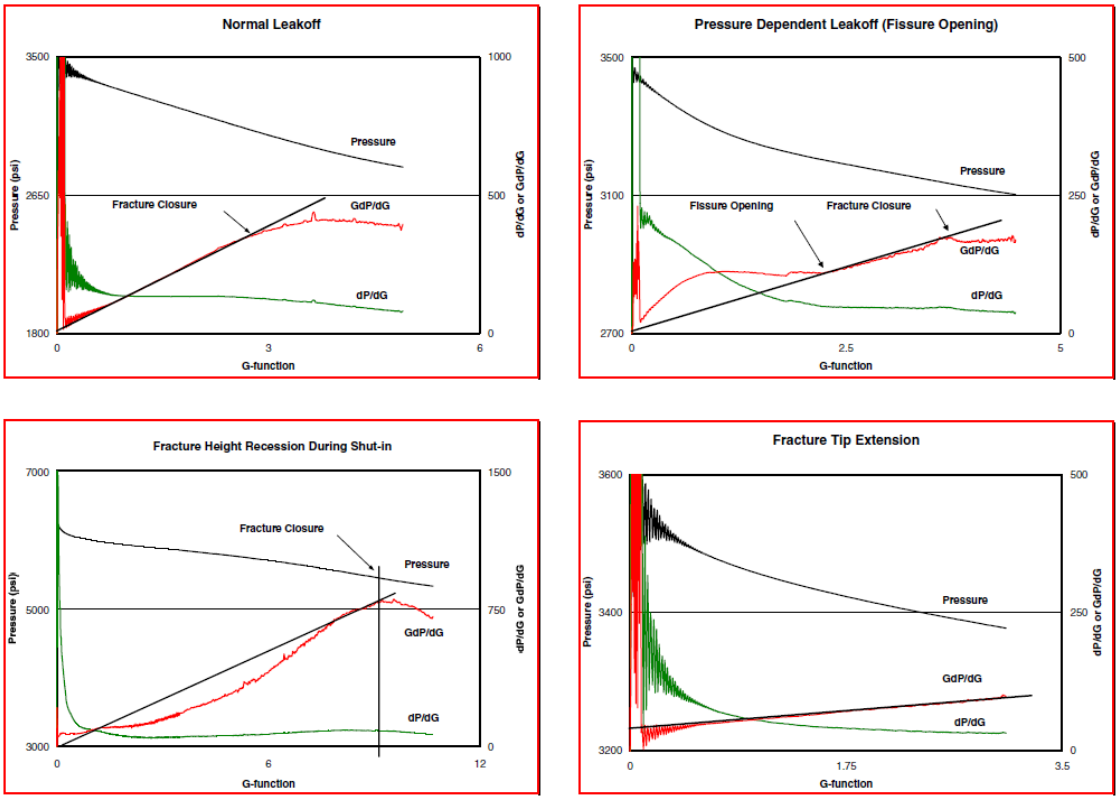

Figure 1-3 G-function characteristics for different leakoff mechanisms (Craig et al. 2000)

Besides the composite G-function diagnostic approach as discussed above, the other commonly used interpretation method is the Log-log Bourdet derivative method. Instead of using the G-function, the Log-log Bourdet derivative presentation takes

advantage of traditional pressure transient analysis (PTA) methods by employing superposition time function and its Bourdet derivative, as shown in Eq. (1.26) and (1.27). All flow regimes can be identified from this single plot, as shown in Figure 1-4. For before closure analysis, there is a 3/2-slope in the model, which indicates the closure process of normal leakoff. The finding was first proposed by (Mohamed et al. 2011) and further illustrated by (Marongiu-Porcu 2014; Marongiu-Porcu et al. 2011; Marongiu-Porcu et al. 2014) and Bachman(Bachman et al. 2013; Bachman et al. 2012).

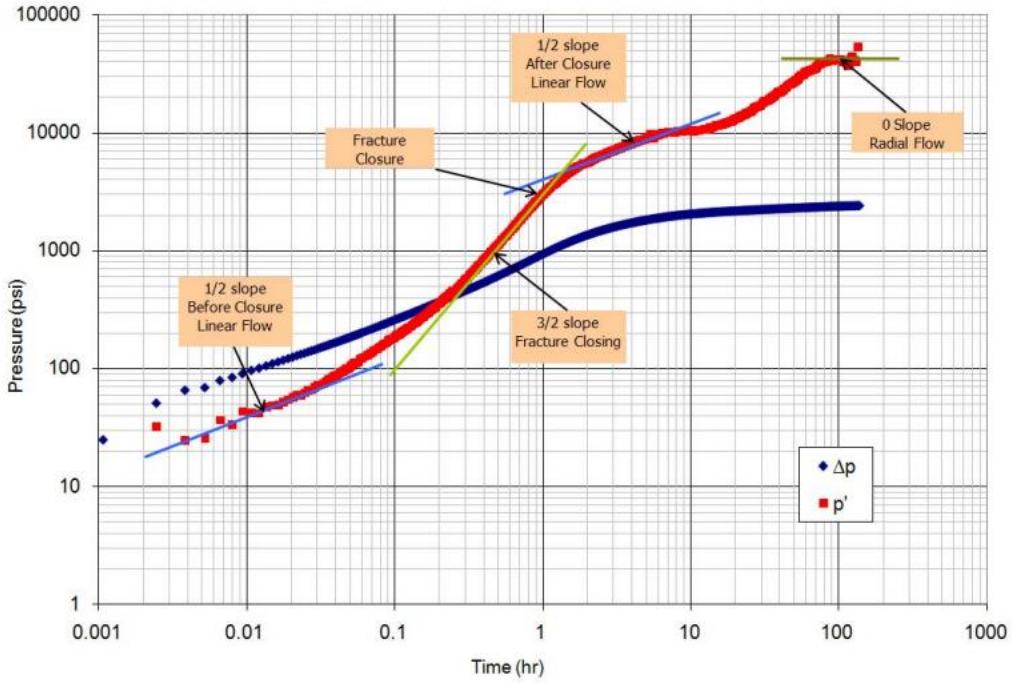

Figure 1-4 Representation of log-log diagnostic plot (Mohamed et al. 2011)

One should notice that different time functions have been used in the works of (Marongiu-Porcu 2014; Marongiu-Porcu et al. 2011; Marongiu-Porcu et al. 2014) and (Bachman et al. 2013; Bachman et al. 2012). The superposition time (τ) is employed to

build diagnostic curve by Marongiu-Porcu, while the equivalent time function is used by Bachman. The superposition time by Marongiu-Porcu model is given as,

$$\tau = \frac{t_p + \Delta t}{\Delta t} = 1 + \frac{1}{\Delta t_D} \tag{1.26}$$

and, its Bourdet derivative can be calculated as,

$$\tau \frac{d\Delta p_w}{d\tau} = -\left(\Delta t_D + {\Delta t_D}^2\right) \frac{d\Delta p_w}{d\Delta t_D} \tag{1.27}$$

However, the equivalent time function

$$t_{er} = \frac{t_p \Delta t}{t_p + \Delta t} = \frac{\Delta t_D}{1 + \Delta t_D} \tag{1.28}$$

and, its Bourdet derivative is,

$$t_{er} \frac{d\Delta p_w}{dt_{er}} = \left(\Delta t_D + {\Delta t_D}^2\right) \frac{d\Delta p_w}{d\Delta t_D} \tag{1.29}$$

Compare Eq.(1.26) with (1.28) and Eq. (1.27) with (1.29), we can find that the superposition time is just the reciprocal of the equivalent time, and the only difference in their Bourdet derivative is a negative sign.

Actually, Marongiu-Porcu shows that, the 3/2-slope in the log-log Bourdet derivative plot can be derived from Nolte G time function (NGTF) model (Marongiu-Porcu 2014; Marongiu-Porcu et al. 2011; Marongiu-Porcu et al. 2014). This provides the inherent consistency between these two diagnostic approaches. The Bourdet derivative for normal leakoff can be derived by substituting Eq. (1.19) into Eq. (1.27),

$$\tau \frac{d\Delta p_w}{d\tau} = -\frac{2 r_p C_L \sqrt{t_p}}{c_f} \left(\Delta t_D + {\Delta t_D}^2\right) f(\Delta t_D) \tag{1.30}$$

The definition of $f(\Delta t_D)$ can be found in Eq. (1.15), and its analytical approximation is listed in Eq. (1.17). The slope of Bourdet derivative curve in different time regions then can be calculated out from these equations. It has been proven that for normal leakoff on the log-log plot, the Bourdet derivative curve has a unit slop in the very early time and then transitions to the 3/2-slope (Marongiu-Porcu 2014). One should note that in Figure 1-4, the early time unit slope is masked by a ½ slope derivative trend, which will be discussed in Chapter II.

1.2.2 Mayerhofer model

Besides the Nolte G-function, the Mayerhofer method (Mayerhofer and Economides 1993, 1997; Mayerhofer et al. 1995) is another commonly used FCT analysis model. In this model, leakoff is decoupled into two major categories. One is fluid leaking though the fracture face, which is treated as the flow skin, and the other is linear flow of filtrate into formation. The total pressure drop should be the sum of pressure loss in these two parts.

$$\Delta p(t_j) = \Delta p_r(t_j) + \Delta p_{face}(t_j) \tag{1.31}$$

where, $\Delta p_{face}(t_j)$ and $\Delta p_r(t_j)$ are pressure drop at any time point through filter cake and in the reservoir, respectively.

The pressure drop in the reservoir can be computed with Eq. (1.32)

$$\Delta p_r = \left(a_p q\mu/kh\right)\sqrt{a_t \pi t/\mu\phi c_t x_f^2} \tag{1.32}$$

where, a_p and a_t are constants, and $a_p = 141.2$, $a_t = 0.000264$ in oilfield units; q is the flow rate; μ is the fluid viscosity; k, ϕ and h are formation permeability, porosity and height; c_t is the total compressibility; x_f is the fracture half-length.

The varying fracture-face skin factor is,

$$s = [\pi k R_0 R_D(t)]/2x_f \tag{1.33}$$

where,

$$R_D(t) = \frac{R_s}{R_0} = \sqrt{\frac{t_n}{t_m}} \tag{1.34}$$

and t_m is total pumping time, and t_n is the total time from the start of pumping.

With all formulations above from Eq. (1.31) to (1.34), the pressure gradient during pumping ($R_D(t) = 1$) can be derived as,

$$\Delta p(t_m) = 4a_p \sqrt{\frac{a_t \pi t}{\mu \phi c_t}} \left[\sum_{j=1}^{m} \left(\frac{q_{Ij}}{A_{p,j}} - \frac{q_{Ij-1}}{A_{p,j-1}} \right) \sqrt{t_n - t_{j-1}} \right] + \left(2a_p \mu_f \pi R_0 / A_{p,m}\right) R_{D,m} q_{Im} \tag{1.35}$$

where, q_{Ij} is the leakoff rate at any time point during pumping; A_p is the permeable fracture area.

By subtracting the pressure loss during pumping from the total pressure change, the pressure drop during fracture closing can be written as,

$$\Delta p(t_n) = [p_i - p(t_n)] - [p_i - p(t_m)]$$

$$= 4a_p\sqrt{\frac{a_t\pi t}{\mu\phi c_t}}\left[\sum_{j=1}^{m}\left(\frac{q_{Ij}}{A_{p,j}} - \frac{q_{Ij-1}}{A_{p,j-1}}\right)\sqrt{t_n - t_{j-1}}\right]$$

$$+\left[\sum_{j=m}^{n}\left(\frac{q_{Fj}}{A_{p,j}} - \frac{q_{Fj-1}}{A_{p,j-1}}\right)\sqrt{t_n - t_{j-1}}\right] \quad (1.36)$$

$$-\left[\sum_{j=1}^{m}\left(\frac{q_{Ij}}{A_{p,j}} - \frac{q_{Ij-1}}{A_{p,j-1}}\right)\sqrt{t_m - t_{j-1}}\right]$$

$$+\left(2a_p\mu_f\pi R_0/A_{p,m}\right)\left(R_{D,n}q_{Fm} - R_{D,m}q_{Im}\right)$$

where, q_{Fj} is the leakoff rate during closing, and given as,

$$q_{Fj} = -c_f A_f \frac{d\Delta p(t_j)}{d\Delta t_j} \quad (1.37)$$

Assumption of an initial value of fracture area (A_f), fracture face resistant (R_0) and reservoir permeability (k) is required for iterative computation. According to Mayerhofer, Eq. (1.36) not only satisfies the physics of filtration and linear elastic mechanics, but also preserves the material balance function. A modified Mayerhofer model is proposed by Valko and Economides (Valko and Economides 1997), in which the initial assumption of these factors is not required, and the complicated derivation will not be represented in this context.

Usually in conventional reservoir treated with crosslinked fluid, a significant pressure drop could occur when the fluid leaks though the filter cake due to its ultra-low permeability. As anticipated, the effect of fracture surface resistance will be much reduced for fracturing in a tight formation (Mayerhofer et al. 1995).

1.2.3 Hagoort model

(Hagoort 1981) assumed the pressure transient was a result of the superposition of two pressure transients: one associated with the imaginary continuing injection, and the other with the imaginary production starting from the end of injection. Furthermore, the model focused on the early-time pressure decline immediately after shut-in, when Hagoort believed that the production transient is the dominant factor in comparison with the injection transient. Therefore, the problem is reduced to solve the pressure response of a linear flow from a formation with an initial pressure at ISIP, into a hydraulic fracture with infinite conductivity, and producing at a constant rate (injection rate).

Besides, fracture storage effect was included in the model by material balance function and linear elastic theory. This solution therefore can be designated as the model for leakoff dominated by formation flow. (Koning and Niko 1985) and (Barree et al. 2009) used the Hagoort solution in their work and rewrote it as Eq.(1.38). It is clear that the first term in the right of Eq.(1.38) is exactly same with traditional linear flow from formation into an infinite-conductivity hydraulic fracture; the second term is associated with the fracture storage effect.

$$p_{wD} = \sqrt{\pi \Delta t_D} - C_{fbcD} \left(\frac{\pi}{2}\right)^2 \left(1 - e^{\varepsilon^2 \Delta t_D} \operatorname{erfc}\left(\varepsilon \sqrt{\Delta t_D}\right)\right) \tag{1.38}$$

where,

$$p_{wD}(\Delta t_D) = \frac{kh}{141.2qB\mu} \left[p_w(t_p) - p_w(t_p + \Delta t)\right] \tag{1.39}$$

$$\Delta t_D = \frac{0.0002637k\ \Delta t}{\phi \mu c_t {x_f}^2} \tag{1.40}$$

$$\varepsilon = \frac{2}{\pi C_{fbcD}} \tag{1.41}$$

$$C_{fbcD} = \frac{5.615\ C_{fbc}}{2\pi\phi c_t h {x_f}^2} = \frac{0.8936 C_{fbc}}{\phi c_t h {x_f}^2} \tag{1.42}$$

Here, C_{fbc} is the before closure fracture storage constant, and it is defined as,

$$C_{fbc} = 0.3562\ c_f A_f \tag{1.43}$$

The above pressure solution described in Eq. (1.38) will result in a straight line on a graph of $p_w(t_p + \Delta t)$ versus $\sqrt{\Delta t}$ for formation linear flow before closure, as shown in Figure 1-5. Different with G-function plot, the closure events in the square root plot should be picked at the inflection point on the pressure vs. sqrt(t) curve. Suggested by Barree(Barree et al. 2009), the inflection point should be the point with maximum amplitude of first derivative. This method is therefore used as an alternative way to determine fracture closure event.

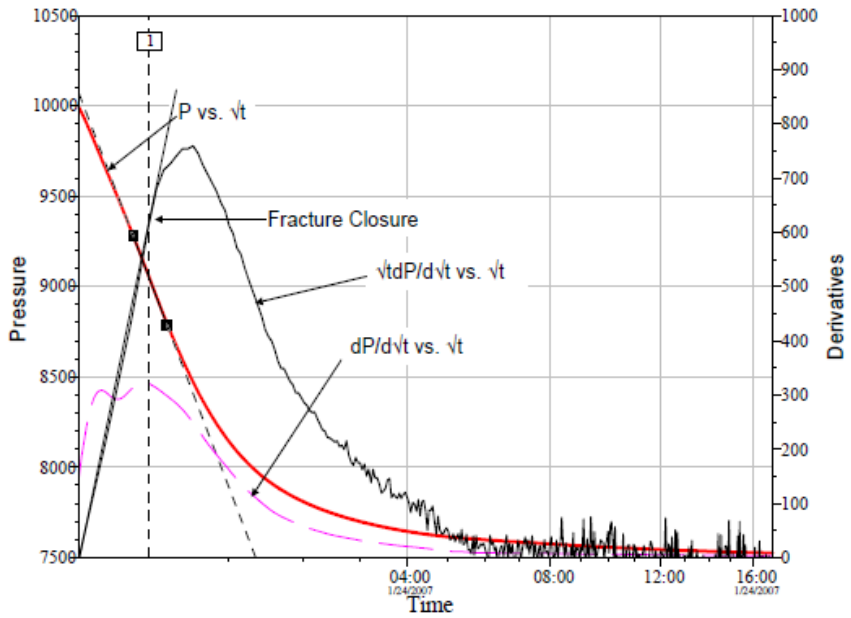

Figure 1-5. Normal leakoff indicated by Hagoort square root time method (Barree et al. 2009)

From its derivation, we can find that Hagoort model can only be used for the analysis in a very short period immediately after shut-in. The duration of the time is dependent on the injection time. In other words, the validity of the model could last long for the injection in a long time. If the injection time is short, and it takes a much longer time to close, which happens very often for FCT in tight formation, the linear flow system cannot be reduced to a producing well with a constant rate from a formation with an initial reservoir pressure at ISIP. This is the major reason why long-lasting ½-slope in log-log plot, which is sometimes interpreted as fracture linear flow, is rarely observed during closing in practice.

1.3 Abnormal leakoff

Although all above models are based on ideal/normal leakoff situation, (Craig et al. 2000; Craig et al. 2000) observed only a few instances of normal leakoff in low permeability sandstones. In a statistical study over a large database, they found that normal leakoff behavior was observed in only 8.9% of the FCTs in Piceance Basin Mesaverde sandstones, while pressure-dependent leakoff (50.5%) is the most common leakoff behavior, followed by fracture tip extension (34.7%). (McGowen et al. 2007; Stegent et al. 2004) reported similar findings. In this section, the features of diagnostic plot for each of the abnormal leakoff behaviors will be elaborated.

1.3.1 Pressure dependent leakoff (PDL)

As suggested by many researchers (Barree 1998; Fan and Chen 1997; Gulrajani and Nolte 2000), a high leakoff rate at early time is probably caused by the creation of new fracture surfaces. Referring to Carter leakoff model (Carter 1957) in Eq. (1.1), the initial leakoff rate at this new surface is much higher because the rate is inversely proportional to the square root of contacting time with the fluid. There two most likely scenarios accounting for the new created surface: natural fissures related pressure dependent leakoff (PDL) and tip extension. In tight fissured formation, where natural fractures can be connected during fracturing, pressure dependent leakoff behavior in FCTs is commonly observed (Craig et al. 2000; Warpinski 1985).

As shown in the top-right plot in Figure 1-3, when PDL occurs, the diagnostic plot by Gdp/dG is a concave down curve. The finish of the downward derivation from linearity, or the start point of straight line through the origin, is believed to be the closure event of these reopened natural fractures. The bottomhole pressure at this time point therefore can be picked as their opening/closure pressure. After that, leakoff from the main fracture into matrix is the dominant factor for the pressure response (Barree et al. 2009). On the log-log diagnostic Bourdet derivative, it seems that the PDL behavior has a smaller apparent slope compared with the typical 3/2-slope in normal leakoff, as shown in Figure 1-6.

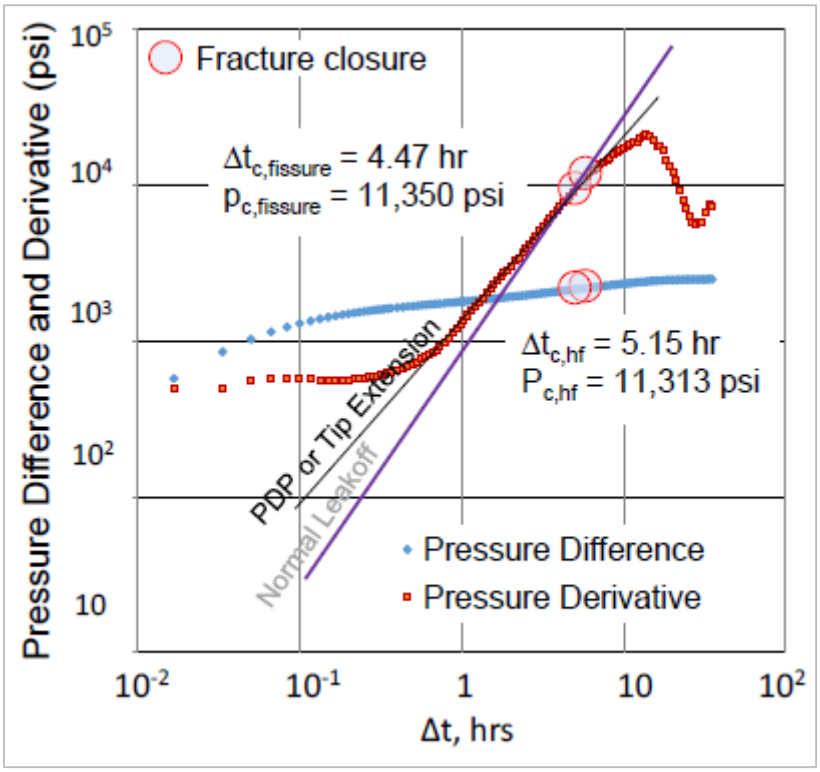

Figure 1-6 PDL behavior on the log-log diagnostic Bourdet derivative (Xue and Ehlig-Economides 2013)

There are several models have been proposed to simulate PDL behavior in last couple decades. (Walsh 1981) provides a model to calculate fracture permeability under variable confining pressure.

$$k = k_0 \left[J \ln\left(\frac{\sigma^*}{\sigma - p}\right)\right]^3 \quad (1.44)$$

where, k_0 is reservoir permeability under in-situ conditions; σ is normal stress on the fissure; σ^* is the reference stress state; and J is a constant. Both $\sigma^*$and J are required to be determined from field data.

For each leakoff mechanisms introduced by (Howard and Fast 1957), (Castillo 1987) conclude a model to account for PDL with different coefficients.

Warpinski (Warpinski 1985) adding net pressure into Walsh model.

$$v = \sqrt{\frac{k_o \phi C^3}{2\mu t g}} \Bigg((\sigma - p_i) \Bigg\{ \left[\ln \frac{\sigma^*}{\sigma - p_i} \right]^3 + 3 \left[\ln \frac{\sigma^*}{\sigma - p_i} \right]^2 + 6 \left[\ln \frac{\sigma^*}{\sigma - p_i} \right] + 6 \Bigg\} - (\sigma - p_0) \Bigg\{ \left[\ln \frac{\sigma^*}{\sigma - p_i} \right]^3 + 3 \left[\ln \frac{\sigma^*}{\sigma - p_0} \right]^2 + 6 \left[\ln \frac{\sigma^*}{\sigma - p_0} \right] + 6 \Bigg\} \Bigg)^{1/2} \quad (1.45)$$

where, p_i and p_0 are initial reservoir pressure and treatment pressure, respectively.

According to Meyer and Jacot (Meyer and Jacot 2000), there are two most commonly used models for natural fracture related pressure dependent leakoff. For the first one, the created fracture has two different but constant leakoff coefficients, as expressed in Eq. (1.46). When fracture pressure is above the closure pressure of natural fissures (p_{fo}), the fracture system has a larger leakoff coefficient, C_{L1}; while, when fracture pressure is below p_{fo}, $p_w < p_{fo}$, it has a smaller value, C_{L2}. For the second model represented in Eq. (1.47), fracture has a variable leakoff coefficient when fracture pressure is above p_{fo}; and a constant leakoff coefficient after the closure of natural fractures, same with previous model.

$$C_L(p_w) = \begin{cases} C_{L1} & p_w \geq p_{fo} \\ C_{L2} & p_w < p_{fo} \end{cases} \tag{1.46}$$

From the definition, it can be figured out that typically $C_{L1} > C_{L2}$.

$$C_L(p_w) = \begin{cases} C_{L1} \exp\left(-\beta \dfrac{p_{ws} - p_w}{p_{ws} - p_{fo}}\right) & p_w \geq p_{fo} \\ C_{L2} & p_w < p_{fo} \end{cases} \tag{1.47}$$

where,

$$C_{L1} = C_L(p_w = p_{ws}) \tag{1.48}$$

$$C_{L2} = C_L(p_w < p_{fo}) \tag{1.49}$$

$$\beta = \ln\left(\frac{C_{L1}}{C_{L2}}\right) \tag{1.50}$$

From above equation we can figure out that the decline manner of the leakoff coefficient is fixed for a certain case when C_{L1}, C_{L2}, p_{ws} and p_{fo} are constant. Another model proposed by Barree (Barree 1998; Barree and Mukherjee 1996) has a similar form with Eq. (1.47), but has a free variable (C_{dp}) which controls the decline manner of the leakoff coefficient, as expressed in Eq. (1.51).

$$C_L(p_w) = \begin{cases} C_{L1} \exp\left[C_{dp}\left(p_w - p_{fo}\right)\right] & p_w \geq p_{fo} \\ C_{L2} & p_w < p_{fo} \end{cases} \tag{1.51}$$

The difference between fissure opening pressure and main fracture closure pressure, $p_{fo} - p_c$, could have a significant impact on the production. According to Mullen and Enderlin (Mullen and Enderlin 2010), if the difference is relatively large, flow capacity of these fissures will be deprived by the overwhelming confining pressure. Fissures therefore might have little contribution to the production. If the difference is

small, these “closed natural fissures” could be more permeable than the formation matrix (Branagan et al. 1996), and they could be the major contributor to the production.

For the formation where natural fissure related PDL happens, proppant screenout could be a potential problem during following main stimulation (Rollins and Hyden 1998). To avoid premature screenout, pad with larger volume is usually required.

1.3.2 Tip extension

Tip-extension phenomenon means that fracture continue propagating even after the shut-in, which conflicts with the pre-assumption of Nolte G-function model. Generally, tip-extension is typically caused by the ultra-low permeability or leakoff rate in tight formations (Barree et al. 2009; Craig et al. 2000). Furthermore, formations where tip extension happen usually have a poor production and limited economic potential (Craig et al. 2000; Rollins and Hyden 1998).

The typical feature of tip-extension on Gdp/dG is shown in the bottom-left plot in Figure 1-3. There is a straight line before closure. The line is not through the origin, but has a positive intercept with the composite derivative axis (Barree and Mukherjee 1996).

Currently, there is no model to simulate the tip-extension phenomenon.

1.3.3 Transverse storage and height recession

Transverse storage and height recession are two distinct concepts, but are believed to have similar pressure response when they happen. Transverse storage is

associated with a secondary fracture system. If the natural fracture system is connected during treatment, it can take and store an amount of fluid from the main fracture. Since the natural fissure usually suffer a higher confining pressure than the main fracture, part of the stored fluid in natural fissures could be squeezed back into the main fracture, which will resupply the main fracture and reduce the pressure decline rete in the whole fracture system.

One should note that the natural fracture system is involved in both pressure dependent leakoff (PDL) and transverse storage. That which of them could be the dominant factor is determined by the leakoff rate from the natural fissures and the decline rate of natural fracture width. If the former is much larger, enhanced leakoff rate, or PDL behavior can be expected; while if the leakoff rate from natural fissures is small, and they close in a rapid manner, transverse storage effect can be observed.

As to height recession, it usually happens when the fracture extends out of the target zone into overlying or underlying layers, where leakoff rate is relatively small and local formation stress is higher than that in target zone. Similar to natural fracture related transverse storage, fluid in the fracture beyond the target zone leaks into formation at a slower rate than the decline rate of fracture width at this section. Part of fluid in this section thus will be expelled back into the fracture in target layer, and height recession occurs.

As shown in the bottom-left plot in Figure 1-3, transverse storage or height recession typically has a “belly” below the linearity through the origin on Gdp/dG curve (Barree 1998; Barree et al. 2009; Barree and Mukherjee 1996). In many cases, after the

end of transverse storage/height recession, normal leakoff behavior, which is characteristic by constant fracture surface area and constant leakoff coefficient dominated by matrix, will occur (Barree et al. 2009). On the log-log diagnostic Bourdet derivative, transverse storage/height recession seems to have a steeper slope compared with the typical 3/2-slope in normal leakoff, or a belly-shape curve under the 3/2-slope line, as shown in Figure 1-7.

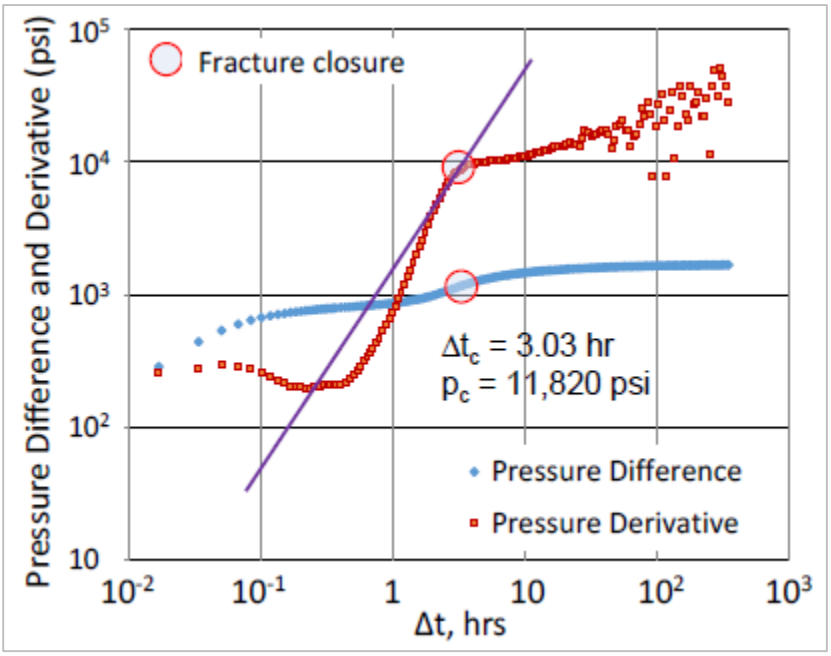

Figure 1-7 Transverse storage/height recession on the log-log diagnostic Bourdet derivative (Xue and Ehlig-Economides 2013)

Currently, no model has been proposed to illustrate transverse storage/height recession behavior for the FCT analysis.

1.3.4 Multiple apparent closures

According to Barree (Barree 1998), multiply apparent closures are frequently observed from field data. One field example has been discussed by Xue and Ehlig-Economides (Xue and Ehlig-Economides 2013), as shown in Figure 1-8. We can find that several straight lines through the origin can be drawn on Gdp/dG curve, and correspondingly, several 3/2-slope lines on the log-log Bourdet derivative plot.

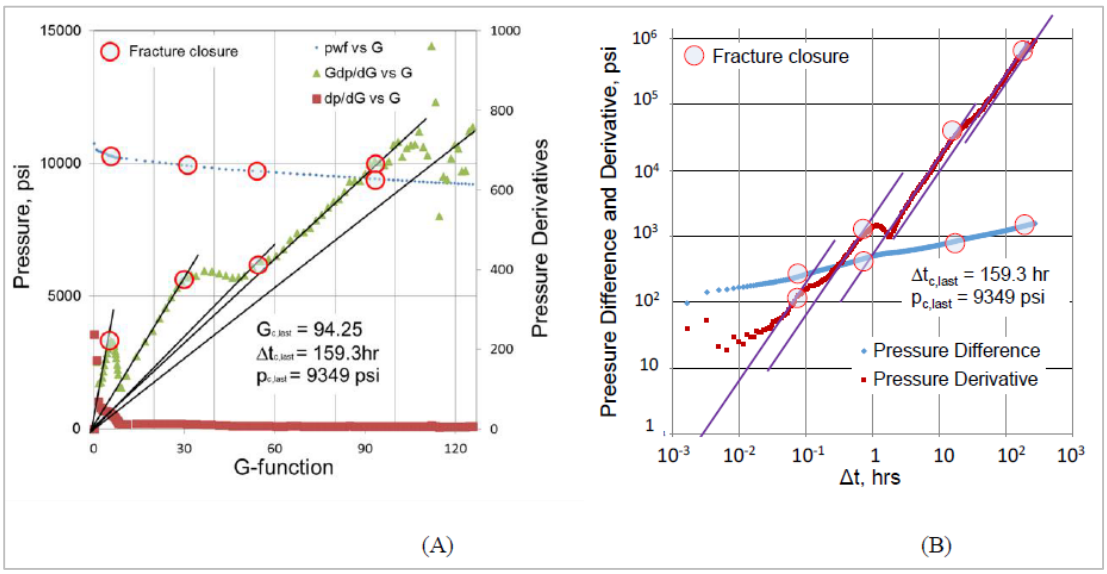

Figure 1-8 Multiple-closure behavior on both Gdp/dG and the log-log diagnostic Bourdet derivative (Xue and Ehlig-Economides 2013)

1.3.5 Multiple leakoff mechanisms

In some cases, more than one above leakoff mechanisms happen at same or different time at FCTs, as shown in Figure 1-9 (Mullen and Enderlin 2010). Both PDL (or tip extension) and transverse storage feature are observed in the same diagnostic curve.

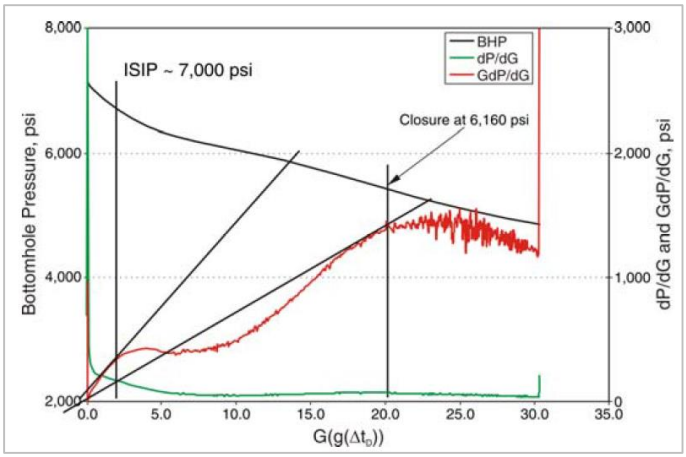

Figure 1-9 Both PDL and transverse storage behavior exist in one FCT (Mullen and Enderlin 2010)

1.4 Problem definition and objectives

From the previous discussion, it is apparent that existing models for commonly observed abnormal leakoff behaviors are only qualitative and do not provide quantitative parameters. The major objective of this research is to build a model to simulate these abnormal leakoff behaviors and the physics behind them to quantify all factors that govern these behaviors. The following commonly observed flow regimes and non-ideal leakoff behavior will be covered: wellbore storage, early fracture linear flow, pressure-dependent leakoff (PDL), transverse storage, tip-extension and multiple-closure behavior. Finally, we will try to build a comprehensive model that could simulate all these listed normal and abnormal leakoff mechanisms.

1.5 Research summary

Chapter I starts from the introduction of fracture calibration test (FCT), and then several most commonly used before-closure models and diagnostic methods are discussed. For those often observed abnormal leakoff behavior, their potential physics and diagnostic curve feature are provided. The major research problem is defined and the objective specified.

In Chapter II, several commonly observed flow regimes and abnormal leakoff behaviors are modeled, including wellbore storage effect, early linear flow, tip extension, pressure dependent-leakoff (PDL), multiple-closure behavior, and transverse storage effect. Pressure solutions for those flow regimes and leakoff mechanisms are

derived, and more parameters are able to be quantified, including natural fracture leakoff coefficient and its possible extension.

Several field examples from Horn River Shale are interpreted in Chapter III. Compared with traditional diagnostic model, the new derived PDL model and the decoupled fracture model are able to explore more information of natural fracture system if they are opened during treatment. Mostly, the interpretation result provides a good explanation of the production performance.

In Chapter IV, several primary conclusions from this research are listed.

CHAPTER II

ABNORMAL LEAKOFF BEHAVIOR MODELLING

Chapter I illustrates three major existing before-closure models: Nolte G-function model, Mayerhofer and Hagoort model. All these model are based on ideal leakoff condition and they are so oversimplified that none of them are able to quantify any abnormal leakoff mechanisms, whose potential physics and representation in diagnostic plots are presented previously. A series of new model will be developed in this chapter pertinent to these abnormal leakoff behaviors.

Based on traditional Nolte G-function, which is to calculate leakoff fluid volume during and after injection, pressure solution is derived in this chapter for each specific abnormal leakoff mechanism by considering their unique leakoff physics. All the following flow regimes and leakoff behavior will be modeled: wellbore storage effect, early linear flow, tip extension, pressure dependent-leakoff (PDL), multiple-closure behavior, and transverse storage effect.

2.1 Wellbore storage effect (WBS)

WBS is usually the first behavior we expect to see in traditional build-up and drawdown tests in conventional reservoir. Due to the compressibility, fluid stored in wellbore will expand when pressure is reduced, or shrink when pressure is building up. Because of huge difference in compressibility, wells producing or injected with gas typically has a much longer and more dominant WBS effect than those with liquid.

As to FCT, water-based fracturing fluids are the major treatment fluid used in the field. Among them, fresh water, with or without friction reducer, is the most widely used fluid in unconventional reservoir, like gas-shale, tight sand, etc. Since water is slightly compressible, the stored fluid in the wellbore will keep expanding after shut-in with the declining pressure. Because wellbore string volume is supposed to be constant, the expansion of water in it will force the incremental volume into the fracture, which is sometimes called "after-flow" effect (McClure et al. 2014; Nguyen and Cramer 2013). Theoretically, the fluid expansion, or "after-flow" phenomenon, will not stop until the bottomhole pressure drops to a constant value. In other words, WBS effect always exists during the whole pressure falloff after shut-in. However, except for that in the very early time immediately after shut-in, the pressure drop rate is so slow that WBS effect is usually negligible. Therefore, WBS is traditionally believed to happen only at very early time after shut-in, which is reasonable. To find its potential mechanisms, the early WBS will be elaborated in this section, and the long-lasting WBS behavior will be discussed together with tip-extension behavior in **Section 2.3.2**.

As well-known in well testing community, when WBS occurs, there will a unit-slope in both log-log Bourdet derivative and pressure difference curve. Mathematically, the pressure solution can be written as,

$$C = \frac{q_p B}{24 \frac{\Delta p}{\Delta t}} \tag{2.1}$$

where, C is the WBS coefficient, bbl/psi; q_p is the pumping rate in the unit of bbl/day, not bbl/minute. Δp is the pressure difference after shut-in, psi; Δt is the elapsed time after shut-in in hour.

From above equation, we can find that the pressure solution is very simple and no formation or fracture properties are involved. The reason is because the early WBS occurs in a very short time immediately after shut-in, before fracture or formation flow become the dominant flow mechanism. Another important point with WBS is that the pressure decline rate is almost constant in a relatively high level during this time, as indicated in Eq. (2.1). Now, the question will be what happens behind the fast decline pressure at early beginning of falloff?

If the pressure is recorded in the surface, the wellhead treating pressure (WHTP) can be expressed as (Mack and Warpinski 2000),

$$WHTP = p_c + p_{net} + \left(\Delta P_{pipe\ friction} + \Delta P_{near\ wellbore\ friction}\right) - p_{hyd} \quad (2.2)$$

where, p_c is the closure pressure and assumed to be constant, psi; $\Delta P_{pipe\ friction}$ is the pressure loss in wellbore due to friction; p_{hyd} is the hydrostatic pressure of the fluid in the string; $\Delta P_{near\ wellbore}$ is the pressure loss near wellbore, and it consists of friction components through perforation, fracture tortuosity and perforation misalignment friction.

Since p_{hyd} and p_c are constant in the left side of Eq. (2.2), the decline of recorded pressure, WHTP, could be caused by the decline of one or all of these three terms: p_{net}, $\Delta P_{pipe\ friction}$ and $\Delta P_{near\ wellbore}$. In other words, that whether early WBS effect is strong or weak, and the duration of WBS, is mainly dependent on the falloff rate

of net pressure (p_{net}), and the dissipation of friction along the wellbore string and at near-wellbore area ($\Delta P_{pipe\ friction} + \Delta P_{near\ wellbore}$). Therefore, we can conclude that early WBS behavior would be strong at following scenarios.

1) Rapid decline of net pressure at early time immediately after shut-in. It could happen when the treated formation has a high leakoff rate, or some other permeable sub-layers are connected by natural fissures, or fracture continue growing after shut-in, which is also called tip-extension and will be elaborated later.
2) Large amount of pressure loss associated with friction in the wellbore and near-wellbore area. This part of pressure loss could be a result of many factors: injection rate, perforation number and diameter, fracture trajectory near the wellbore, the connection between perforation and created fracture. Unfortunately, it is almost impossible to calculate all of them out. Besides, this part of pressure loss will dissipate rapidly after shut-in, which is another important source of rapid pressure drop at early time after shut-in. Therefore, strong WBS behavior might be a sign of large pressure loss due to the friction in the wellbore string or at the near-wellbore vicinity.

In summary, early WBS effect happens only when there is a big net pressure drop or a large amount of pressure dissipation associated with friction in the wellbore and near-wellbore area. The rapid net pressure decline could be caused by high leakoff rate, including pressure dependent leakoff (PDL), and tip-extension.

2.2 Fracture linear flow

As occasionally observed in practice, there is an early ½-slope (before 3/2-slope) at the Bourdet derivative curve on log-log plot, as shown in Figure 1-4. Since ½-slope usually indicates linear flow in traditional pressure transient analysis, the early time ½-slope might be the pressure response of fracture linear flow. As noted in the previous section, to see the ½ slope behavior without any evidence of wellbore storage highlights an important difference between the FCT response and standard pressure buildup behavior for a hydraulically fractured well. The following reasons may account for this flow regime:

1) relatively high leakoff rate at tip area;
2) existence of "dry tips" or tip extension after shut-in;

In this section, all these factors will be illustrated in detail to explain the apparent fracture linear flow.

2.2.1 High leakoff rate at tip area

According to classic Carter leakoff model, fluid leakoff rate is inversely proportional with square root of contacting time, as illustrated in Eq. (1.1). It is clear that the new created fracture surface has a higher leakoff rate than in those sections where leakoff has started earlier. In other words, leakoff rate in the fracture tip area is much faster than that behind this section. Therefore, fluid tends to flow from wellbore or fracture near wellbore to the tip to supply the higher leakoff rate in this area. This factor therefore could be one of the reasons for fracture linear flow.

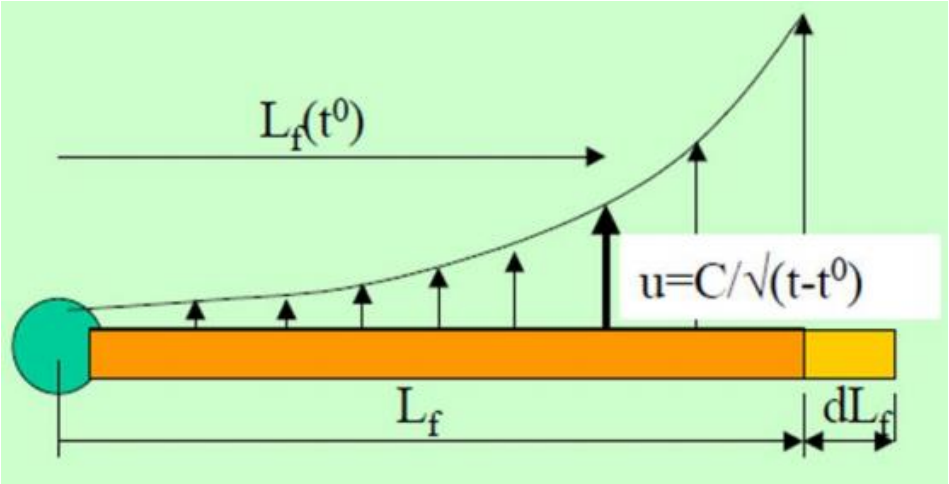

Figure 2-1 Representation of Carter leakoff model (Bachman et al. 2012)

2.2.2 Dry fracture tips and tip extension

As observed directly or indirectly by many researchers (Barree et al. 2013; Medlin and Masse 1984; Warpinski 1985; Yew and Liu 1993), there is a process zone in the tip area during fracture propagation. Two parts are included in this zone: the fluid lag region or dry fracture surface behind the tip, and a damage zone beyond it, as shown in Figure 2-2. Fluid pressure in the fluid lag region is less than closure pressure (i.e. minimum horizontal stress), and may even less than the pore pressure for some very tight formations. In other words, the net pressure in this area is negative.

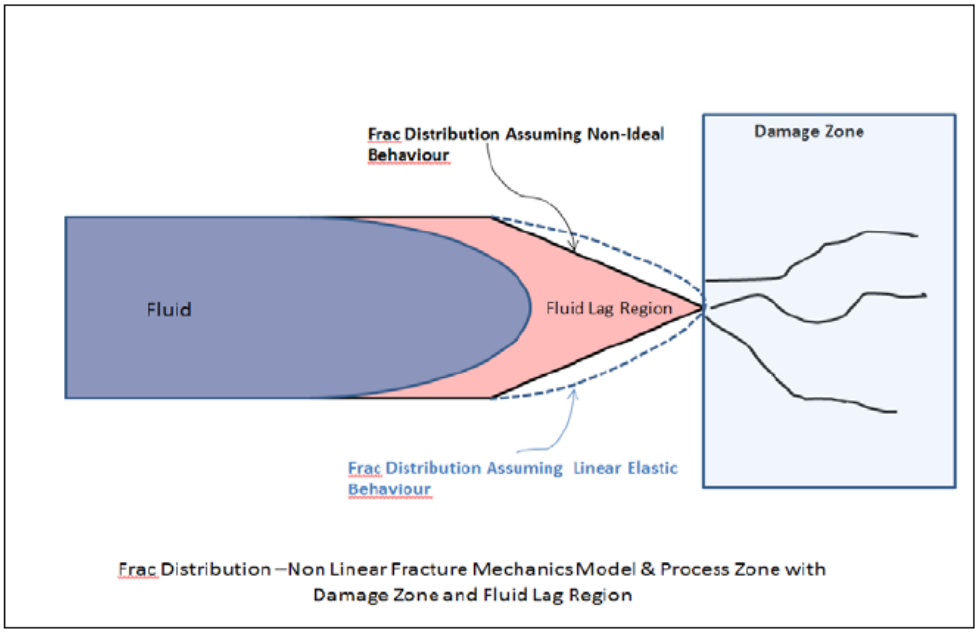

Figure 2-2. Description of process zone and the fluid lag zone (Barree et al. 2013)

According to Barree (Barree et al. 2013), the formation of the fluid lag zone is probably caused by the fact that fluid leakoff rate through the new created fracture is even higher than the rate that fluid can be delivered along the fracture. While, this explanation is probably unacceptable because hydraulic fracture is thought to have a much higher conductivity or flow capacity than formation matrix, not to mention in the tight formation like the gas-/oil-shale. Actually, the evidence of the fluid lag zone can be found from the linear elastic fracturing model (LEFM). The most commonly used mechanics model with LEFM in hydraulic fracturing community is derived by (Sneddon 1946; Sneddon 1951; Sneddon and Elliott 1946). In the Sneddon model, following assumptions on the crack property and boundary conditions are made.

1) The crack is in ellipse shape;

2) The crack is very thin $(-c \le y \le c, x = 0)$ in the interior of an infinite elastic solid, as shown in Figure 2-3;

3) The boundary conditions at $x = 0$ are as follows.

   a. There is no shear stress along $y - axis$: $\tau_{xy} = 0,$ for all values of y.

   b. The Griffith crack is opened under the uniform internal pressure: $\sigma_x = -p_0, |y| \le c$.

   c. The strain along $y - axis$ beyond crack tips is 0: $u_x = 0, |y| \ge c$.

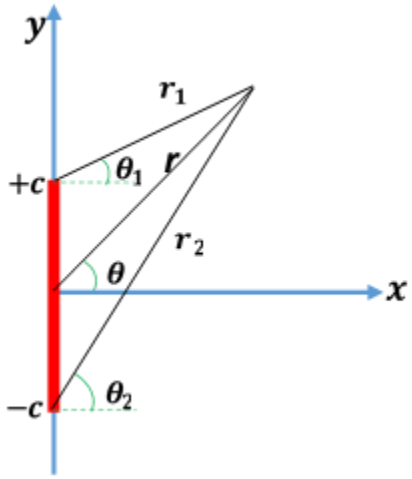

Figure 2-3 Coordinate of fracture in Sneddon model

The derived pressure solution is,

$$\frac{1}{2}(\sigma_y - \sigma_x) = p_0 \frac{r}{c}\left(\frac{c^2}{r_1 r_2}\right)^{3/2} \cos\theta \cos\left[\frac{3}{2}(\theta_1 + \theta_2)\right] \tag{2.3}$$

$$\frac{1}{2}(\sigma_y + \sigma_x) = p_0 \left[\frac{r}{\sqrt{r_1 r_2}} \cos\left(\theta - \frac{1}{2}\theta_1 - \frac{1}{2}\theta_2\right) - 1\right] \tag{2.4}$$

$$\tau_{xy} = -p_0 \frac{r}{c}\left(\frac{c^2}{r_1 r_2}\right)^{3/2} \cos\theta \ \sin\left[\frac{3}{2}(\theta_1 + \theta_2)\right] \tag{2.5}$$

With above equations, stress change at any point around the crack can be calculated, and one simulation result is shown in Figure 2-4 and Figure 2-5. Figure 2-4 describe the stress change of σ_x and σ_y, respectively. Figure 2-5 exhibit the final stress status after the creation the crack. In this example, the fracture is lying at $y - axis$ between $-500\text{ft} \leq y \leq 500\text{ft}$. The negative value in these plots indicates that the local stress is at the reverse direction of the positive according to the sign convention. All those 4 plots show that stress field is changed dramatically around the created crack, especially at the small vicinity beyond tips. Unlike the compressive stress at the side of crack, stress around the tip is the tensile stress, and the magnitude of the tensile stress is so overwhelming that the crack cannot be arrested from continuing propagating. In other words, because of the tensile stress singularity beyond the tip, stress distribution from the Sneddon model is not stable.

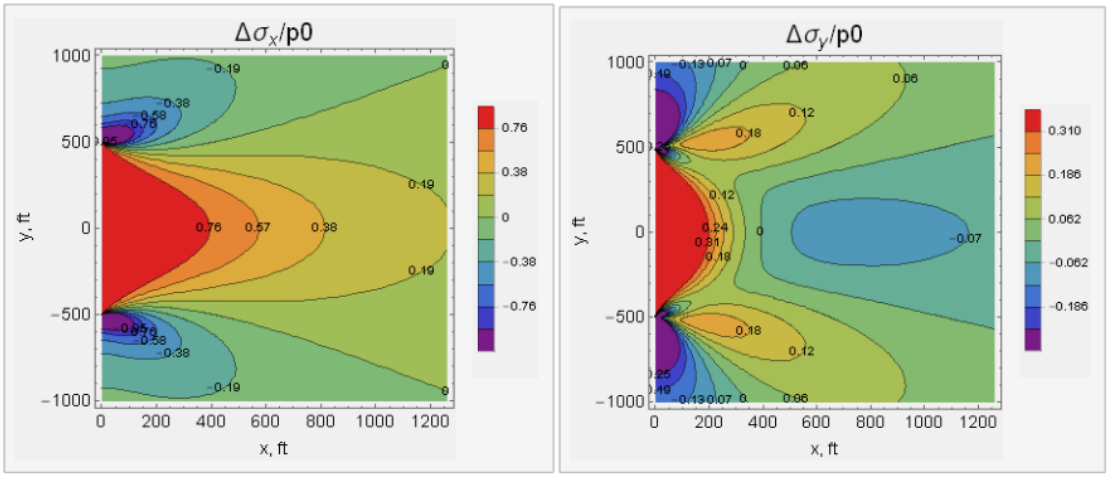

Figure 2-4 σ_x and σ_y change around the created crack

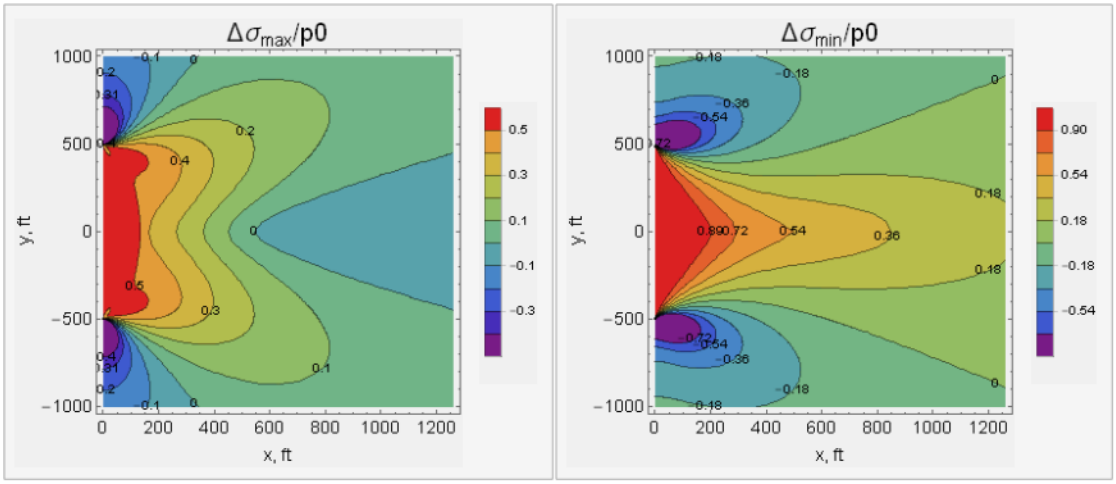

Figure 2-5 Local σ_{max}, σ_{min} change around the created crack

Two major issues in the assumption are believed to be responsible for this unpractical stress singularity beyond the tip. One is that the internal pressure is uniform, which in hydraulic fracturing is probably not the fact. The friction related pressure gradient is thought to be much more than estimated from viscous theory (Warpinski 1985). Unfortunately, there is currently no analytical model of the stress field for

variable internal pressure. Another factor accounting for the stress singularity is the assumption that the strain beyond the tip is zero, which is challenged because of the fluid lag zone or dry-tip. (Sneddon 1951) developed a distict model for the case in which restriction on the strain is released from the boundary condition. Its pressure solution is derived as shown in Eq.(2.6) - (2.8).

$$\sigma_x = -\frac{p_0}{2\pi}[2(\theta_1 - \theta_2) - \sin(2\theta_1) + \sin(2\theta_2)] \tag{2.6}$$

$$\sigma_y = -\frac{p_0}{2\pi}[2(\theta_1 - \theta_2) + \sin(2\theta_1) - \sin(2\theta_2)] \tag{2.7}$$

$$\tau_{xy} = \frac{p_0}{2\pi}[\cos(2\theta_2) - \cos(2\theta_1)] \tag{2.8}$$

The simulation result for this model is exhibited in Figure 2-6. From these two plots we can figure out that the stress singularity disappears in this model. One should note that, the internal pressure between two "hydraulic tips" ($-500\text{ft} \leq y \leq 500\text{ft}$), are still uniform, but the real fracture tips, defined as zero strain, are beyond these hydraulic tips. As the only difference between these two models is the restriction on tip strain, we can conclude that the stress singularity can be removed if the crack is allowed to continue propagating freely. The second model therefore seems to be more practical than the first one.

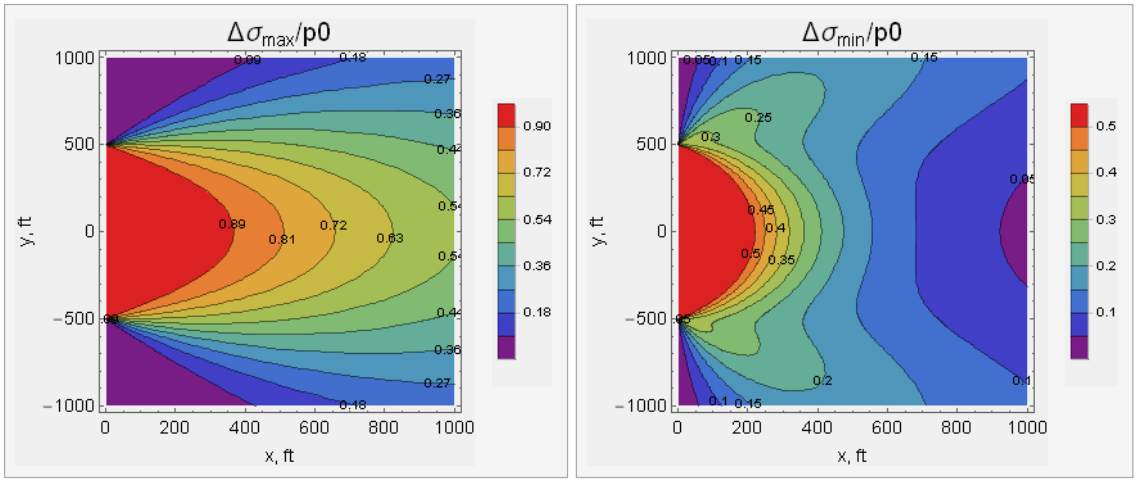

Figure 2-6 Local σ_{max} and σ_{min} change around the created crack without strain restriction in tips

Back to the discussion about the fluid lag zone as shown in Figure 2-2, the existence of a process zone can eliminate the stress singularity in the tip, as described in the second model. Since the fluid pressure close to the tip is much lower than that close to the wellbore during injection, fluid will continue flow into the tip area after shut-in. Fracture linear flow will happen when the fluid flows from the wellbore or near wellbore fracture area to the tip. And, if the fluid pressure is still relatively high as fluid reaches the tip, the tip can continue growing for some distance into the damage zone or even further, which is observed as the tip extension after shut-in. The existence of the fluid lag zone and the tip-extension are consistent with fracture linear flow after shut-in.

In summary, several evidences show that part of fluid in the wellbore and fracture near wellbore can still be delivered to the tip area even after shut-in. If the flow rate through the fracture is more than the leakoff rate into the formation through the fracture face, the pressure response might be dominated by the fracture linear flow and

tip-extension. Therefore, fracture linear flow is possible to appear early after shut-in, and it is probably the physics of ½ slope in the diagnostic plot. Actually, tip-extension could also be the possible factor for the early flow regime with a slope less than 1, which will be discussed later.

2.2.3 Model for fracture linear and fracture radial flow

Followed the conclusion that fracture linear flow might happen during FCTs, its pressure solution and duration will be introduced in this section.

(Al-Thawad and Jamiol Ahmady 2014) derived a model, which is in the integration form and in Laplace domain, on the early fracture linear flow and bilinear flow. (Pattay 1998) listed another model for fracture linear flow for vertical fracture in vertical wells, which is given as Eq. (2.9).

$$p_{wD} = \frac{2}{C_{fD}} \sqrt{\pi \eta_{fD} t_{Dx_f}} \tag{2.9}$$

where, C_{fD} is the dimensionless fracture conductivity. The definition of p_{wD}, C_{fD}, η_{fD} and t_{Dx_f} are listed as follows.

$$p_{wD} = \frac{kh\left(p_{wf} - p_i\right)}{\delta\ qB\mu} \tag{2.10}$$

$$C_{fD} = \frac{k_f w_f}{k x_f} \tag{2.11}$$

$$\eta_{fD} = \frac{k_f\ \phi\ c_t}{k\ \phi_f\ c_{ft}} \tag{2.12}$$

$$t_{Dx_f} = \frac{\delta\, k\, t}{\phi\, \mu\, c_t\, x_f^2} \tag{2.13}$$

where, x_f, k_f, w_f, ϕ_f and c_{ft} are fracture half-length, permeability, width, porosity and compressibility. δ is the unit conversion factor. Actually, in combination with Eq. (1.2), c_{ft} can be expressed with fracture compliance (c_f) if there no tip-extension,

$$c_{ft} = -\frac{1}{V_f}\frac{dV_f}{dp_{wf}} = -\frac{1}{(A_f w_f)}\frac{A_f dw_f}{dp_{wf}} = \frac{c_f}{w_f} \tag{2.14}$$

Substituting Eq. (2.14) into Eq. (2.12), we can get,

$$\eta_{fD} = \frac{k_f\, \phi\, c_t\, w_f}{k\, \phi_f\, c_f} = \frac{C_{fD}\phi\, c_t\, w_f}{c_f} \tag{2.15}$$

Eq. (2.9) confirms that ½-slope would appear in the log-log diagnostic plot if fracture linear flow happens. One should note that, linear flow indicates that fracture is in the channel shape, which is likely the case in vertical well. While, in horizontal wells designed for multiple transverse fractures, radial fracture geometry might be created in the FCT which is typically treated with a small volume of fluid. Instead of linear flow, radial flow might happen in the fracture at early time. Then, we are likely to see a flat derivative trend in the log-log diagnostic plot.

Although fracture linear or radial flow might happen, they are not frequently observed. The reason is that the duration of fracture linear or radial flow is very short, they are easily masked by the wellbore storage behavior and the following leakoff behaviors. The duration of the fracture linear flow can be estimated by Eq. (2.16) (Lee et al. 2003).

$$t_{L_fD} = \frac{0.1\, C_{rD}^2}{\eta_{fD}^2} \tag{2.16}$$

where, η_{fD} is the dimensionless hydraulic diffusivity defined same with Eq. (2.12); t_{L_fD} is the dimensionless time, same as Eq. (2.15); C_{rD} is the dimensionless fracture conductivity, and is a little different with Eq. (2.11),

$$C_{rD} = \frac{k_f w_f}{\pi k x_f} \tag{2.17}$$

In summary, fracture linear or radial flow could be proven by several factors, like high leakoff rate at tip area, the existence of fracture process zone/dry tips, and tip-extension. In the log-log derivative plot, fracture linear or radial flow will exhibit ½-slope or flat trend, respectively. Besides, this flow regime is very short-lived, and could easily be masked by early wellbore storage behavior.

2.3 Tip extension

In the last section, tip extension is explained by the existence of a fluid lag zone and the theoretical linear elastic fracturing model (LEFM). As long as the fracture continues growing, the assumption of constant fracture area during closure is violated for both modified Mayerhofer method and the Nolte G-function method. The interpretation result from these models could result in unpredictable error. In this section, three models will be developed to quantify this commonly observed abnormal leakoff behavior.

2.3.1 Tip extension without wellbore storage effect

To investigate the impact of tip extension on the pressure response, the leakoff is assumed to be same as normal leakoff except for it applies for a growing fracture. Although the pressure solution given by Eq. (1.19) from Nolte model is incorrect when tip extension occurs, the material balance function in Eq. (1.7), is still valid if there is no other deviation from the ideal leakoff model. If the treatment fluid is incompressible and no fluid enter into fracture from wellbore after shut-in, e.g. there is no wellbore storage effect, the material balance function given in Eq. (1.7) states that the reduction of fracture volume should be the same as the incremental volume of leakoff fluid from fracture into the formation. Based on these assumptions, the pressure transient function for a fracture with tip extension can be derived.

Starting from the material balance function used in Nolte G-function model, we first assume that the fracture continues propagating at the same rate after shut-in as that during pumping, or the area exponent, α, is a constant before and after shut-in. During an elapsed time Δt_{te} after shut-in at t_p, the fracture surface area grows from A_{fo} to A_{f1}. According to Nolte (Nolte et al. 1993), there is a power law relationship between fracture area and the elapsed time, as shown in Eq.(2.18).

$$\frac{A_f}{A_{fo}} = \left(\frac{t}{t_p}\right)^{\alpha} \tag{2.18}$$

where, A_f is the fracture area at any time t during its propagation; A_{fo} is the fracture surface area at end of pumping. Therefore, the final fracture surface area after tip-extension can be calculated as,

$$A_{f1} = A_{fo}\left(\frac{t_{p1}}{t_p}\right)^{\alpha} \tag{2.19}$$

where,

$$t_{p1} = t_p + \Delta t_{te} \tag{2.20}$$

Since the fracture propagates in the same way during tip-extension period after shut-in with that before, the cumulative leakoff volume at any time during tip-extension$\left(t_p \le t \le t_{p1}\right)$ can be calculated with Eq. (1.10), but the pumping time t_p should be replaced with the elapsed time t. The leakoff volume during tip extension thus can be written as,

$$V_{l,p} = 2\, r_p C_L \sqrt{t} A_f g(0,\alpha) \qquad t_p \le t \le t_{p1} \tag{2.21}$$

Substitute A_f with Eq. (2.18) and (2.19), the cumulative leakoff volume function during fracture extension before and after shut-in can be written as,

$$V_{l,p} = 2\, r_p C_L A_{f1} {t_{p1}}^{-\alpha} g(0,\alpha) t^{\alpha+1/2} \qquad t_p \le t \le t_{p1} \tag{2.22}$$

Then, combine Eq. (2.21) and the material balance function as shown in Eq. (1.7). We can get,

$$\frac{V_{frac}}{A_f} = \frac{V_p - V_{l,p}}{A_f} = \frac{V_p}{A_f} - 2\, r_p C_L \sqrt{t} g(0,\alpha) \qquad t_p \le t \le t_{p1} \tag{2.23}$$

By substituting Eq. (2.23) into Eq. (1.9), the pressure transient solution can be developed as follows.

$$\frac{d\Delta p_w}{dt} = -\frac{1}{c_f}\frac{d}{dt}\left(\frac{V_{frac}}{A_f}\right)$$

$$= -\frac{1}{c_f}\left[V_p\frac{d}{dt}\left(\frac{1}{A_f}\right) - r_p C_L g(0,\alpha)\frac{1}{\sqrt{t}}\right] \tag{2.24}$$

$$= \frac{1}{c_f}\left[-\frac{\alpha V_p {t_{p1}}^{\alpha}}{A_{f1}t^{\alpha+1}} + \frac{r_p C_L g(0,\alpha)}{\sqrt{t}}\right] \qquad t_p \le t \le t_{p1}$$

Integrating both side of Eq. (2.24), we can get,

$$p_{ws} - p_w(t) = \frac{V_p {t_{p1}}^{\alpha}}{c_f A_{f1}}\left(\frac{1}{{t_p}^{\alpha}} - \frac{1}{t^{\alpha}}\right) + \frac{2r_p C_L g(0,\alpha)}{c_f}\left(\sqrt{t} - \sqrt{t_p}\right) \tag{2.25}$$

$$t_p \le t \le t_{p1}$$

or,

$$p_{ws} - p_w(t) = \frac{V_p}{c_f A_{fo}}\left(1 - \frac{{t_p}^{\alpha}}{t^{\alpha}}\right) + \frac{2r_p C_L g(0,\alpha)}{c_f}\left(\sqrt{t} - \sqrt{t_p}\right) \tag{2.26}$$

$$t_p \le t \le t_p + \Delta t_{te}$$

With Eqs. (2.25) or (2.26), pressure at any time during tip extension can be calculated out if the fracture surface at the end of pumping or propagation can be determined. For Eqs. (2.25) and (2.26), we can find that the first term in its right, is the pressure transient associated only with tip growth, while the second term is that related with fluid leakoff during tip-extension. Since tip-extension is generally believed to happen in tight formations, pressure drop by leakoff process would be negligible compared with that by tip extension. It is the main reason that the first term would generally be the dominant factor for the pressure solution during tip-extension.

When the fracture stop propagating, the pressure behavior is similar to the normal leakoff except for the definition of pumping time, t_p. Similar to Eq. (1.19), the pressure solution for after tip-extension can be written as,

$$p_w(\Delta t_D{}' = 0) - p_w(\Delta t_D{}') = \frac{\pi r_p C_L \sqrt{t_{p1}}}{2c_f} G(\Delta t_D{}', \alpha) \qquad \Delta t_D{}' > 0 \tag{2.27}$$

where,

$$G(\Delta t_D{}', \alpha) = \frac{4}{\pi}[g(\Delta t_D{}', \alpha) - g(\Delta t_D{}' = 0, \alpha)] \tag{2.28}$$

$$\Delta t_D{}' = \frac{t - t_{p1}}{t_{p1}} = \frac{t - t_p - (t_{p1} - t_p)}{t_p + \Delta t_{te}} = \frac{\Delta t_D - \Delta t_{teD}}{1 + \Delta t_{teD}} \tag{2.29}$$

Here,

$$\Delta t_{teD} = \frac{\Delta t_{te}}{t_p} \tag{2.30}$$

Compared Eq. (2.27) with Eq. (1.19), we can find the pressure solution after end of tip-extension is very similar with that in normal leakoff. Therefore, by adjusting injection time from t_p in Eq. (1.19) to t_{p1} in Eq. (2.27), and definition of dimensionless time from Δt_D in Eq. (1.12) to $\Delta t_D{}'$ in Eq. (2.29), pressure decline after the end of tip-extension can be diagnosed and analyzed with same method as that in normal leakoff condition.

Pressure transient behavior can be resolved with Eq. (2.26) and (2.27) if the following assumptions can be satisfied:

1) Little fluid enters into fracture after shut-in.
2) Frac fluid is incompressible.

3) Fracture compliance is constant.
4) Fracture propagates at the same rate after shut-in as that before.
5) Fracture surface area at end of pumping or propagating can be determined or assumed.
6) Normal leakoff except for the tip-extension.

The Bourdet pressure derivative can also be derived by substituting Eq. (2.26) and (2.27) into Eq. (1.27),

$$\tau \frac{d\Delta p_w(\Delta t_D)}{d\tau} = \frac{\alpha V_p}{c_f A_{fo}} \frac{\Delta t_D}{(1+\Delta t_D)^{\alpha}} + \frac{r_p C_L \sqrt{t_p} g(0,\alpha)}{c_f} \sqrt{1+\Delta t_D}\, \Delta t_D \qquad 0 \le \Delta t_D \le \Delta t_{teD} \tag{2.31}$$

$$\tau \frac{d\Delta p_w(\Delta t_D)}{d\tau} = \frac{2 r_p C_L \sqrt{t_p}}{(1+\Delta t_{teD}) c_f} f\left(\frac{\Delta t_D + \Delta t_{teD}}{1+\Delta t_{teD}}\right) \qquad \Delta t_D \ge \Delta t_{teD} \tag{2.32}$$

Again, for the two terms in the left of Eq. (2.31), the first one represents the pressure response related with tip-extension, while the second, related with leakoff process. For the cases when formation is tight enough that the leakoff mechanism is negligible compared with tip-extension, the curve trend of Bourdet derivative is dominated by the firm term. The curve will first show a unit slope at very early time, and then, it would bend to a more flat trend with a slope at $(1-\alpha)$ when Δt_D is growing large, which can be demonstrated mathematically from Eq. (2.31). Therefore, depending on the value of α, which typically ranges between ½ to 1 during injection, the log-log Bourdet derivative of pressure might have a slope between 0 to ½. The early ½-slope or

flat curve immediately after shut-in, which is diagnosed as apparent fracture linear flow or radial flow in previous section, could be the feature of tip-extension.

One should note that, if tip extension does not happen, Δt_{teD} is 0, and Eq. (2.32) can be reduced to Eq. (1.30), which is the Bourdet derivative for normal leakoff.

Usually, if tip-extension is observed from diagnostic plots, the corresponding pressure or time at its end can be read out directly from these plots. If we assumes that the dimensionless time duration defined in Eq. (2.30) is known, we are able to investigate the effect of tip extension on the pressure transient. A simulations has been run with the input data in Table 2-1. Figure 2-7 shows the bottomhole pressure curve for tip-extension when $\Delta t_{teD} = 1$, which means that fracture continued propagating after shut-in until $t = t_p + \Delta t_{teD} t_p = 2t_p$. We can find from the pressure falloff plot that pressure dives much faster at early time during tip extension than the following period.

Table 2-1 Input data for the simulation of tip-extension without WBS

r_p	1
h_f, ft.	50
E', psi.	5×10^6
p_{ws} or ISIP, psi.	6000
t_p, minute	5
S_{min}, psi.	5000
q_p, bbl/minute	6
Δt_{teD}	1
α	4/5
C_L, ft/$\sqrt{\text{min}}$	5×10^{-4}

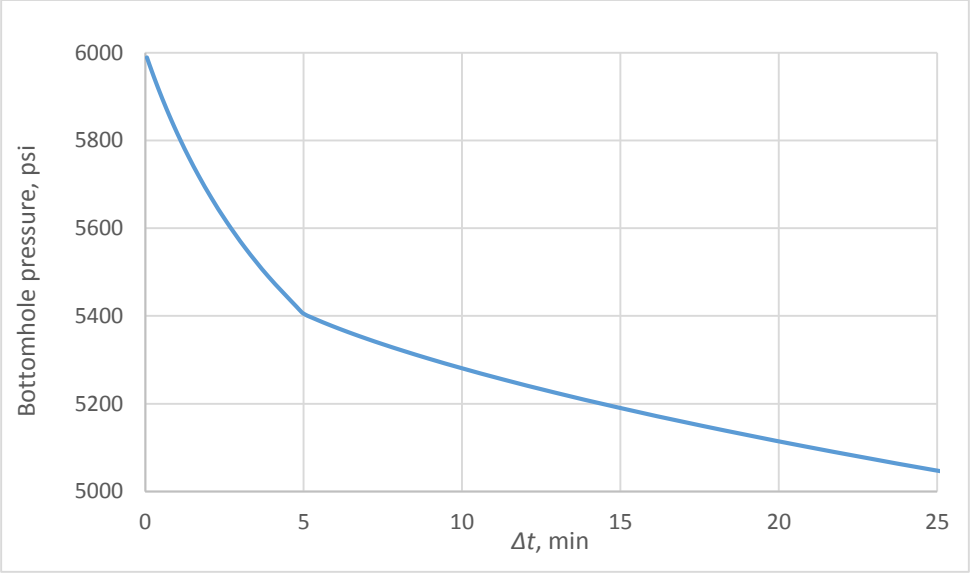

Figure 2-7 Bottomhole pressure for tip extension without WBS

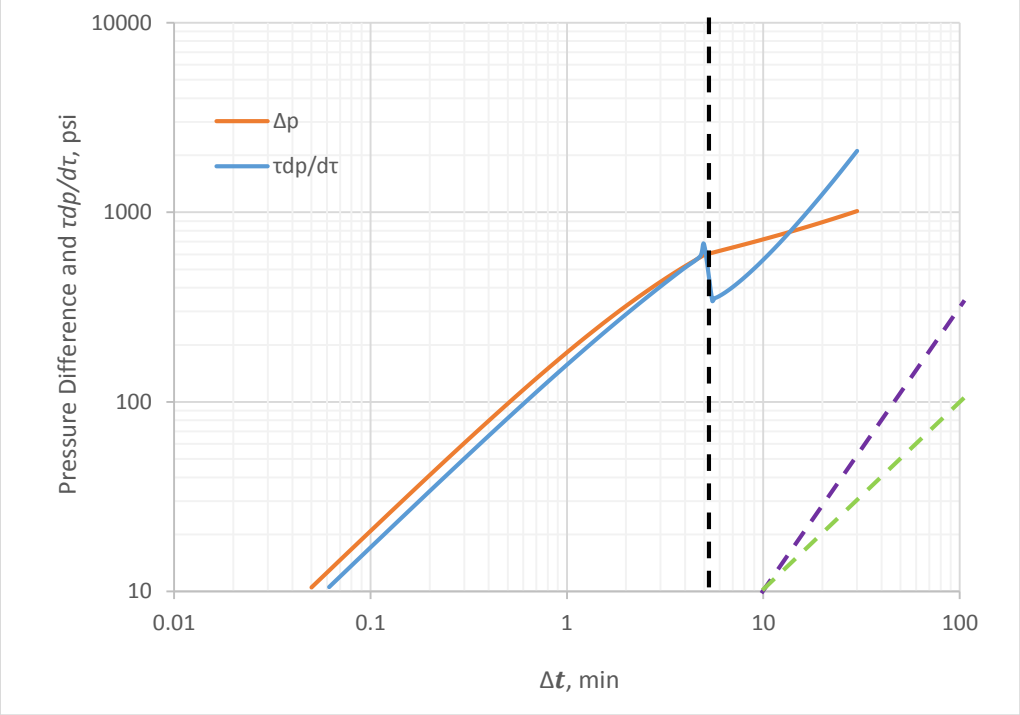

Figure 2-8 Log-log Bourdet derivative diagnostic plot for tip extension without WBS

Figure 2-8 and Figure 2-9 are diagnostic plots for tip extension. On the log-log diagnostic Bourdet derivative plot, the black dashed line indicates the pumping time before shut-in. The dramatic decline indicates the end of tip-extension, or the transition from tip-extension behavior to the normal leakoff. The dramatic transition in both plots is caused by the assumption that the fracture continues propagating at same rate after shut-in as before, and then is arrested immediately at $\Delta t = \Delta t_{teD}$ when the pressure reaches a critical propagation pressure, which is defined as the pressure below which propagation ceases. It is probably more reasonable to assume that the propagation rate should decline gradually to zero after shut-in, which will be discussed later in this section.

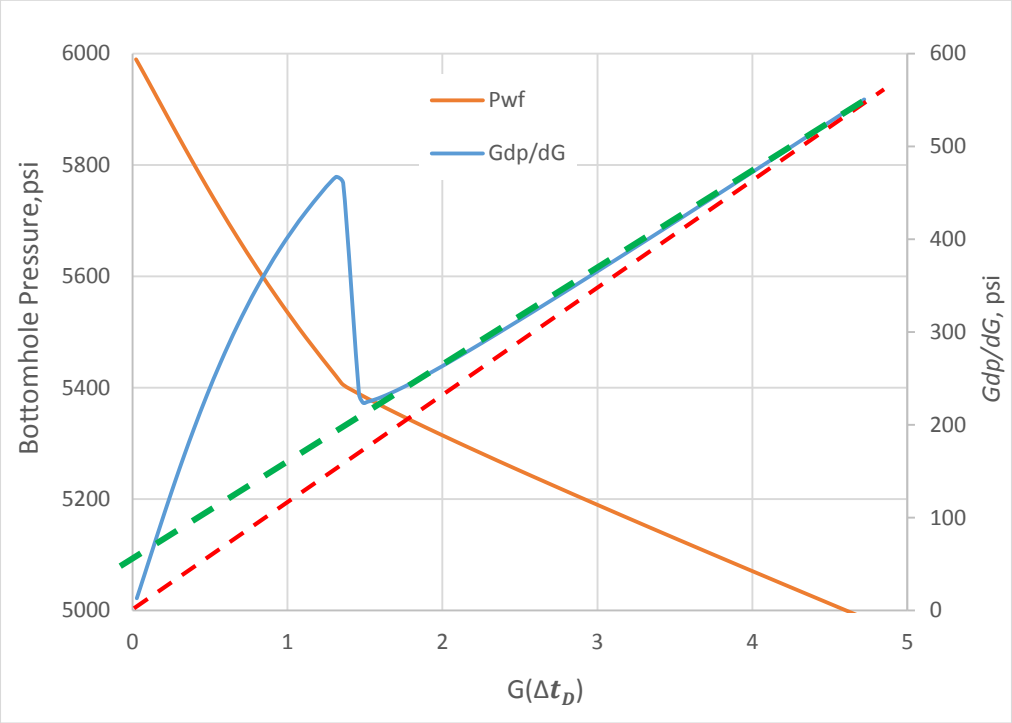

Figure 2-9 Composite G-function plot for tip extension without WBS

In the G-function plot in Figure 2-9, the abrupt increase at very beginning time is caused by tip extension. After that, normal leakoff takes over. Two characteristic lines exhibited in Figure 2-9 are represented by two extrapolated straight lines in red and green. The green is the for the data points before $G(\Delta t_{teD}) = 4$, and the red is for the whole time range. If the fracture closes in a relatively short time after tip-extension, or the data is recorded for only a short time, the available pressure data after tip-extension could be limited, likes the case before $G(\Delta t_{teD}) = 4$ and represented by the green line in Figure 2-9. Similar to commonly observed feature as shown in Figure 1-3, the extrapolated green line lies above the origin and has a positive intercept on the pressure axis. However, if it takes a long time for the fracture to close and all pressure points during closing are recorded, we are likely to observe that Gdp/dG would approach to the asymptote which can be extrapolated through the origin. Both signatures indicated by the green and red lines can be explained mathematically by the pressure solution in Eq. (2.27). Since a practical dimensionless tip-extension duration is probably less than 10, when the $\tau dp/d\tau$ curve in log-log plot is undergoing the transition from unit slope to 3/2 slope, more attention is required in the tip extension analysis with log-log diagnostic Bourdet derivative plot.

Sensitivity analysis on more factors will be elaborated later in the **section 2.3.3**, where the dramatic changes in the diagnostic plots are diminished with a gradual decline manner of area exponent ($\boldsymbol{\alpha}$) during tip-extension.

2.3.2 Tip extension with wellbore storage effect

Since fluid expansion during pressure falloff potentially is one of the major fluid source of tip-extension, WBS in a long time duration after shut-in, will be modeled in this section. As has been discussed in **2.1 Wellbore storage effect (WBS)**, fluid will expand as long as the stored fluid pressure declines. In other words, the "after-flow" will not stop during the whole pressure falloff test. However, strong wellbore storage behavior typically only happens at very early time immediately after shut-in because of rapid pressure drop during this time. As discussed previously, the early short time WBS is mainly caused by dissipation of friction in the wellbore and near-wellbore area, or the fast decline of net pressure, which could be the result of PDL or tip-extension. Friction components during injection is difficult to quantify because of the complicated communication condition between wellbore and fracture. However, the rapid decline of net pressure caused by abnormal leakoff behaviors is able to be estimated. In this section, fluid expansion effect will be involved and modeled in the whole pressure falloff after shut-in.

Besides the created fracture, the wellbore will be involved in the pressure transient system. Then, the after-flow volume is able to be included by the new material balance function, as shown in Eq. (2.33).

$$V_p + V_{AF} = V_{frac} + V_{l,p} \tag{2.33}$$

where, V_{AF} is the after-flow volume caused by slightly compressibility of frac fluid after shut-in, which is the only difference with previous model without wellbore storage effect. V_{AF} at any time after shut-in can be calculated with Eq. (2.34),

$$V_{AF} = V_w * c_w * \Delta p_w(t) \tag{2.34}$$

One should note that the volume incremental of the stored fluid in the fracture caused by pressure decline is not included into the material balance function. To study the pressure behavior for the case where tip extension happens, the fracture is assumed to propagate in the same manner as previous model. By substituting Eq. (2.33) into Eq. (1.6), the pressure resolution during tip extension after shut-in can be derived as follows.

$$\begin{aligned}
\frac{d\Delta p_w}{dt} &= -\frac{1}{c_f}\frac{d}{dt}\left(\frac{V_{frac}}{A_f}\right) \\
&= -\frac{1}{c_f}\left[\frac{1}{A_f}\frac{dV_{frac}}{dt} - \frac{V_{frac}}{{A_f}^2}\frac{dA_f}{dt}\right] \\
&= -\frac{1}{c_f}\left[-\frac{1}{A_f}\frac{dV_{l,p}}{dt} + \frac{1}{A_f}\frac{dV_{AF}}{dt} - \frac{V_p + V_{AF} - V_{l,p}}{{A_f}^2}\frac{dA_f}{dt}\right] \\
&= \frac{1}{c_f}\left[\frac{1}{A_f}\frac{dV_{l,p}}{dt} - \frac{1}{A_f}C_w V_w\frac{d\Delta p_w}{dt} + \frac{V_p + V_{AF} - V_{l,p}}{{A_f}^2}\frac{dA_f}{dt}\right]
\end{aligned} \tag{2.35}$$

As $\frac{d\Delta p_w}{dt}$ shows up in both sides of the function, it can be solved by rearranging the equation as,

$$\frac{d\Delta p_w}{dt} = \frac{\frac{dV_{l,p}}{dt} + \frac{V_p + V_{AF} - V_{l,p}}{A_f}\frac{dA_f}{dt}}{c_f A_f + c_w V_w} \tag{2.36}$$

Substituting Eq. (2.18), (2.19), (2.22)and (2.34) into Eq. (2.36), we can get,

$$t\frac{d\Delta p_w}{dt} = \frac{r_p C_L A_{f1} g(0,\alpha) t^{\alpha+1/2} + \alpha V_p\left(t_p + \Delta t_{te}\right)^{\alpha} + \alpha c_w V_w \Delta p_w\left(t_p + \Delta t_{te}\right)^{\alpha}}{c_f A_{fo} t^{\alpha} + c_w V_w\left(t_p + \Delta t_{te}\right)^{\alpha}} \tag{2.37}$$

By solving Eq. (2.37), the solution of pressure transient behavior during tip-extension can be obtained as,

$$p_{ws} - p_w(t) = \frac{2r_p C_L A_{f1} g(0,\alpha)\left(\sqrt{t} - \sqrt{t_p + \Delta t_{te}}\right)t^{\alpha} + V_p\left[t^{\alpha} - \left(t_p + \Delta t_{te}\right)^{\alpha}\right]}{c_f A_{f1} t^{\alpha} + c_w V_w \left(t_p + \Delta t_{te}\right)^{\alpha}} \quad (2.38)$$

$$t_p \leq t \leq t_p + \Delta t_{te}$$

Eq. (2.38) can be used to calculate the pressure at any time during tip extension. If $c_w = 0$ or $V_w = 0$, which means there is no wellbore storage effect, Eq. (2.38) can be reduced to Eq. (2.26). It proves the consistence of these two model. Furthermore, the difference between pressure drops in these two models is only caused by the wellbore storage effect, it therefore might be quantified by the difference.

$$J_{WBS} = \frac{\Delta p_{w-no\ WBS} - \Delta p_{w-WBS}}{\Delta p_{w-no\ WBS}} \quad (2.39)$$

where, $J_{WBS}$is the index of wellbore storage effect which is introduced to indicate the relative contribution of pressure drop from wellbore storage. $\Delta p_{w-no\ WBS}$ and Δp_{w-WBS} are pressure drop without and with wellbore storage respectively, and they can be calculated from Eq. (2.26) and (2.38). After substituting Eq. (2.26) and (2.38) into Eq. (2.39), the equation can be simplified as,

$$J_{WBS} = \frac{1}{1 + \frac{V_{frac}}{c_w V_w p_{net}}\ (1 + \Delta t_D)^{\alpha}} \quad (2.40)$$

From above equation, we can find that wellbore storage effect (J_{WBS}) would be obvious if the after-flow volume is comparable to or even larger than the volume of created fracture, which more likely happens when the injection volume is limited and the wellbore has a large volume.

Because pressure decline much faster during tip extension than any later time, it is more likely that wellbore storage effect happens at very early time of falloff. Although the effect could be negligible for the falloff after tip-extension, where pressure decline is pretty flat, fluid compressibility is also coupled into material balance function to keep consistent with the pressure solution during tip extension. Similar to previous model, fluid leakoff during tip extension is treated as continuous pumping time. The pressure solution derivation is shown as follows.

$$\frac{d\Delta p_w}{dt} = -\frac{1}{c_f}\frac{d}{dt}\left(\frac{V_{frac}}{A_f}\right)$$

$$= -\frac{1}{c_f A_{f1}}\frac{dV_{frac}}{dt}$$

$$= -\frac{1}{c_f A_{f1}}\left[-\frac{dV_{l,p}}{dt} + \frac{dV_{AF}}{dt}\right]$$

$$= \frac{1}{c_f A_{f1}}\left[\frac{dV_{l,p}}{dt} - \frac{dV_{AF}}{dt}\right]$$

$$= \frac{2r_p C_L A_{f1}\sqrt{t_{p1}}}{c_f A_{f1}}\frac{dg(\Delta t_D{}', \alpha)}{dt} - \frac{c_w V_w}{c_f A_{f1}}\frac{d\Delta p_w}{dt} \tag{2.41}$$

Rearrange Eq. (2.41), and integrate both sides of the equation, we can get,

$$p_w(\Delta t_D{}' = 0) - p_w(\Delta t_D{}') = \frac{\pi r_p C_L A_{f1}\sqrt{t_{p1}}}{2\left(c_f A_{f1} + c_w V_w\right)} G(\Delta t_D{}', \alpha) \qquad t \geq t_p + \Delta t_{te} \tag{2.42}$$

The definition of $\Delta t_D{}'$ and $G(\Delta t_D{}', \alpha)$ is same as Eq. (2.29) and Eq. (2.28). With Eq. (2.38) and (2.42), pressure transient solution can be simulated for the cases where both wellbore storage and tip extension are observed. The assumptions for this model are as following.

1) Fracture compliance is constant.
2) Fracture propagates in the same rate after shut-in with that before.
3) Fracture surface area at end of pumping or propagating can be determined or estimated.
4) Normal leakoff except for the tip-extension and wellbore storage effect.

Also, the Bourdet derivative for this case can be developed by substituting Eq. (2.38) and (2.42) into Eq. (1.27). The derivative is so complicated that the analytical solution is not listed here.

A series of simulations are run to investigate the composite effect of WBS and tip extension in FCTs. For this discussion, the input data is similar to previous **Section 2.3.1** except for several additional parameters of wellbore, as shown in Table 2-2. Two different sizes of wellbore are taken as examples to illustrate the impact of wellbore storage effect on the pressure behavior after shut-in. The total injection volume for both wells are same with previous example, at 30 bbl.

Table 2-2 Input parameters and their values for simulations of tip-extension with WBS

c_w, psi^{-1}	3×10^{-6}
Small wellbore volume	
r_w, in.	4.8
L_w, ft.	5000
Large wellbore volume	
r_w, in.	8.4
L_w, ft.	15,000

Figure 2-10 shows that wellbore storage can buffer the decline of bottomhole pressure, and this effect is more apparent for the well with a larger wellbore. From both diagnostic plots shown in Figure 2-11 and Figure 2-12, we can find that WBS effect has a relatively weak impact on composite derivatives. Therefore, it can be concluded that, for the well injected through a medium or small size string, wellbore storage effect can be neglected if the pumping volume is not too small. Same to previous model, the dramatic drop in diagnostic curves indicates the end of tip-extension, and it is caused by the assumption that fracture continues growing in the same manner as that during injection, and then is arrested when its internal pressure drops to a critical value.

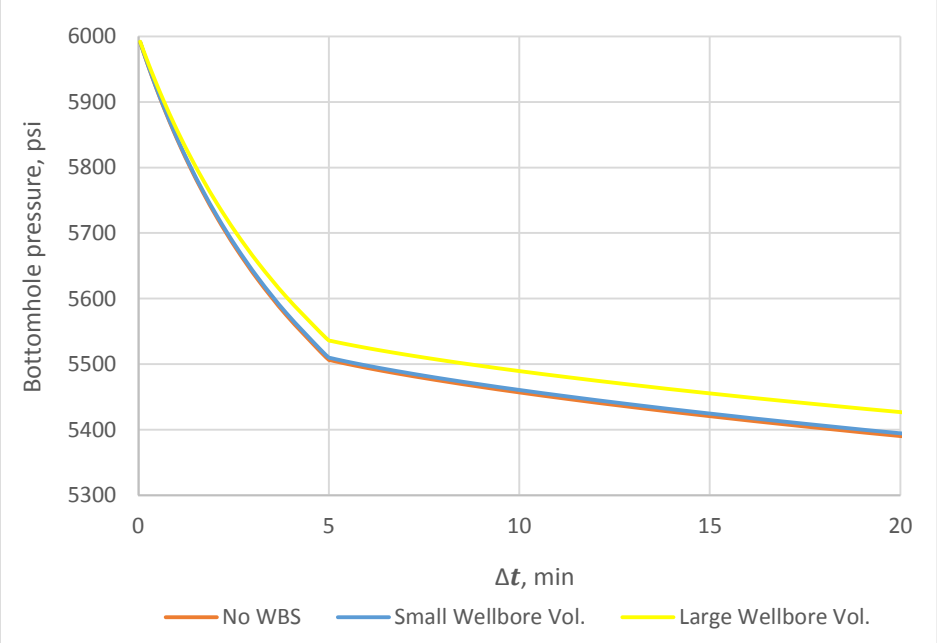

Figure 2-10 Pressure falloff for tip extension with and without WBS (Inj. Vol.=30 bbl)

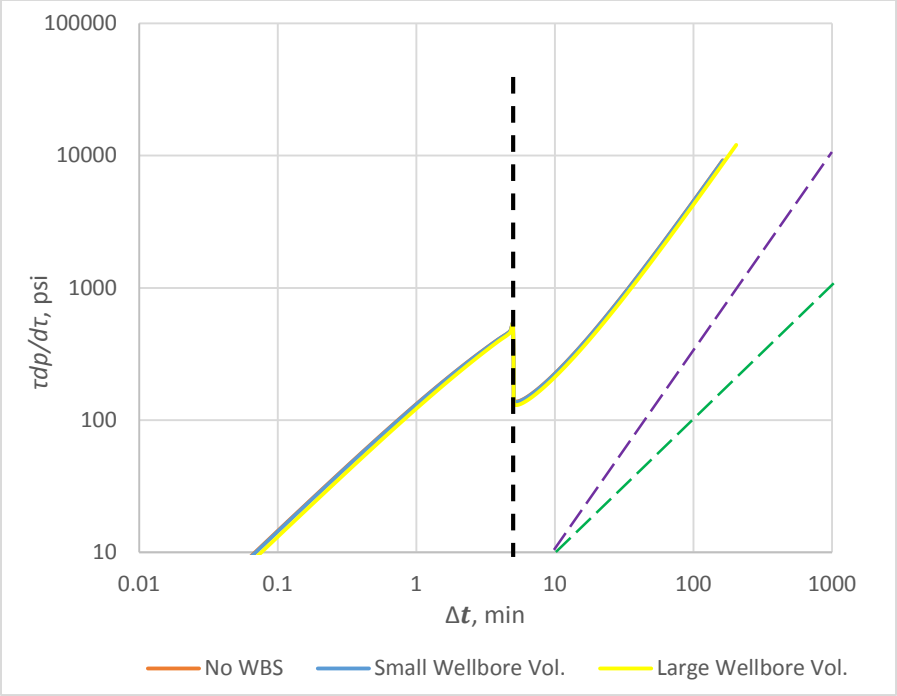

Figure 2-11 Log-log diagnostic Bourdet derivative plot for tip extension with and without WBS (Inj. Vol.=30 bbl)

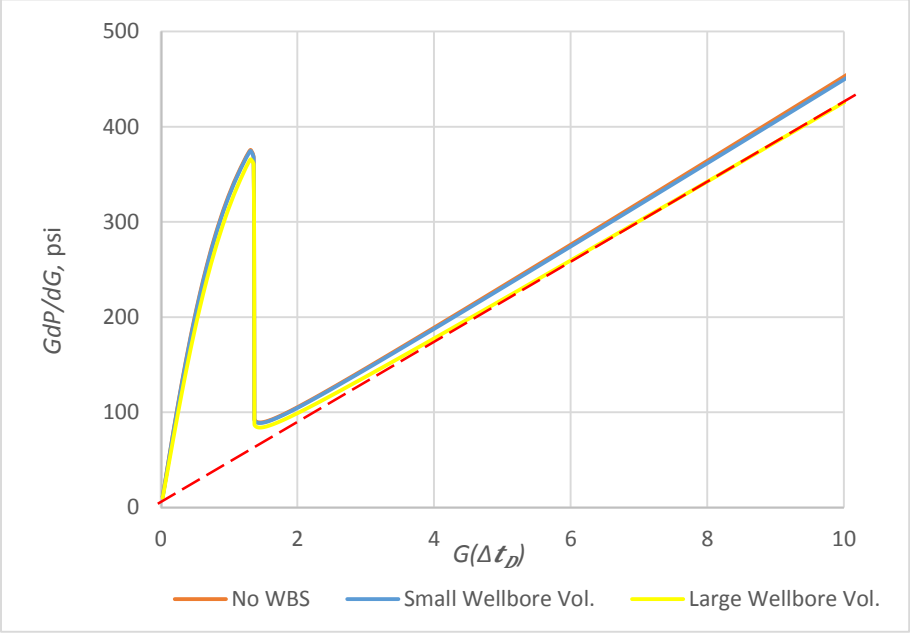

Figure 2-12 G-function plot for tip extension with and without WBS (Inj. Vol.=30 bbl)

Besides the volume of string, the injection size is another significant factor for WBS. As discussed previously, the wellbore storage will be more apparent if the pumping volume is very limited, which is the common practice for FCTs in tight formations. A series simulations are run with smaller injection volume at 12 bbl. For the FCT with small size injection, the wellbore storage effect on the pressure response is illustrated by Figure 2-13, and two diagnostic plots by Figure 2-14 and Figure 2-15. Compared with previous example with larger pumping volume, WBS effect is much more apparent, especially when the wellbore volume is relatively large.

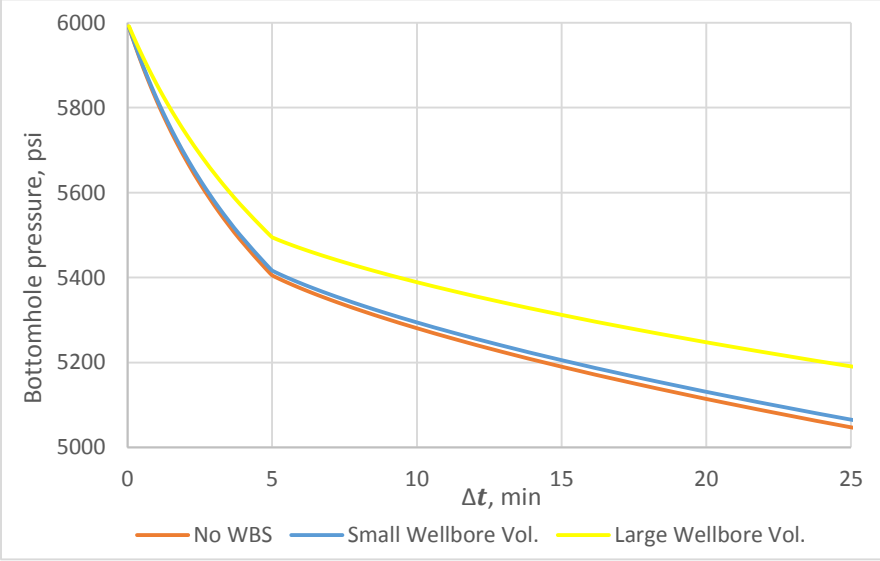

Figure 2-13 Wellbore storage effect on FCTs with small injection volume and tip-extension (Inj. Vol.=12 bbl)

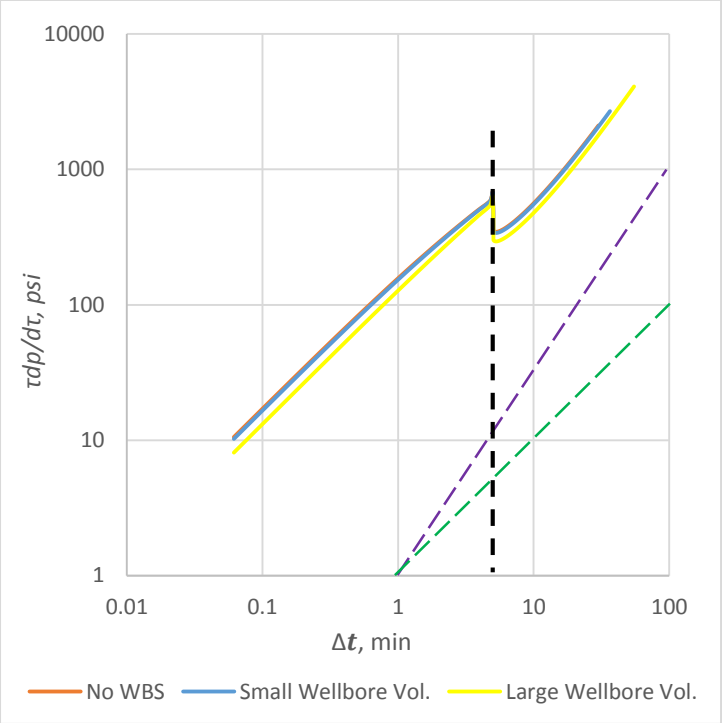

Figure 2-14 WBS effect on $\tau dp/d\tau$ for FCTs with small injection volume and tip-extension (Inj. Vol.=12 bbl)

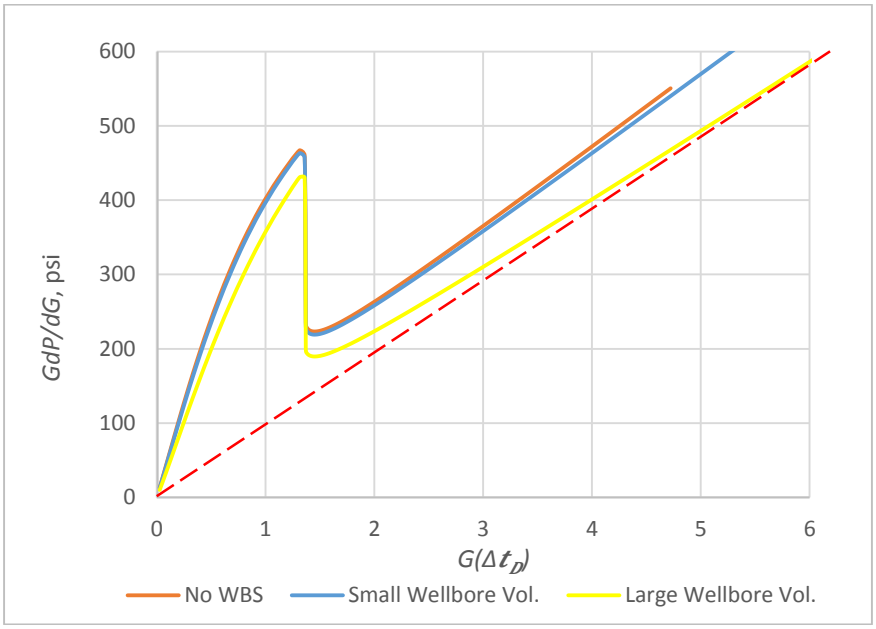

Figure 2-15 WBS effect on Gdp/dG for FCTs with small injection volume and tip-extension (Inj. Vol.=12 bbl)

From previous two sets of examples with different injection sizes and wellbore volumes, we can conclude that the impact of wellbore storage effect (WBS) on pressure response depends on the ratio of wellbore volume over pumping volume. If the ratio is small, WBS can be negligible; otherwise, WBS should be taken into consideration when calculating leakoff coefficient and fluid efficiency from before-closure analysis.

2.3.3 Tip extension with variable area exponent (α)

As we mentioned in previous two tip-extension models, the dramatic drop of diagnostic curve is caused by the assumption that the area exponent is constant during tip extension after shut-in until the decaying fracture pressure reaches a critical pressure level, which could be named as the minimum fracture propagation pressure. Then the fracture is arrested and the area exponent drops immediately to zero from the constant value close to 1. Although there is no model to quantify the decline behavior of the area exponent, intuitively, it is more likely to drop off from initial value to zero gradually. In this way, the fracture propagation rate is allowed to slow down to zero during tip-extension. Several decline manners of the area exponent are modeled here to investigate their impact on pressure behavior and to obtain a smooth diagnostic curve. All studied decline manners are defined as follows, and α_0 is the initial value of area exponent during pumping and at shut-in.

1) Linear decline of area exponent (α).

$$\alpha = \frac{t_{p1} - \mathrm{t}}{t_{p1} - t_{p0}} \alpha_0 \tag{2.43}$$

2) Logarithm decline of area exponent (α).

$$\alpha = \frac{\mathrm{Log}(t_{p1}) - \mathrm{Log}(t)}{\mathrm{Log}(t_{p1}) - \mathrm{Log}(t_{p0})}\alpha_0 \tag{2.44}$$

3) Exponential decline of area exponent (α).

$$\alpha = \frac{\mathrm{Exp}(c\ t_{p1}) - \mathrm{Exp}(c\ t)}{\mathrm{Exp}(c\ t_{p1}) - \mathrm{Exp}(c\ t_{p0})}\alpha_0 \tag{2.45}$$

where, c is the coefficient which can control the decline rate of α. Four series of c are tested as $c = -1,\ -0.01,\ 0.01$ and 1. Eq. (2.45) can be reduced to Eq. (2.43) when c approaches to zero.

4) Square-root decline of area exponent (α).

$$\alpha = \frac{\sqrt{t_{p1}} - \sqrt{t}}{\sqrt{t_{p1}} - \sqrt{t_{p0}}}\alpha_0 \tag{2.46}$$

Besides area exponent described in Eq. (2.43) to (2.46) and wellbore storage effect discussed in previous model, several other parameters are involved in the pressure solution as shown in Eq. (2.26) and (2.27): injection size, pumping time, tip-extension duration, formation leakoff coefficient, etc. A series of sensitivity study have been done to investigate their impact on the pressure behavior on diagnostic plots when tip-extension occurs.

1) Sensitivity study on decline behavior of the area exponent (α)

The area exponent, α, is the factor controlling fracture propagation rate. To obtain a smooth curve of composite pressure derivative ($\tau dp/d\tau, Gdp/dG$), it should be assumed to diminish gradually from its initial value to zero. All decline behaviors of area exponent are plotted in Figure 2-16. Although to predetermine the decline behavior of

area exponent is difficult, it is likely close to one or lying between two of these manners. In this example, we arbitrarily assume that fracture in all cases continue growing for the same time as injection time, $\Delta t_{teD} = 1$. Therefore, fracture starting with a slower decline rate of area exponent tends to result in a longer tip-extension. For instance, in the case of exponential decline with $c = 1$, fracture continue growing after shut-in almost in the same rate with that before, and then drops to zero sharply at end of tip-extension. It is pretty similar to two previously discussed models, and longer fracture growth is expected in this case. To the other extreme, fracture starting with a fast decline of area exponent, like in the case of exponential decline with $c = -1$, fracture propagation is arrested effectively after shut-in. Tip-extension distance in this case will be so limited that it may be not able to be detected. Therefore, different decline models lead to different fracture length increments after shut-in. Fracture dynamic half-lengths for all decline behaviors are plotted in Figure 2-17 with the input data listed in Table 2-3.

Table 2-3 Input data for simulations of tip-extension with declining α

h_f, ft.	50
E', psi.	5×10^6
p_{ws} or ISIP, psi.	6000
t_p, minute	5
q_p, bbl/minute	6
Δt_{teD}	1
C_L, ft/$\sqrt{\text{minute}}$	5×10^{-3}

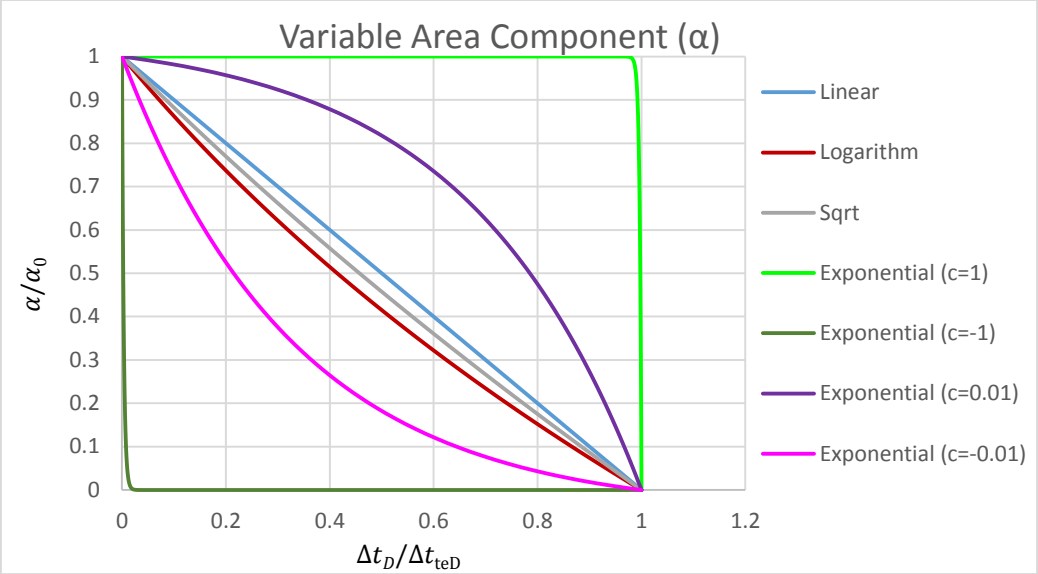

Figure 2-16 Different decline models of area exponent

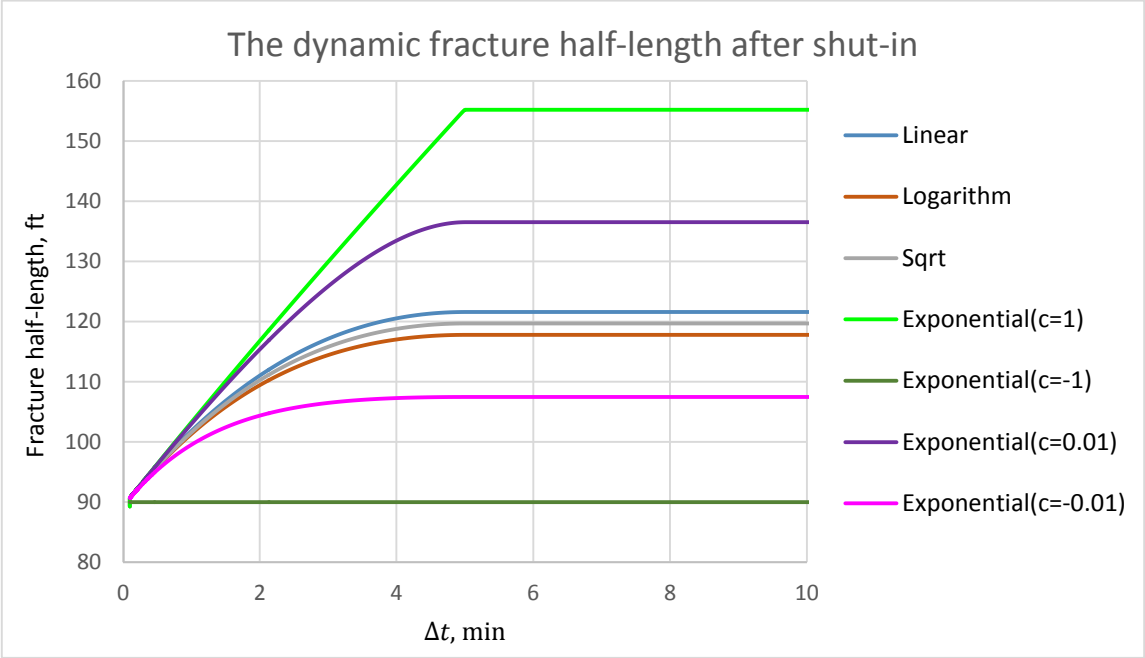

Figure 2-17 Dynamic fracture half-length after shut-in for all α decline behaviors

For those decline behaviors, their impact on the pressure response after shut-in is plotted in Figure 2-18 to Figure 2-20. As mentioned previously, for the case with a fast early decline rate of α, like the exponential model with $c = -1$, very limited tip-extension is expected. Therefore, its pressure response will be very similar to normal leakoff, not only in the plot of bottomhole pressure (Figure 2-18), but also in diagnostic plots (Figure 2-19 and Figure 2-20). While for the opposite extreme, α drops so slow at beginning that it almost can be viewed as constant until the pressure reaches a critical value. After that, it drops to zero dramatically. Pressure response in this case is pretty similar to two previously discussed models where α is assumed to be constant after shut-in and same as before. For each decline rate between these two limits, there is a smooth concave-down curve in the Gdp/dG curve during tip-extension, which is similar to the signature of pressure dependent leakoff (PDL) as shown in Figure 1-3. The major difference between these two abnormal leakoff behaviors is that the normal leakoff after PDL is a straight line, while that after tip-extension behavior is an asymptote. This signature could be confusing if more than one abnormal leakoff mechanisms happen at the same time, or the recorded data is not long-lasting enough, or the tip-extension distance is limited. Furthermore, the altitude of bump is directly related to its propagation decline rate. Faster decline rate at beginning, or longer new-created fracture during tip extension, result in faster bottomhole pressure decline and higher altitude of the bump in Gdp/dG curve.

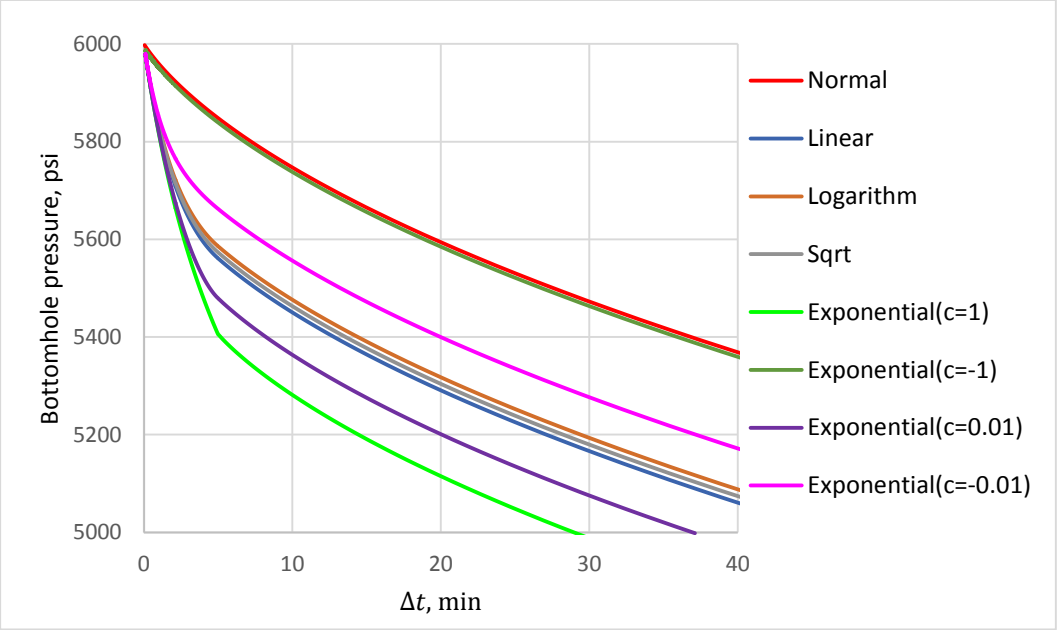

Figure 2-18 Bottomhole pressure for each propagation-rate decline models during tip extension

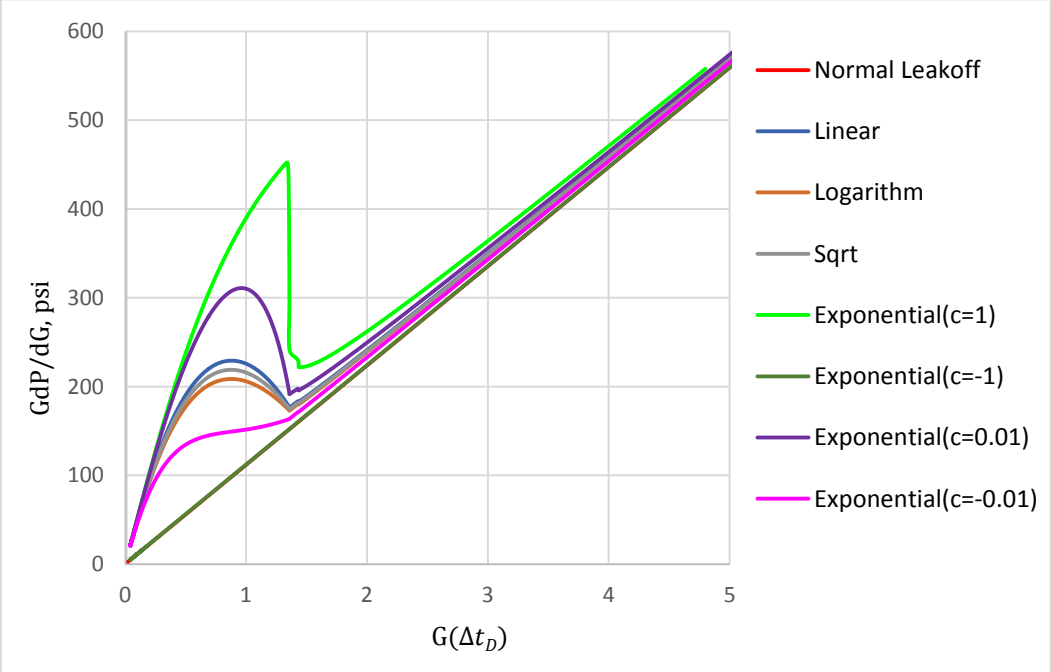

Figure 2-19 G-Derivative plot for different propagation-rate decline models during tip extension

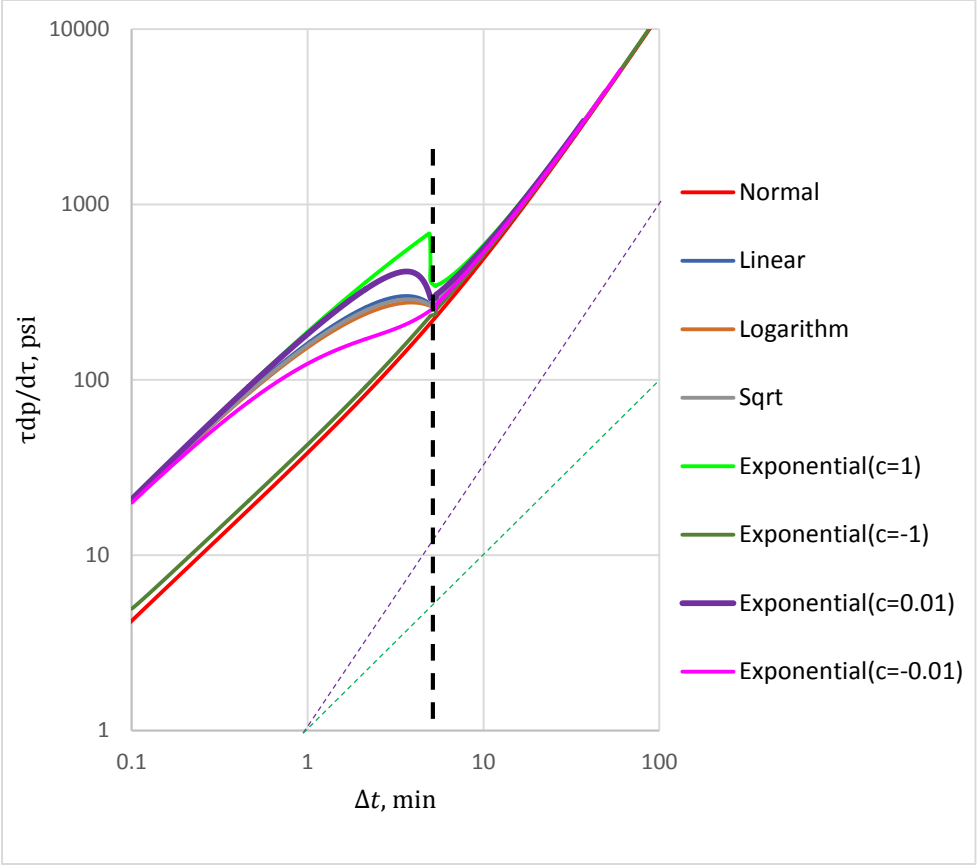

Figure 2-20 Bourdet Derivative plot for different propagation-rate decline models during tip extension

With the propagation rate slowing down during tip-extension, we can see there is a transition in both diagnostic plots shown Figure 2-19 and Figure 2-20. Since the end of hump in the semilog G-function plot indicates the finish of rapid net pressure decline, it thus can be taken as the end time of tip-extension, or Δt_{teD} in previously new derived model. As to the log-log diagnostic plot, if the transition happens before $\Delta t_D = 1$, it will start with a unit slop and then switches to a more flat level until the end of tip-extension. However, if the transition happens during $\Delta t_D = 1{\sim}10$, which probably is the reasonable tip-extension duration range, the transition of tip-extension will superposes

with that of log-log Bourdet derivative transition from unit to 3/2 slope. In this case, more attention needs to be paid when picking the end time of tip-extension from the log-log plot.

As mentioned before, the G-function diagnostic curve after tip-extension tends to approach the asymptote which extrapolating through the origin. And, if only part of data after tip-extension is available, the extrapolated straight line is expected, which have a positive intercept on pressure-axis. This signature is valid for all tip-extension behavior, and can be found in Figure 2-19. Besides, fractures with longer tip-extension tends to have a bigger intercept on pressure axis.

2) Sensitivity study on leakoff coefficient

To investigate the impact of leakoff coefficient on the pressure falloff behavior when tip-extension occurs, exponential decline model of α with $c = -0.01$ is selected as an example. All the rest parameters are same with Table 2-3. Three leakoff coefficients are studied in this section: $C_L = 1 \times 10^{-4}$ ft/$\sqrt{\text{min}}$, 2×10^{-4} ft/$\sqrt{\text{min}}$, 4×10^{-4} ft/$\sqrt{\text{min}}$. From the bottomhole pressure profile in Figure 2-21, we can find that these three curves almost coincide with each other. It suggests that during early time of tip-extension, when fracture continues growing in a fast rate, the pressure decline is mainly contributed by tip-extension, while the impact of leakoff process is negligible. After the fracture growth slows down, the leakoff through fracture surface will take over, which can be presented by the enhanced difference in pressure decline curve.

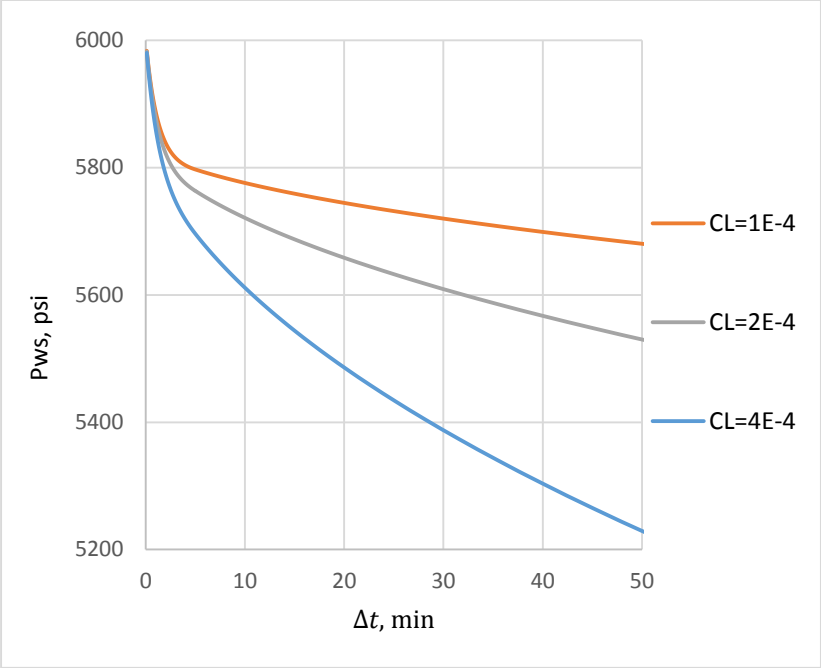

Figure 2-21 Bottomhole pressure for cases with same tip-extension behavior but different leakoff coefficients

Log-log diagnostic plot in Figure 2-22 also exhibits that these curves are close with each other at very early time during tip-extension, and the leakoff process becomes the dominant factor when the tip growth slows down. The final position of 3/2-slope stands for different formation leakoff coefficients.

Similar results can be concluded from G-function diagnostic plot, shown in Figure 2-23. We can find that fracture with larger leakoff coefficient lies above that with smaller one. The slope of the each extrapolated straight line is mainly controlled by the formation leakoff coefficient.

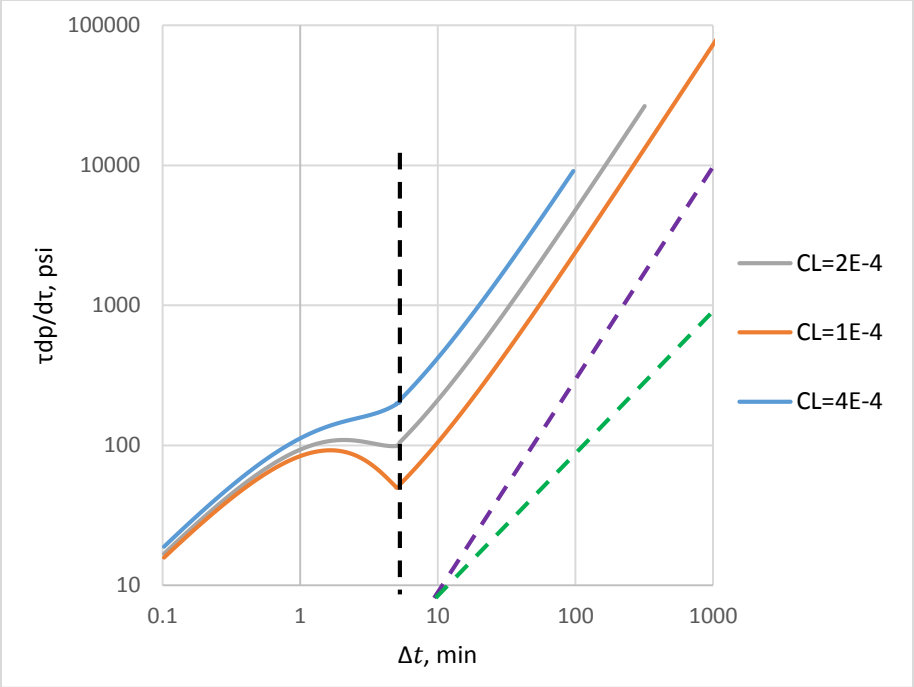

Figure 2-22 Effect of leakoff coefficient on Bourdet derivative curve with tip-extension

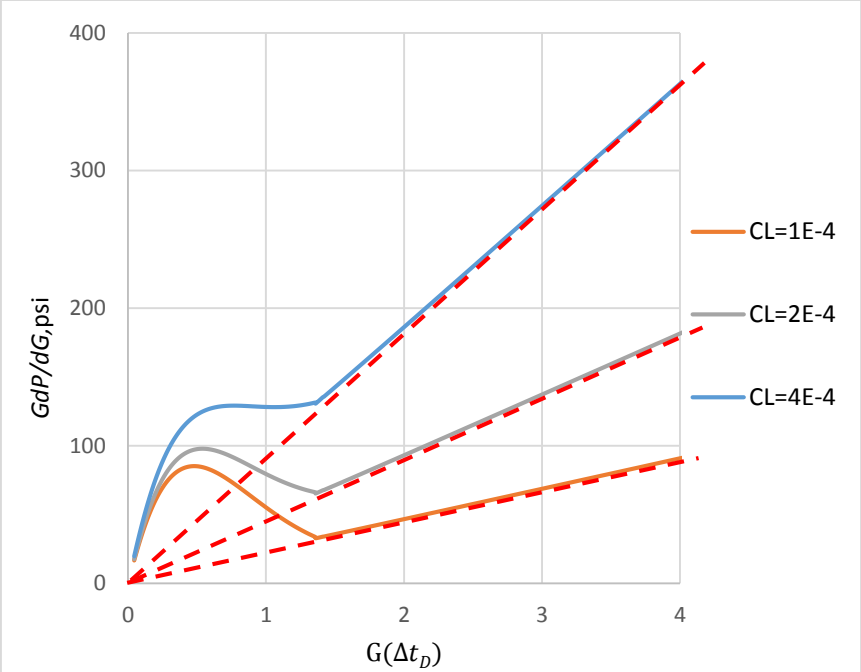

Figure 2-23 Effect of leakoff coefficient on *Gdp/dG* with tip-extension

3) Sensitivity study on tip-extension duration

Tip-extension duration, or pressure difference between the shut-in pressure and the minimum propagation pressure, is another important factor for the tip-extension distance. Three dimensionless tip-extension durations are tested for sensitivity study, $\Delta t_{teD} = 0.5, 1$ and 2. Assuming the area exponent decline exponentially with $c = -0.01$, $C_L = 1 \times 10^{-4}$ ft/$\sqrt{\text{min}}$, the rest input parameters are same with these in Table 2-3.

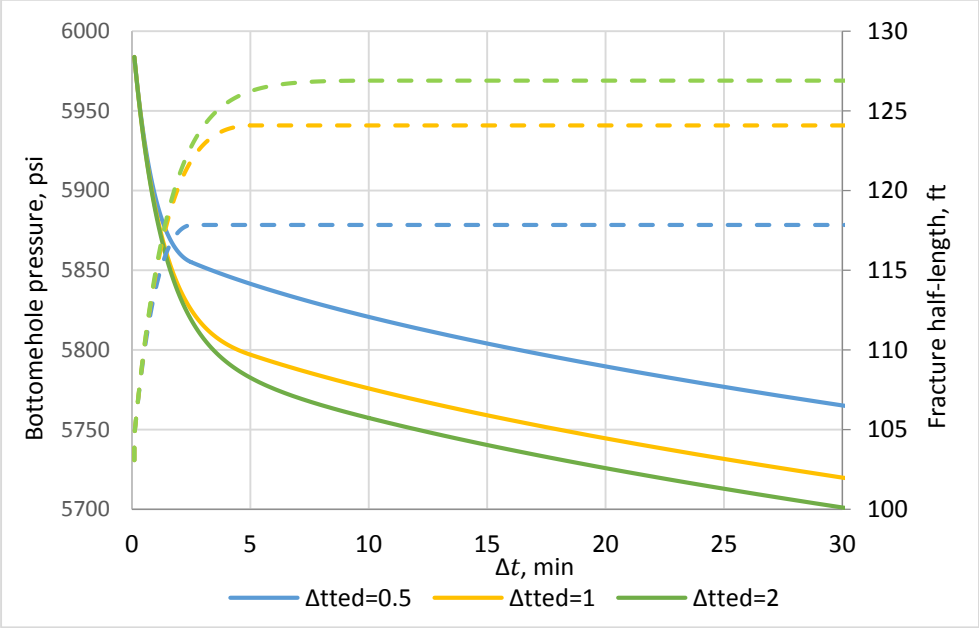

Figure 2-24 Dynamic fracture length and pressure decline after shut-in with different tip-extension durations

Figure 2-24 exhibits fracture extension after shut-in and the pressure falloff behavior. In the same decline behavior of area exponent, longer tip-extension period, or longer new-created fracture length after shut-in, results in a larger pressure drop. It is

especially true in the tight formation, where the early time fast pressure drop is likely caused by tip-extension, rather than by leakoff process.

Figure 2-25 and Figure 2-26 are diagnostic plots for these three different tip-extension durations. The dashed lines in Figure 2-25 indicate the pumping times of all three cases in the real time. Firstly, we can find that, all G-function derivative curves, or log-log Bourdet derivative, coincide in the later time, which is the normal leakoff after tip-extension. During tip-extension, longer duration results in a longer fractures, larger pressure drop, and higher hump in altitude above the later extrapolated straight line in composite G-function plot.

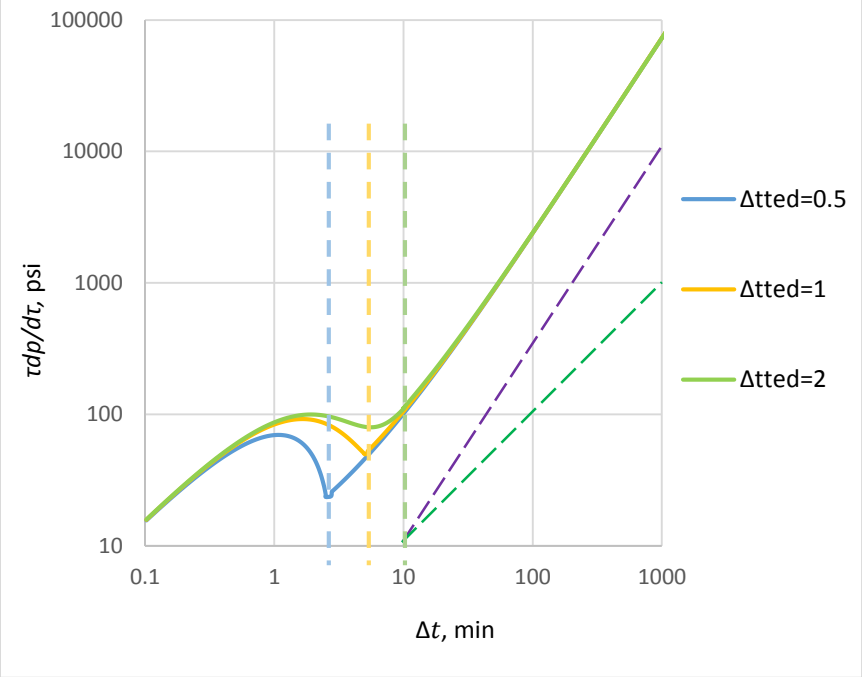

Figure 2-25 $\tau dp/d\tau$ diagnostic plot for tip-extension with different duration (exponential decline behavior with $c = -0.01$)

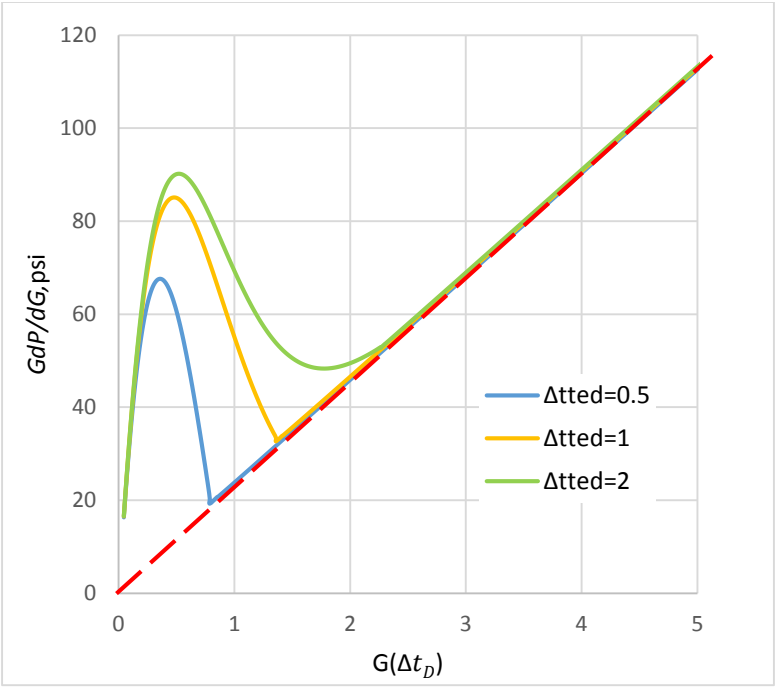

Figure 2-26 Gdp/dG diagnostic plot for tip-extension with different duration (exponential decline behavior with $c = -0.01$)

4) Sensitivity study on injection size

In this case, four different injection times are tested with same pumping rate: $V_p = 15\text{bbl}, 30\text{bbl}, 60\text{bbl}$ and 120bbl. The leakoff coeffcient is assumed to be $C_L = 5 \times 10^{-4}\ \text{ft}/\sqrt{\text{min}}$, and the area exponent decline exponentially with $c = -0.01$. Besides, tip-extension duration is same for all cases at $\Delta t_{teD} = 1$. All the rest parameters are same with these listed in Table 2-3.

The pressure profile and fracture extension after shut-in are shown in Figure 2-27. With same dimensionless duration, tip-extension seems has a much greater impact on the pressure response for the case with a small injection volume.

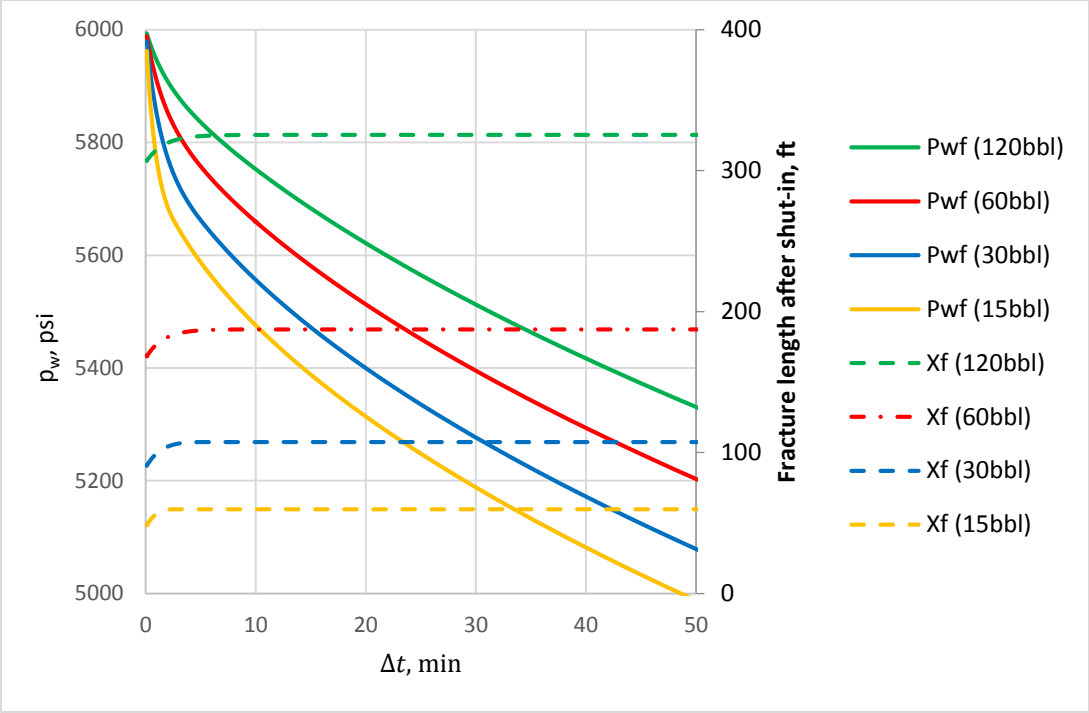

Figure 2-27 Bottomhole pressure profile and fracture length after shut-in for different injection sizes

Table 2-4 Tip-extension distance for different pumping volumes

Injection Volume, bbl	Origianl Fracture Half-length,ft	Final Fracture Half-length,ft	Tip-extension Distance, ft	Increment ratio, %
15	46.93	59.79	12.86	27.4
30	89.25	107.45	18.2	20.4
60	166.92	187.25	20.33	12.2
120	305.75	325.27	19.52	6.4

Figure 2-28 $\boldsymbol{Gdp/dG}$ curves for different injetion sizesexhibits the G-function derivative plots for different injection volumes. It is clear that long fracture created with large volume of fluid, tends to have a Gdp/dG curve close to the straight line through the origin. Or, tip-extension behavior is not as apparent in large injection treatment as

that in small. Table 2-4 can be used to illustrate this phenomenon. Longer tip-extension is likely to be created when larger volume of fluid is injected. However, the incremental ratio of the fracture length during tip-extension is reduced with the increasing of pumping size. This is the direct reason for the decaying tip-extension feature in the larger injecting. If the ratio decreases to zero, the tip-extension behavior will disappear, and the pressure response will be much same with that in normal leakoff.

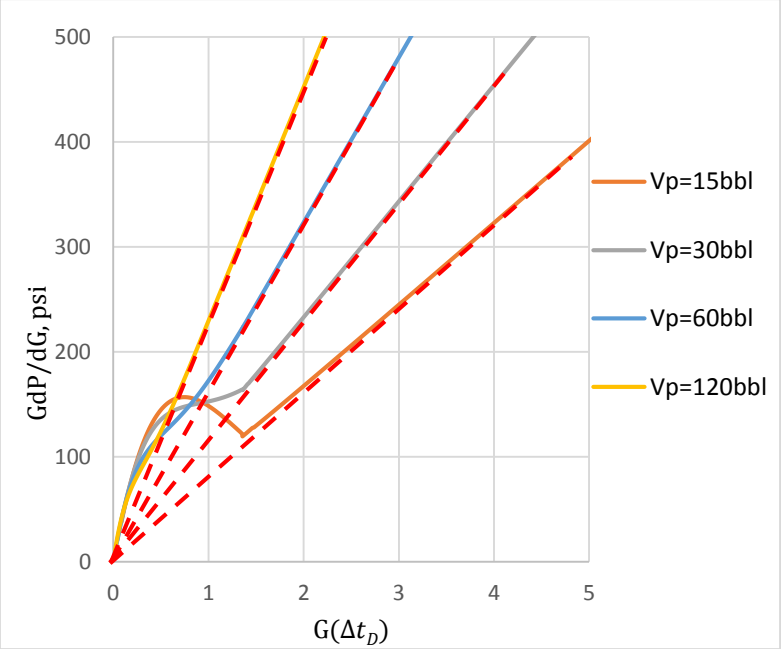

Figure 2-28 Gdp/dG curves for different injection sizes

Similar phenomenon can be observed in the log-log diagnostic plot in Figure 2-29. With same pumping rate and different injection volumes, the injection times for all cases are different and indicated in in Figure 2-29. Vertical dashed lines in the plot indicate the injection time for each case. These parallel lines at later time with 3/2-slope

stands for different fracture surface areas, or fracture lengths created by different injection volumes.

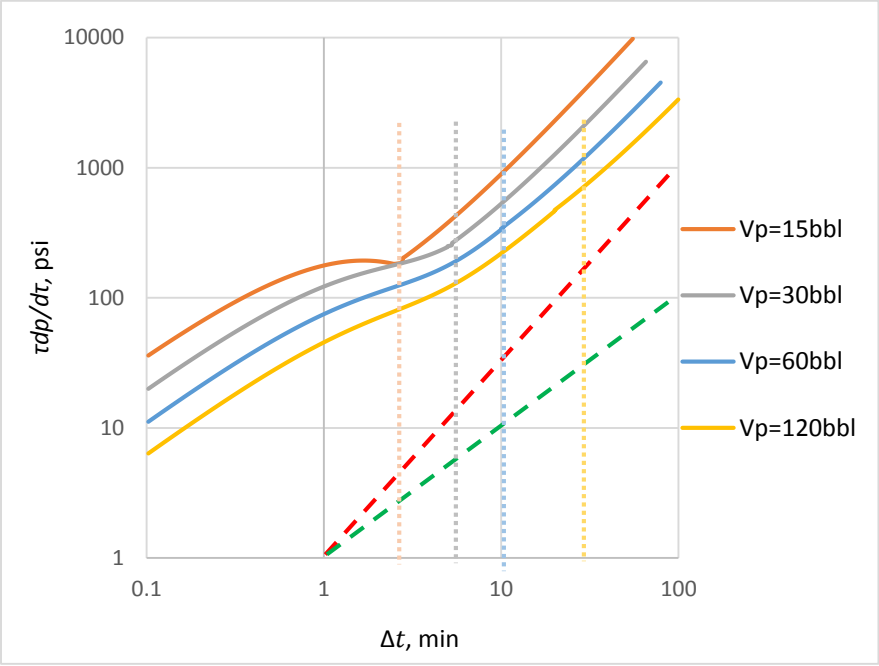

Figure 2-29 $\tau dp/d\tau$ curves for different injection sizes

In summary, if tip-extension happens, its composite G-function will approach to an asymptote, which is extrapolated through the origin. If the fracture closes in a short time after tip-extension, or the recorded data is not long enough, the extrapolated line of the Gdp/dG curve after tip-extension is likely to have a positive intercept with the derivative axis, which is the common practice to identify tip-extension with the composite G-function method. Besides, rapid pressure decline associated with tip-extension tends to strengthen WBS behavior at early time after shut-in. This effect tends

to be more transparent for the treatment with small injection. Furthermore, a smooth diagnostic curve is able to be drawn with a declining area exponent during tip-extension.

2.4 Pressure dependent leakoff (PDL)

Pressure dependent leakoff is one of most commonly observed abnormal leakoff behavior in the FCTs. Generally, it is believed to happen as a result of reopening the natural fracture system. Large amount of fluid flows into these natural fissures, so that a relatively large apparent leakoff coefficient can be obtained. After the closure of these natural fissures, normal leakoff will take over, which typically has a smaller leakoff coefficient. In this section, starting from two commonly used leakoff coefficient model for PDL (Meyer and Jacot 2000), pressure solution are derived for the FCT analysis.

2.4.1 Natural fissure related PDL with a constant leakoff coefficient when $p_w > p_{fo}$

In this case, existing closed natural fissures reopened during hydraulic fracturing have a constant leakoff coefficient when $p_w \geq p_{fo}$, and then switch to a constant and smaller value when the fracture pressure declines below p_{fo}. We assume there is no wellbore storage effect and no other abnormal leakoff mechanisms except for pressure dependent leakoff. Starting from material balance equation, the pressure transient behavior can be derived for these two periods with constant but different leakoff coefficients respectively.

For $p_w \geq p_{fo}$, the constant leakoff coefficient indicates that Nolte function can be employed for this section, as shown in Eq. (2.47), which is similar to Eq. (1.19).

$$p_{ws} - p_w(\Delta t_D) = \frac{\pi r_p C_{L1}\sqrt{t_p}}{2c_f}\, G(\Delta t_D, \alpha) \qquad 0 \le \Delta t_D \le \Delta t_{fcD} \tag{2.47}$$

Where, C_{L1} is the leakoff coefficient for $p_w \ge p_{fo}$; $G(\Delta t_D, \alpha)$ is same as Eq. (1.21); Δt_{fcD} is the dimensionless time when fissure closed, or when $p_w = p_{fo}$.

For $p_w < p_{fo}$, natural fissures are assumed to totally closed and lose all conductivity. Therefore, leakoff into formation matrix is the dominant mechanism of fracture fluid loss, which can be described as normal leakoff. Assume the leakoff coefficient of matrix is C_{L2}. Since C_{L2} is constant, Nolte function again can be used, as shown in Eq. (2.48).

$$p_{fo} - p_w(\Delta t_D) = \frac{\pi r_p C_{L2}\sqrt{t_p}}{2c_f}\left[\, G(\Delta t_D, \alpha) - \, G\left(\Delta t_{fcD}, \alpha\right)\right] \qquad t_D \ge \Delta t_{fcD} \tag{2.48}$$

p_{fo} can be solved from Eq. (2.47) by substituting $\Delta t_D = \Delta t_{fcD}$,

$$p_{fo} = p_{ws} - \frac{\pi r_p C_{L1}\sqrt{t_p}}{2c_f}\, G\left(\Delta t_{fcD}, \alpha\right) \tag{2.49}$$

Substituting Eq. (2.49) into Eq. (2.48), we can get,

$$p_{ws} - p_w(\Delta t_D) = \frac{\pi r_p \sqrt{t_p}}{2c_f}\left[C_{L2} G(\Delta t_D, \alpha) + (C_{L1} - C_{L2}) G\left(\Delta t_{fcD}, \alpha\right)\right] \qquad \Delta t_D \ge \Delta t_{fcD} \tag{2.50}$$

If the leakoff coefficient into matrix is C_{L2}, then that into natural fracture when it opens should be $(C_{L1} - C_{L2})$. From the right side of Eq. (2.50), we can find that the effect of each constant leakoff coefficient on the pressure drop can be expressed by the linear combination of the leakoff coefficient with its lasting duration expressed by G-function. In other words, the leakoff system around the created hydraulic fracture can be

decoupled into two separated scenarios: matrix and natural fissures. Furthermore, if there more than one set of natural fissures with different opening pressures, and each set has a constant leakoff coefficient as assumed in this model, multiple closure events could be observed from the diagnostic plot. This will be explain in more detail later in the simulation result analysis and the case study in next chapter.

The Bourdet derivative can be developed by substituting Eq. (2.47) and (2.48) into Eq. (1.27).

$$\tau\frac{d\Delta p_w}{d\tau} = -\frac{2r_p C_{L1}\sqrt{t_p}}{c_f}\left(\Delta t_D + {\Delta t_D}^2\right) f(\Delta t_D, \alpha) \qquad 0 \le \Delta t_D \le \Delta t_{fcD} \tag{2.51}$$

$$\tau\frac{d\Delta p_w}{d\tau} = -\frac{2r_p C_{L2}\sqrt{t_p}}{c_f}\left(\Delta t_D + {\Delta t_D}^2\right) f(\Delta t_D, \alpha) \qquad \Delta t_D \ge \Delta t_{fcD} \tag{2.52}$$

From above two equations, it can be concluded that the only difference between the Bourdet derivatives for these two sections is the leakoff coefficient. On log-log diagnostic Bourdet derivative plot, this difference could result in different position of these two parts of Bourdet derivative curve. The second part can be obtained by switch the first part downward by $\mathrm{Log}(C_{L2}/C_{L1})$ on log-log diagnostic Bourdet derivative plot. In other words, the gap between these two parts of curve is determined by the ratio of these two constant leakoff coefficients.

A simple simulation is performed to show the basic feature of PDL with two constant leakoff coefficients. The input data needed is listed in Table 2-5. Figure 2-30 shows the pressure falloff after shut-in. It can be easily figured out that early time, when natural fissures are involved in the leakoff, has a much sharper pressure decline.

Table 2-5 Input data for the simulation of PDL with two costant leakoff coefficients

r_p	1
h_f, ft.	50
E', psi.	5×10^6
p_{ws} or ISIP, psi.	6000
p_{fo}, psi	5400
t_p, minute	5
S_{min}, psi.	5000
q_p, bbl/minute	6
α	4/5
C_{L1}, ft/$\sqrt{\text{min}}$	2.5×10^{-4}
C_{L2}, ft/$\sqrt{\text{min}}$	1×10^{-4}

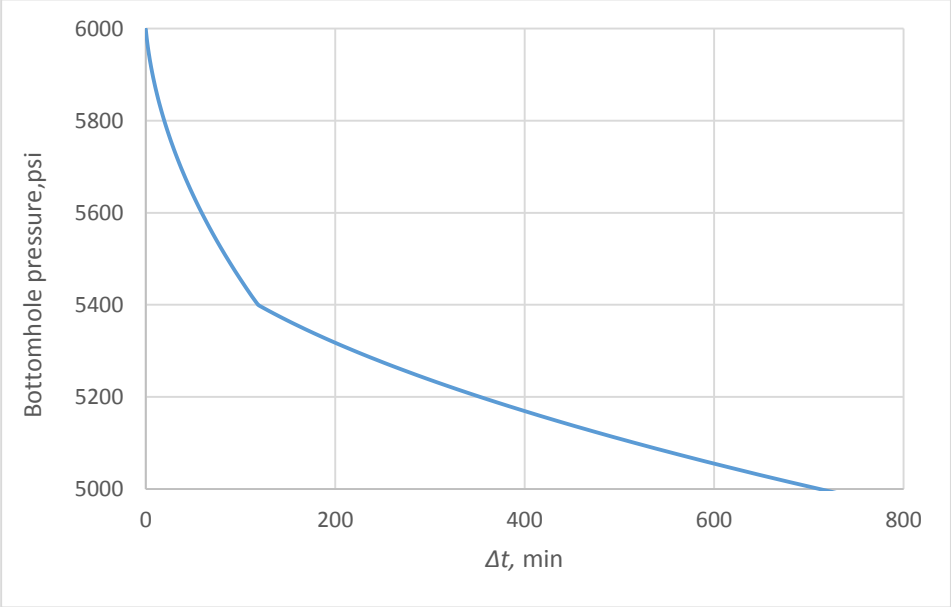

Figure 2-30 Bottomhole pressure for PDL with 2 constant leakoff coefficients

The diagnostic plots presented by log-log diagnostic Bourdet derivative plot and G-function plots are shown in Figure 2-31 and Figure 2-32, respectively. For log-log diagnostic plot, there are two inconsistent 3/2-slopes, and the dramatic drop is the

indication of closure of natural fissures, or the end of PDL. The pressure in this point is the closure stress of natural fractures. From each 3/2-slope, the adherent leakoff coefficient can be calculated out with the new derived pressure solution. Besides, it can be found that the second 3/2-slope line can be reached by switch the first downward by log(2.5), which is the leakoff coefficient ratio in the logarithm scale.

Furthermore, if more than two sets of leakoff coefficient involved in the fracture system, which could happen if more than one set of natural fissures in different directions are connected during treatment, there will be more 3/2-slopes in the Bourdet derivative curve. Each 3/2-slope stands for a constant system leakoff coefficient. This phenomenon has been observed (Xue and Ehlig-Economides 2013), and usually named as “multiple closure events”, as shown in Figure 1-8.

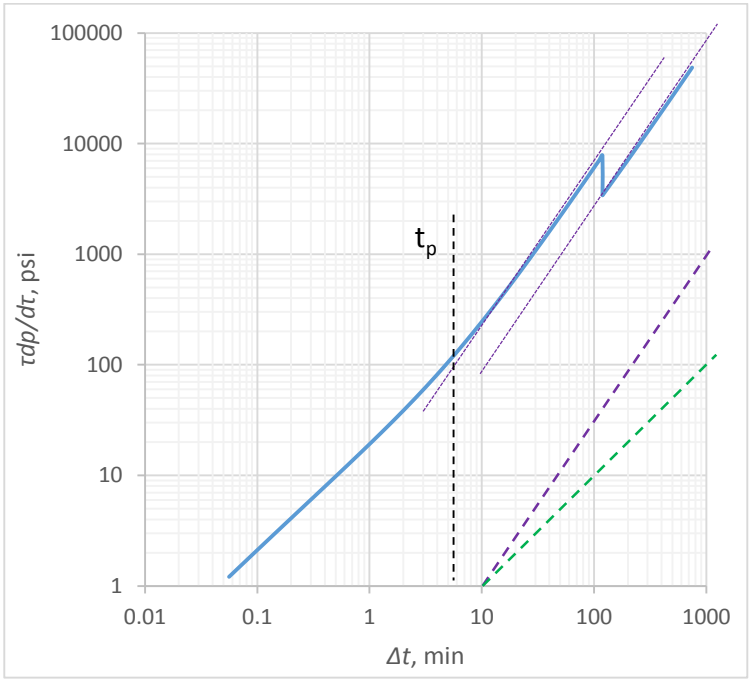

Figure 2-31 Log-log diagnostic Bourdet derivative plot of PDL with two constant leakoff coefficients

Similar finding in G-function plot has been noticed, as shown in Figure 2-32. There are two straight lines with different slopes and both can be extrapolated through the origin. Each of them stands for a distinct system leakoff coefficient. Similar to two 3/2-slope straight lines in log-log diagnostic plot, each leakoff coefficient can be computed out. One should note that these two extrapolated straight lines in the G-function plot correspond to the two 3/2-slope lines in the log-log Bourdet derivative plot. Same closure event, closure pressure can be picked and therefore, same leakoff coefficients and fracture geometry can be calculated from these two diagnostic plots.

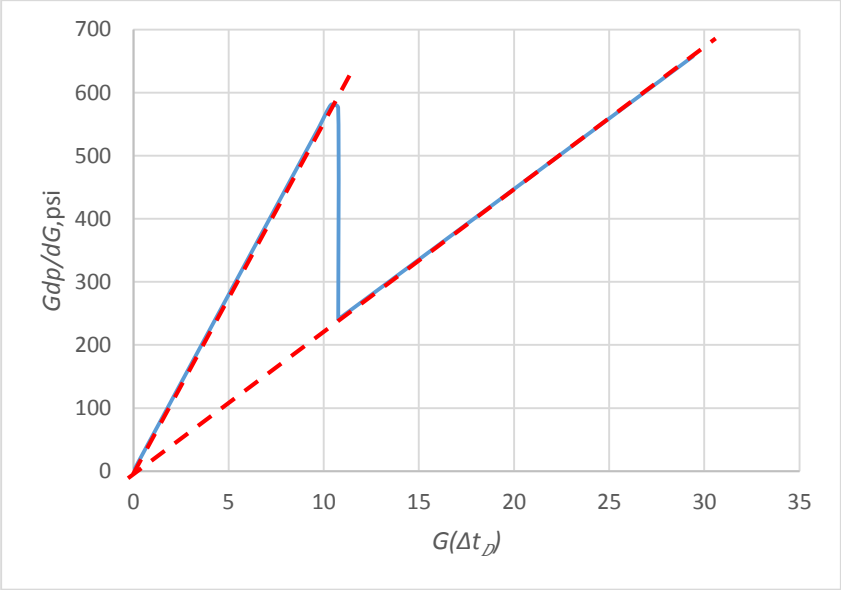

Figure 2-32 G-function plot of PDL with two constant leakoff coefficients

2.4.2 Natural fissure related PDL with a variable leakoff coefficient when $p_w > p_{fo}$

This model has been described in Eq. (1.47). Again, no other non-ideal leakoff mechanism occurs except for PDL. With this assumption, we can find that Eq. (1.10)

and (1.15) are still valid with the fact that C_L is not constant but a function of pressure change, which is what we are trying to solve. The derivation of pressure falloff solution is based on the material balance function, as shown in Eq. (1.7). Similar to previous model, the pressure solution will be separated into two parts because there are two different leakoff mechanisms during pressure decline.

For $p_w \geq p_{fo}$, by substituting $C_L(p_w)$ in Eq. (1.47) into (1.15) with $\theta = 1/2$, we can get,

$$\frac{d\Delta p_w}{d\Delta t} = \frac{2r_p\, C_{L1}\, exp\left(-\beta \frac{\Delta p_w}{p_{ws} - p_{fo}}\right)}{c_f \sqrt{t_p}} \frac{dg(\Delta t_D, \alpha)}{d\Delta t} \qquad p_w \geq p_{fo} \qquad (2.53)$$

or,

$$exp\left(\beta \frac{\Delta p_w}{p_{ws} - p_{fo}}\right) \frac{d\Delta p_w}{d\Delta t} = \frac{2r_p\, C_{L1}}{c_f \sqrt{t_p}} \frac{dg(\Delta t_D, \alpha)}{d\Delta t} \qquad p_w \geq p_{fo} \qquad (2.54)$$

Integrate both sides of Eq. (2.54), we can get the pressure drop solution during PDL period as,

$$p_{ws} - p_w(\Delta t_D) = \frac{p_{ws} - p_{fo}}{ln\left(\frac{C_{L1}}{C_{L2}}\right)} \ln\left\{1 + \frac{2r_p\, C_{L1}\sqrt{t_p}}{c_f} \frac{ln\left(\frac{C_{L1}}{C_{L2}}\right)}{p_{ws} - p_{fo}} [g(\Delta t_D, \alpha) - g(0, \alpha)]\right\} \qquad (2.55)$$

$$p_w \geq p_{fo}$$

Matrix leakoff with constant leakoff coefficient will take over after PDL, and the pressure solution is exactly same with previous model, as shown in Eq. (2.48).

Similarly, the Bourdet derivative during PDL can be derived as follows.

$$\tau\frac{d\Delta p_w}{d\tau} = -\frac{\left(\Delta t_D + {\Delta t_D}^2\right) f(\Delta t_D, \alpha)}{\frac{c_f}{2r_p\, C_{L1}\sqrt{t_p}} + \frac{ln\left(\frac{C_{L1}}{C_{L2}}\right)}{p_{ws} - p_{fo}}[g(\Delta t_D, \alpha) - g(0, \alpha)]} \tag{2.56}$$

$$0 \le \Delta t_D \le \Delta t_{fcD}$$

One should note that if there is no PDL, or $C_{L1} = C_{L2}$, Eq. (2.56) can be reduced to Eq. (1.30), which proves the consistence between these two PDL models.

Back to the assumption of the newly derived PDL model, by using a variable leakoff coefficient before natural fracture closure, a smooth transition can be drawn to connect the two leakoff scenarios: one at very early time after shut-in with a relatively high leakoff coefficient at C_{L1}, the other happening after the closure of natural fracture with a constant leakoff coefficient. The resulting curve is more practical than previous model with two constant leakoff coefficients. However, the variable leakoff coefficient model, as expressed in Eq. (1.47), is not based on any physical model or laboratory work. Also, the decline manner of leakoff coefficient is fixed, so it does not have any freedom to change the curve shape during transition section. Therefore, the model is not able to match most of the real field data, Analog to Eq. (1.51), a new exponential transition function with a decline controlling factor (ω) is created to avoid the inherent problem of Eq. (1.47), and shown as following.

$$C_L(p_w) = \begin{cases} C_{L1} & p_w > p_{fo} \\ (C_{L1} - C_{L2}) \dfrac{\mathrm{Exp}\left(\omega \dfrac{p_w}{p_{ws}}\right) - \mathrm{Exp}\left(\omega \dfrac{p_{fo}}{p_{ws}}\right)}{\mathrm{Exp}(\omega) - \mathrm{Exp}\left(\omega \dfrac{p_{fo}}{p_{ws}}\right)} + C_{L2} & p_{ci} > p_w \geq p_{fo} \\ C_{L2} & p_{ci} > p_w > p_c \end{cases} \quad (2.57)$$

with p_{ci} at time Δt_{ci} defined as the start of normal closure behavior ending with the final closure pressure, p_c at time Δt_c. For $p_{ci} > p_w \geq p_{fo}$, at least some of the natural fissures have closed, and the leakoff coefficient drops from C_{L1} to C_{L2} gradually with the pressure change and controlled by ω. The decline controlling factor, ω, can be adjusted to match the field data with different curve trend during transition in the real practice.

A simulation is tested with the input data listed in Table 2-5 except $C_{L1} = 1 \times 10^{-4}$ ft/$\sqrt{\text{min}}$ and $C_{L2} = 1 \times 10^{-5}$ft/$\sqrt{\text{min}}$. And, the system leakoff coefficient is expressed by Eq. (1.47). Bottomhole pressure profile is shown in Figure 2-33. Figure 2-34 shows the change of leakoff coefficient with pressure and elapsed time. We can find that, at early time, leakoff coefficient drops much faster than later time. Besides, when fracture pressure falls below natural fissure opening pressure, p_{fo}, matrix leakoff will be the dominant mechanism, and then the leakoff coefficient is assumed to be constant.

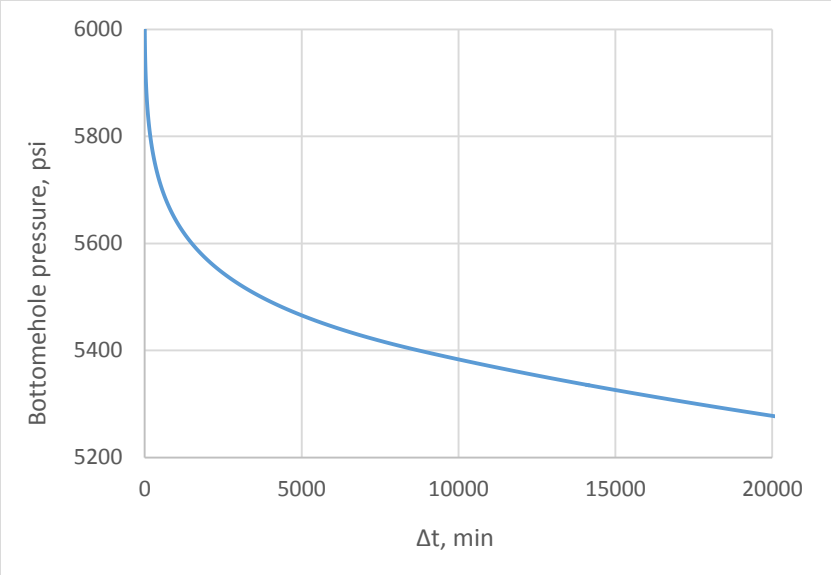

Figure 2-33 Bottomhole pressure profile

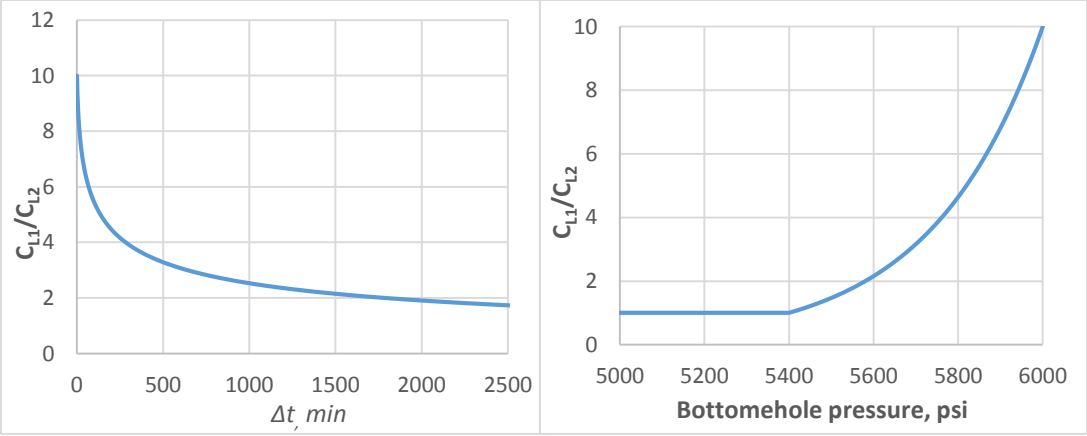

Figure 2-34 Leakoff coefficient changes with elapsed time and pressure

Figure 2-35 and Figure 2-36 are diagnostic plots for this example. We can find that, in the log-log diagnostic plot, there is a straight line at very early time, followed by a transition section until the final straight line with 3/2-slope. Both the early unit slope line and the final line with 3/2-slope are indication of normal leakoff. They stand for the

initial and final condition of fracture system. The transition section occasionally has a straight line in the log-log diagnostic plot, which has a slope ranging between unit and 3/2. The starting time of 3/2-slope thus can be taken as the end of PDL, and the pressure at this point can be picked as the natural fissure opening pressure. Besides, the end time of PDL and natural fracture closure pressure can also be picked from Gdp/dG diagnostic plot, as shown in Figure 2-36. The hump signature above the extrapolated straight line from data in the later time is the most direct characteristic for PDL behavior. After that, the curve will switch to the straight line. The start point of the curve back to the straight line can be taken as the end time of PDL, and the pressure at this point as closure or opening pressure of natural fissures. In some case, another extrapolated line could be drawn from the early time data, which is corresponding to the early unit slope in the log-log diagnostic plot, and can be used to estimate the initial leakoff situation of fracture system.

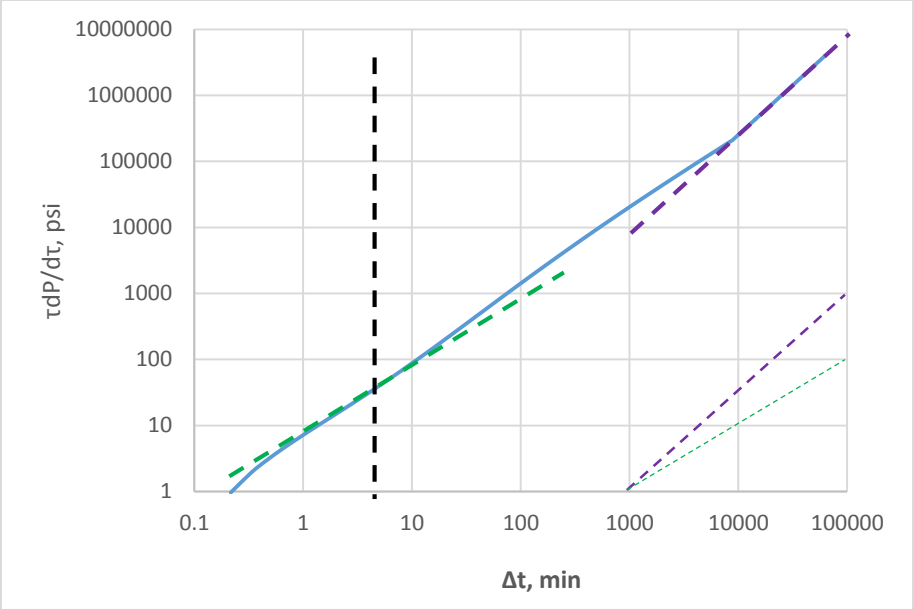

Figure 2-35 $\tau dp/d\tau$ diagnostic plot for PDL with variable leakoff coefficient

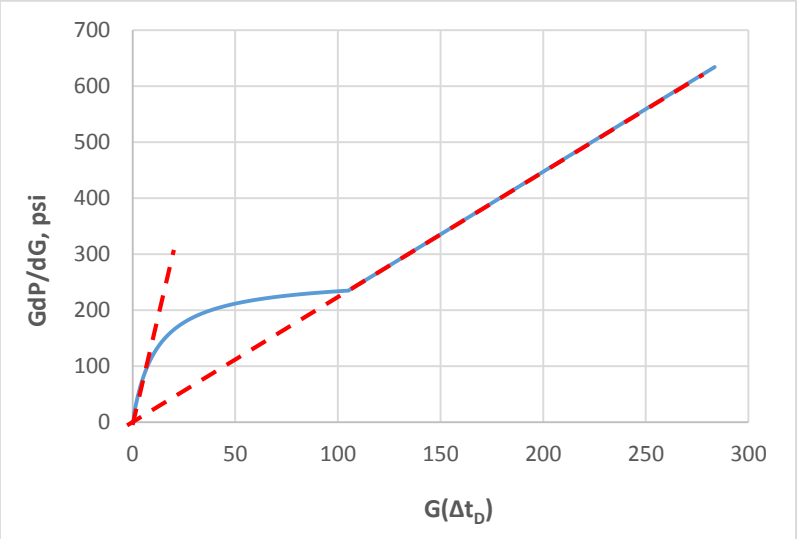

Figure 2-36 Gdp/dG diagnostic plot for PDL with variable leakoff coefficient

A series of sensitivity study has been done to investigate the impact of leakoff into natural fissures on the diagnostic plots. For all of these cases, the only difference is

the initial leakoff coefficient, C_{L1}. Bottomhole pressure falloff profile is exhibited in Figure 2-37, and the diagnostic curves are shown in Figure 2-38 and Figure 2-39. We can find that the final 3/2-slope is easily be identified. Before that, the early unit or 3/2-slope straight line also can be picked out, which stands for the initial leakoff condition. If the difference between the initial and final leakoff coefficient is relatively small, these two lines with 3/2-slope will be very close to each other. In the extreme situation, when these two leakoff coefficients are same, which means normal leakoff behavior rather than PDL behavior, these two 3/2-slope lines will coincide with each other. The larger the leakoff coefficient difference is, the bigger the distance between these two lines. After the end of PDL, all curves converge to one 3/2-slope lines which is the behavior of normal leakoff by formation matrix. In the semilog G-function plot in Figure 2-39, all curves with different original leakoff coefficients show the concave-down feature. And, the larger the original leakoff coefficient is, the faster it declines to the final level, and the shorter duration of PDL behavior in diagnostic plot. Also, the early extrapolated straight line could be drawn, and it corresponds to the early 3/2-slope or unit slope line in log-log diagnostic plot. This initial leakoff coefficient is possible to be calculated out from the early 3/2-slope in the log-log Bourdet derivative, or from the first extrapolated line in the G-function.

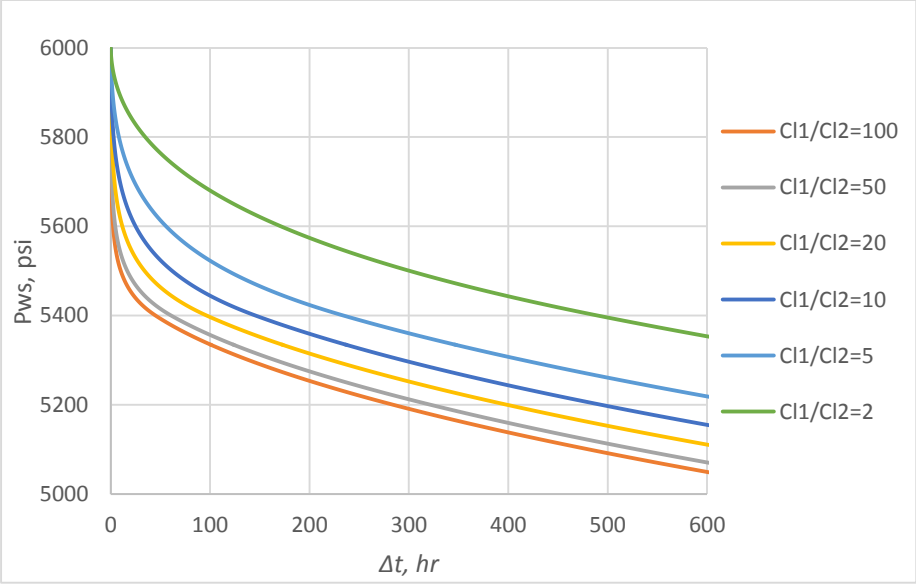

Figure 2-37 Bottomhole pressure profile of PDL with different initial leakoff coefficients

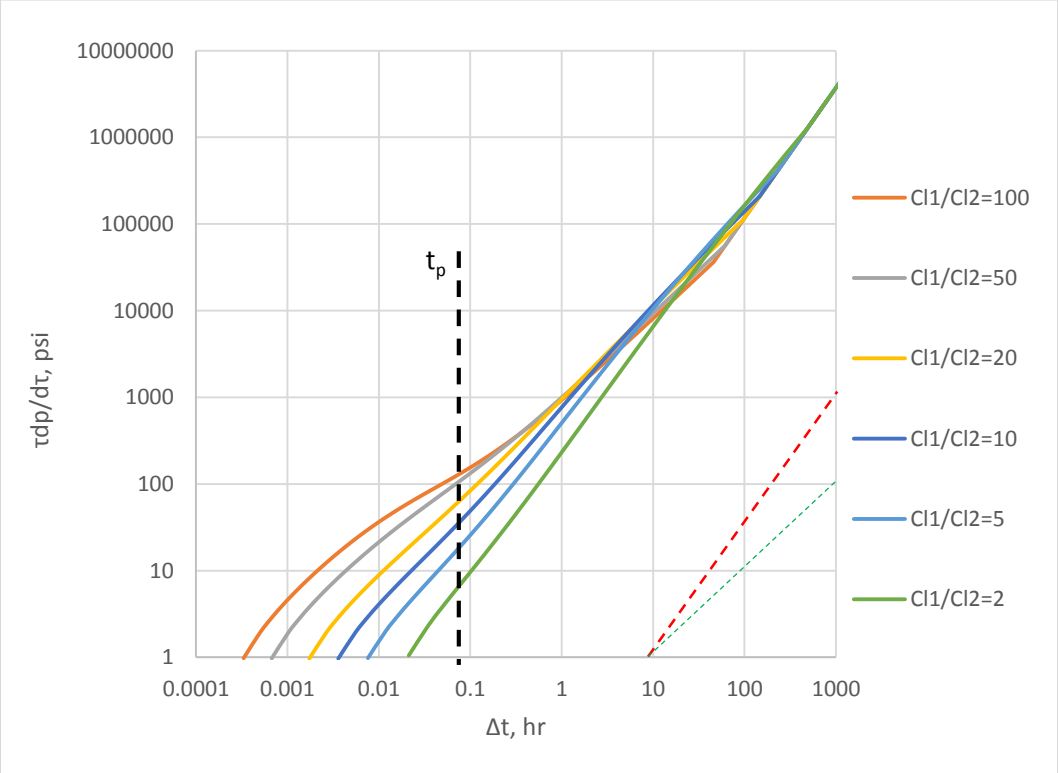

Figure 2-38 $\tau dp/d\tau$ diagnostic plot for PDL with variable leakoff coefficient

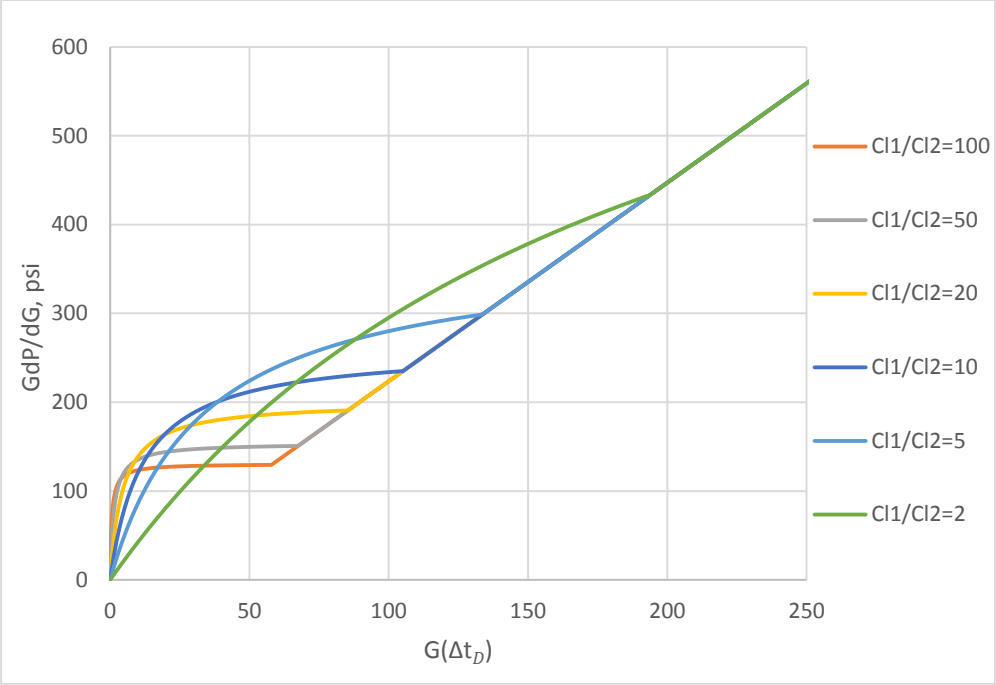

Figure 2-39 Gdp/dG diagnostic plot for PDL with variable leakoff coefficient

One should note that for $\Delta t_D = 1{\sim}10$, there is a slope transition from unit to 3/2 for poroelastic closure in normal leakoff. While Figure 2-38 shows transitions from the early 3/2-slope to the later, with moderate to high permeability reopened fracture networks, the transition could be from unit to unit or unit to 3/2, and closure of natural fissures could occur at the end of unit slope behavior in these cases as shown in Figure 2-40 with $C_{L2} = 1 \times 10^{-4}$ ft/$\sqrt{\text{min}}$. Compared with those in Figure 2-38, the transition time to the final 3/2-slope in Figure 2-40 is much earlier, and most curves in this plot do not have early 3/2-slope straight line, unit slope line instead.

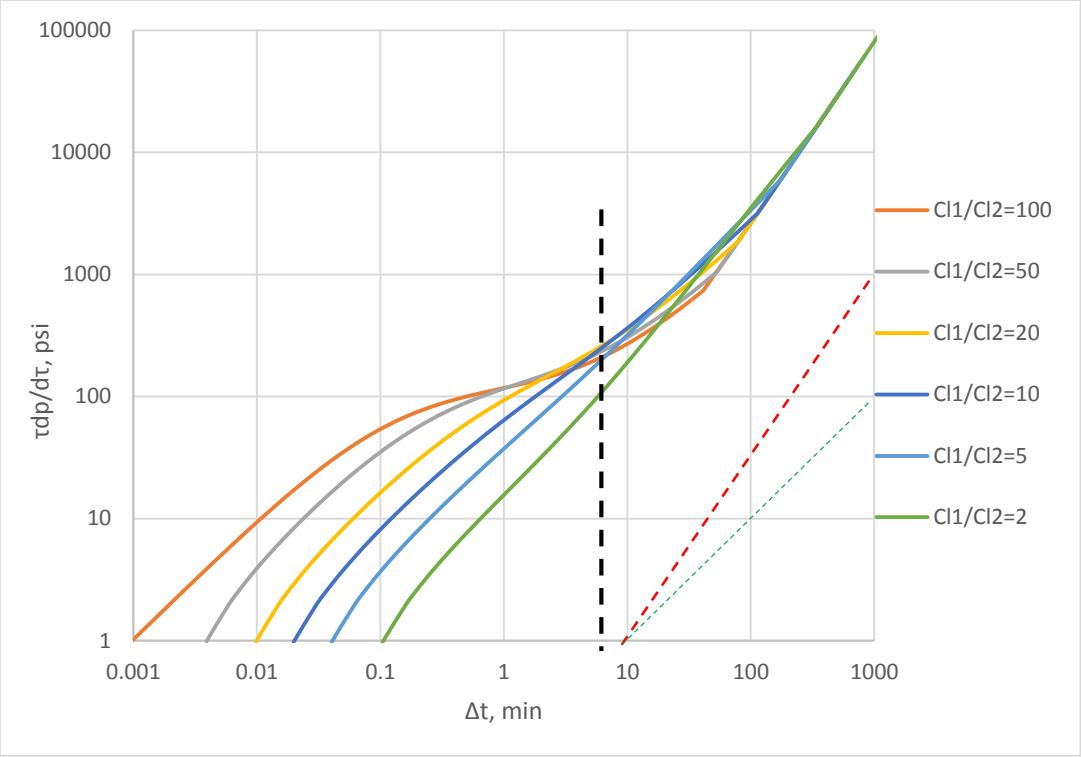

Figure 2-40 $\tau dp/d\tau$ plot for PDL with variable leakoff coefficient (C_{L2} = 1×10^{-4} ft/√min)

Because both tip extension and PDL can have an early unit slope trend and a hump above the extrapolated straight line, there might be interpretation ambiguities. Three simulations, one with PDL and two with tip-extensions, are tested with the input data listed in Table 2-6. For these two tip-extension, one is assumed to have a limited tip growth after shut-in, at about 20%, while the other have a large length incremental ratio, at about 182%. The pressure decline profiles are exhibited in Figure 2-41 Bottomhole pressure falloff curve and their diagnostic plots in Figure 2-42 and Figure 2-43.

Table 2-6 Input data for both PDL and Tip-extension case

Fracture model	PKN
α	4/5
t_p, minute	5
q_p, bbl/minute	6
r_p	1
p_{ws} or ISIP, psi.	6000
E', psi.	5×10^6
C_{L2} or C_{Lm}, ft/$\sqrt{\text{min}}$	1×10^{-4}
h_f, ft.	50
PDL	
C_{L1}, ft/$\sqrt{\text{min}}$	1×10^{-3}
p_{fo}, psi.	5800
Tip extension – short extension	
c	-0.01
Δt_{teD}	1
Tip extension - long extension	
c	0.01
Δt_{teD}	3

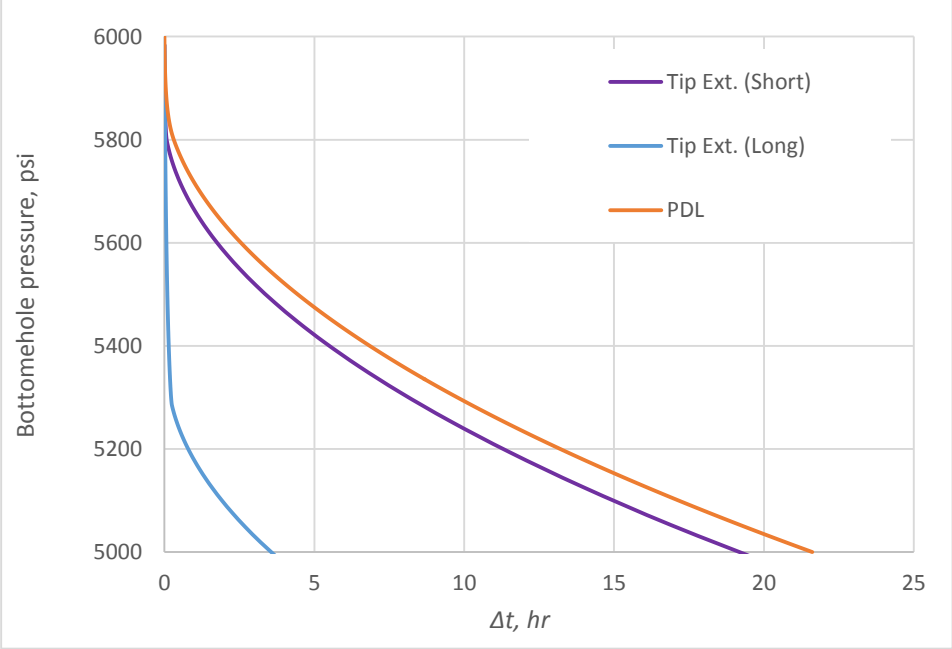

Figure 2-41 Bottomhole pressure falloff curve of PDL and tip-extensions

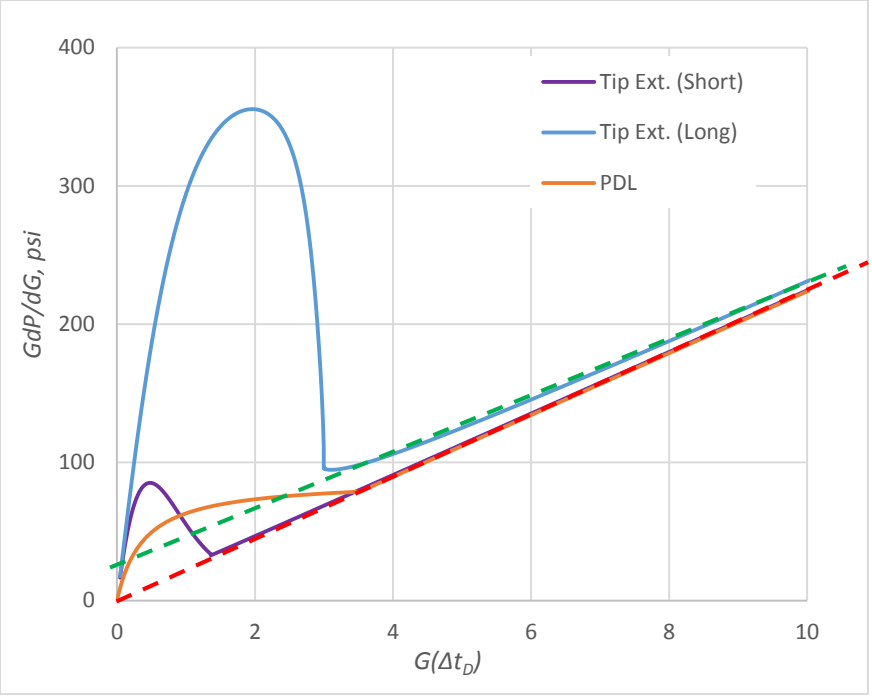

Figure 2-42 Gdp/dG plot for PDL and tip-extensions

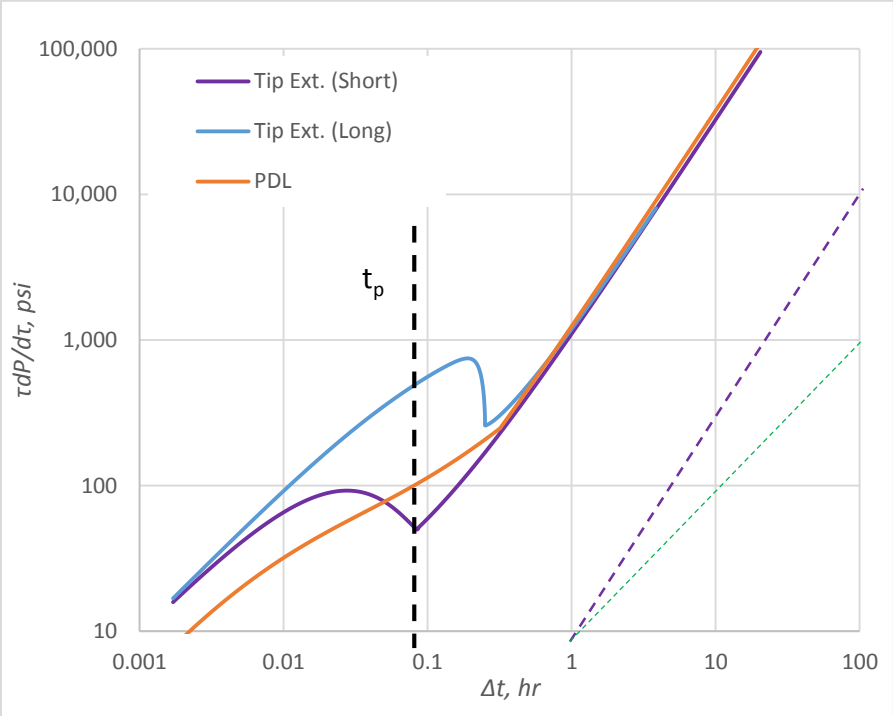

Figure 2-43 $\tau dp/d\tau$ plot for PDL and tip-extensions

We can find that curve shapes in both diagnostic plots are similar, it seems to be difficult to distinguish between these two leakoff mechanisms. Here, several points will be introduced to distinguish PDL with tip extension behavior. To begin with, the curve after the end of tip-extension should approach to its asymptote, which can be drawn through the origin and shown as the red dashed line in Figure 2-42. Or, an extrapolated line catching limited curve after the tip-extension lies above the origin, shown as the red line in Figure 2-42. This feature is especially obvious for the case with large tip-extension. Besides, tip-extension typically has a much faster pressure decline at beginning than normal leakoff process, and it might be even faster than PDL phenomenon. Therefore, its pressure declines even more rapidly at early time after shut-in, as illustrated in Figure 2-41. However, for the case with limited tip-extension, its behavior is so close to the characteristic of PDL that it might be difficult to tell them apart.

In summary, pressure solution for PDL behavior has been developed in this section, and it can be used to estimate initial leakoff coefficient at early time after shut-in when natural fractures are reopened. Also, if there multiple sets of natural fissures are connected, which can be observed by multiple-closure events, the leakoff coefficient for each specific set of natural fractures are able to be calculated out. From the simulation result, it can be concluded that the start point of the later normal leakoff, indicated by 3/2-slope in log-log diagnostic plot or the extrapolated straight line through the origin, could be picked as the closure natural fracture. Depending on the closure time of natural fissures, their closing process could have a unit slope in log-log diagnostic plot if it

closes before $\Delta t_D = 1$, or a 3/2-slope after $\Delta t_D = 10$. Another important issue is that it might be ambiguous between PDL and tip extension (with a limited fracture growth after shut-in).

2.5 The decoupled fracture model

For both fissures related PDL models discussed above, the fluid flow into natural fractures are treated as leakoff from main fracture. Although it is a simple way to investigate the non-ideal leakoff behavior before natural fracture close, some physical process is ignored in both models, like the leakoff process from natural fractures into formation matrix. Therefore, it is necessary to decouple the leakoff process into two parts: one is the matrix leakoff from main fracture, and the other is that from natural fractures. In this way, the role of both natural fracture and main fracture properties in fluid leakoff and pressure transient can be investigated separately. Besides pressure dependent leakoff, this model can also be extended to analyze the behavior of transverse storage effect, which will be discussed in the later context.

2.5.1 Natural fractures with constant leakoff coefficient and fracture compliance

In this model, natural fissures and main fracture are treated separately, but they share the same pressure system and material balance function, as depicted in Figure 2-44. We first assume that all properties of natural and main fractures listed in Figure 2-44 are constant. Besides, natural fractures will totally close and lose its volume at or below its opening/closure pressure, p_{fo}, and also no more fluid can leak into it when it

closes. The fracture compliances for main fracture and natural fissures could be different but both are constant.

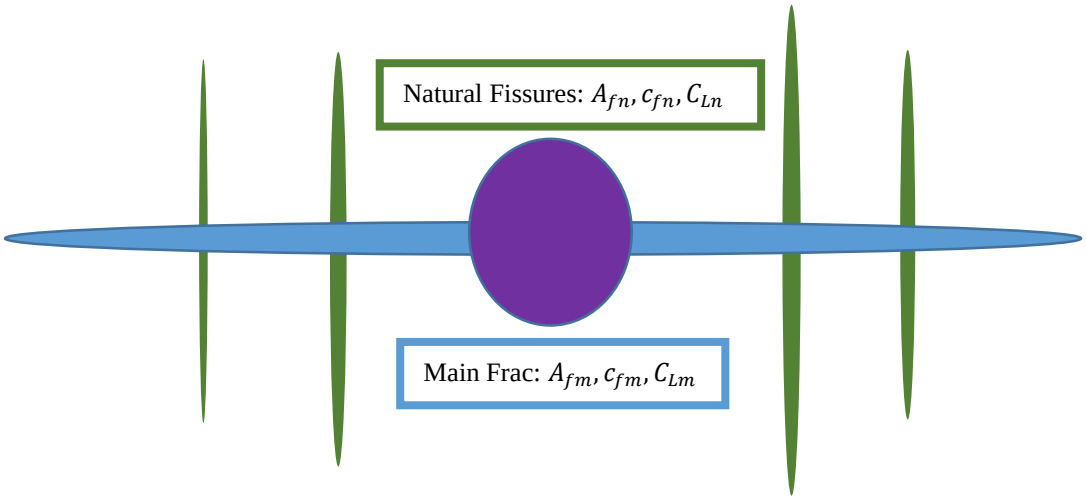

Figure 2-44 The sketch of decoupled natural and main fracture system

The material balance function for this model can be written as,

$$V_{l,mf} + V_{frac,mf} + V_{l,nf} + V_{frac,nf} = V_p \tag{2.58}$$

where,

$V_{l,mf}$ is the cumulative leakoff volume from main fracture;

$V_{frac,mf}$ is the volume of main fracture;

$V_{l,nf}$ is the cumulative leakoff volume from all natural fissures;

$V_{frac,nf}$ is the total volume of all natural fissures;

For simplicity, all natural fissures are treated as one single fracture which initiate at the same time as the main fracture. Then, before the closure of natural fissures, $V_{l,mf}$, $V_{l,nf}$ can be related with pressure change by Eq. (1.14), and $V_{frac,mf}$, $V_{frac,nf}$ can be

expressed as a relationship with pressure with Eq. (1.6). After differentiation with respect to time, Eq. (2.58) can be written as,

$$\frac{d\Delta p_w}{d\Delta t_D} = \frac{2r_p\sqrt{t_p}\left(C_{Lm}A_{fm} + C_{Ln}A_{fn}\right)}{c_{fm}A_{fm} + c_{fn}A_{fn}} \frac{dg(\Delta t_D, \alpha)}{d\Delta t} \qquad 0 \le \Delta t_D \le \Delta t_{fcD} \tag{2.59}$$

where, Δt_{fcD} is the dimensionless time when natural fissures close or $p_w = p_{fo}$. The pressure solution can then be developed as,

$$p_{ws} - p_w(\Delta t_D) = \frac{\pi r_p\sqrt{t_p}\left(C_{Lm}A_{fr} + C_{Ln}\right)}{2\left(c_{fm}A_{fr} + c_{fn}\right)} G(\Delta t_D, \alpha) \qquad 0 \le \Delta t_D \le \Delta t_{fcD} \tag{2.60}$$

where, A_{fr} is the surface area ratio between main fracture and total natural fracture,

$$A_{fr} = \frac{A_{fm}}{A_{fn}} \tag{2.61}$$

After fracture pressure decreasing below p_{fo}, natural fissures totally close on their faces and will not take any fluid from main fracture, so for $p_w < p_{fo}$, $V_{l,nf} = 0$ and $V_{frac,nf} = 0$. Then, similar to the derivation of Eq. (2.60), the pressure solution for $p_w \le p_{fo}$ can be written as,

$$p_{fo} - p_w(\Delta t_D) = \frac{\pi r_p\sqrt{t_p}C_{Lm}}{2c_{fm}}\left[G(\Delta t_D, \alpha) - G\left(\Delta t_{fcD}, \alpha\right)\right] \qquad \Delta t_D \ge \Delta t_{fcD} \tag{2.62}$$

Δt_{fcD} in Eq. (2.62) can be calculated out from Eq. (2.60). Bourdet derivative then can be calculated as follows.

$$\tau\frac{d\Delta p_w}{d\tau}=-2r_p\sqrt{t_p}\left(\frac{C_{Lm}A_{fr}+C_{Ln}}{c_{fm}A_{fr}+c_{fn}}\right)\left(\Delta t_D+{\Delta t_D}^2\right)f(\Delta t_D,\alpha)$$
$$0\le\Delta t_D\le\Delta t_{fcD} \tag{2.63}$$

$$\tau\frac{d\Delta p_w}{d\tau}=-2r_p\sqrt{t_p}\left(\frac{C_{Lm}}{c_{fm}}\right)\left(\Delta t_D+{\Delta t_D}^2\right)f(\Delta t_D,\alpha)\qquad \Delta t_D\ge\Delta t_{fcD} \tag{2.64}$$

Comparing the Bourdet derivative with that of normal leakoff in Eq. (1.30), we can find that the only difference for Eq. (2.63) is the term in the first parentheses. This term includes the properties of both natural and main fracture. Eq. (2.63) can be reduced to Eq. (1.30) if the volume of natural fractures is assumed to be zero.

It is obviously that the only difference between Eq. (2.63) and Eq. (2.64) is the term in their first parentheses in the left, $\frac{C_{Lm}A_{fr}+C_{Ln}}{c_{fm}A_{fr}+c_{fn}}$ and $\frac{C_{Lm}}{c_{fm}}$, which is the essential reason for the shape of the diagnostic plots. In other words, the hump, belly shape or straight line curve of the semi-log G-function is determined by the ratio of leakoff rate over the reduction rate of fracture volume. Mathematically, the ratio in decoupled fracture model can be expressed as,

$$r\left(A_{fr},C_{Lm},C_{Ln},c_{fm},c_{fn}\right)=\frac{C_L}{c_f}=\begin{cases}\left(\dfrac{A_{fr}+C_{Ln}/C_{Lm}}{A_{fr}+c_{fn}/c_{fm}}\right)\dfrac{C_{Lm}}{c_{fm}} & p_w\ge p_{fo}\\ \dfrac{C_{Lm}}{c_{fm}} & p_w<p_{fo}\end{cases} \tag{2.65}$$

where, C_L and c_f are leakoff coefficient and fracture compliance for the whole fracture system. Natural fracture is included in the system before its closure. The ratio is weighted by fracture surface area by adding A_{fr} into the function.

To simplify Eq. (2.65), the following ratios are defined.

$$C_{Lr} = \frac{C_{Lm}}{C_{Ln}} \tag{2.66}$$

$$c_{fr} = \frac{c_{fm}}{c_{fn}} \tag{2.67}$$

Then, Eq. (2.65) can be written as,

$$r(A_{fr}, C_{Lr}, c_{fr}) = \frac{C_L}{c_f} = \begin{cases} \left(\dfrac{A_{fr} + 1/C_{Lr}}{A_{fr} + 1/c_{fr}}\right)\dfrac{C_{Lm}}{c_{fm}} & p_w \geq p_{fo} \\ \dfrac{C_{Lm}}{c_{fm}} & p_w < p_{fo} \end{cases} \tag{2.68}$$

From Eq. (2.68), we can conclude that the signature of diagnostic plots depends on the relative amplitude of these three ratios, A_{fr}, C_{Lr} and c_{fr}.

If occasionally, $\frac{A_{fr}+1/C_{Lr}}{A_{fr}+1/c_{fr}} > 1$, or $c_{fr} > C_{Lr}$, high leakoff rate through natural fracture will result in PDL or multiple-closure behavior; if $\frac{A_{fr}+1/C_{Lr}}{A_{fr}+1/c_{fr}} = 1$, or $c_{fr} = C_{Lr}$, Eq. (2.63) and Eq. (2.64) will be identical, and the diagnostic curve will be exactly same with that in normal leakoff; if $\frac{A_{fr}+1/C_{Lr}}{A_{fr}+1/c_{fr}} < 1$, or $c_{fr} < C_{Lr}$, the storage effect of natural fissures, or transverse storage effect, indicated by the belly shape curve below extrapolated straight line through the origin, will be observed. The following simulation result will demonstrate this finding.

A simple simulation here is to show the effect of leakoff from natural fissures on the pressure transient behavior. For the following 3 cases in this section, the only different input factor is the leakoff coefficient from natural fractures into matrix. Besides, for all 3 cases, the fracture compliance and surface area of natural fracture equals to these of main fracture.

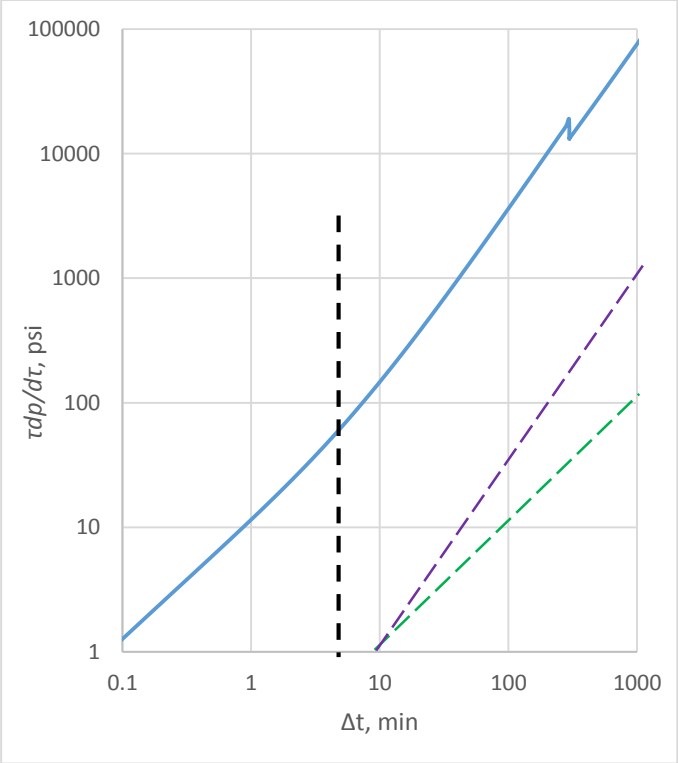

Figure 2-45 Log-log diagnostic Bourdet derivative plot for the Decoupled Fracture Model with 2 constant leakoff coefficients (C_{Lm}=1/2C_{Ln})

For the first case, the leakoff coefficient of natural fissures is 2 times of that of main fracture, which means that fluid leaks off faster from natural fissures into matrix than that from main fracture. A multiple-closure signature shows up in both log-log diagnostic plot and G-function plot, as shown in Figure 2-45 and Figure 2-46, respectively. The dramatic drop at these two plots indicate the closure event of natural fissures, and the bottomhole pressure at this point could be picked as opening/closure pressure of nature fractures. The inconsistency of two parts before and after the dramatic drop is caused by the assumptions that natural fracture has a constant fracture compliance, leakoff coefficient and fracture surface area before its closure, and all drop to zero

immediately after that. To smoothen the curve, the transient behavior of these three parameters should be taken into consideration during closing of natural fractures. In the following sections, more detail will be discussed for different decline behaviors of fracture compliance, leakoff coefficient (PDL) and fracture surface area.

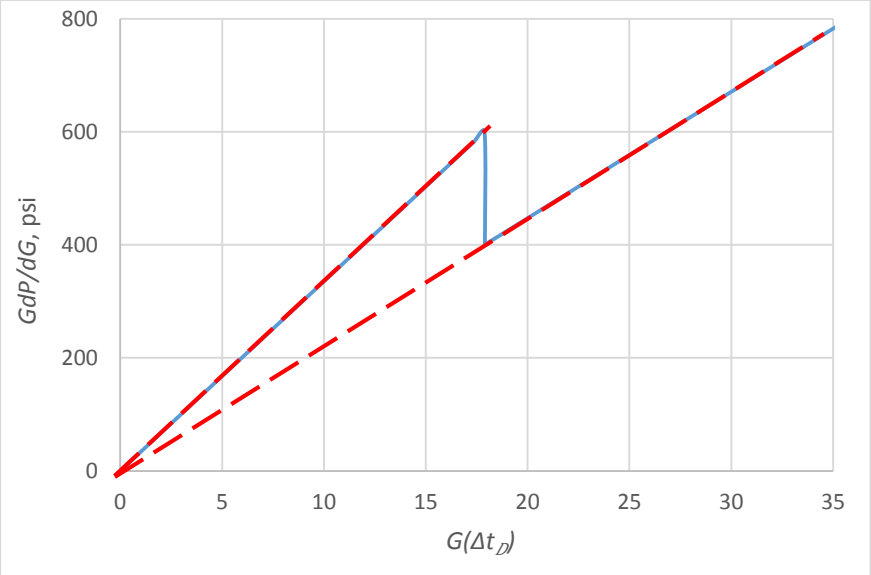

Figure 2-46 G-function plot for the Decoupled Fracture Model with 2 constant leakoff coefficients ($C_{Lm}=1/2C_{Ln}$)

For the second case, the leakoff coefficient of natural fractures is same as that of main fracture, which indicates that fluid in natural fissure leaks off into formation at the same rate with that in main fracture. The diagnostic plots in Figure 2-47 and Figure 2-48 show that, the pressure behavior of this case is exactly same as that in normal leakoff where no natural fractures are involved in the leakoff system. In other words, natural

fractures could be connected during the treatment even when the apparent normal leakoff behavior is observed.

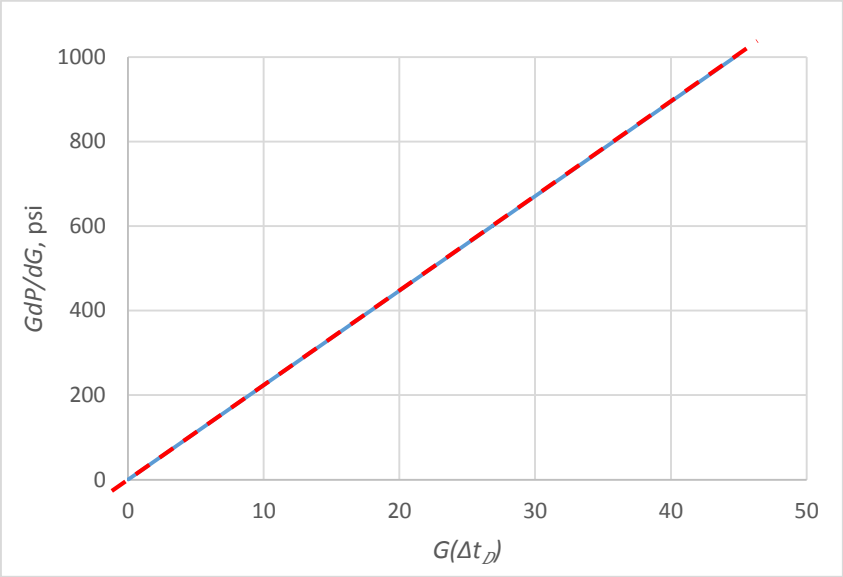

Figure 2-47 G-function plot for the Decoupled Fracture Model with 2 constant leakoff coefficients (C_{Lm}= C_{Ln})

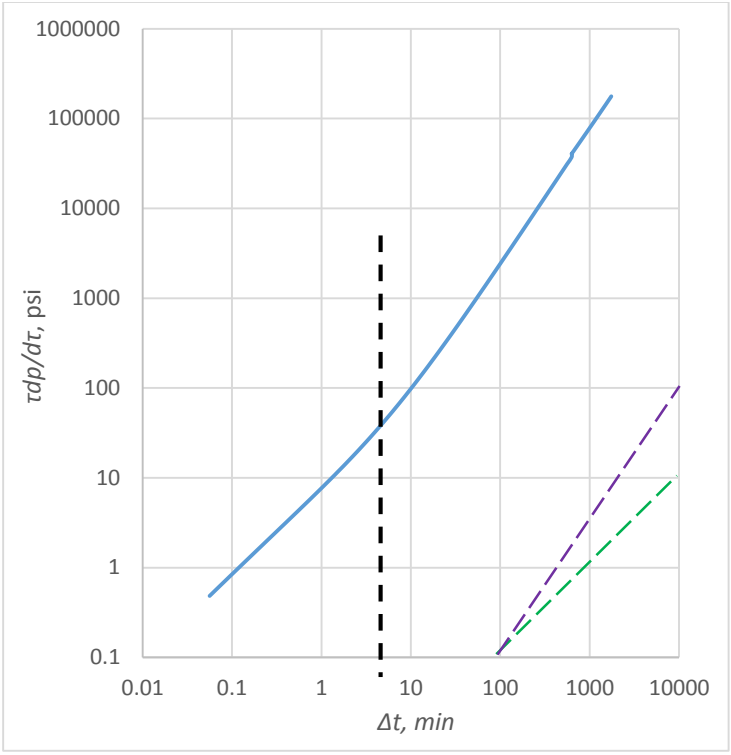

Figure 2-48 Log-log diagnostic Bourdet derivative plot for the Decoupled Fracture Model with 2 constant leakoff coefficients (C_{Lm}= C_{Ln})

For the third case, the leakoff coefficient of natural fissures is half of that of main fracture. It indicates that natural fissures has a lower leakoff rate, which is supposed to be the main factor for the transverse storage effect, as discussed before. Again, the dramatic drop in the diagnostic plots is the indication of closure event of natural fractures. The inconsistency is caused by the assumption of inconsistency of nature fracture compliance, leakoff coefficient and total fracture surface area. If the broken curve can be smoothen, the concave-up curve in both log-log diagnostic plot and G-function plot can be interpreted as transverse storage behavior.

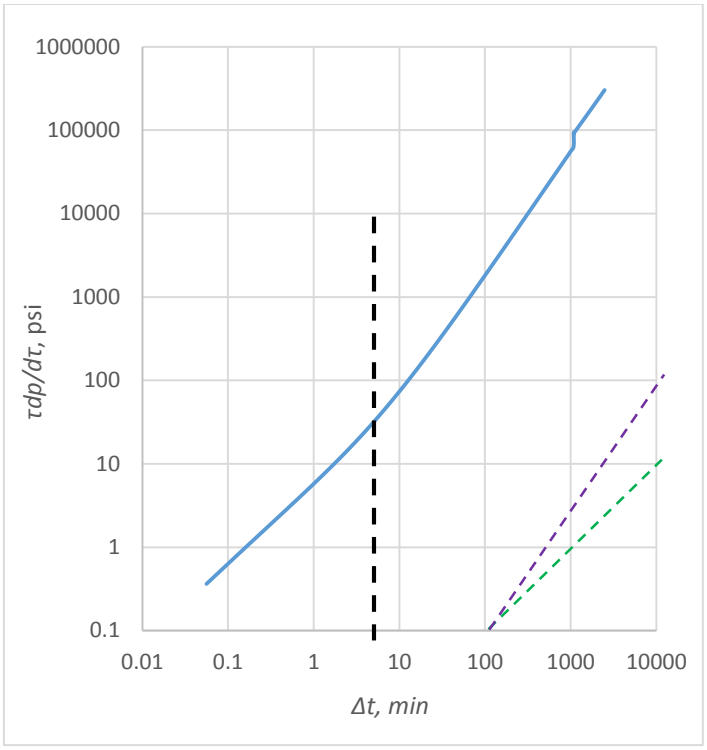

Figure 2-49 G-function plot for the Decoupled Fracture Model with 2 constant leakoff coefficients (C_{Lm}= 2C_{Ln})

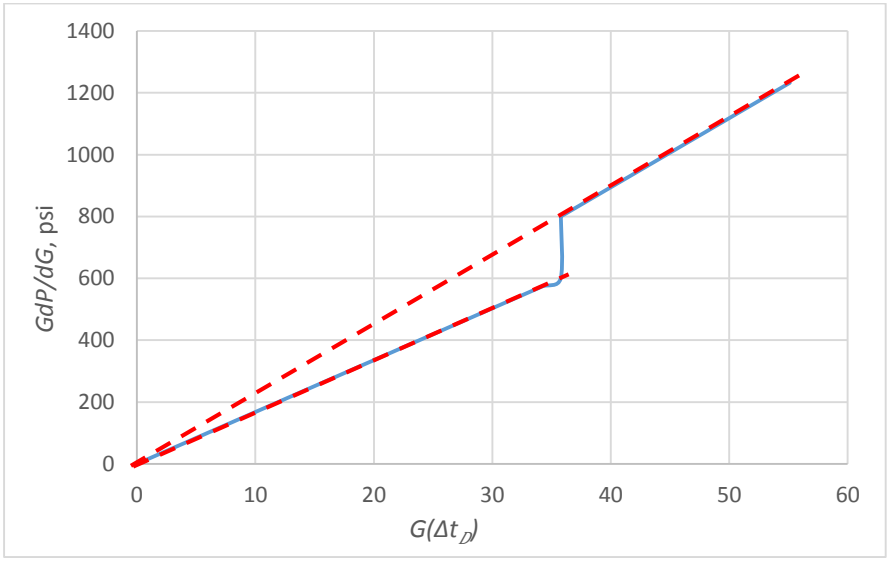

Figure 2-50 Log-log diagnostic Bourdet derivative plot for the Decoupled Fracture Model with 2 constant leakoff coefficients (C_{Lm}= 2C_{Ln})

From these 3 cases, we can conclude that, depending on properties of natural fissures, they could behavior as PDL, transverse storage or even normal leakoff. Besides the leakoff coefficient discussed in this section, fracture compliance and fracture surface ratio could also have similar effect on the pressure transient.

2.5.2 Natural fissures with pressure-dependent leakoff (PDL) coefficient and constant fracture compliance

As has been proposed by many researchers, the reopened natural fissures could reserve a part of flow capacity even when they close on their surfaces after their internal pressure drops below closure pressure. These "closed" natural fractures could be propped open in a small scale by unconformable contact between surfaces or by formation fines (Ehlig-Economides and Economides 2011; McClure et al. 2014). Although the residual aperture and conductivity is fairly limited, those "closed" natural fractures still could be much more permeable than the formation matrix (Branagan et al. 1996), especially in tight formation. Therefore, in this model, a residual natural fracture leakoff coefficient, C_{Ln2} in Eq. (2.69), is assigned for the "closed" natural fissures. Since these natural fissures typically suffers larger confining stress and have poorer flow capacity than main fractures, the residual leakoff coefficient, C_{Ln2}, is supposed to be much smaller than that of main fractures. Besides, the storage volume of natural fissures, is neglected after closure with the assumption that void volume between two natural fracture faces is very limited and does not change much with the declining pressure. Before closure, the leakoff coefficient of natural fissures is pressure dependent.

Meanwhile, the matrix leakoff coefficient from main fracture is assumed to be constant during pressure falloff. Similar to variable leakoff coefficient model in Eq. (1.47), the leakoff coefficient model of natural fracture can be expressed as,

$$C_{Ln}(p_w) = \begin{cases} C_{Ln1} \exp\left(-\beta \dfrac{p_{ws} - p_w}{p_{ws} - p_{fo}}\right) & p_w > p_{fo} \\ C_{Ln2} & p_w \le p_{fo} \end{cases} \tag{2.69}$$

where,

$$C_{Ln1} = C_{Ln}(p_w = p_{ws}) \tag{2.70}$$

Starting from the material balance function as shown in Eq. (2.58), the pressure solution can be derived as following,

$$\begin{aligned} & p_{ws} - p_w(t) \\ & = \frac{(p_{ws} - p_{fo})}{\ln\left(\frac{C_{Ln1}}{C_{Ln2}}\right)} \ln\left\{\left(1 + \frac{C_{Ln1}}{A_{fr}\, C_{Lm}}\right)\left(\frac{C_{Ln1}}{C_{Ln2}}\right)^{\frac{2A_{fr}\, C_{Lm}\, r_p\sqrt{t_p}\,[g(\Delta t_D,\alpha) - g(0,\alpha)]}{(p_{ws} - p_{fo})(A_{fr}\, c_{fm} + c_{fn})}}\right. \\ & \qquad \left. - \frac{C_{Ln1}}{A_{fr}\, C_{Lm}}\right\} \qquad 0 \le \Delta t_D \le \Delta t_{fcD} \end{aligned} \tag{2.71}$$

$$\begin{aligned} p_{ws} - p_w(t) &= \frac{\pi r_p \sqrt{t_p}\left(C_{Lm} A_{fr} + C_{Ln2}\right)}{2 c_{fm} A_{fr}} \left[G(\Delta t_D, \alpha) - G\left(\Delta t_{fcD}, \alpha\right)\right] \\ & \qquad \Delta t_D \ge \Delta t_{fcD} \end{aligned} \tag{2.72}$$

Eq. (2.71) can be reduced to Eq. (2.60) by assuming that the leakoff coefficient of natural fractures is constant, or $C_{Ln1} = C_{Ln2}$, and can also be reduced to Eq. (2.55) if the leakoff only happens at main fractures with same leakoff model described in Eq.

(2.69) or Eq. (1.47). Therefore, mutual corroboration of these models proves their consistence.

The Bourdet derivatives for this case are so complicated that they will not written in an analytical form in this context.

One simulation assuming $C_{Lm} = C_{Ln1} = 10C_{Ln2}$ is taken as an example, and the rest input parameters are listed in Table 2-7. Figure 2-51 and Figure 2-52 are its diagnostic plots. We can find that transverse storage behavior shows up because $C_{Lm} \geq C_{Ln}$, and PDL feature can also be observed from the concave-down curve in the first part of G-function.

Table 2-7 Input data for simulations of decoupled fracture model with variable C_{Ln}

t_p, minute	5
q_p, bbl/minute	6
r_p	1
p_{ws} or ISIP, psi.	6000
A_{fr}	1
E', psi.	5×10^6
Main fracture	
Fracture model	PKN
h_{mf}, ft.	50
S_{min}, psi.	5000
C_{Lm}, ft/$\sqrt{\text{min}}$	2×10^{-4}
Nature fracture	
Fracture model	PKN
h_{nf}, ft.	50
p_{fo}, psi.	5400
C_{Ln1}, ft/$\sqrt{\text{min}}$	2×10^{-4}
C_{Ln2}, ft/$\sqrt{\text{min}}$	2×10^{-5}

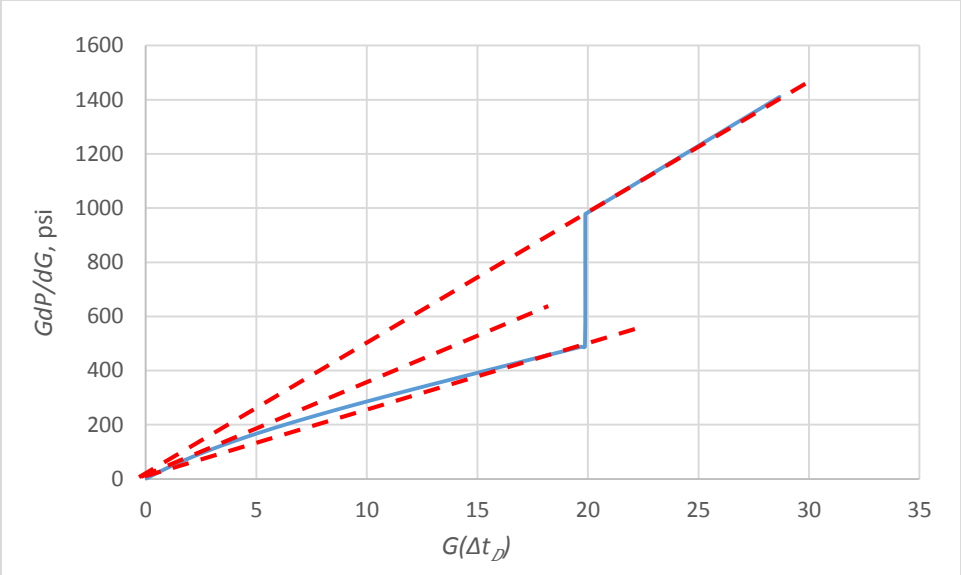

Figure 2-51 G-function plot for the Decoupled Fracture Model with variable C_{Ln}

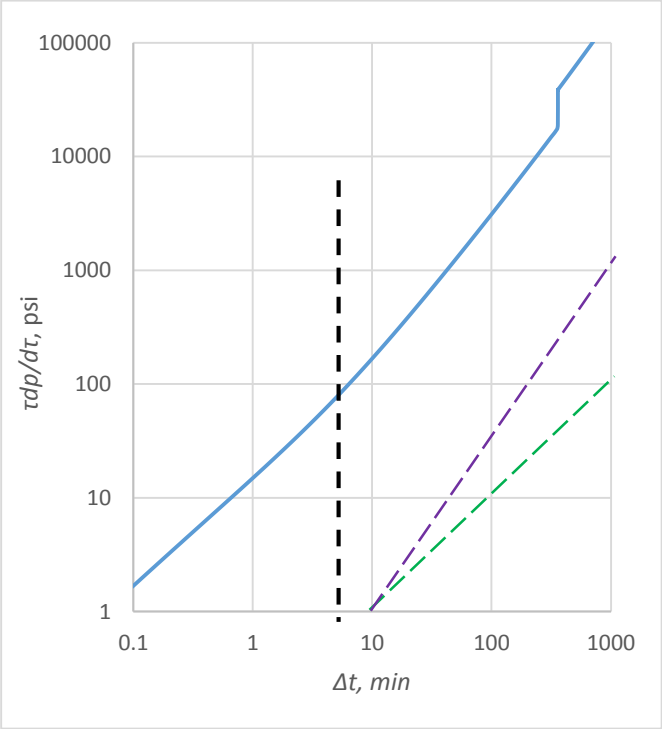

Figure 2-52 Log-log diagnostic plot for the Decoupled Fracture Model with variable C_{Ln}

Although the inconsistency of system leakoff coefficient during and after natural fracture closure has been removed by introducing a variable leakoff coefficient before closure and a residual value after that, as expressed by Eq. (2.69), curves in both diagnostic curves are not consistent in the connection. Two separated straight behavior can be picked, and each is controlled by one distinct leakoff behavior. It indicates that adjusting leakoff mechanism is not enough to smooth the curve, and the other factors that should be responsible to the broken diagnostic curve are compliance and total surface area of natural fracture. Since both factors are assumed to be constant before closure, and assigned to be zero after that without any gradual transition. To develop a model that can match field data with a smooth curve, a declining fracture compliance or surface area should be assigned to the natural fissure system.

2.5.3 Natural fractures with pressure-dependent fracture compliance and leakoff coefficient

As discussed in previous model, the discontinuity in diagnostic plots is resulted from the assumption that the natural fracture compliance and surface area are constant during closure, and both jump to zero immediately when pressure drops below the closure pressure. It is an ideal free closing process. Since the possible existence of fracture surface unconformity, the closing process could be more complicated. With the declining of internal pressure in the natural fracture, two opposite fracture surfaces will approach to each other. These unconformable asperities, or toughness in both sides of fractures, are supposed to first contact each other before other part. Then more and more

stress, which originally is loaded on the liquid in the fracture, will be transferred onto these contacted asperities. Fracture closing rate will be much slowed even when the leakoff rate is almost same with before. Mathematically, natural fracture compliance is reduced from its original value all the way to zero.

As described in last paragraph, many factors are involved during the closing process, like altitude, strength and number of asperities. Currently there is few theoretical or experienced models available on this issue. McClure and Ribeiro have proposed a similar model for this phenomenon (McClure et al. 2014; Ribeiro and Horne 2013). In their models, fracture is assumed to close freely when fracture aperture larger than a certain width. Below it, asperities will contact with each other and take more and more loading. An experienced function proposed by Barton and Bandis (Bandis et al. 1983; Barton et al. 1985) is employed to describe the relationship between stress and strain during the closure of joints. Barton and Bandis model is based on plenty of laboratory tests on dry rock joints. According to McClure (McClure et al. 2014), the relationship between the "in contact" fracture width with the applied effective stress can be written as,

$$w_{fn} = \frac{w_{fr0}}{1 + 9\sigma_n'/\sigma_{n,ref}} \tag{2.73}$$

When asperities start to touch each other, fracture has a width at w_{fr0}, which is named as residual void aperture by McClure (McClure et al. 2014), and the fracture pressure at this time is same to closure pressure, and the effective pressure (σ_n') at this

pressure point equals to zero. $\sigma_{n,ref}$ is the effective stresses applied to reduce the "in contact" joint width by 90% of residual void aperture.

Since Eq. (2.73) should be consistent with Eq.(1.2) at the pressure point when the effective pressure (σ_n') is zero. By combining these equations, the relationship between w_{nf0} and $\sigma_{n,ref}$ in Eq. (2.73) with c_f in Eq.(1.2) is,

$$\sigma_{n,ref} = \frac{9 w_{fr0}}{c_{fn0}} \tag{2.74}$$

where, c_{nf0} is the natural fracture compliance when the fracture is open and is closing freely.

Then the "in contact" fracture compliance can be derived as,

$$c_{fn} = c_{nf0} \left(\frac{w_{fr0}}{w_{fr0} + c_{nf0}\, \sigma_n'} \right)^2 \tag{2.75}$$

where the effective pressure, σ_n', can be written as,

$$\sigma_n' = \sigma_{resistant} - p_w(t) \tag{2.76}$$

Although this model has been tried in some issues on hydraulic fracturing mechanics, several fatal defects need to be pointed out, which probably the main reason for the disagreement of its simulation result with the real data. First of all, Barton and Bandis model is based on the statistic data of experimental tests on dry rock joint. With the increasing loading, deformation at early time only happens on the contact roughness. While, hydraulic fractures are more like to be an undrained porous media. The pressurized liquid is able to support the fracture, redistribute pressure and stress around the fracture, and also able to soften strength of the saturated rock asperities in some

cases. Poroelastic effect cannot be excluded by just taking effective normal stress as shown in Eq. (2.76). Besides, it is difficult to determine residual void aperture (w_{nf0}), and the result is pretty sensitive to this parameter. Moreover, it is arbitrary to pick closure pressure at the point when asperities start to contact. Since there is still a residual aperture at this pressure point, fluid pressure should be higher than the closure pressure for the majority part of fracture except for limited toughness area. And this error will be enlarged for the cases with big residual void aperture (w_{nf0}). Therefore, Barton and Bandis model is far from adequate to simulate the closing process of a "in contact" hydraulic fracture.

Due to so many uncertainties associated with Barton and Bandis model, a more comprehensive and practical model on decline behavior of natural fracture compliance is hypothesized as Eq. (2.77). In this model, natural fracture compliance decreases from its initial value at ISIP to zero at closure pressure. After that, natural fracture is assumed to be totally closed on its surface.

$$c_{fn}(p_w) = \frac{\mathrm{Exp}(b\ p_w/p_{ws}) - \mathrm{Exp}(b\ p_{fo}/p_{ws})}{\mathrm{Exp}(b\ ) - \mathrm{Exp}(b\ p_{fo}/p_{ws})} c_{fn0} \tag{2.77}$$

where, c_{fn0} is the natural fracture compliance at end of pumping. b is the coefficient which controls the decline rate of c_{fn}. Several sets of b are tested. Actually, almost all monotone decline behaviors can be simulated with different controlling coefficient, b.

Besides, it assumes that the leakoff coefficient from natural fractures into matrix follows the exponential decline model described as Eq. (2.69), same with that in last section.

Based on the material balance function, a semi-analytical model is built to calculate pressure decline curves in different decline behaviors of natural fracture compliance.

As has been mentioned, if natural fractures are believed to be connected during injection, to preserve properties of natural fractures in the model, it is better to decouple the fracture system into natural and main fracture. Then, all of their properties can be studied separately or combined as a whole. With many more factors involved in the model than previous models, it is better to start with the sensitivity study on their impact on pressure response during pressure falloff.

1) Diagnostic plots for variable natural fracture compliance

The dilated natural fracture can not only increase fluid leakoff from main fracture, but can also enhance fracture storage volume. As suggested by Barree (Barree et al. 2009), transverse storage effect could be much more overwhelming than PDL even when the latter is pretty large. Similar result can be observed in our model. Figure 2-53 is semilog G-function diagnostic plot for the case that natural fracture has a higher leakoff rate than main fracture. It demonstrates that the belly shape of the diagnostic plot for transverse storage behavior could be caused by the reduction of natural fracture compliance, rather than by the relative small leakoff coefficient of natural fractures.

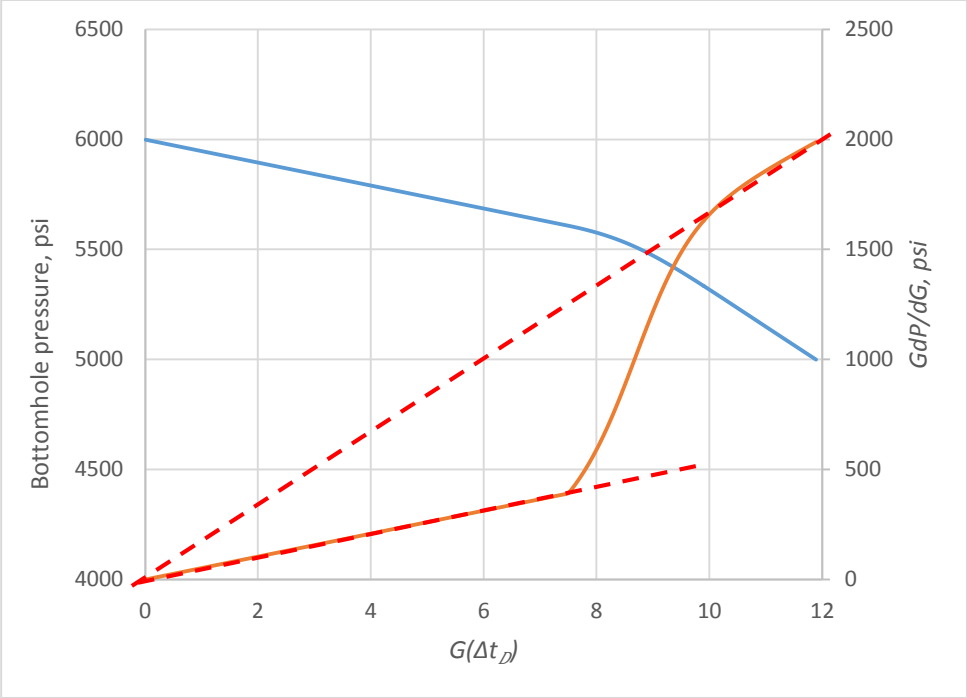

Figure 2-53 Gdp/dG plot for the decoupled fracture model ($C_{Ln} > C_{Lm}$)

2) Sensitivity study on decline behavior of natural fracture compliance (c_{fn})

Table 2-8 Input data for sensitivity study on te decline behavior of c_{fn}

h_f, ft.	50
E', psi.	5×10^6
p_{ws} or ISIP, psi.	6000
t_p, minute	5
p_{fo}, psi.	5400
S_{min}, psi.	5000
q_p, bbl/minute	6
α	4/5
A_{fr}	0.5
C_{Lm}, ft/$\sqrt{\text{min}}$	1×10^{-4}
C_{Ln1}, ft/$\sqrt{\text{min}}$	1×10^{-4}
C_{Ln2}, ft/$\sqrt{\text{min}}$	1×10^{-4}

First of all, the natural fracture is assumed to have an initial fracture compliance (c_{nf0}) at 1.571×10^{-5} ft/psi, which is pre-required by Barton and Bandis model in Eq. (2.73). The rest of input data is listed in Table 2-8. To see the impact of decline behavior of both models, the pressure-dependent leakoff behavior is excluded by assuming that natural fracture has a constant leakoff coefficient all the time.

For both Barton and Bandis model with different residual fracture widths (w_{fr0}) and exponential model with several decline coefficients (b), the pressure-dependent natural fracture compliance is plotted in Figure 2-54. The scattering lines consisting of dots are exponential model with different bs, while the other lines consisting of triangular are Barton and Bandis model with different w_{fr0}s. We can find that these decline behaviors generally follow similar trend. The major difference for two models is that the natural fracture compliance after closure is zero for exponential decline model, while it is not for Barton and Bandis model, and continues dissipating even when the internal pressure is lower than closure stress. Depending on the scale of asperities, different decline rates of fracture compliance are observed for Barton and Bandis model. Wider residual fracture aperture is more likely to take larger pressure drop before approaching to a relatively small and stable width. The variable compliance in this pressure range would have a great impact on the shape of diagnostic curve and the way to determine closure pressure, which will covered in detail in the following discussion.

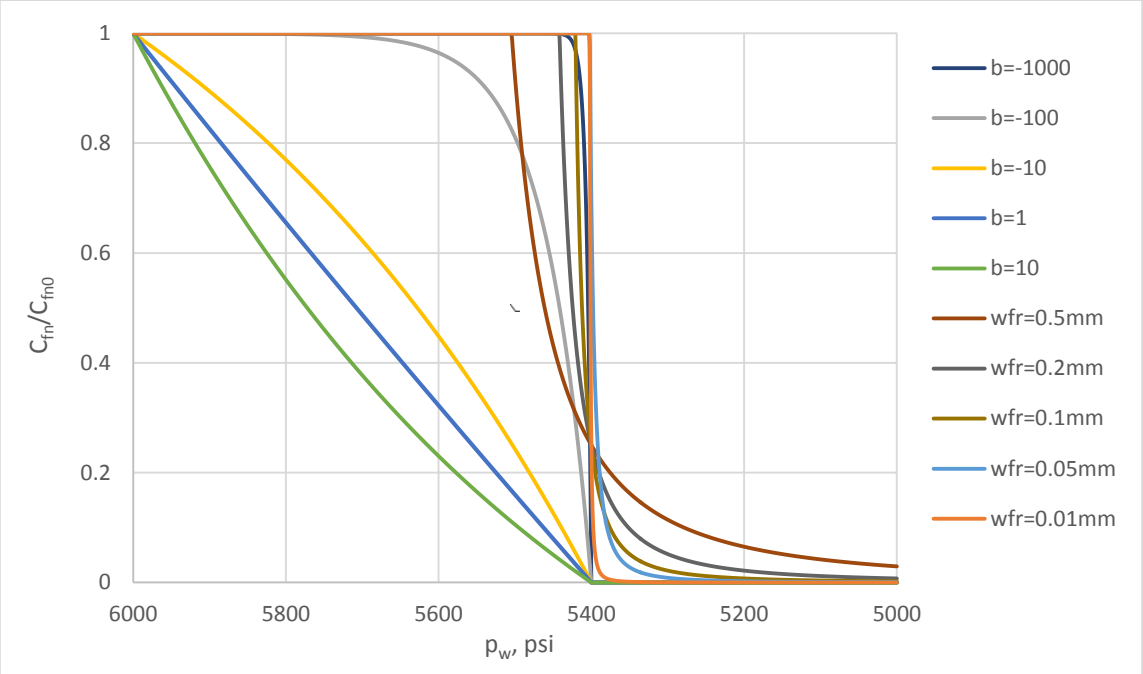

Figure 2-54 Pressure-dependent natural fracture compliance with different decline behaviors

Figure 2-55, Figure 2-57 are semilog G-function diagnostic plots for different decline behaviors in exponential and Barton and Bandis model, respectively. And, Figure 2-57 exhibits all the corresponding curve in log-log diagnostic plot. Generally speaking, the difference among all cases with different decline behaviors of C_{fn} is more transparent in semilog G-function plot, as shown in Figure 2-55 and Figure 2-56. Another finding is that in cases with a faster decline of C_{fn} at later time, like $b = -1000$ and -100 in exponential model and $w_{fr0} \leq 0.1$ mm in Barton and Bandis model, their concave-up semilog G-function curve tend to be deeper, and surge more rapidly to the final level at later time. As a comparison, cases with moderate decline rates, or with wide residual fracture apertures, are more likely to have shallow "belly"

curves. In practice, variable shapes of diagnostic plots has been observed frequently. The decline behavior of fracture compliance could be one of reasons.

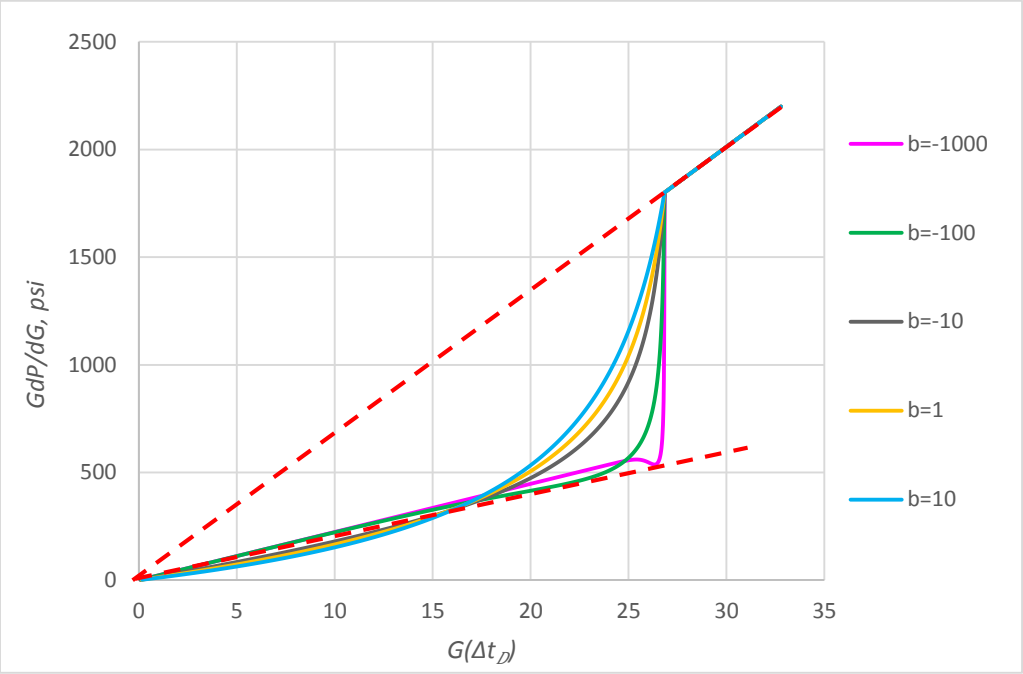

Figure 2-55 Gdp/dG plot for the decoupled fracture model with different decline behaviors of C_{fn} (Exponential decline model)

Another significant point can be found from Figure 2-55 and Figure 2-56 is that, two extrapolated straight lines can be drawn from each specific curve. As has been discussed before, the straight line indicates normal leakoff condition. Since fracture compliance does not change much at early time for both fracture compliance models, the leakoff at this time thus can be treated as normal leakoff, and it is the first extrapolated straight line. Furthermore, this part of curve can be taken advantage to estimate some natural fracture properties, like total natural fracture length. The second extrapolated

straight line happens at later time. After closure of natural fracture, fracture compliance will be a constant in exponential model, and will approach to a constant in Barton and Bandis model. Therefore, the situation is close to normal leakoff dominated by main fracture.

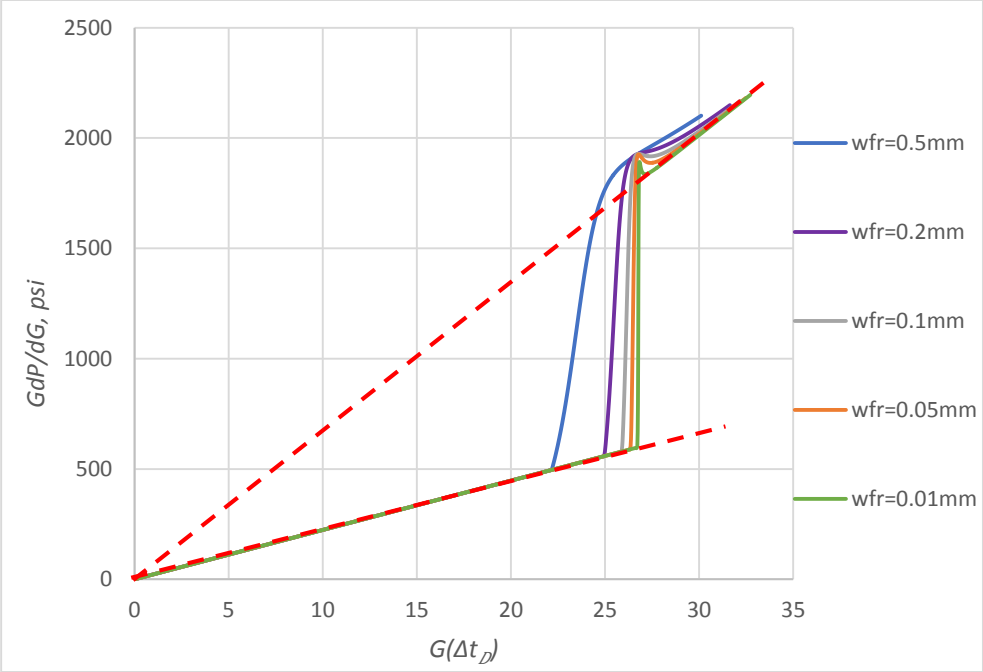

Figure 2-56 Gdp/dG plot for the decoupled fracture model with different decline behaviors of C_{fn} (Barton and Bandis model)

By comparing Figure 2-55 and Figure 2-56, we can find several differences between these two decline models of natural fracture compliance: exponential and Barton and Bandis model. First, the start point of the latter extrapolated straight line could be picked as the closure event according to exponential decline model. However, in Barton and Bandis model, it lies in the transition section between two extrapolated

straight lines, as denoted as the pink solid square in curves in Figure 2-56. Besides, because of the residual fracture aperture, fracture compliance will continue decreasing at later time when internal pressure is even lower than closure stress. In the semilog G-function plot in Figure 2-56, we can find that in the later time, it takes some time for the curve to approach to the final extrapolated straight line. And, more time is required for the fractures with wider residual fracture aperture.

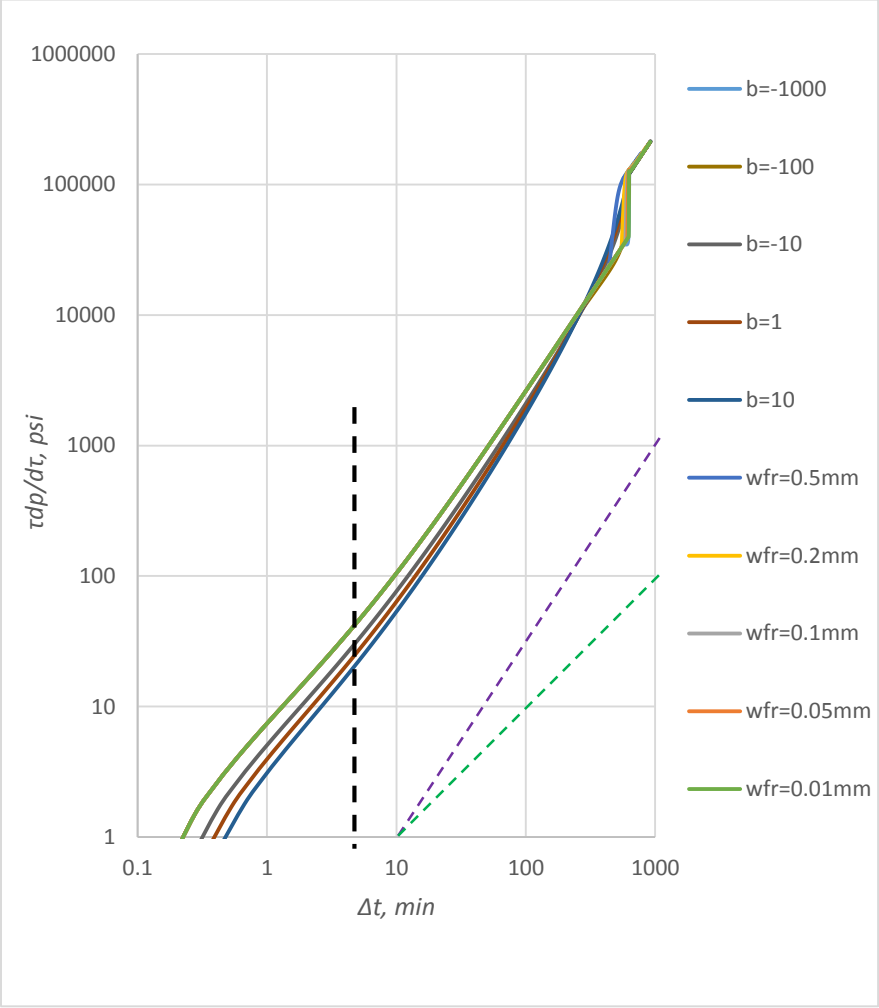

Figure 2-57 Log-log diagnostic plot for decoupled fracture model with different decline behaviors of C_{fn}

The log-log diagnostic plot for all decline behaviors of both fracture compliance models is shown in Figure 2-57. First of all, two straight lines with 3/2-slope can be found for each specific curve. These two straight lines are corresponding to these two extrapolated lines through the origin in semilog G-function plot in Figure 2-55 and Figure 2-56. Similarly, the first 3/2-slope line can be used to estimate total extension and closure stress of natural fracture, and the later to calculate these of main fracture.

3) Both leakoff coefficient and compliance of natural fractures are pressure-dependent

Table 2-9 Input data for simulations of decoupled fracture model with variable C_{Ln} and c_{fn}

r_p	1
h_f, ft.	50
E', psi.	5×10^6
p_{ws} or ISIP, psi.	6000
t_p, minute	5
p_{fo}, psi.	5400
S_{min}, psi.	5000
q_p, bbl/minute	6
α	4/5
A_{fr}	0.5
C_{Lm}, ft/$\sqrt{\text{min}}$	1×10^{-4}
C_{Ln1}, ft/$\sqrt{\text{min}}$	1×10^{-4}
C_{Ln2}, ft/$\sqrt{\text{min}}$	1×10^{-5}
Decline behavior of natural fracture compliance	Exponential decline model with $b = -100$

In this section, leakoff coefficient from natural fracture into matrix is assumed to decease with the shrinking fracture width, and approaches to a constant residual value, as

described in Eq. (2.69). One simulation is run with the input data listed in Table 2-9, and its diagnostic plots are shown in Figure 2-58 and Figure 2-59.

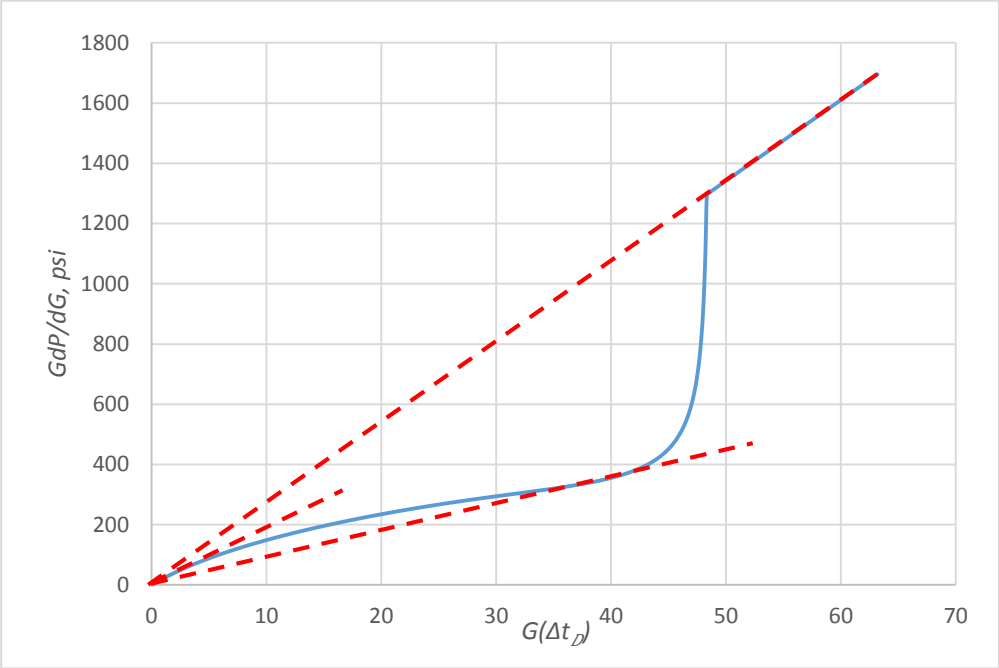

Figure 2-58 Gdp/dG plot for decoupled fracture model with pressure-dependent compliance and leakoff coefficient of natural fractures

It can be figured out that both PDL and transverse storage effect show up in both semilog G-function plot and log-log diagnostic plot, as shown in Figure 2-58 and Figure 2-59. The straight line in the semilog G-function plot at the very beginning time of falloff, or the straight line with unit slope in log-log plot, is the indication of high initial leakoff rate with almost constant fracture compliance in the natural fractures. The second extrapolated straight line through the origin in the semilog G-function plot, or the first straight line with 3/2-slope in log-log diagnostic plot, happens close to the end of PDL

and before the dramatically decline of natural fracture compliance. At this time, natural fracture has lost majority of its leakoff coefficient. Final leakoff coefficient and initial fracture compliance therefore could be estimated from data in this part. The last straight line in the semilog G-function plot, or the second straight line with 3/2-slope in log-log diagnostic plot, shows up when natural fractures have almost closed. Properties of main fracture, like closure pressure, fracture length and leakoff coefficient from main fracture, thus could be estimated from data in this section.

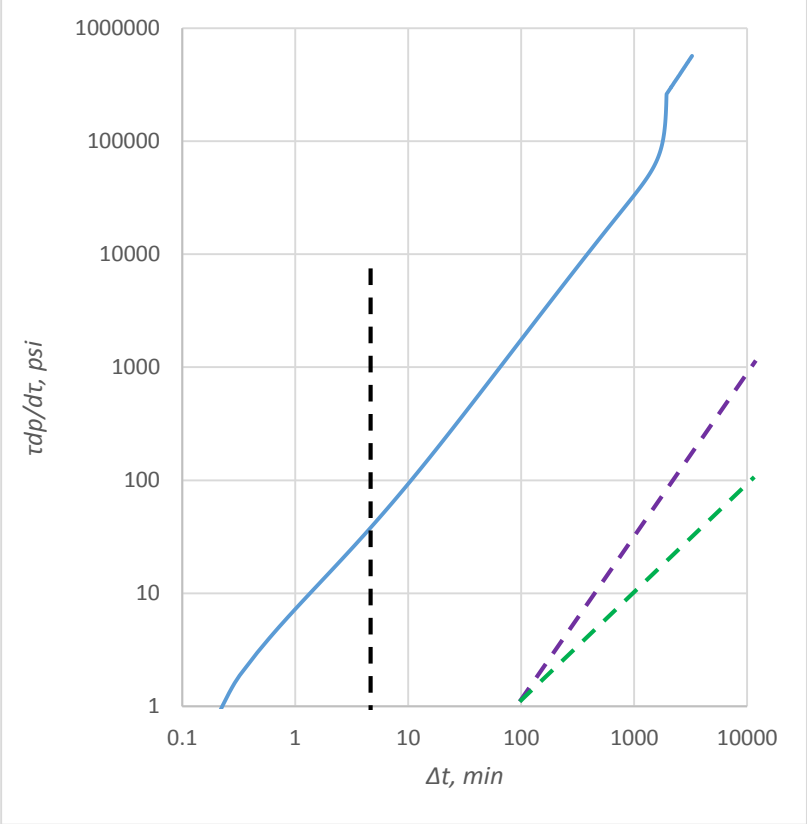

Figure 2-59 Log-log diagnostic plot for decoupled fracture model with pressure-dependent compliance and leakoff coefficient of natural fractures

4) Sensitivity study on natural fracture extension

The effect of natural fracture extension on the feature of diagnostic curve is tested in this section. All the input parameters are same with these in Table 2-9 except for A_{fr}, which is the surface area ratio of main fracture with natural fracture. A wide range of A_{fr} is examined from 0.1 to 10. Small value of A_{fr} indicates the large extension of natural fractures.

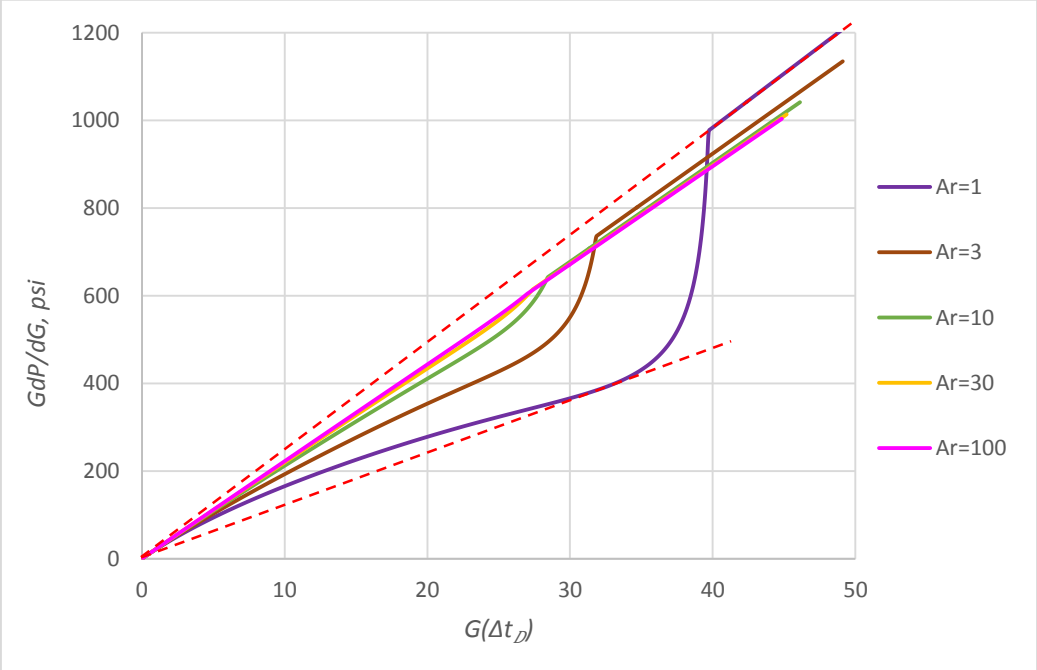

Figure 2-60 Gdp/dG plot for decoupled fracture model with variable natural fracture extension

From semilog G-function plot in Figure 2-60, we can find that cases with larger natural fracture extension, or smaller A_{fr}, are more likely to have a deeper belly below the final extrapolated straight line, and also a higher hump above the second line. While

for the case with a big A_{fr}, such as when $A_{fr} = 10$, the main fracture is dominant in the fracture system. The diagnostic plot has a very shallow belly and a minimum hump, which is pretty close to that in normal leakoff. Similar conclusion can be drawn from the log-log diagnostic plot in Figure 2-61. Therefore, the behavior of PDL and/or transverse storage would be weighted by the connected natural fracture extension in the diagnostic plots. Larger extension of natural fractures tends to boost the signature of hump when PDL happens, and the belly shape when transverse storage is observed.

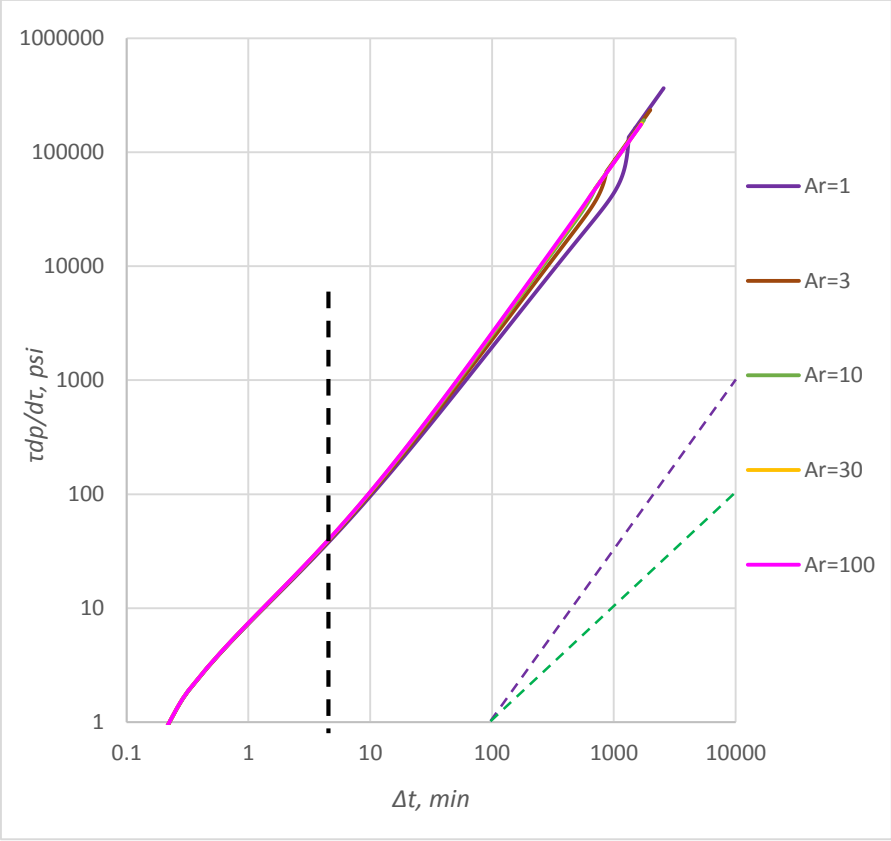

Figure 2-61 Log-log diagnostic plot for decoupled fracture model with variable natural fracture extension

As has been discussed above, the inconsistency of diagnostic curves can be avoided by assuming that natural fractures have a declining fracture compliance and a declining leakoff coefficient during closing. It could be the fact only if the new-created natural fracture faces are unconformable contact with each other. However, since the majority length of natural fractures is created by the tensile stress applied by the internal hydraulic pressure, it is a doubt that whether the fresh fracture surfaces are unconformable or not. In the next section, we will explore another more likely scenario for the closing of natural fractures.

2.5.4 Natural fractures with pressure-dependent natural fracture extension

Since the impact of unconformable contact would be minimum in the fresh tensile failure crack, the changing of fracture compliance probably is not the main factor for the signature of transverse storage effect. The declining fracture area during closing is more likely to be the major factor for the transverse storage behavior than fracture compliance and leakoff coefficient. In this section, we assume that the leakoff area is the only variable during closing of natural fracture, and its fracture compliance and leakoff efficient are constant. Similar to the declining model of fracture compliance in Eq. (2.77), the natural fracture surface area is also assumed to decline exponentially with a controlling factor, d.

$$A_{fn}(p_w) = \frac{\mathrm{Exp}(d\ p_w/p_{ws}) - \mathrm{Exp}(d\ p_{fo}/p_{ws})}{\mathrm{Exp}(d\ ) - \mathrm{Exp}(d\ p_{fo}/p_{ws})} A_{fn0} \qquad (2.78)$$

where, A_{fn0} is the fracture area at the end of injection.

A series of sensitivity study has been done on the coefficient d in Eq. (2.78), and three ratios in Eq. (2.68): A_{fr}, C_{Lr} and c_{fr}.

1) Sensitivity study on the decline rate of natural fracture surface area

With a wide range of d from -1000 to 1000, we can find that all the possible decline manners could be included within this range, as shown in Figure 2-62. When d is very small, like $d = -1000$ and -100, natural fracture surface area does not change much at early time, and then jumps to zero rapidly at later time. For the other extreme, when $d = 1000$ or 100, the surface area recedes in a fast rate immediately after injection. The most direct impact of decline rate of natural fracture surface area on pressure response is mainly on the leakoff rate from natural fractures. Fast decline rate at early time diminishes the leakoff area and also leakoff rate, and fluid in natural fractures would be squeezed back into main fracture, which will retard its closure. Transverse storage behavior therefore could be observed in this case.

With the input parameters listed in Table 2-10, cases with different decline rates of natural surface area are tested and their diagnostic plots are shown in Figure 2-63 and Figure 2-64.

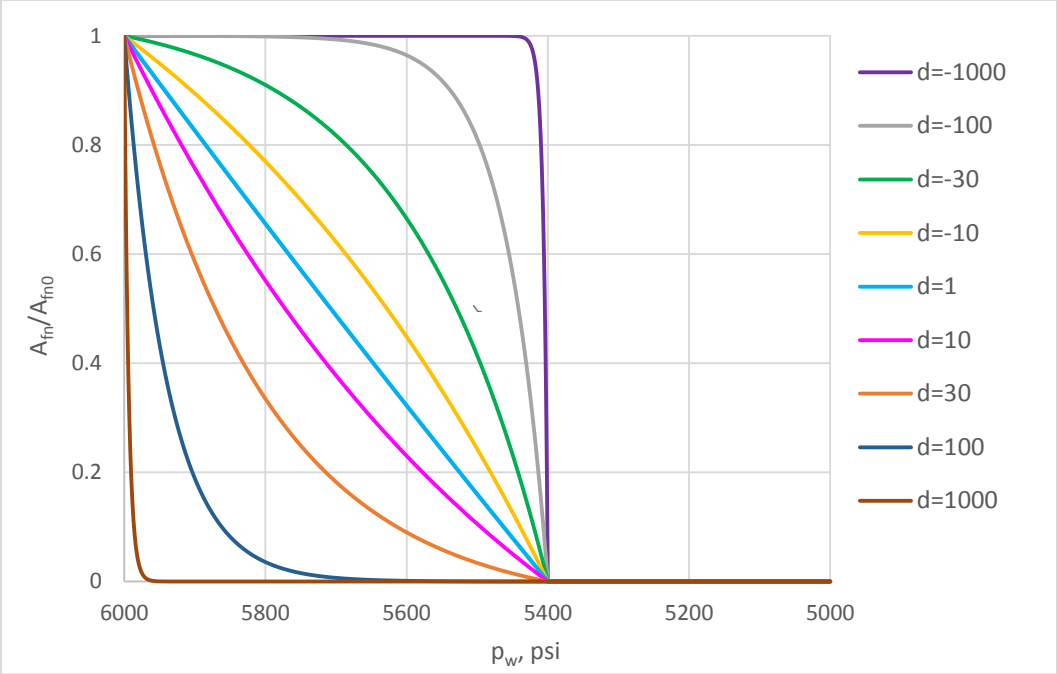

Figure 2-62 Exponential decline of natural fracture surface area with variable decline rates

Table 2-10 Input data for simulations of decoupled fracture model with variable A_{fn}

r_p	1
h_f, ft.	50
E', psi.	5×10^6
p_{ws} or ISIP, psi.	6000
t_p, minute	5
p_{fo}, psi.	5400
S_{min}, psi.	5000
q_p, bbl/minute	6
α	4/5
Main fracture model	PKN
Natural fracture model	PKN
C_{Lm}, ft/$\sqrt{\text{min}}$	1×10^{-4}
C_{Ln}, ft/$\sqrt{\text{min}}$	2×10^{-5}
A_{fr}	0.5
c_{fr}	1

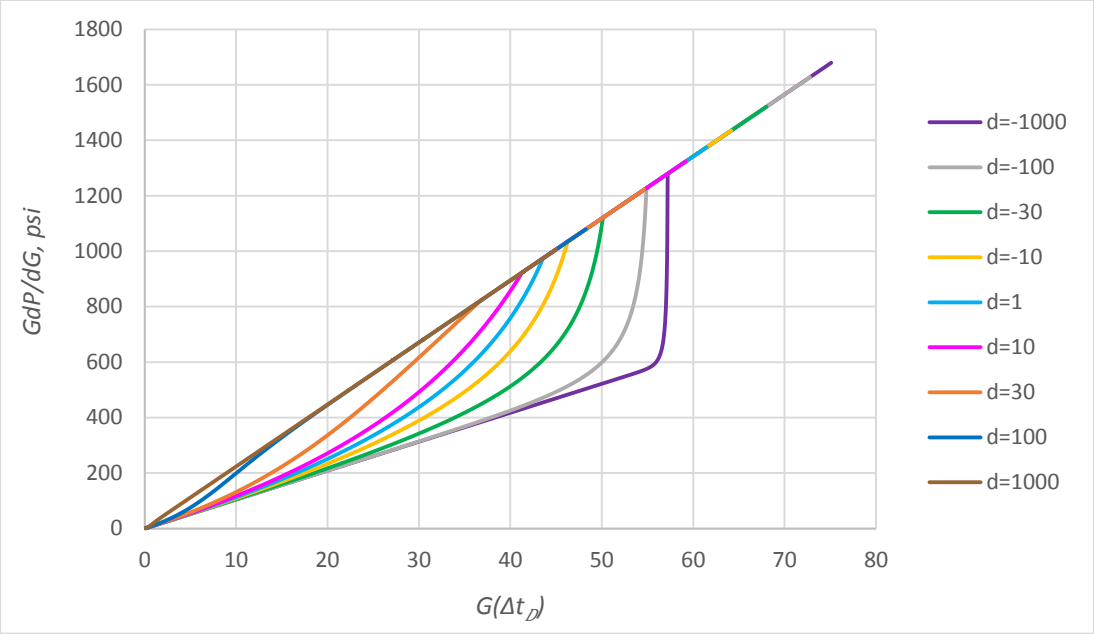

Figure 2-63 Gdp/dG plot for decoupled fracture model with variable decline behaviors of natural fractures surface area

For each diagnostic curves in semilog G-function plot shown in Figure 2-63, two extrapolated straight line could be drawn through the origin. The early one happens before the rapid decline of natural fracture surface area. This period is relatively long for the cases with small decline rate at beginning, like when $d = -100$ and -1000. While for the cases with fast decline rate at early time, such as when $d = 100$ and 1000, the belly shape curve below the extrapolated line could be so shallow and the time duration is so limited that the transverse storage behavior may be undetectable. The situation would be even worse if wellbore storage or other factors happen at early time. Anyway, if the first extrapolated straight line can be drawn at the case when transverse storage happens, it is possible to estimate the total extension of natural fractures.

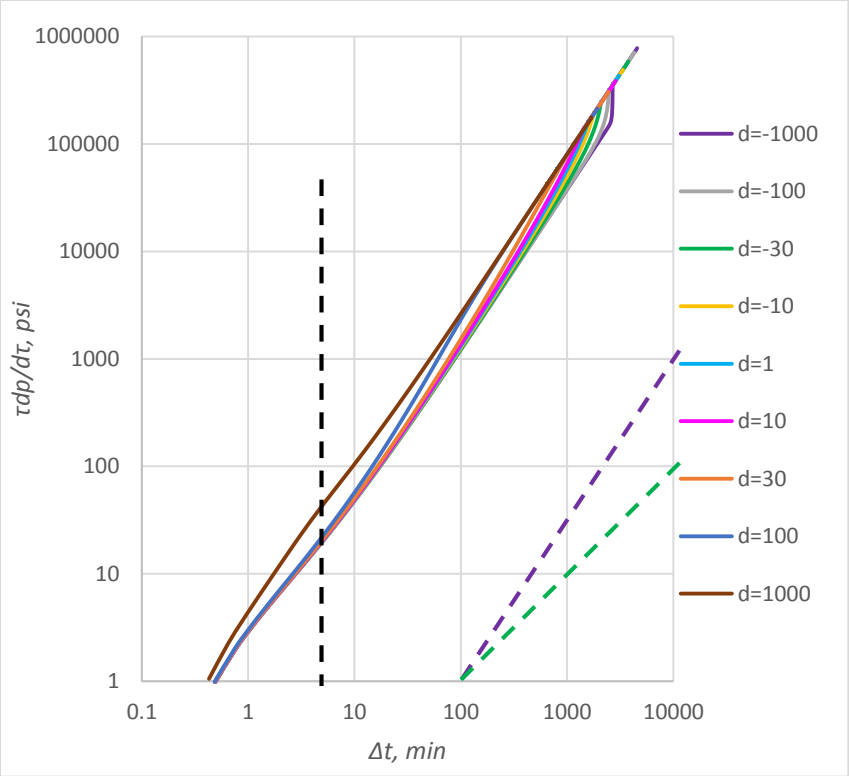

Figure 2-64 Log-log diagnostic plot for decoupled fracture model with variable decline behaviors of natural fractures surface area

For the other extrapolated straight line in semilog G-function, it occurs after the closure of natural fractures, and fluid leaks off mostly through the main fracture. The geometry of main fracture and its closure stress therefore could be calculated through the data in this section.

Similar findings could be figured out from the log-log diagnostic plot in Figure 2-64. Two straight lines with 3/2-slope could be found, and each is corresponding to the extrapolated straight line in semilog G-function plot. Together with G-function plot, it can be used to determine the data section that could be taken to calculate fracture lengths of both natural and main fracture.

2) Sensitivity study on leakoff coefficient ratio, C_{Lr}

In this section, the impact of natural fracture leakoff capacity on the pressure response of the whole fracture system will be discussed. The pumping and formation parameters are assumed to be same with these in Table 2-10 except the leakoff coefficient of natural fractures, C_{Ln}, which will the variable for the sensitivity study. Five sets of C_{Lr}s are tested, $C_{Lr} = 5, 1.5, 1, 2/3$ and 0.2. Besides, the closure of natural fractures follows the exponential decline model of fracture surface area with $d = 30$.

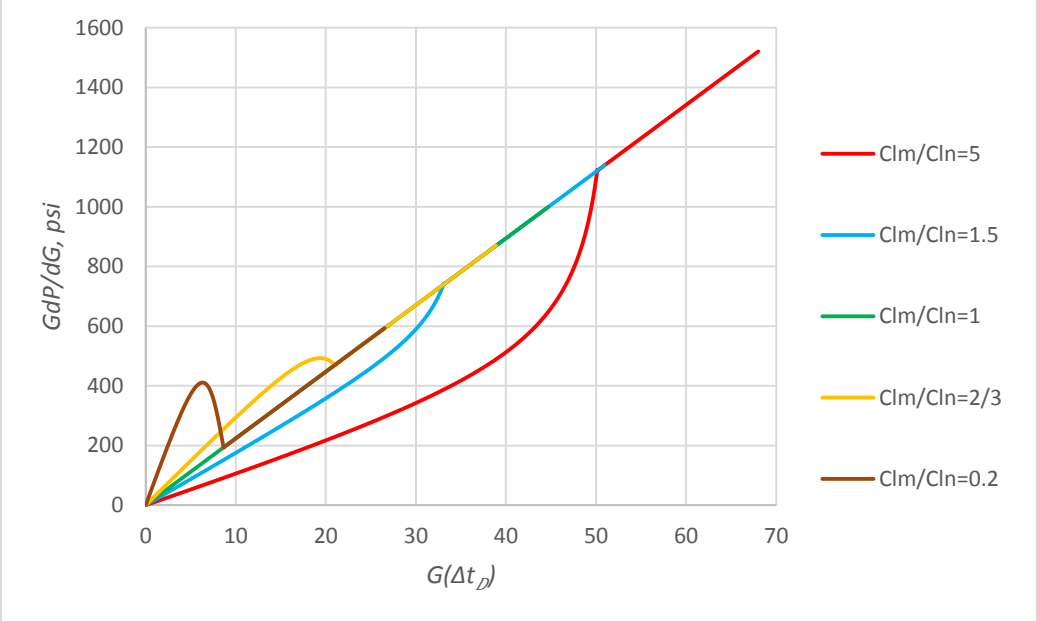

Figure 2-65 Gdp/dG plot for decoupled fracture model with a declining surface area of natural fractures

Actually, the shape of the diagnostic curve can be roughly pre-determined by Eq. (2.68). When C_{Lr} is smaller than c_{fr}, which is 1 in this case, PDL behavior is expected. Transverse storage signature is supposed to happen when $C_{Lr} > c_{fr}$. If by accident,

$C_{Lr} = c_{fr}$, two expressions in Eq. (2.68) are identical, and the pressure response will be exactly same with that with normal leakoff.

All diagnostic plots in semilog G-function are exhibited in Figure 2-65. Same with the conclusion drawn from Eq. (2.68), we can find that PDL happens when $C_{Lr} < c_{fr} = 1$, and transverse storage behavior when $C_{Lr} > c_{fr} = 1$. Besides, high leakoff rate from natural fracture tends to boost the PDL effect, so that the first extrapolated straight line will have a large slope, and also a high hump above the final extrapolated line. In the other end, natural fractures with low leakoff rate will have a deep belly curve.

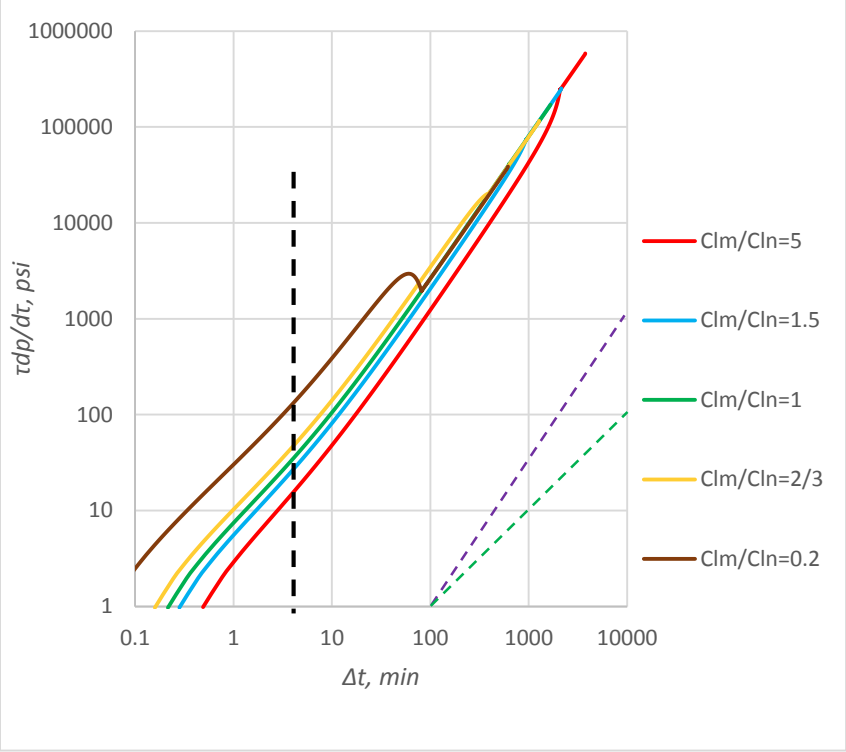

Figure 2-66 Log-log plot for decoupled fracture model with a declining surface area of natural fractures

Similarly, two straight lines with 3/2-slope can be drawn in log-log diagnostic plot, and they are corresponding to these two extrapolated lines in semilog G-function plot. For the cases with PDL, the first straight line lies in the left of the second, while for cases with transverse storage behavior, the first in the right. These two line will merge into one when normal leakoff occurs.

3) Sensitivity study on fracture compliance ratio, c_{fr}

Table 2-11 Input data for the sensitivity study of c_{fr} with decoupled fracture model

r_p	1
h_f, ft.	50
E', psi.	5×10^6
p_{ws} or ISIP, psi.	6000
t_p, minute	5
p_{fo}, psi.	5400
S_{min}, psi.	5000
q_p, bbl/minute	6
α	4/5
Main fracture model	PKN
Natural fracture model	PKN
C_{Lm}, ft/$\sqrt{\text{min}}$	1×10^{-4}
C_{Lr}	2/3
A_{fr}	0.5
Natural fracture surface area decline behavior	Exponential decline with $d = -30$

In previous section, it assumes that compliance of natural fracture is same with that of main fracture. However, because of the geometric difference and formation isotropic, these two fracture compliances are probably not same to each other. In this section, several sets of fracture compliance ratios are tested to examine its impact on the

pressure response. The input data is listed in Table 2-11, and the diagnostic curves are shown in Figure 2-67 and Figure 2-68.

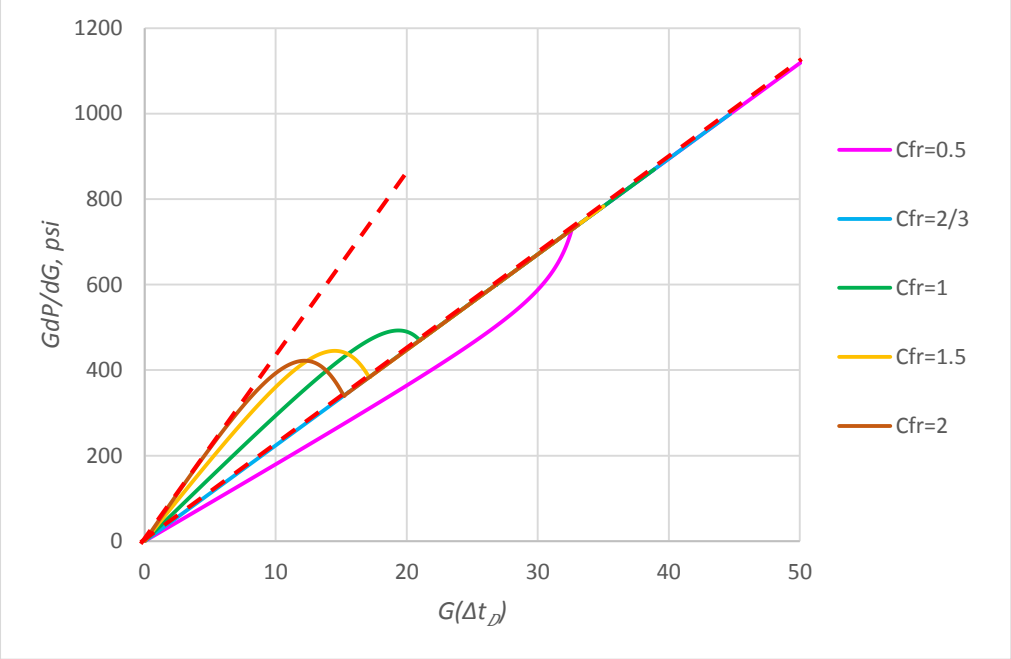

Figure 2-67 Gdp/dG plot for decoupled fracture model with a declining surface area of natural fractures and variable fracture compliance ratios (d=-30, Cl_m/Cl_n=2/3, Ar=0.5)

The result again demonstrates the conclusion we made in last section based on the Eq. (2.68). PDL behavior, indicated by a hump above the extrapolated straight line through the origin in semilog G-function plot, will show up when c_{fr} is bigger than C_{Lr}, which is 2/3 in this case. When $c_{fr} < C_{Lr} = 2/3$, such as $c_{fr} = 0.5$ in Figure 2-67, the belly shape below the extrapolated line usually interpreted as transverse storage effect. Besides, two extrapolated straight lines can be drawn in the semilog G-function curve.

The latter one should be used to estimate parameters of main fracture, and then, natural fracture surface area could be estimated with the data in the first extrapolated line.

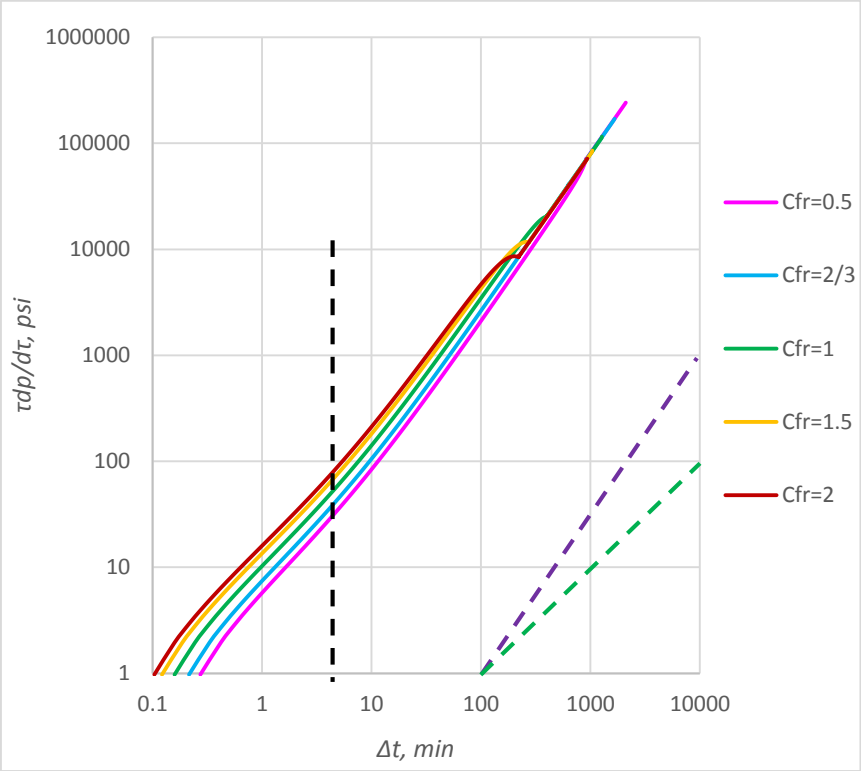

Figure 2-68 Log-log diagnostic plot for decoupled fracture model with a declining surface area of natural fractures and variable fracture compliance ratios (d=-30, Cl_m/ Cl_n=2/3, Ar=0.5)

Similarly, two straight lines with 3/2-slope in the log-log diagnostic plot in Figure 2-68 correspond to these two extrapolated lines in the semilog G-function plot. And they also could be taken as the helpful reference to pick the closure events of both types of fractures, and the data range of two extrapolated lines in G-function plot.

4) Sensitivity study on fracture surface area ratio, A_{fr}

During treatment in tight formation or naturally fractured reservoir, natural fractures are likely to be connected. The wide spread microseismic cloud is usually taken as the well-developed natural fracture networking. Therefore, it is necessary to investigate the impact of total extension of the natural fracture on the pressure response during fracture injection test. In this section, the fracture leakoff coefficient ratio (C_{Lr}) is assumed to be 5, which means that natural fracture has a poor leakoff capacity. The rest input data is same with that in Table 2-11, and the resulting diagnostic curves are plotted in Figure 2-69.

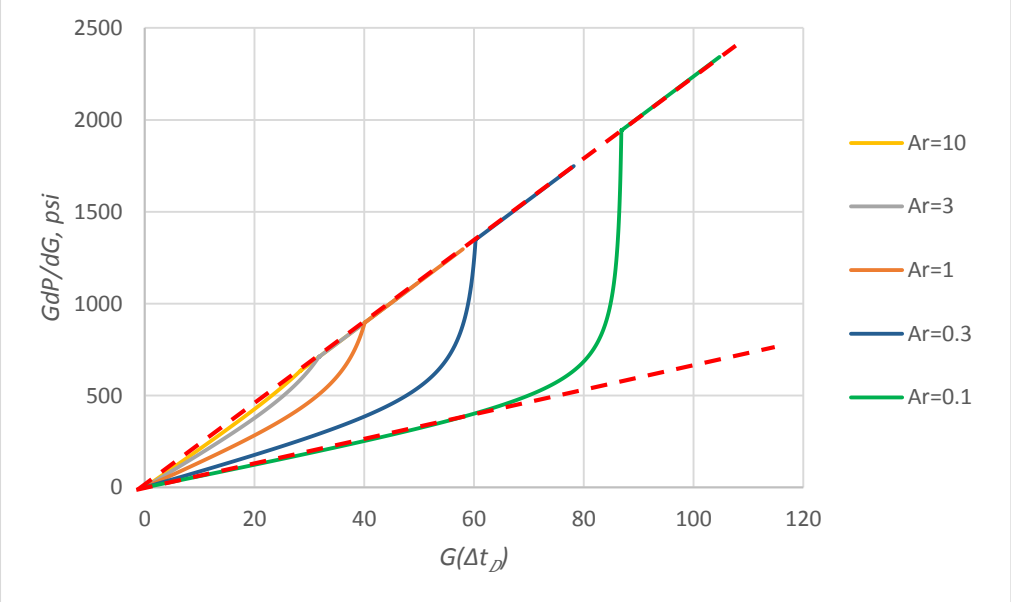

Figure 2-69 Gdp/dG plot for decoupled fracture model variable natural fracture extension (d=-30, Cl_m/Cl_n=5)

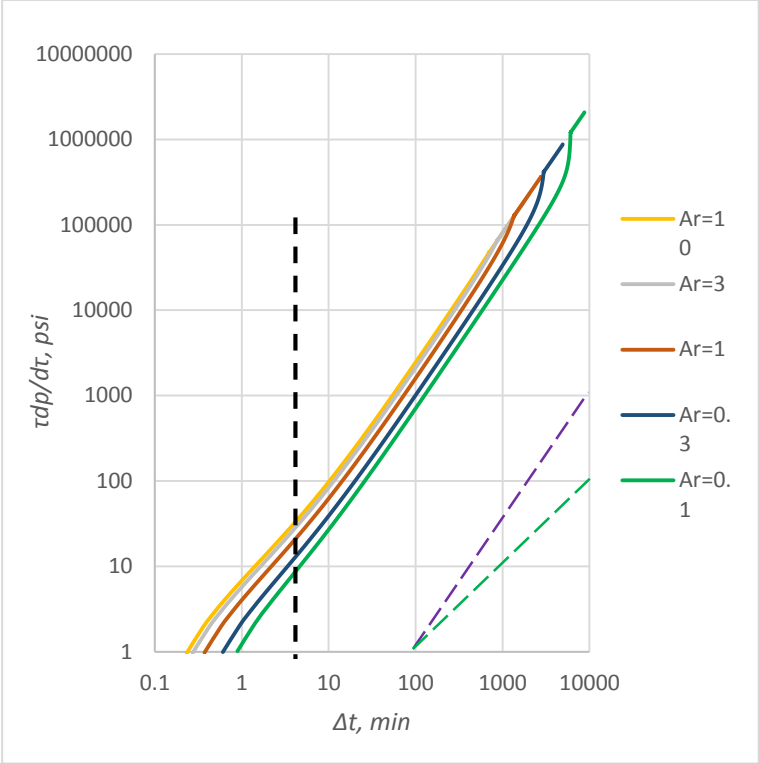

Figure 2-70 Log-log diagnostic plot for decoupled fracture model variable natural fracture extension (d=-30, Cl_m/Cl_n=5)

For the case when $A_{fr} = 0.1$, which means that the total fracture surface of natural fracture is 10 times of that of main fracture, natural fracture is very well developed and it is the dominant in the whole fracture system. For the sake of poor leakoff capacity through natural fractures, transverse storage effect is observed, and large extension of natural fracture network tends to exaggerate the behavior. A deep belly curve therefore can be found below the final extrapolated straight line. While for the other extreme when $A_{fr} = 10$, main fracture dominates the fracture system and the impact from natural fracture is minimum. The transverse storage effect is not that obvious and the belly is pretty shallow below the extrapolated line.

In the log-log diagnostic plot, two straight line with 3/2-slope could be picked from each curve. Same to previous discussion, the first one stands for the fracture system with both main and natural fractures, while the second only for the main fracture. In this sensitivity study, we can find that the distance between these two lines will be minimum if the natural fracture extension is limited. The leakoff from the fracture system changes little before and after closure of natural fractures. However, for the case with large natural surface area over main fracture, more fluid will flow back into main fracture during natural fracture closing, and the supplement will result in obvious transvers storage behavior in diagnostic plots.

Again, by analyzing these two extrapolated straight lines in semilog G-function plot or these two 3/2-slope lines in log-log diagnostic plot, it is possible to estimate the extension of both main fracture and natural fractures.

In summary, decoupled fracture model can be used to estimate more properties from FCTs than traditional Nolte G-function model and the PDL model in last section. Depending on properties of natural fracture, it can behave as PDL, transverse storage or even normal leakoff. To obtain a realistic smooth curve from the decoupled fracture model, one of or both these two parameters, fracture compliance or surface area of natural fracture, is required to decline gradually to zero during the closure of natural fissures. Since fractures are mainly created by tensile failure, fracture compliance might not change much, and the fracture length recession could happen during natural fracture closing.

2.6 Summary of Chapter II

In this chapter, most of the potential leakoff regimes, or leakoff behaviors are discussed, including wellbore storage effect (WBS), early fracture linear flow which indicated by the ½-slope before elastic closing process, fracture tip-extension, pressure dependent-leakoff (PDL), multiple apparent closure events and transverse storage behavior. Several important points should be concluded from the discussion and modeling work.

1. Early WBS behavior mainly caused by two factors: the pressure loss associated with friction in the wellbore and near-wellbore vicinity, and the rapid decline of net pressure, which might result from tip-extension and PDL.
2. There are several factors accounting for the early fracture linear or radial flow, such as high leakoff rate at tip area, the existence of dry tips and tip extension. A ½-slope or flat trend in log-log diagnostic plot might be observed if fracture linear or radial flow happen. However, this flow regime is very likely masked by the early wellbore storage effect.
3. If tip-extension takes place, its composite G-function curve tends to approach an asymptote, which is extrapolated through the origin. If the fracture closes shortly after tip-extension, or the recorded data is not long enough, the extrapolated straight line would lies above the origin and have a positive intercept, which however is the common practice to identify tip extension by Barree method.

4. In the newly developed PDL model, the leakoff contributed by natural fissures is able to be estimated, e.g. the initial leakoff coefficient of the whole fracture system can be calculated out.
5. Besides leakoff coefficient of natural fracture, its extension is included in the decoupled fracture model. Both PDL and transverse storage mechanisms can be analyzed in the model.
6. In some cases, it might be ambiguous between PDL and tip extension (with a limited fracture growth after shut-in) because they are sharing similar diagnostic curves.

CHAPTER III

FIELD CASE STUDY

Several commonly observed abnormal leakoff mechanisms, including tip-extension, PDL and transverse storage, are modeled in Chapter II. Besides, the WBS behavior and early linear flow are also covered. The application in really field FCT analysis will be demonstrated to show the advantage of the new-derivated models.

In this chapter, four fracture calibration tests (FCTs) from different horizontal wells will be taken as examples for the discussion. All wells were drilled in the same well pad (as shown in Figure 3-1) in Horn River Basin (HRB), which is the largest shale gas field and located in the northeastern corner of British Columbia in west Canada. According to published papers (Johnson et al. 2011; Reynolds and Munn 2010), the GIP of shale gas in HRB is estimated at around 500 TCF, and the marketable resources at about 78 TCF.

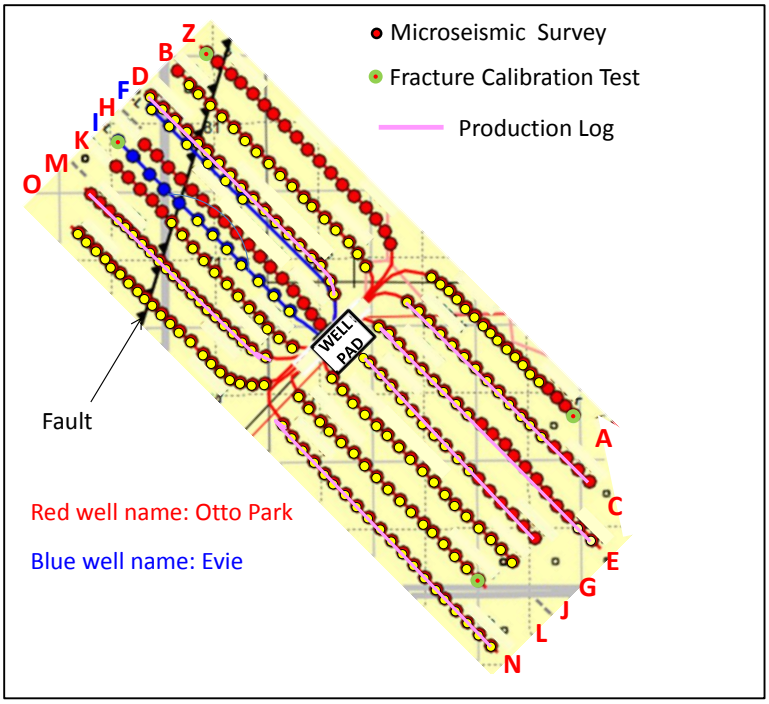

Figure 3-1 Schematic of Horn River horizontal well pad(Ehlig-Economides et al. 2012)

In this well pad, wells in the northwest side of the pad were drilled through a fault, as mapped in Figure 3-1. This fault has a great influence on the completion and production performance (Ehlig-Economides et al. 2012), which will be discussed later.

Horn River Group (HRG) is comprised of several layers of interest, including the Muskwa, Otter Park, Klua (sometimes known as Evie), and sometimes a Middle Devonian Carbonate (MDDC) layer between Klua and Otter Park, as shown in the schematic chart in Figure 3-2. Ft. Simpson shales, which overlays above the HRG, is thick and clay rich; Keg River Formation is the tight limestone zone and underlays below the HRG. These two layers are acting as the outer barrier to terminate the potential fracture propagation in HRG (Beaudoin et al. 2011). According to Beaudoin et al. (Beaudoin et al. 2011), several other factors could be the potential barrier, such as the

observed strong horizontal stress difference for different lateral layers, which is caused by tectonic stress, the exist of clay-rich layer and MDDC formation between Otter Park and Klua, and also the highly laminated rock fabric in the zone of interest. Generally, the primarily pay zones are Muskwa and Otter Park members, where the deposit can be described as grey to black organic-rich shales. In additional to these two main targets, the Klua/Evie member is likely to be next active pay zone.

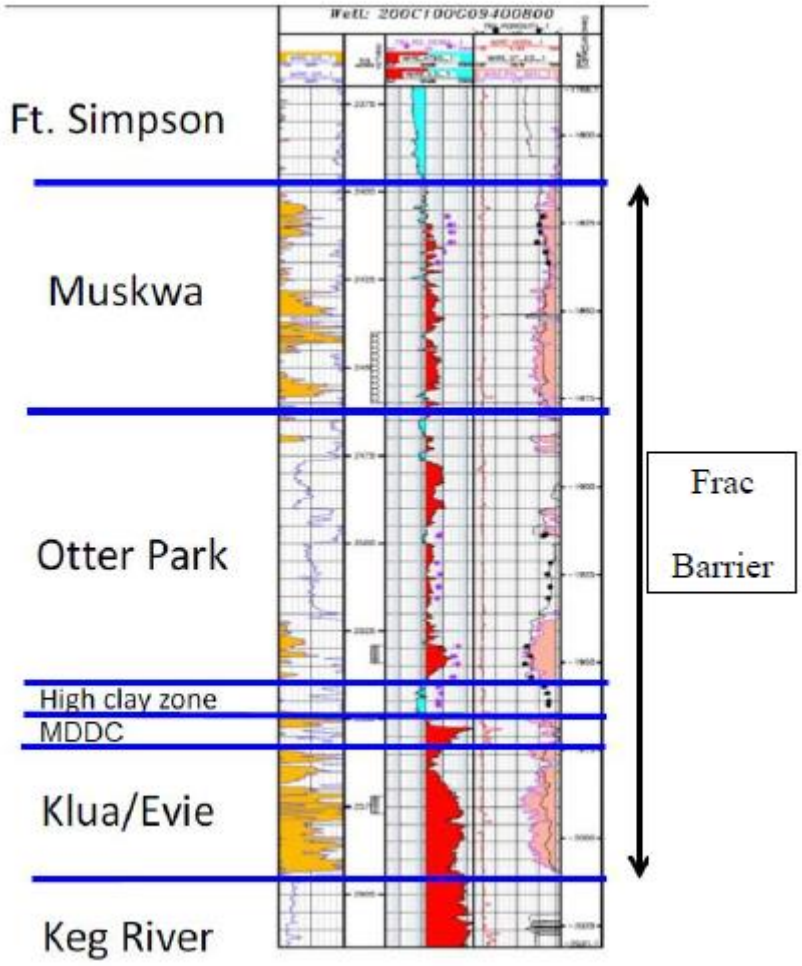

Figure 3-2 Zones of interest in Horn River formation(Beaudoin et al. 2011)

For four tested horizontal wells in our dataset, three of them (Well A, Z and L) were drilled in Otter Park formation, and the rest one (Well I) in Klua/Evie. Since the average thickness of HRG could be up to 400ft (Ehlig-Economides et al. 2012; Reynolds and Munn 2010), and the injection volume for these four fracture calibration tests are very limited, ranging from 31 to 126 bbl, it is likely that fracture will not reach the overlain and underlain barriers. The fracture geometry could be in radial shape, and the radial fracture model will be employed for the following analysis.

3.1 Fracture calibration test (FCT) analysis for Well A

The FCT was performed in the toe stage of Well A with a single preformation at 8932.2 ft TVD in Otter Park member. About 31.45 bbl fresh water was injected into the well in 6.67 minutes with a rate at 4.72 bbl/min, as shown in Figure 3-3. The bottomhole pressure was monitored for about 350 hours after shut-in.

Figure 3-4 and Figure 3-5 exhibit the diagnostic plots with log-log Bourdet derivative and composite G-function, respectively. From both plots, we can find that PDL behavior happens. Two 3/2-slope lines can be drawn in the log-log diagnostic plot. The first line is likely to happen when natural fractures are reopened during treatment, and they have a higher leakoff coefficient than main fracture. The deviation point from the first 3/2-slope line could be taken as the start point of natural fracture closure ($\Delta t = 0.52$ hr), and the whole closure process finishes when the curve switch to the second extrapolated straight line at $\Delta t = 5.39$ hr. The closure process of natural fracture may happen in the way of fracture length recession. In other words, the surface area change

of natural fissures with time is likely to be the reason for the transition from the first 3/2-slope line to the second. Then, the closure pressure at start and at end of closure could be picked at 7211 psi and 6426 psi, respectively.

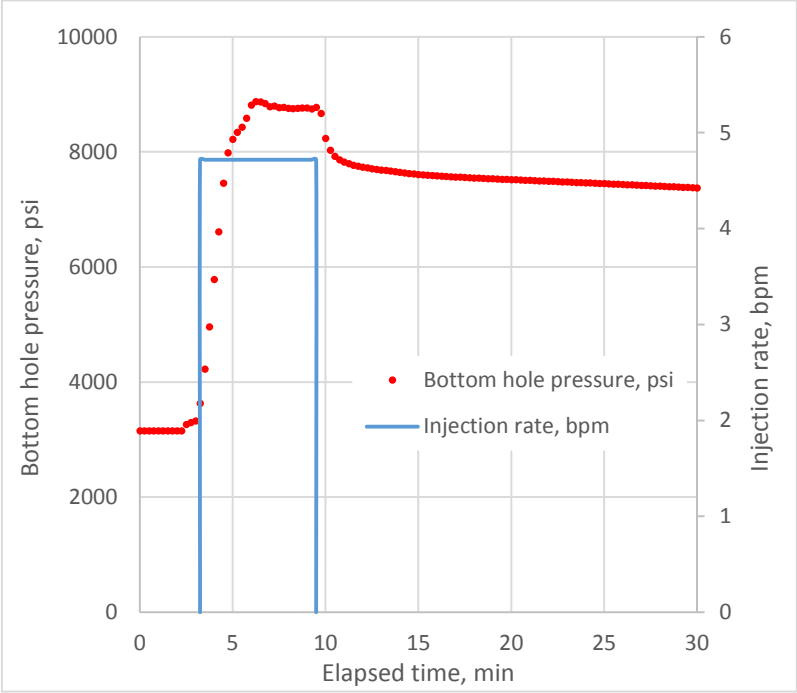

Figure 3-3 Bottomhole pressure change and injection profile for Well A

Same closure events and closing process can be picked from the composite G-function plot. Two extrapolated straight lines drawn from the origin in G-function diagnostic curve, are corresponding to these two 3/2-slope lines in the log-log diagnostic plot.

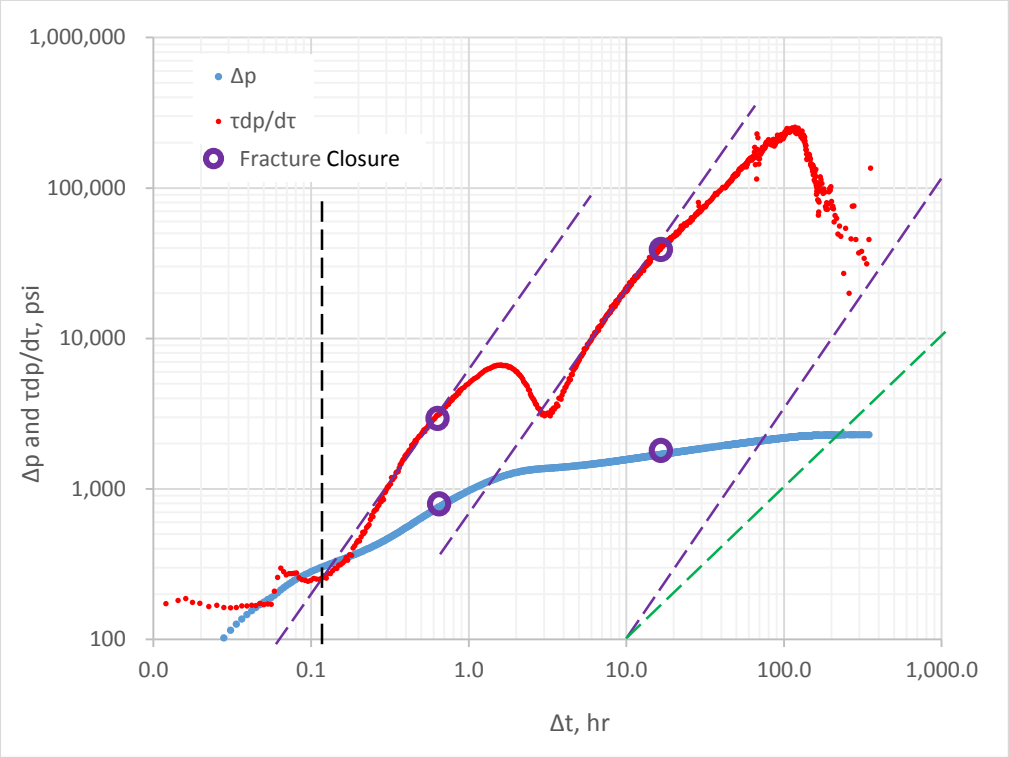

Figure 3-4 Log-log diagnostic plot for Well A

Before the end of natural fracture closure, fluid can leak off into formation through both main fracture and the residual natural fracture faces. While after that, natural fissures are supposed to be totally closed and have no contribution either to fluid storage or to leakoff process. Then, the leakoff through main fracture will be the dominant leakoff mechanism. The deviation point from the second 3/2-slope line in the log-log diagnostic plot, or correspondingly, the second extrapolated line in the G-function plot, therefore could be picked as he closure event of main fracture. The closure pressure and closure time can be read out directly from the log-log diagnostic plot. In this case, main fracture closes at $\Delta t = 11.47$ hr, and the closure pressure is 6266 psi, which probably is the local minimum horizontal stress.

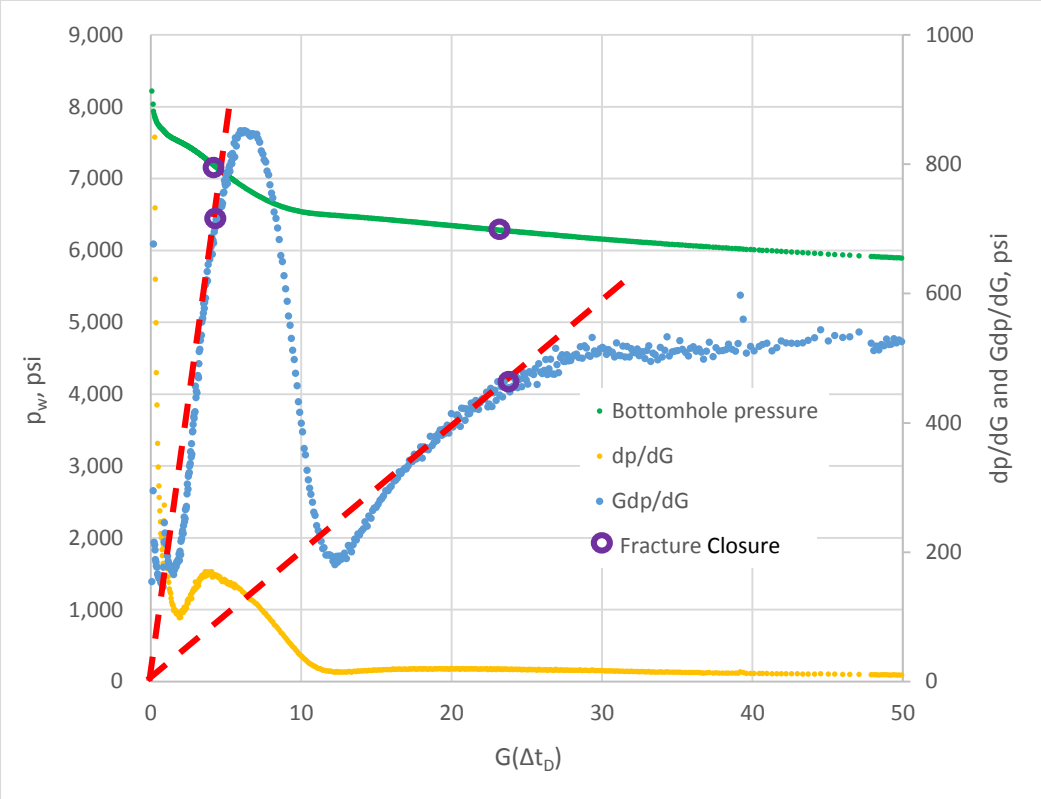

Figure 3-5 Composite G-function diagnostic plot for Well A

Another important parameter to be determined with before-closure analysis is the leakoff coefficient. For this case, results of 3 different diagnostic models will be discussed and compared.

1) Traditional Nolte G-function model

First, with the traditional Nolte G-function model as given in Chapter I, fluid efficiency, fracture extension and leakoff coefficient are able to be determined, as listed in the following table. One should note that, in the traditional Nolte G-function model, natural fracture, or PDL behavior, is not involved during its derivation. The

interpretation is exactly same with that in normal leakoff case even when the PDL or any other abnormal leakoff behavior is observed.

Table 3-1 Results from before-closure analysis with traditional Nolte G-function model for Well A

η	0.932
R_f, ft	73.58
C_L, ft/$\sqrt{\text{min}}$	9.87×10^{-5}
Closure pressure, psi	6266
Closure stress gradient, psi/ft	0.702

2) PDL model

In this model, natural fracture is treated as part of matrix, but with a higher leakoff coefficient when it is opened, as described in Eq. (1.46) or (1.47). However, except for higher leakoff coefficient, natural fractures do not have any other properties, like fracture with, extension, etc. Another issue with the model is on the closure time of natural fracture. As has been discussed, it is physically more convincing that natural fracture should has a fracture extension recession before closure. There will be some differences in the interpretation result on that whether the start time point or the end time should be picked as the closure event. Clearly, the natural fracture leakoff coefficient will be overestimated if the start time is taken as its closure, and underestimated if the end time is taken. In this dissertation, to simplify the analysis without reducing accuracy of the result, the geometric mean value of both times are taken as the closure event of natural fissures. The interpretation results are shown as following.

Table 3-2 Results from before-closure analysis with PDL model for Well A

R_f, ft	46.48
C_{Lm}, ft/$\sqrt{\text{min}}$	6.83×10^{-5}
Closure pressure of main fracture, psi	6266
C_{Ln}, ft/$\sqrt{\text{min}}$	5.23×10^{-4}
Closure pressure of natural fracture at start of closure, psi	7211
Closure pressure of natural fracture at end of closure, psi	6504
C_{Ln}/C_{Lm}	7.65
η	0.814

From above results, we can find that natural fracture has a much higher leakoff coefficient than main fracture, which accounts for the PDL feature in diagnostic plots. The relatively low fluid efficiency is the result from high leakoff rate of natural fracture. Compared the result with that by traditional Nolte G-function model, we can find that the fracture extension is much overestimated previously with Nolte G-function model; and the leakoff coefficient from Nolte G-function model lies between those of two types of fractures from PDL model.

Using the calculated parameters listed in above table as the input in PDL simulator, the generated curve is able to find the characteristic slopes in the recorded data, as shown in Figure 3-6 to Figure 3-8. These characteristic slopes are exactly the ones used for closure identification.

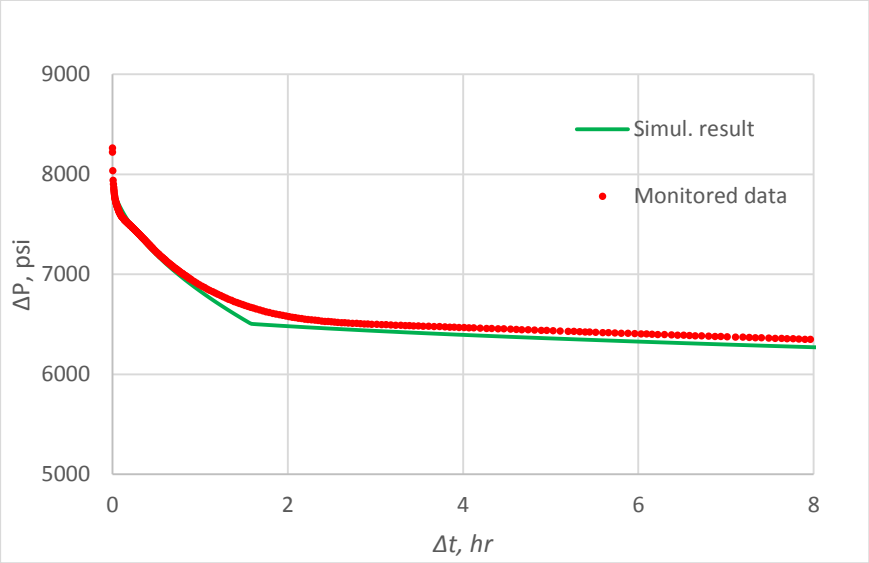

Figure 3-6 History match of the bottomhole pressure of Well A with constant PDL model

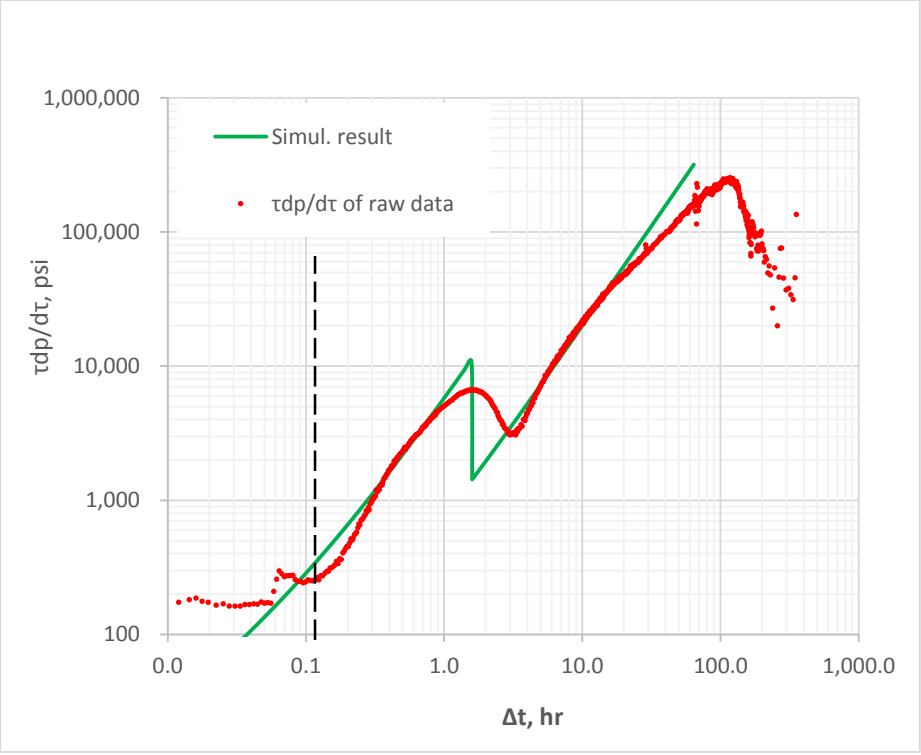

Figure 3-7 History match of the log-log Bourdet derivative of Well A with PDL model

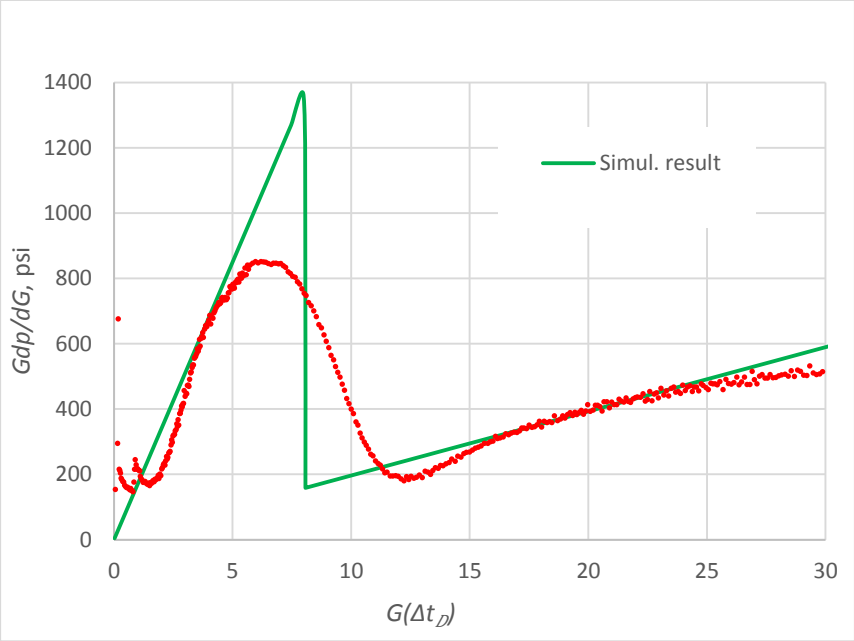

Figure 3-8 History match of the semilog G-function of Well A with PDL model

Although the lines are able to catch all the characteristic trend in the diagnostic plots, the simulation result with a couple straight lines does not match the transition curve very well. Therefore, variable PDL model with a declining leakoff coefficient before natural fracture closure, described by Eq. (2.57), is used. And, the history match with recorded pressure, diagnostic plots are shown as follows.

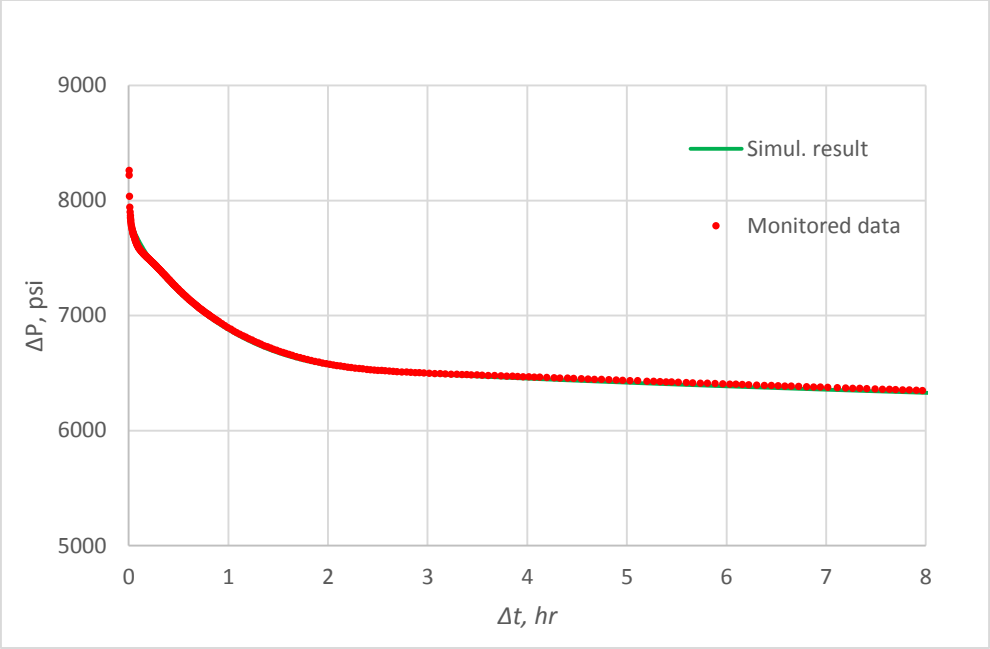

Figure 3-9 History match of the bottomhole pressure of Well A with Variable PDL model

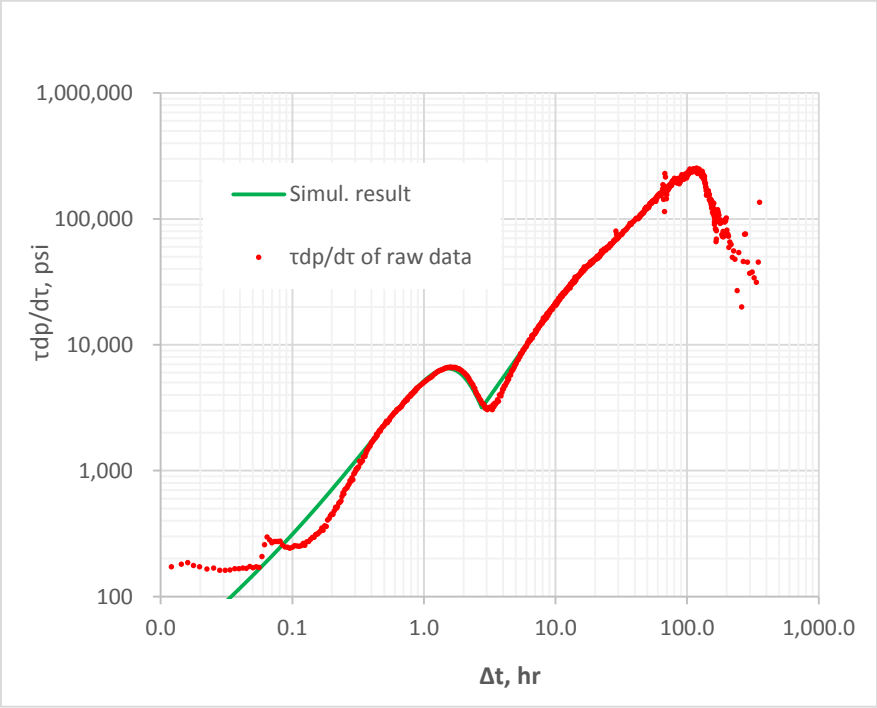

Figure 3-10 History match of the log-log Bourdet derivative of Well A with variable PDL model

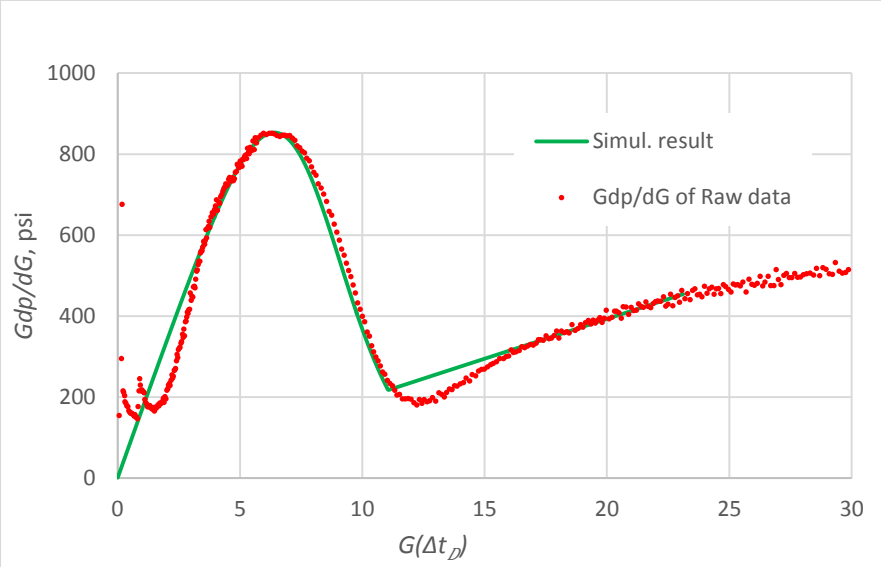

Figure 3-11 History match of the log-log Bourdet derivative of Well A with variable PDL model

The variable pressure-dependent leakoff coefficient used for above history match is plotted as following.

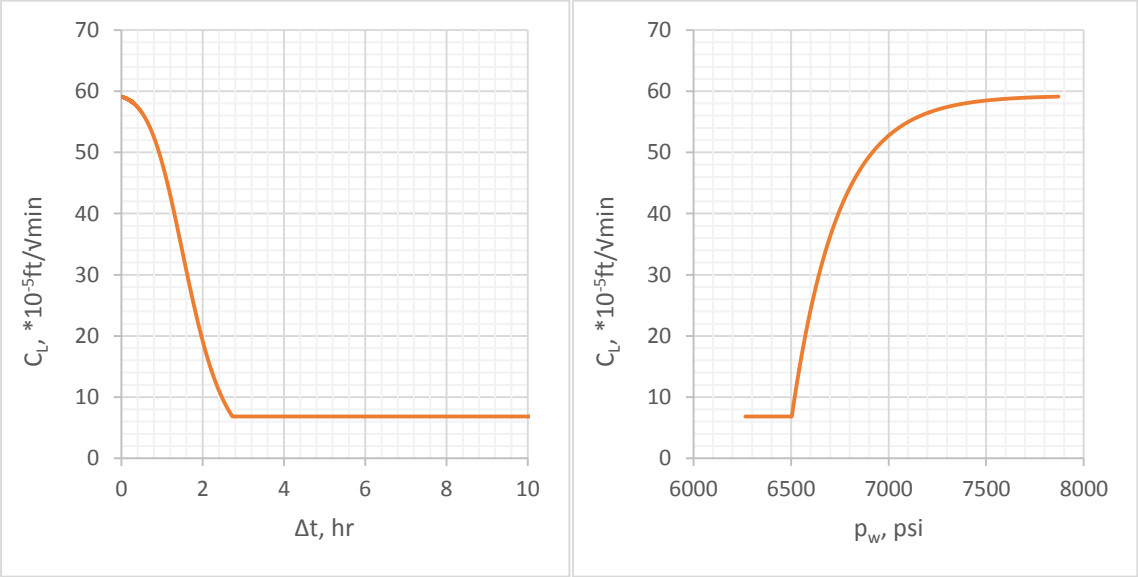

Figure 3-12 Variable leakoff coefficient during pressure falloff with time and pressure

One should understand that, natural fracture extension is not included in above PDL model. In the following interpretation, decoupled fracture model will be used to interpret the data and match the recorded curve with the integrated result.

3) Decoupled fracture model (DFM)

In decoupled fracture model, fracture system is divided into main and natural fractures. They are sharing the same pressure system and material balance, but have properties of their own, like fracture extension, width, leakoff coefficient, etc. As has been discussed in Chapter II, due to the synthetic behavior of natural fracture extension and its leakoff coefficient, it is currently impossible to determine these two parameters from only one data source. However, the corresponding natural fracture extension can be estimated with a pre-assumed leakoff coefficient. Actually, there is a linear relationship between A_{fm}/A_{fn} and C_{Ln}/C_{Lm}, as shown in Eq. (3.1), which can be derived theoretically and proven with the simulation result.

$$A_{fr} = \frac{A_{fm}}{A_{fn}} = \frac{p_1^*}{p_1^* + p_2^*}\left(\frac{C_{Ln}}{C_{Lm}} - 1\right) + 1 \tag{3.1}$$

where, p_1^* and p_2^* are the slope of straight lines before closure of natural and main fracture in the bottomhole pressure curve with G-function, similar with p^* in Figure 1-2. They can be read out from dp/dG curve at each closure time point in the composite G-function plot.

For each C_{Ln}, from 10 to 200 times of C_{Lm}, the corresponding leakoff coefficients, fracture extensions and fluid efficiency are calculated and listed in the following table. The linear relationship between A_{fm}/A_{fn} and C_{Ln}/C_{Lm} are plotted in

the Figure 3-13. Generally speaking, to achieve the same signature of PDL in diagnostic plots, smaller natural fracture leakoff coefficient requires larger fracture surface area, vice versa. Therefore, we can conclude that in this example, natural fractures likely contact some much more permeable layers. And their extension is dependent on the relative altitude of leakoff coefficient through natural fractures into permeable formation with that though main fracture into less permeable zones. For instance, if the permeable formation stimulated by the natural fissures, has a leakoff coefficient 50 times as high as that through main fracture, $C_{Ln}/C_{Lm} = 50$, the surface area of main fracture will be 5.4 time of that of natural fracture. And if $C_{Ln}/C_{Lm} = 20$, the surface area ratio, A_{fr}, will be reduced to 1.48.

Table 3-3 Results from before-closure analysis with decoupled fracture model for Well A

C_{Lm}/C_{Ln}	0.01	0.02	0.033	0.05	0.1
C_{Ln}/C_{Lm}	100	50	30	20	10
$C_{Lm}, \times 10^{-5}\text{ft}/\sqrt{\text{min}}$	6.39	6.23	5.99	5.64	3.67
A_{fm}, ft^2	6820	6489	6006	5319	2247
R_f, ft	46.59	45.45	43.72	41.15	26.75
$C_{Ln}, \times 10^{-3}\text{ft}/\sqrt{\text{min}}$	6.39	3.12	1.80	1.13	0.367
A_{fn}, ft^2	571	1201	2154	3389	12785
A_{fr}	11.93	5.40	2.79	1.48	0.176
η	0.835	0.833	0.830	0.825	0.808

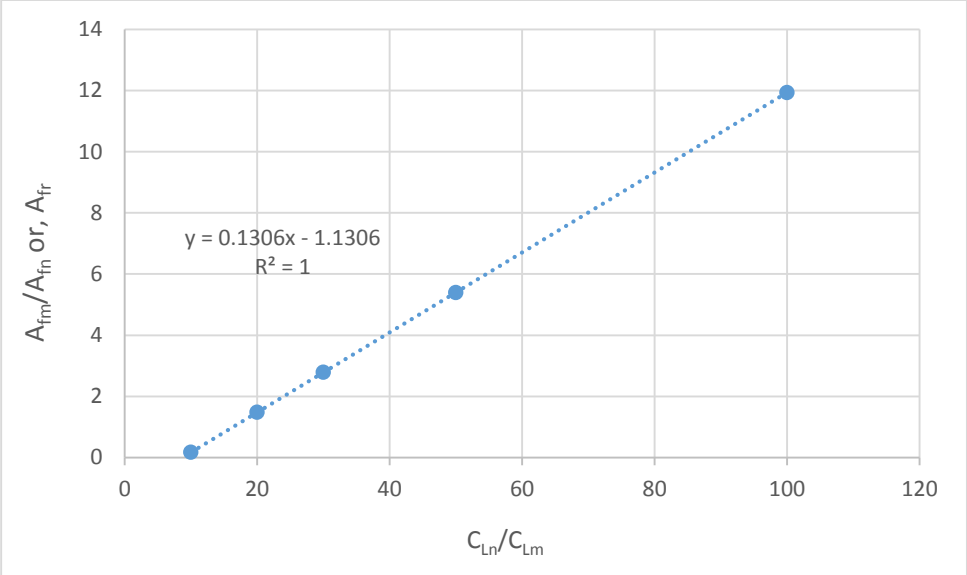

Figure 3-13 Linear relationship between A_{fm}/A_{fn} and C_{Ln}/C_{Lm} of Well A

Two combinations of interpreted result with decoupled fracture model (DFM) from above table, $C_{Ln}/C_{Lm} = 10$ and 30, are taken for instances. Their simulation results in bottomhole pressure, log-log Bourdet derivative and semilog G-function are shown in the Figure 3-14 to Figure 3-16 and Figure 3-17 to Figure 3-19, respectively. We can find that both combinations are able to match the recorded data in a good way.

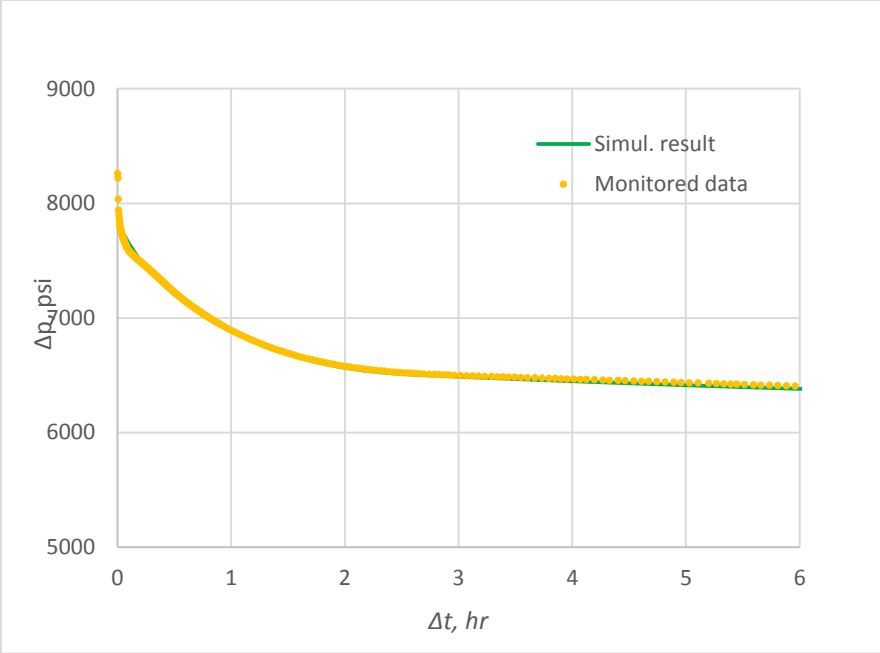

Figure 3-14 History match of the bottomhole pressure with DFM (C_{Ln}/C_{Lm}=10)

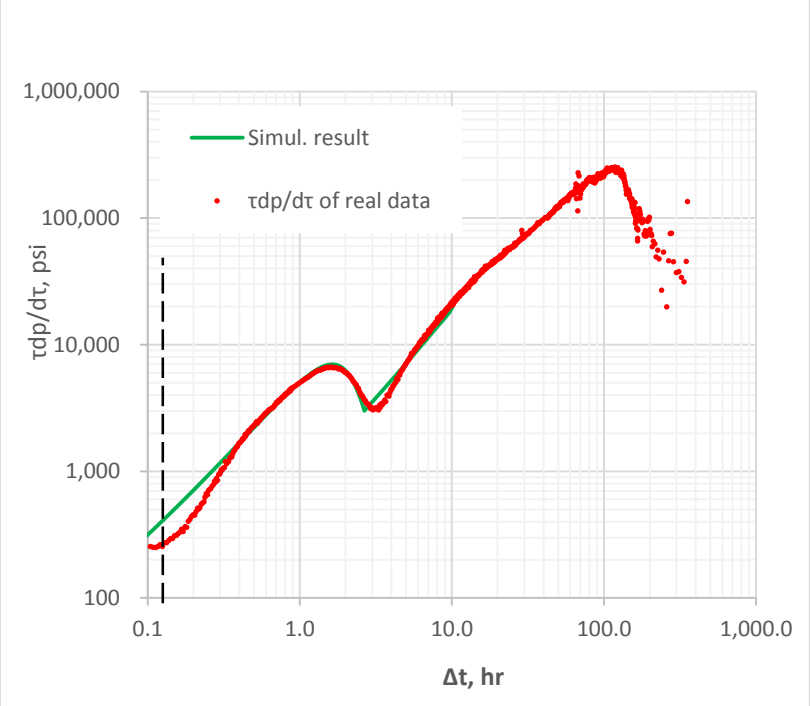

Figure 3-15 History match of the log-log Bourdet derivative with DFM (C_{Ln}/C_{Lm}=10)

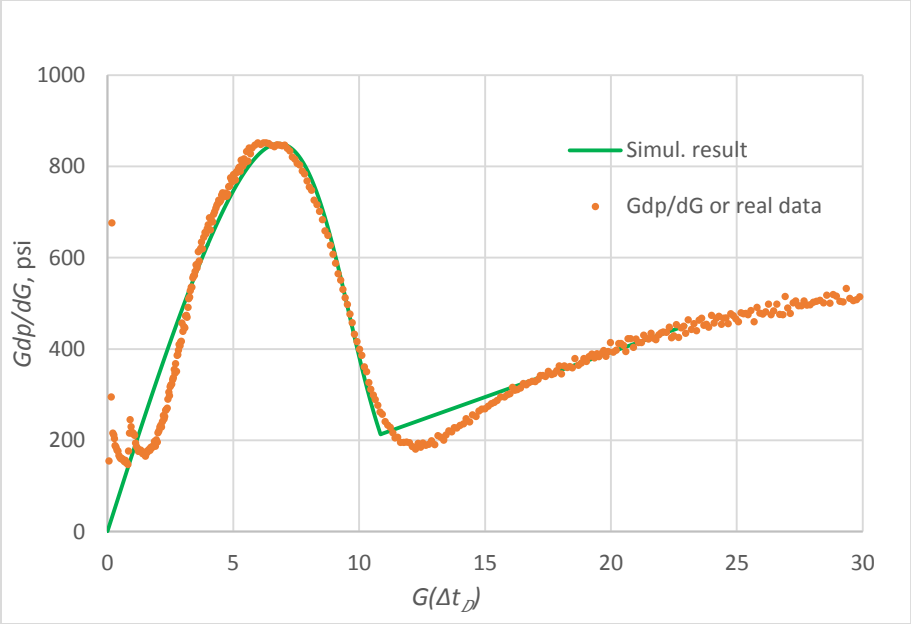

Figure 3-16 History match of the semilog G-function with DFM (C_{Ln}/C_{Lm}=10)

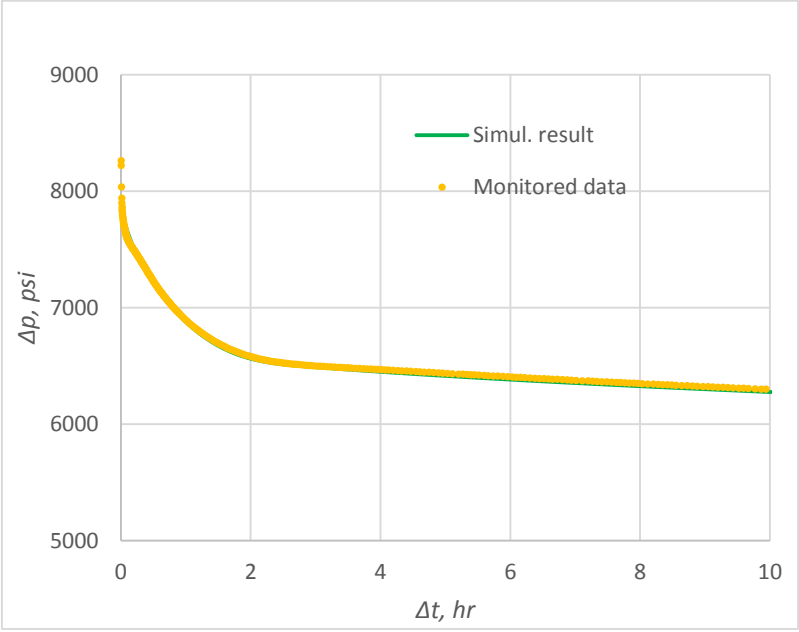

Figure 3-17 History match of the bottomhole pressure of Well A with DFM (C_{Ln}/C_{Lm}=30)

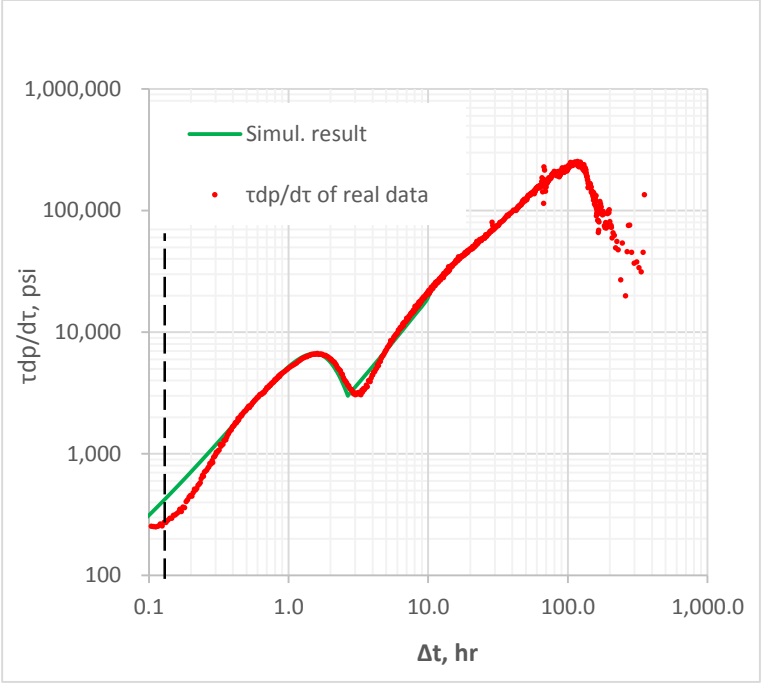

Figure 3-18 History match of the log-log Bourdet derivative with DFM (C_{Ln}/C_{Lm}=30)

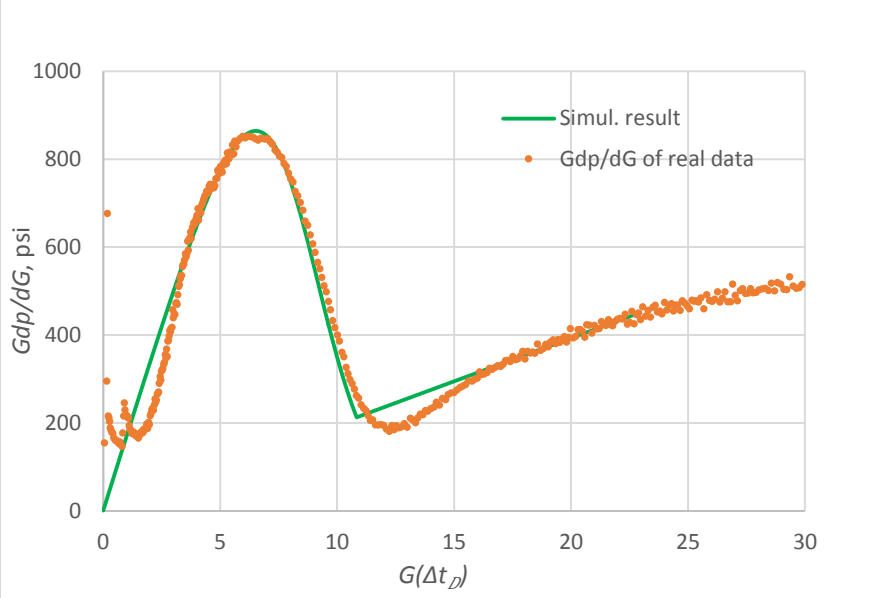

Figure 3-19 History match of the semilog G-function of Well A with DFM (C_{Ln}/C_{Lm}=30)

3.2 Fracture calibration test (FCT) analysis for Well I

Different from other three wells which drilled in Otter Park formation, the target layer of Well I is the Klua/Evie member. The FCT was tested in its toe stage with a single perforation at 9266.21 ft TVD. A total 31.45 bbl fresh water was pumped into the well in 7.13 minutes with a rate at 4.41bbl/min, as shown in Figure 3-20.

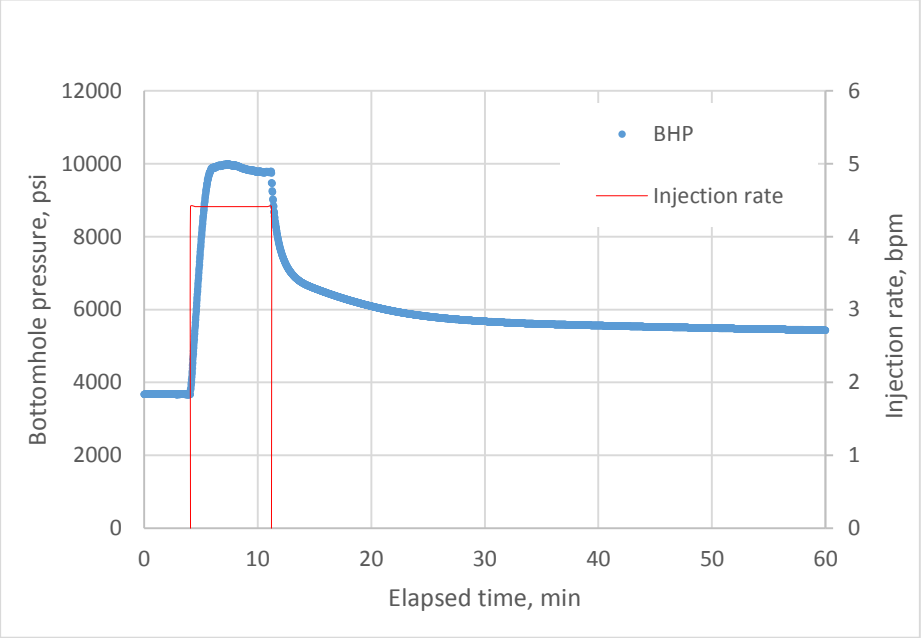

Figure 3-20 Bottomhole pressure change and injection profile for Well I

Figure 3-21 Log-log diagnostic plot for Well I Figure 3-22 are diagnostic plots of well I. The dashed line in the log-log diagnostic plot is the indication of injection time, before which elastic normal closing process has and unit slope. Multiple line with 3/2-slope or unit slope can be picked from the log-log diagnostic plot; and also in the composite G-function plot, many extrapolated straight lines could be drawn through the

origin. The phenomenon is usually named as multiple-closure behavior. If we zoom in on the first closure process in the G-function plot, shown in Figure 3-23, an extrapolated line (the pink dashed line) can be drawn, which lies above the origin and has a positive intercept with the derivative axis. Besides, the calculated semilog G-function derivative seems to approach the asymptote through the origin. Typically, the signature can be interpreted as tip-extension, as discussed in Chapter II.

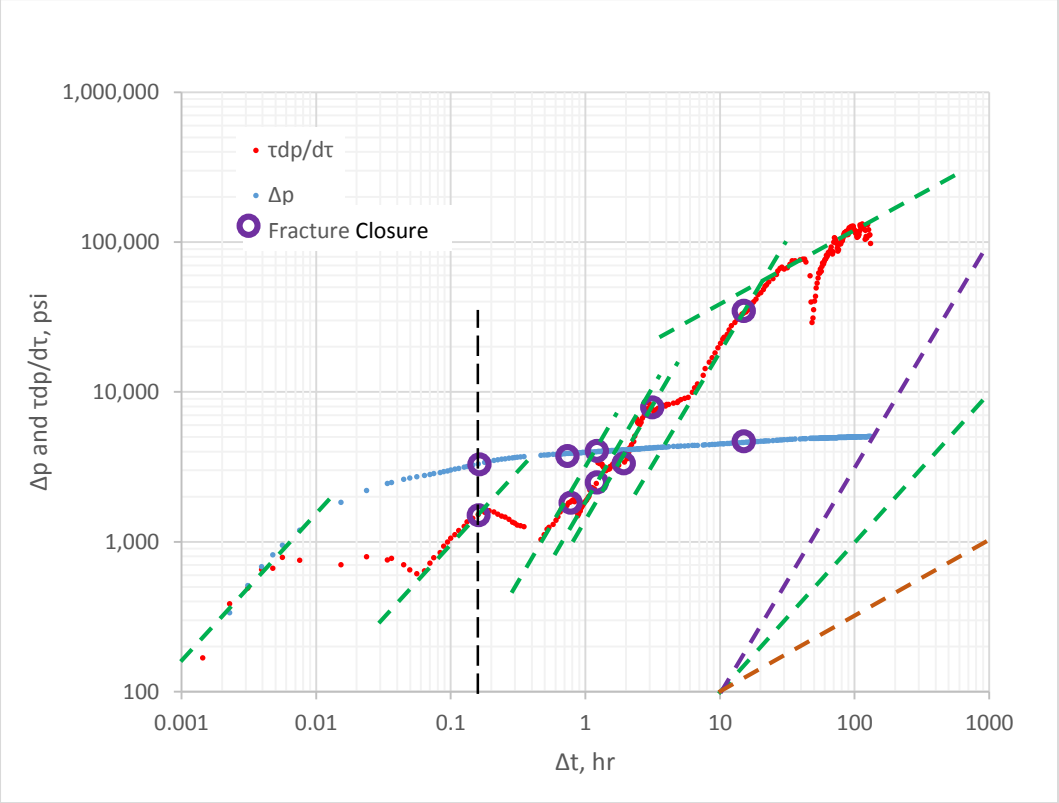

Figure 3-21 Log-log diagnostic plot for Well I

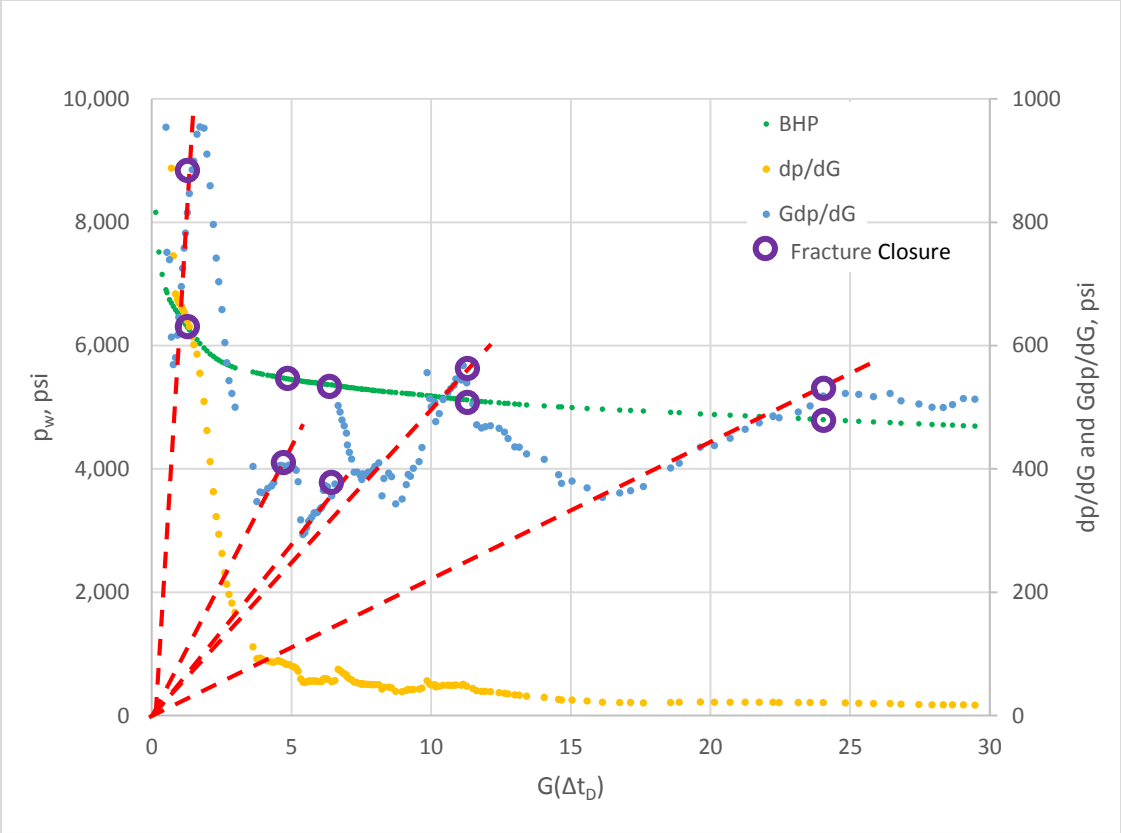

Figure 3-22 Composite G-function diagnostic plot for Well I

First, the finish time of tip-extension can be read out from the semilog G-function plot, at $G_{End\ of\ TE} = 0.764$ or $\Delta t_{End\ of\ TE} = 0.056$ hr. The pressure at this point, which might be taken as the minimum propagation pressure, is 6640.4 psi. After adjusting tip extension with the dimensionless time function defined in Eq. (2.29), the new G-function diagnostic plot could be created and shown in Figure 3-24. It is clear that the new curve has an extrapolated straight line through the origin, same as that in normal leakoff.

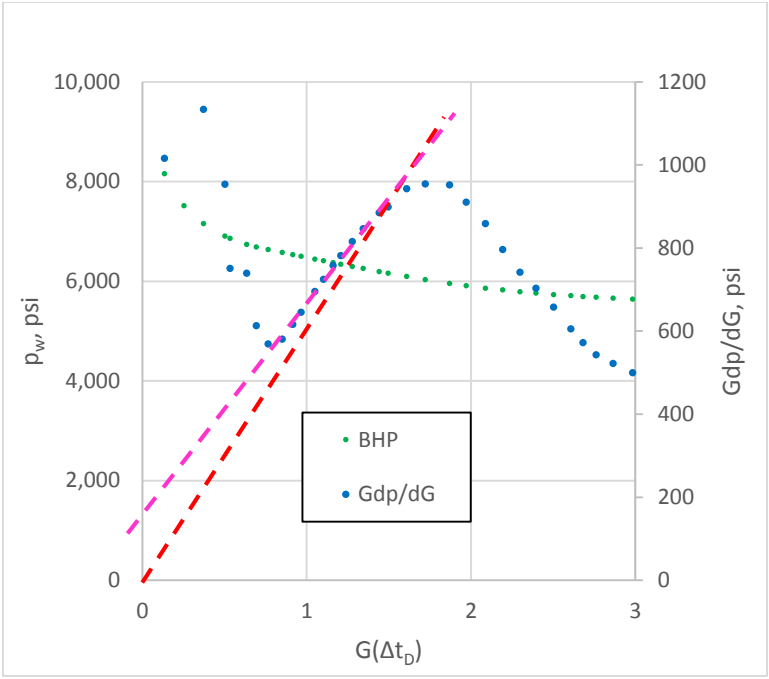

Figure 3-23 Semilog G-function diagnostic plot of the first closure process in Well I

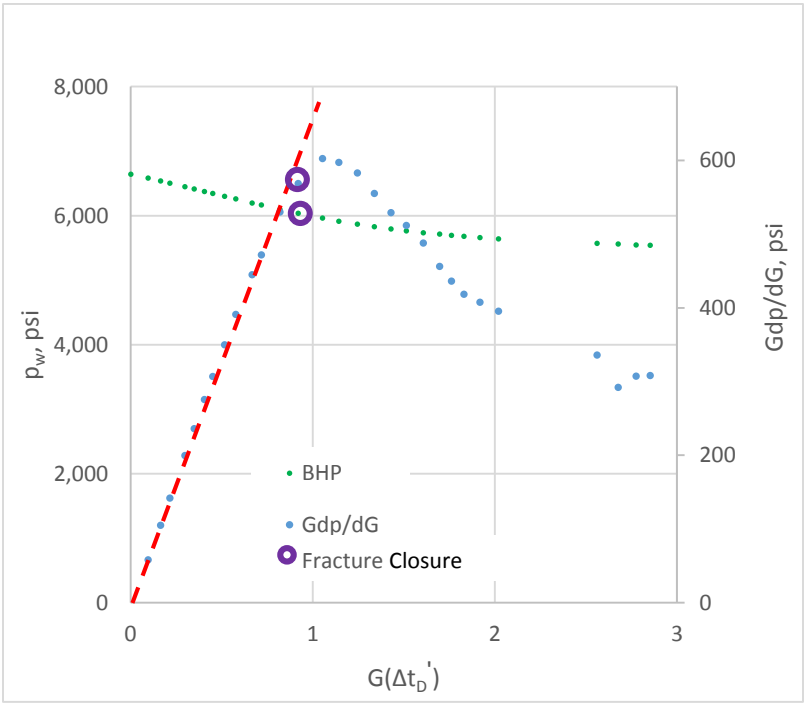

Figure 3-24 Gdp/dG plot of the first closure process after adjusting tip-extension

The log-log diagnostic plot after tip-extension with real time and adjusted time function are shown in Figure 3-25 and Figure 3-26, respectively. Different from the dimensionless time function (Δt_D), the linear relationship between the adjusted time with the real time does not exist anymore, as defined in Eq. (2.29). The non-linear relationship is more transparent at early time after tip-extension, which is exhibited by the distinct curve shapes at early time in Figure 3-25 and Figure 3-26. One should note that the curve during tip-extension is removed by using the adjusted time function. In the diagnostic curves, four straight lines with 3/2-slope and another one with unit slop at very early time before $\Delta \mathrm{t} = t_p$ (indicated by the black dashed line), can be picked out. Since each stands for a closure process, multiple apparent closures happen. It indicates that the fracture system potentially has several pressure-dependent leakoff coefficient during falloff. Physically, one possible scenario is that, several sets of natural fissures, as well as laminated rock fabric, are stimulated during injection. Fluid can penetrate into these fissures, and then leaks off into their surrounded formation. Since each set of natural fissures are suffering different local stress resistances, they are likely to close one by one after shut-in. A part of fracture surface area, or leakoff coefficient, will lose with each closure of natural cracks. Multiple-closure with several system leakoff coefficients therefore could be observed.

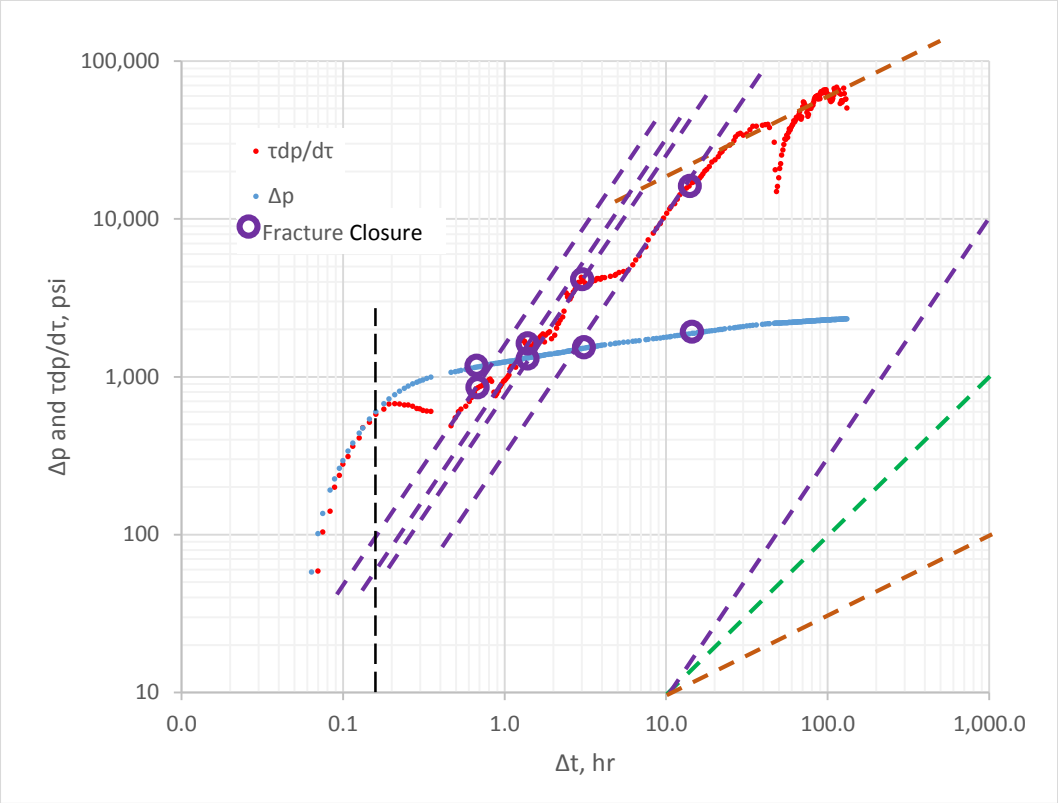

Figure 3-25 Log-log diagnostic plot after tip-extension for Well I with real time

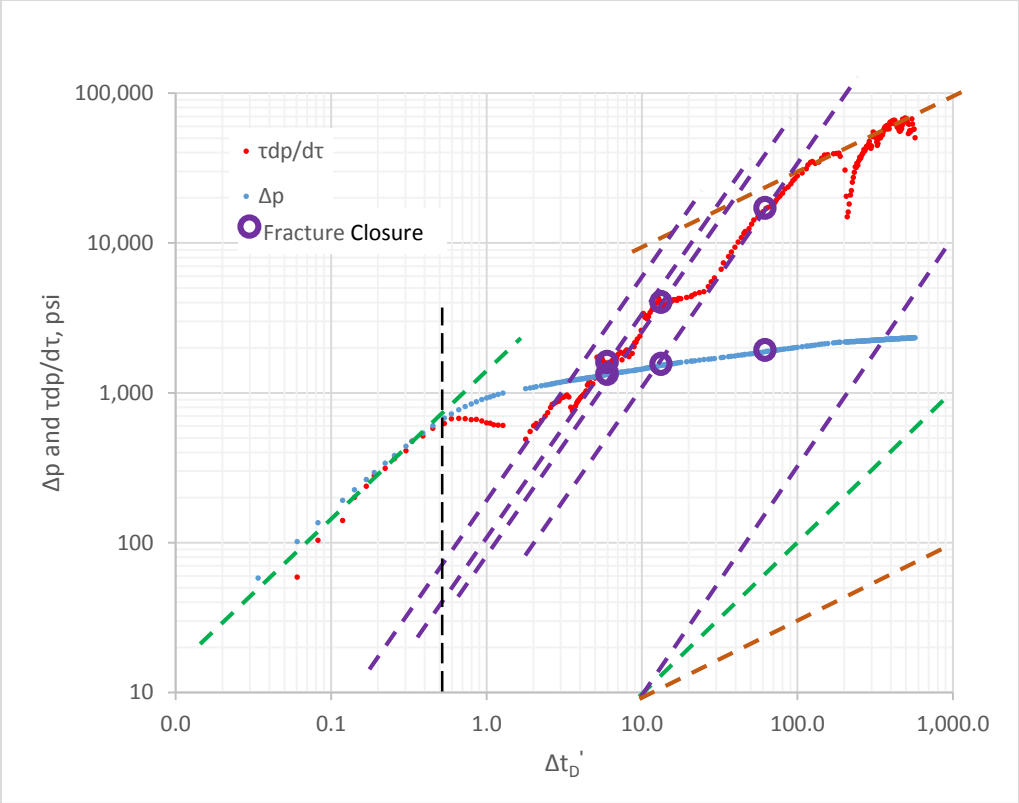

Figure 3-26 Log-log diagnostic plot after tip-extension for Well I with adjusted time function

The composite G-function plot with adjusted time function for the whole pressure falloff are exhibited in the Figure 3-27. Generally, it is pretty similar with the original G-function plot in Figure 3-22. Multiple apparent closures can still be observed. These fives extrapolated lines are corresponding to those five 3/2-sloe lines in the log-log diagnostic plot in Figure 3-26. Same closure events could be identified in both diagnostic curves.

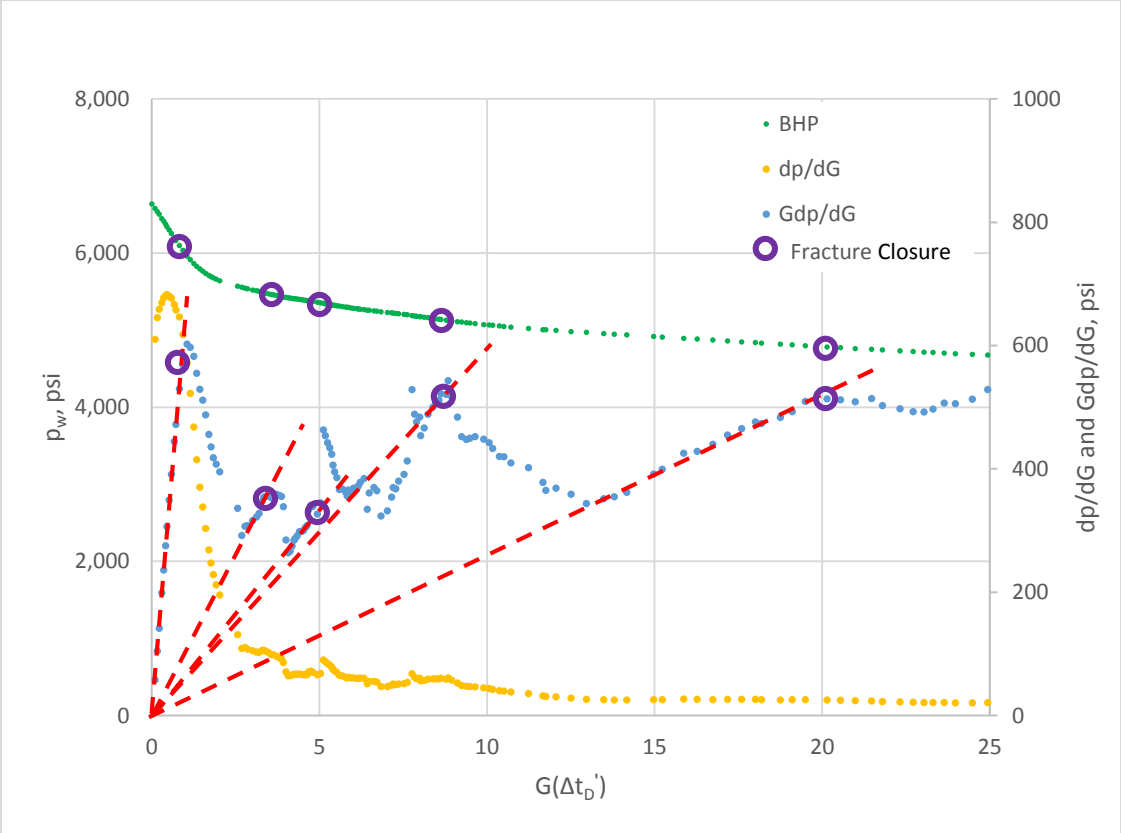

Figure 3-27 Gdp/dG diagnostic plot after adjusting tip-extension

The leakoff coefficient of fracture system is calculated with the traditional Nolte G-function model and PDL, respectively. However, the decoupled fracture model is not feasible in this case. Two more variables, leakoff coefficient and fracture surface area, will be involved by adding one natural fracture into the system, but only one equation could be constituted. In last case in Well A, one set of natural fracture is identified, and there is only one free variable, as shown in Eq. (3.1). Back to this example, 3 sets of natural fracture indicates that there will be 3 undefined variable, which will much complicated for the analysis.

1) Traditional Nolte G-function model

As mentioned before, this model treat the fracture system as normal leakoff, and only the final closure is taken as the closure event. The interpretation result is listed in Table 3-4.

Table 3-4 Results from before-closure analysis with traditional Nolte G-function model for Well I

η	0.934
R_f, ft	70.86
C_L, ft/$\sqrt{\text{min}}$	1.00×10^{-4}
Closure pressure, psi	4784
Closure stress gradient, psi/ft	0.516

2) PDL model

After identifying all the possible closure events from diagnostic plots, the start and end closure pressure for each event can be directly read out. Then, fracture geometry and leakoff coefficient can be calculated out with material balance function. All the result are listed in the following table. And, the change of leakoff coefficient is plotted in Figure 3-28.

Table 3-5 Results from before-closure analysis with PDL model for Well I

R_f, ft	38.6
C_{L1}, ft/$\sqrt{\text{min}}$	1.40×10^{-3}
First closure pressure (Start), psi	6199
First closure pressure (End), psi	5559
C_{L2}, ft/$\sqrt{\text{min}}$	2.38×10^{-4}
Second closure pressure (Start), psi	5474
Second closure pressure (End), psi	5427
C_{L3}, ft/$\sqrt{\text{min}}$	1.52×10^{-4}
Third closure pressure (Start), psi	5358
Third closure pressure (End), psi	5291
C_{L4}, ft/$\sqrt{\text{min}}$	1.34×10^{-4}
Third closure pressure (Start), psi	5121
Third closure pressure (End), psi	4972
C_{L5}, ft/$\sqrt{\text{min}}$	5.90×10^{-5}
Fourth closure pressure, psi	4784
η	0.687

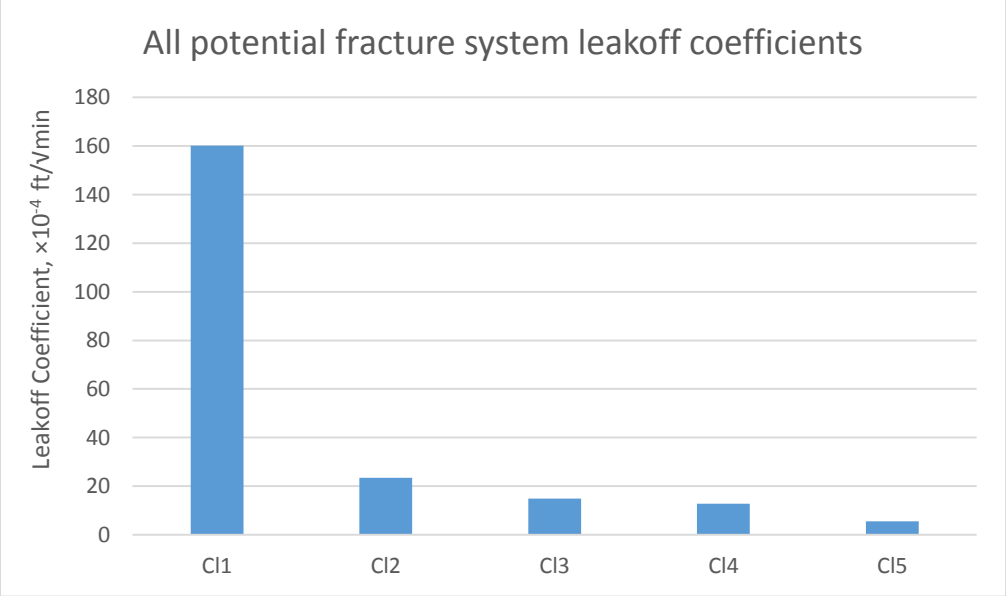

Figure 3-28 Leakoff coefficients during falloff in Well I

With the calculated parameters listed in the above table, PDL simulator is able to generate a curve to generally fit the pressure decline curve (Figure 3-29), and the diagnostic plots (Figure 3-30 and Figure 3-31).

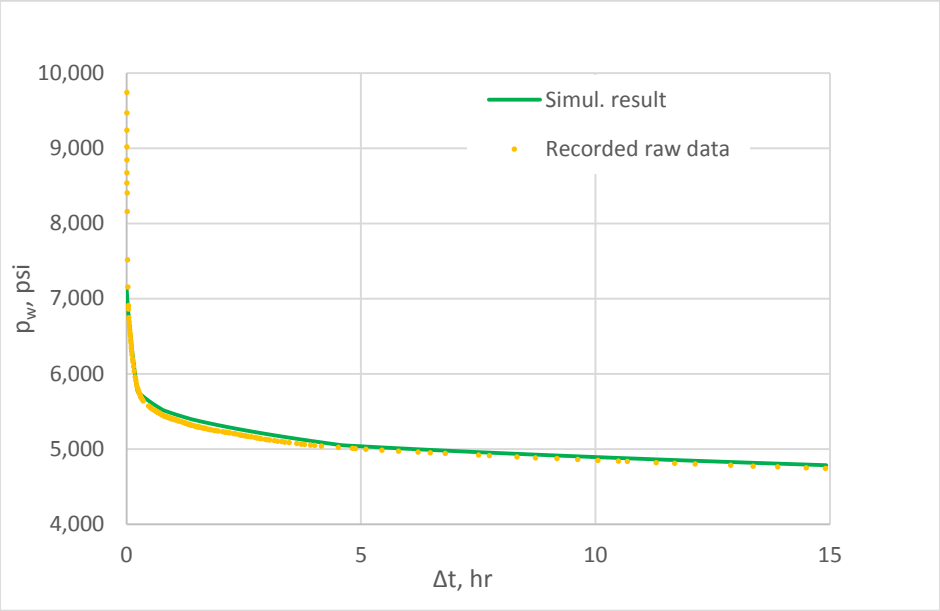

Figure 3-29 History match of the recorded bottomhole pressure of Well I

Figure 3-30 History match of the log-log Bourdet derivative of Well I

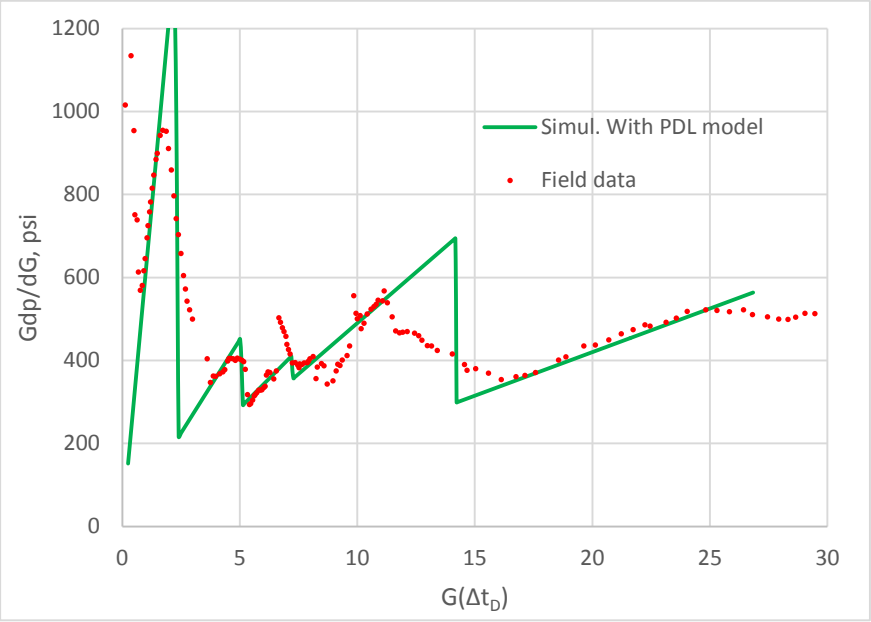

Figure 3-31 History match of the semilog G-function of Well I

Besides, a weak wellbore storage phenomenon is observed at very early time after shut-in (Figure 3-21). Wellbore storage (WBS) coefficient could be quantified as 0.0665 bbl/psi.

3.3 Fracture calibration test (FCT) analysis for Well L

Well L was drilled in Otter Park member. The fracture calibration test was performed in its toe stage at 8979.8 ft TVD. A total volume of 125.8 bbl fresh water was injected into the well in 13.0 minutes with a pumping rate at 9.68bbl/min. The pressure profile during and after injection is monitored and exhibited in Figure 3-32.

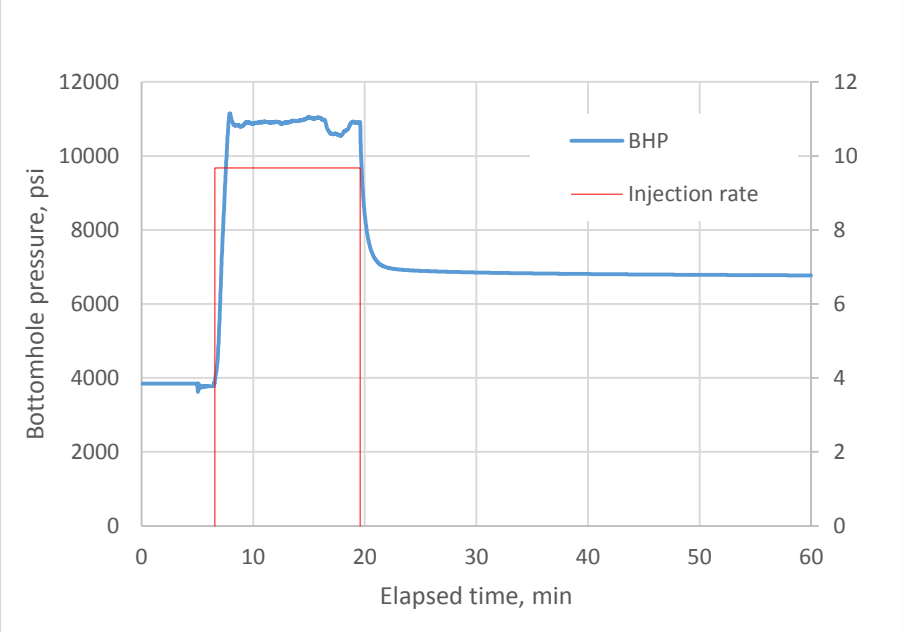

Figure 3-32 Bottomhole pressure change and injection profile for Well L

The diagnostic plots are shown in Figure 3-33 and Figure 3-34. From the both curve, we can see the transverse storage leakoff mechanism. It happens when the leakoff coefficient of natural fracture is so low that the stored fluid in them is squeezed back into main fracture. However, as has been discussed in Chapter II, fracture properties could be estimated from the first 3/2-slope line. Furthermore, more other pressure transient behaviors could also be observed in log-log diagnostic plot. The earliest unit slow should be wellbore storage effect; fracture linear flow, indicated by the first half-slope line, might occurs, which has been discussed in detail in Chapter II; after closure of main fracture, the second half-slope line is likely to be formation linear flow, which could be taken advantage to estimate fracture extension if formation permeability is known.

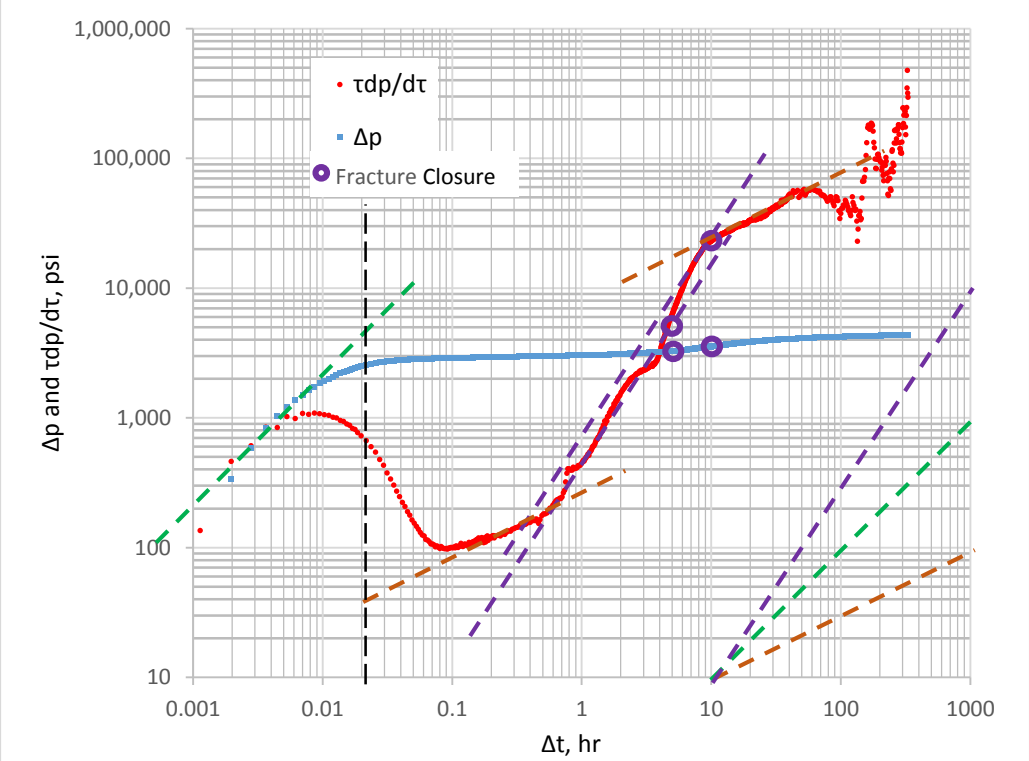

Figure 3-33 Log-log diagnostic plot for Well L

In G-function plot, the belly shape feature under the extrapolated straight line indicates the transverse storage mechanism. Again, these two extrapolated straight lines in the G-function plot correspond to these two line with 3/2-slope in log-log diagnostic plot in Figure 3-33. Same closure events can be picked.

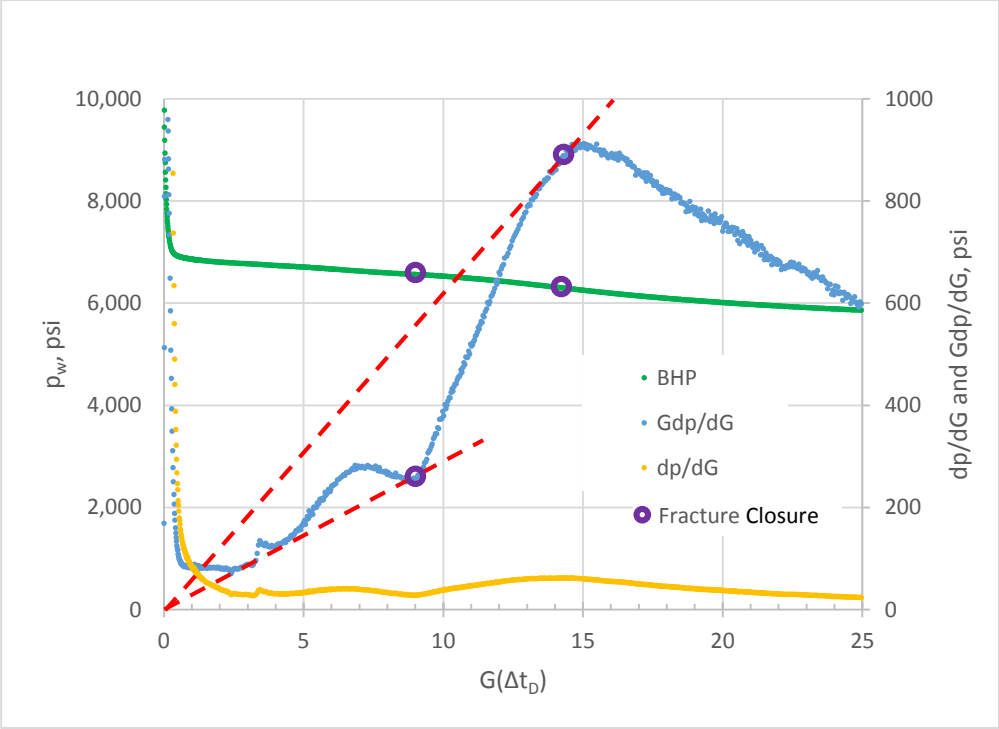

Figure 3-34 Composite G-function diagnostic plot for Well L

1) Traditional Nolte G-function model

Without taking any consideration of natural fracture properties, the traditional Nolte G-function model could estimate the fracture radius, leakoff coefficient and fluid efficiency by assume the fracture system is the ideal leakoff mechanism. The interpretation result is listed in Table 3-6.

Table 3-6 Results from before-closure analysis with traditional Nolte G-function model for Well L

η	0.893
R_f, ft	92.28
C_L, ft/$\sqrt{\text{min}}$	2.85×10^{-4}
Closure pressure, psi	6280
Closure stress gradient, psi/ft	0.699

2) Decoupled fracture model

Similar with the situation in the analysis of Well A, except one of these four parameters is known, leakoff coefficients and fracture extensions of both main and natural fractures, it is currently not able to determine all of them. Therefore, by pre-assuming a leakoff coefficient ratio between these two types of fracture, their extension could be calculated out, as listed in Table 3-7. Again, the linear relationship between A_{fm}/A_{fn} and C_{Ln}/C_{Lm} also exist in Figure 3-35. Figure 3-36 is to show that, generally, natural fracture extension will be limited if its leakoff coefficient is ultra-low, vice versa.

Table 3-7 Results from before-closure analysis with decoupled fracture model for Well L

C_{Lm}/C_{Ln}	2.50	3.33	5	10	100	--
C_{Ln}/C_{Lm}	0.4	0.3	0.2	0.1	0.01	0
$C_{Lm}, \times 10^{-4}\text{ft}/\sqrt{\text{min}}$	1.957	2.425	2.639	2.765	2.842	2.849
A_{fm}, ft^2	12617	19375	22945	25196	26620	26753
R_f, ft	63.37	78.53	85.46	89.56	92.05	92.28
$C_{Ln}, \times 10^{-5}\text{ft}/\sqrt{\text{min}}$	7.826	7.274	5.277	2.765	0.284	0
A_{fn}, ft^2	102,050	62,316	46,057	36,758	31,170	30,655
A_{fr}	0.124	0.311	0.498	0.685	0.854	0.873
η	0.853	0.870	0.881	0.888	0.892	0.893

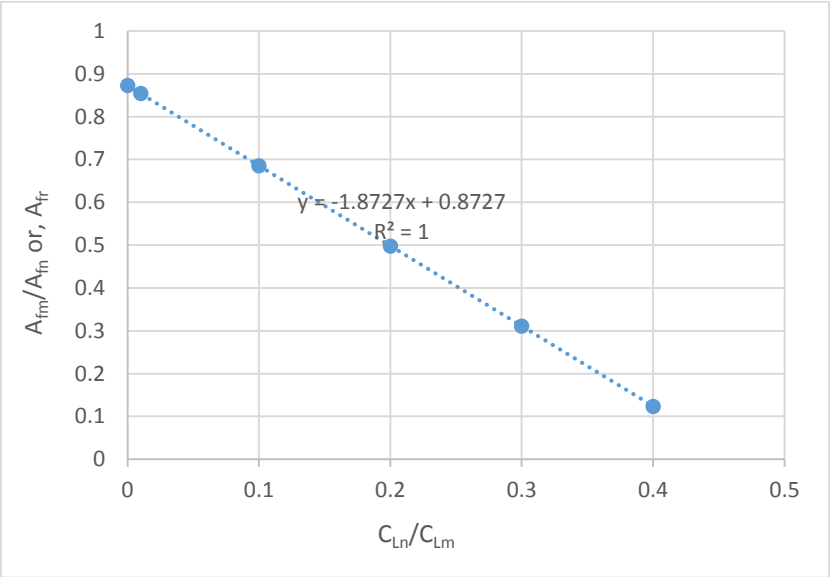

Figure 3-35 Linear relationship between A_{fm}/A_{fn} and C_{Ln}/C_{Lm} in Well L

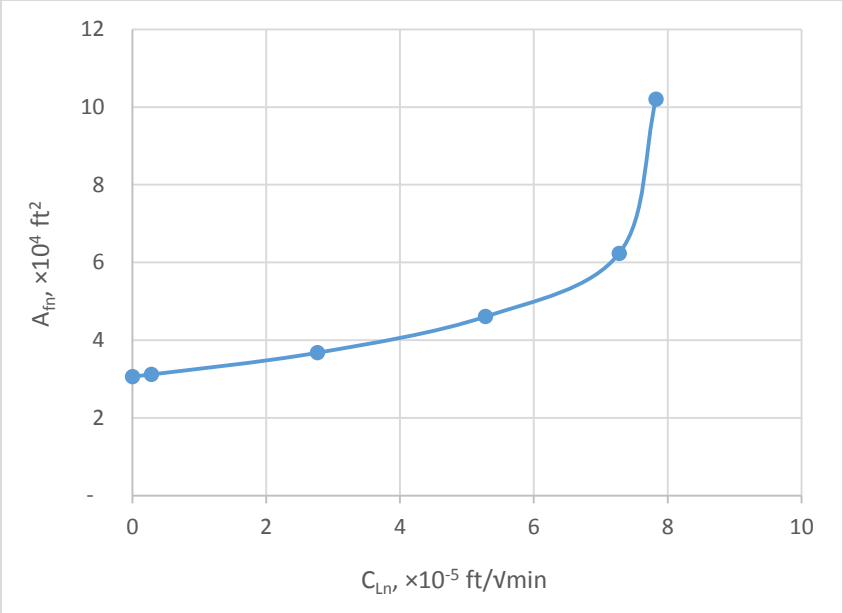

Figure 3-36 Relationship between natural fracture leakoff coefficient with its extension

As shown in the history match for Well A, with all the calculated results shown in Table 3-7, the decouple fracture model (DFM) is able to generate a set of bottomhole pressure, which is able to match the pressure decline curve and also the diagnostic plots. In this case, $C_{Ln} = 0$ is taken for instance, which suggests that fluid in the fracture system is not capable leaks off through the natural fracture surface. The generated data by the DFM simulator has a fairly good match with the recorded data in bottomhole pressure (Figure 3-37), and the diagnostic plots (Figure 3-38 and Figure 3-39).

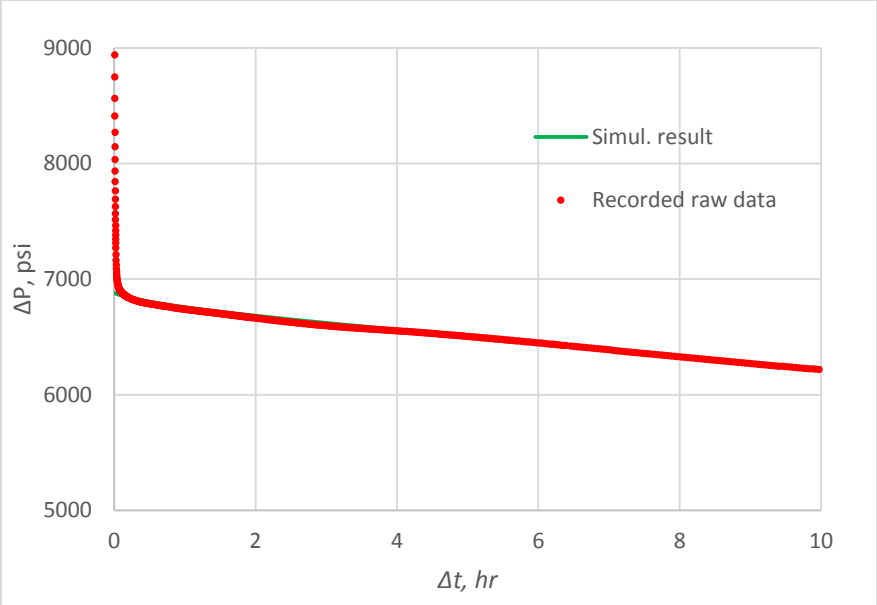

Figure 3-37 History match of the recorded bottomhole pressure of Well L

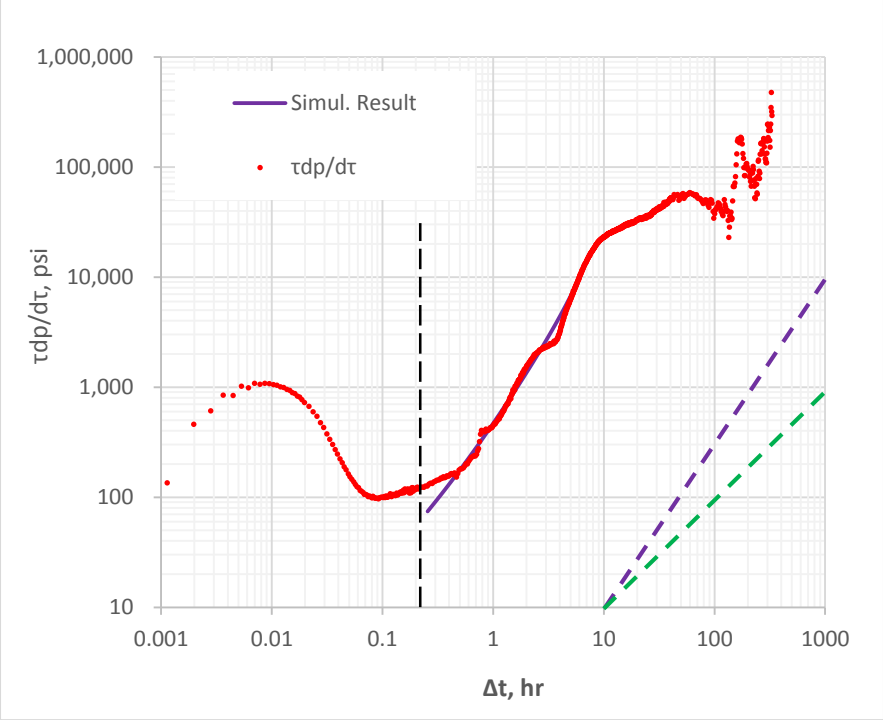

Figure 3-38 History match of the log-log Bourdet derivative of Well L with DFM (C_{Ln}=0)

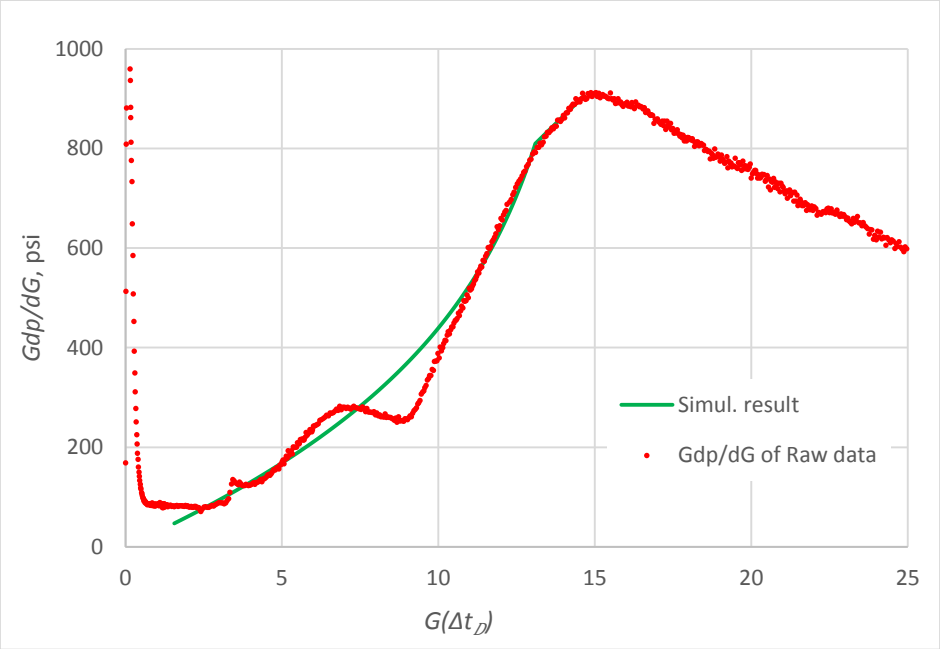

Figure 3-39 History match of the semilog G-function of Well L with DFM (C_{Ln}=0)

Another factor that could be quantified is the wellbore storage effect (WBS), as has been observed in Figure 3-33. The WBS coefficient is calculated as 0.215 bbl/psi.

3.4 Fracture calibration test (FCT) analysis for Well Z

The target layer of the well is the Otter Park member. FCT was tested in its toe stage at 9088.65 ft TVD. Its location in the pad can be found from Figure 3-1. A total volume of 57.87 bbl fresh water was injected into the well in 9.1 minutes with a pumping rate at 6.36bbl/min. The pressure profile during and after injection is monitored and exhibited in Figure 3-40.

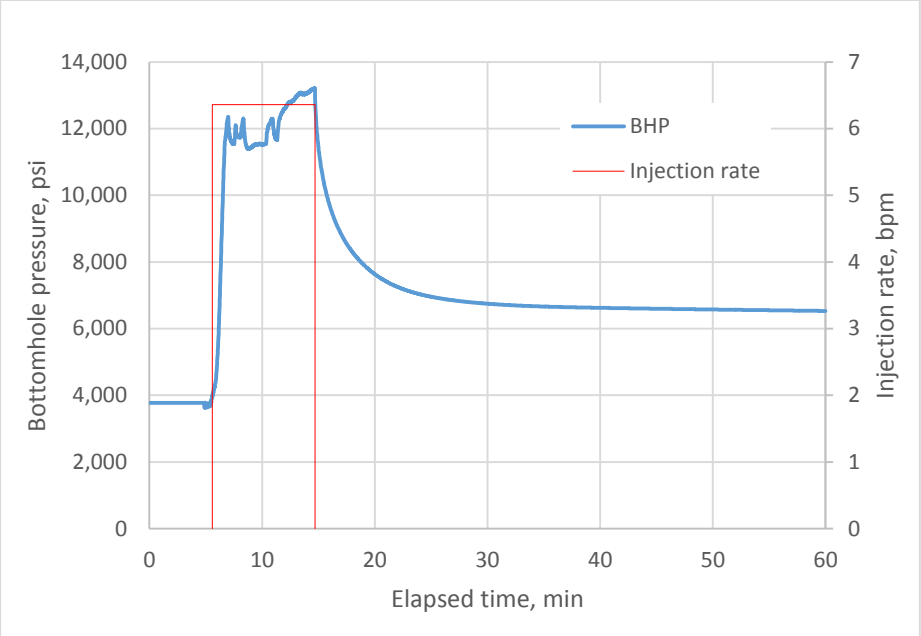

Figure 3-40 Bottomhole pressure change and injection profile for Well Z

The diagnostic plots are shown in Figure 3-41 and Figure 3-42. Similar with Well L, transverse storage behavior is observed before closure. Two 3/2-slope lines can be drawn in the log-log diagnostic plot. These two lines indicate close process of natural and main fracture, respectively. Besides, similar with the FCT in Well L, the early wellbore storage effect (WBS), as well as formation linear flow after closure, are exhibited in the log-log diagnostic plot.

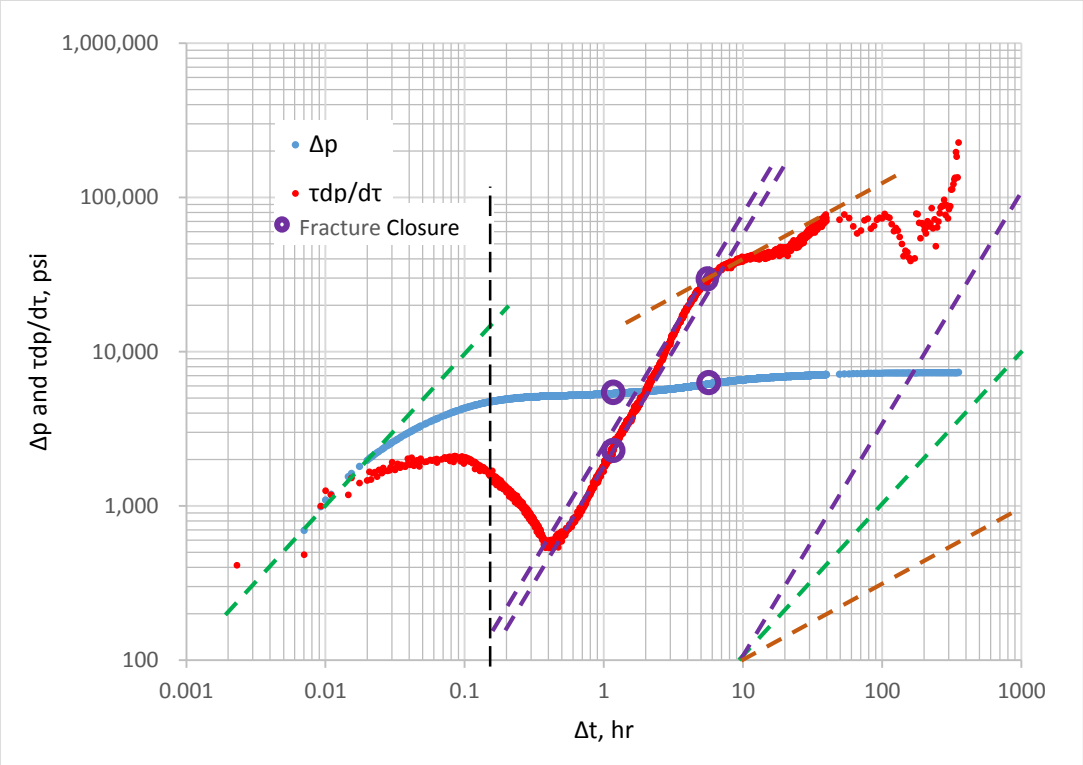

Figure 3-41 Log-log diagnostic plot for Well Z

Two extrapolated straight lines in the G-function plot can be drawn to identify closure events of natural and main fractures. Then their leakoff coefficient and closure pressure can be estimated, respectively.

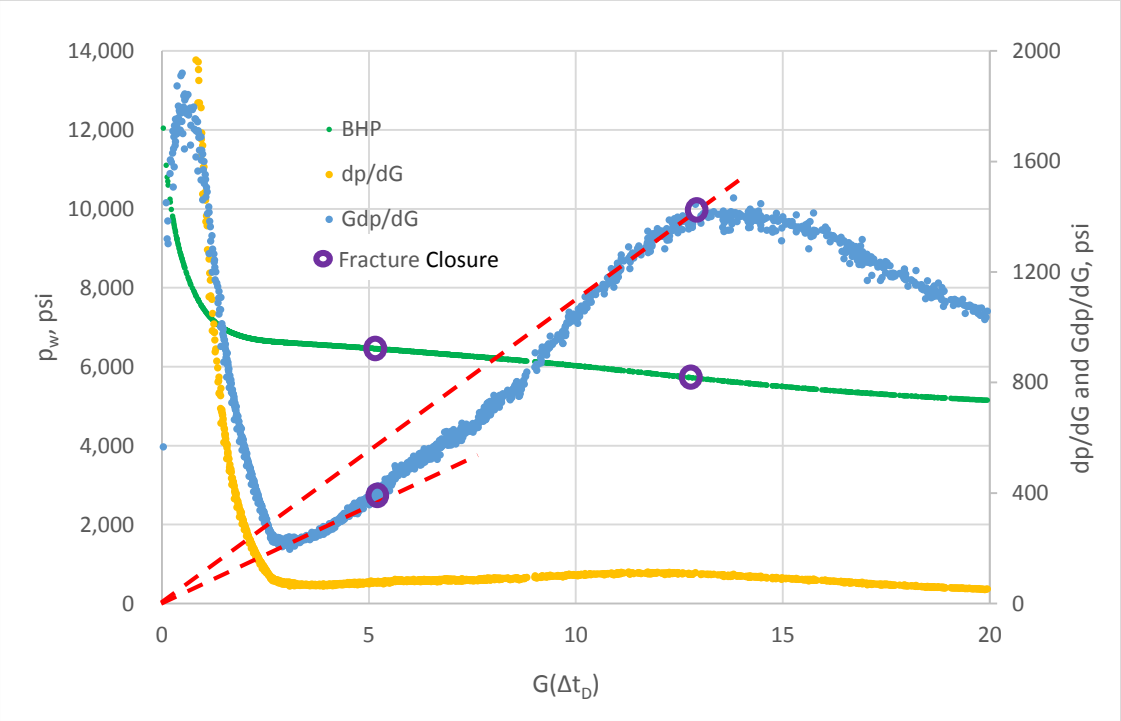

Figure 3-42 Composite G-function diagnostic plot for Well Z

1) Traditional Nolte G-function model

By assuming that no abnormal leakoff mechanisms occurs, the traditional Nolte G-function model is tried to estimated fracture leakoff coefficient. The interpretation result is listed in Table 3-8.

Table 3-8 Results of before-closure analysis with traditional Nolte G-function model for Well Z

η	0.879
R_f, ft	61.26
C_L, ft/$\sqrt{\text{min}}$	4.02×10^{-4}
Closure pressure, psi	5732
Closure stress gradient, psi/ft	0.631

2) Decoupled fracture model

Again, for each assumed C_{Ln}/C_{Lm}, leakoff coefficients and fracture surface areas for both types of fractures are computed, as listed in the following table. The linear relationship between A_{fm}/A_{fn} and C_{Ln}/C_{Lm} is still valid (Figure 3-43). And, natural fracture with lower leakoff coefficient tends to have a smaller extension, as shown in Figure 3-44.

Table 3-9 Results from before-closure analysis with decoupled fracture model for Well Z

C_{Lm}/C_{Ln}	Infinity	10	5	3.33	2.5	2
C_{Ln}/C_{Lm}	0	0.1	0.2	0.3	0.4	0.5
$C_{Lm}, \times 10^{-4}\text{ft}/\sqrt{\text{min}}$	4.015	4.004	3.884	3.773	3.591	3.239
A_{fm}, ft^2	11,791	11,344	11,033	10,407	9,430	7,669
R_f, ft	61.26	60.09	59.26	57.56	54.79	49.41
$C_{Ln}, \times 10^{-5}\text{ft}/\sqrt{\text{min}}$	0	0.4	0.777	1.132	1.436	1.619
A_{fn}, ft^2	7,170	8,220	9,890	12,228	16,072	23,800
A_{fr}	1.644	1.380	1.116	0.851	0.587	0.322
η	0.879	0.875	0.871	0.864	0.854	0.838

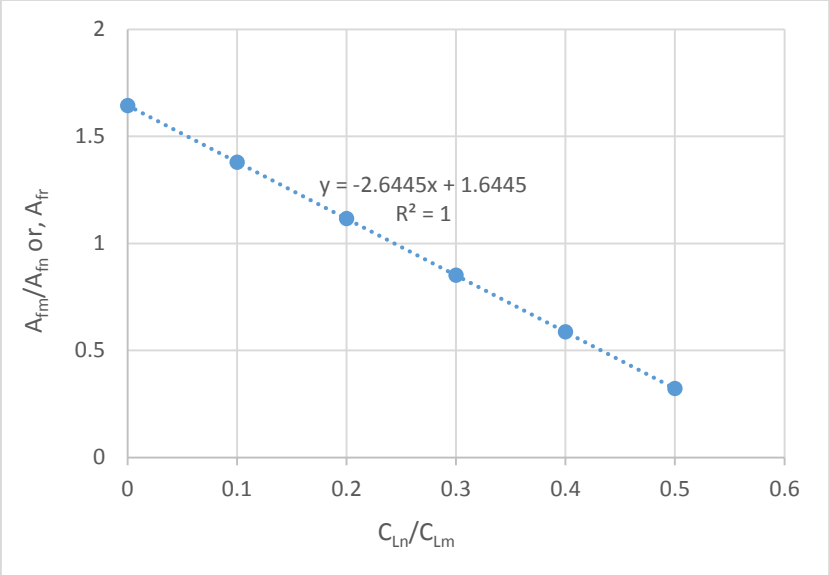

Figure 3-43 Linear relationship between A_{fm}/A_{fn} and C_{Ln}/C_{Lm} in Well Z

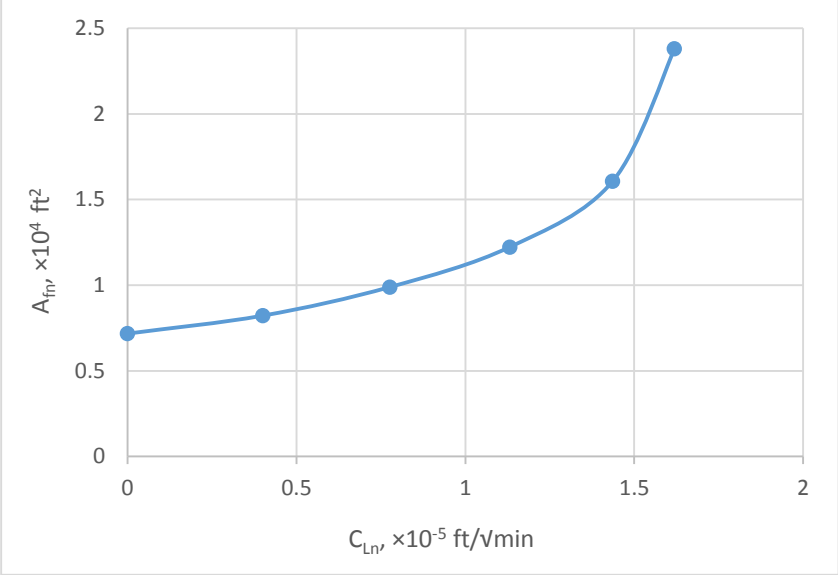

Figure 3-44 Relationship between natural fracture leakoff coefficient with its extension for Well Z

$C_{Ln} = 0$ is taken as the instance for history match. The simulation result has a pretty good fit for the bottomhole pressure (Figure 3-45) and diagnostic plots (Figure 3-46 and Figure 3-47).

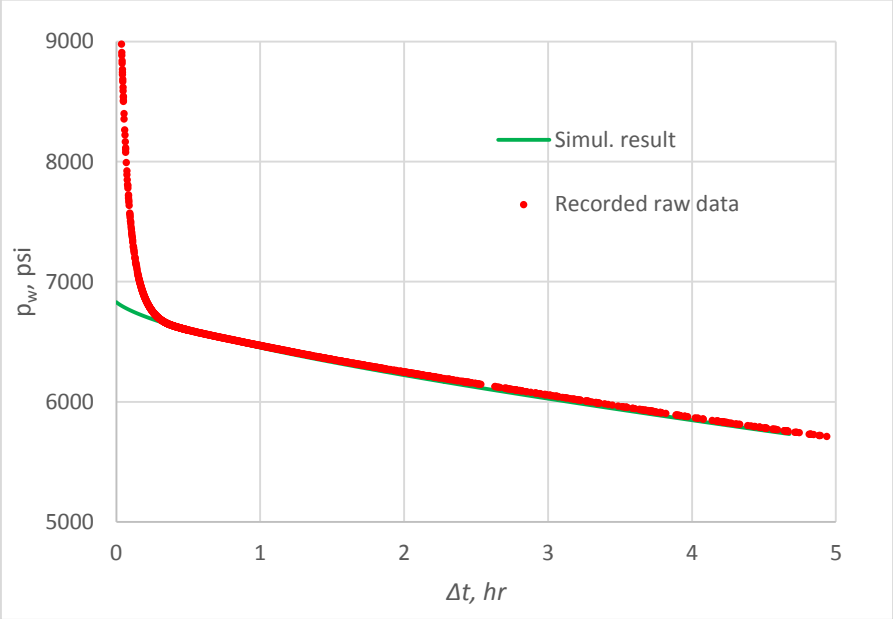

Figure 3-45 History match of the bottomhole pressure of Well Z with DFM (C_{Ln}=0)

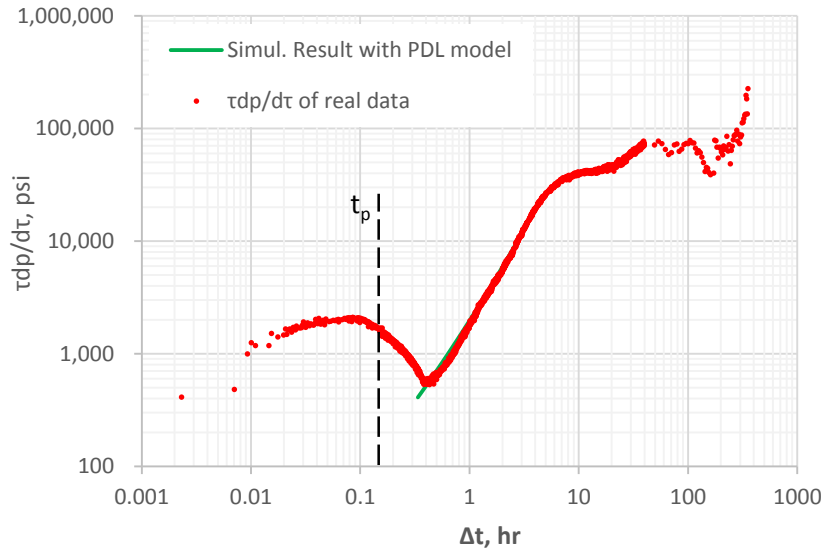

Figure 3-46 History match of the log-log Bourdet derivative of Well Z with DFM (C_{Ln}=0)

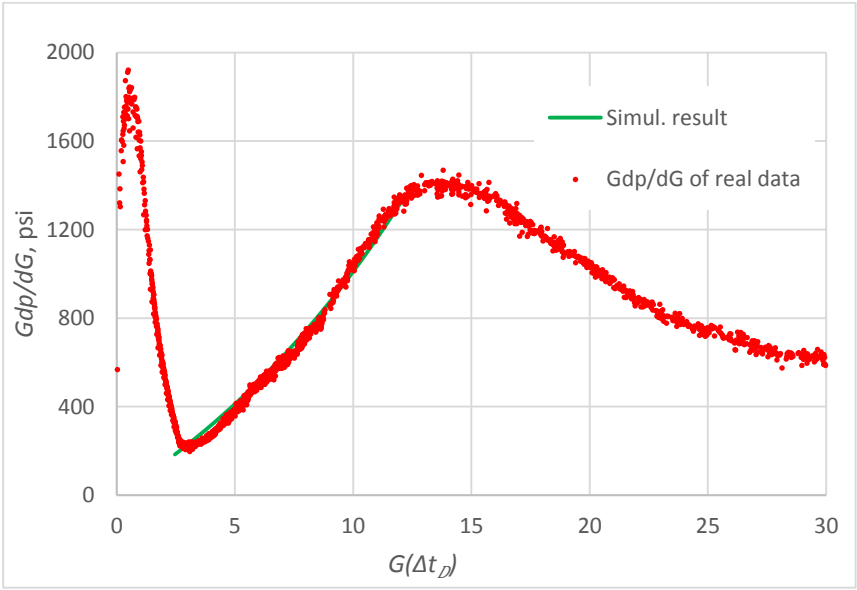

Figure 3-47 History match of the semilog G-function of Well Z with DFM (C_{Ln}=0)

At last, the WBS coefficient is calculated to be 0.272 bbl/psi, which is very close to the value with FCT in Well L.

3.5 Summary of case studies

The summary of FCT interpretation result is listed in Table 3-10. It can be figured out that formation properties could be in great difference among these four wells even they drilled in the same pad. Together with the post-frac gas production rate, as shown in Figure 3-48, the interpretation result for each well will be compared and analyzed. Then, the formation properties could be better described and understood. One should note that in Table 3-10, except for the first and last closure events, three other possible events, as well as their closure pressures and leakoff coefficients, are not listed.

Table 3-10 Summary of before-closure analysis

	Well A	Well I	Well L	Well Z
Formation	Otter Park	Klua	Otter Park	Otter Park
Pumping Vol., bbl	31.45	31.45	125.8	57.87
Pumping time, min	6.666	7.13	13.0	9.1
TVD, ft	8932.2	9266.2	8979.8	9088.6
Closure pressure, psi	6266	4784	6280	5732
Closure stress gradient, psi/ft	0.702	0.516	0.699	0.631
Model	Nolte	Nolte	Nolte	Nolte
C_L, $\times 10^{-4}$ft/$\sqrt{\text{min}}$	0.987	1.00	2.85	4.02
R_f, ft	73.58	70.86	92.28	61.26
Fluid efficiency, η	0.932	0.934	0.893	0.879
Model	PDL	PDL	Decoupled	Decoupled
C_{Ln}, $\times 10^{-4}$ft/$\sqrt{\text{min}}$	5.23	1.34 (C_{L4})	0	0
C_{Lm}, $\times 10^{-4}$ft/$\sqrt{\text{min}}$	0.683	0.590	2.849	4.015
R_f, ft	46.48	38.6	92.28	61.26
A_{fr}	0	0	0.872	1.644
Fluid efficiency, η	0.814	0.687	0.893	0.879

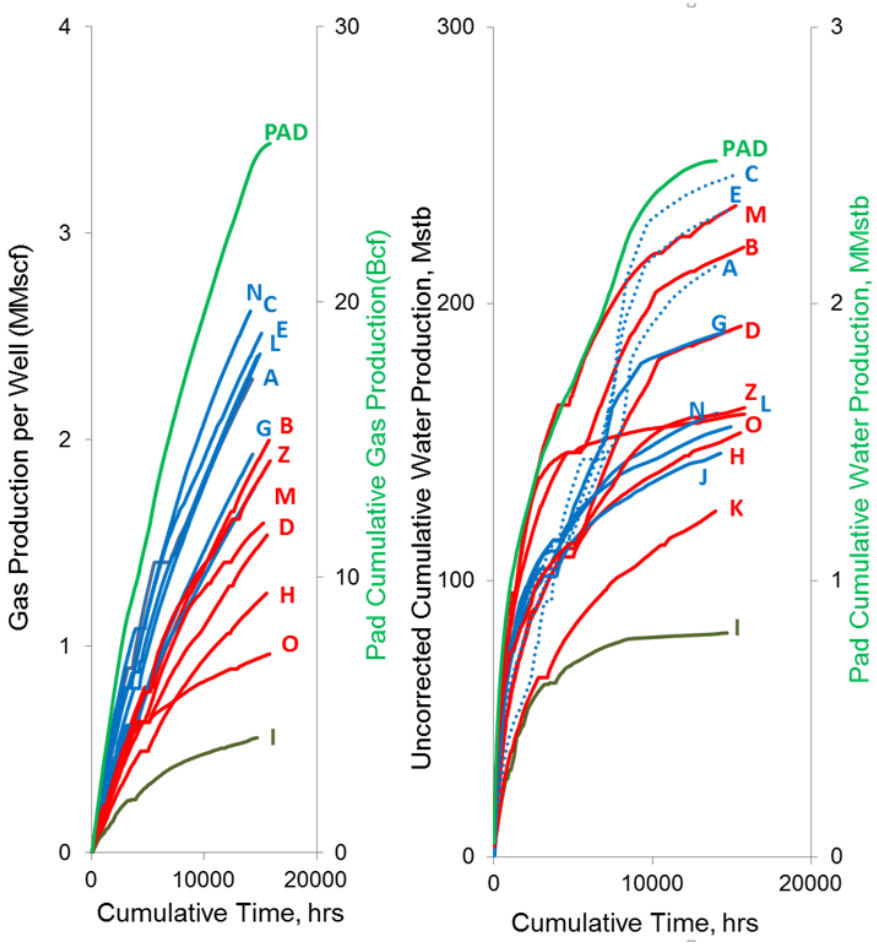

Figure 3-48 Cumulative gas and water production of wells in the pad(Ehlig-Economides et al. 2012)

The first impression on the production profile of all wells in the pad, is that almost all wells located on the fault side have a lower productivity than those on the other side. In other words, the existence of fault could greatly change the mechanical property of the formation. For these four wells with FCT, Well I and Z were drilled on the fault side, we can find that these two wells has a much lower closure stress than the other two on the side without fault. Therefore, fault is one of major factors on well productivity.

Well I, which is the only well located in Klua/ Evie, has a lowest closure gradient, and almost smallest leakoff coefficient as well. It can be expected that the formation is distinct from the overlain Otter Park/Muskwa, and is less permeable than the latter. The lowest production rate confirms the expectation. In its FCT analysis, multiple-closure behavior was observed. Several sets of natural fissures, laminated rock fabric could be activated during treatment, which also can be referred as high uncertainty and complexity. Therefore, it can be concluded that Klua/ Evie might have a smaller permeability, and more complicated rock fabric than the Otter Park/Muskwa members, which is probably the main reason for the low productivity of Well I.

For another well on the side of fault, Well Z, its main fracture has high leakoff coefficients. One possible reason for its low formation stress is that the tested location is very close to the fault, where tectonic stress likely has been released during the formation of fault. Furthermore, natural fractures might be well developed in the vicinity area of the fault. It could be the reason for the observed high fracture leakoff rate. On the other hand, the high flow capacity of these well-developed natural fissures provide an express way for the gas migration. After its generation from kerogen, gas would be likely transported to other layers through the connected natural fissures around the fault. This could be one possible reason for the low production rate of wells on the side of fault even when they were drilled in a permeable formation, like Well Z.

The interpretation result of FCT shows that Well L has a relatively high leakoff coefficient, which indicates that the formation has a relatively high flow capacity. And the well turns out to be the most productive well among these four tested wells.

As to Well A, high leakoff coefficient through natural fractures could be taken as an indication that the hydraulic fracture is able to contact the permeable formation by activated natural fissures. It could be one possible scenario for the relatively high productivity of the well.

In summary, the interpretation result from the FCT with the novel developed models in this dissertation can be used in formation description, especially when abnormal leakoff mechanisms are observed. The properties of natural fractures can be estimated by the PDL and the decoupled fracture model. When these models are involved, FCT could be one of the most beneficial and powerful tools in formation description.

Since early wellbore storage (WBS) behavior has been observed in three of four studied wells. As has been discussed, the early unit-slop curve on log-log derivative or pressure difference are indication of WBS effect. Its effect fades off gradually after the curve departs from the early unit-slope line. Here, we takes the departure point as the end of WBS dominant period. For these three wells with WBS, their durations and calculated coefficients of WBS is listed in Table 3-11. It can be figure out that Well Z has the largest WBS coefficient and longest duration, while WBS is relatively weak in Well I. Together with the pressure response of all wells after shut-in, as shown in Figure 3-49, we might be able to explain the possible scenarios behind the difference WBS behaviors for each well.

Table 3-11 Well storage effect (WBS) for three studied wells

Wells	Duration, s	WBS coefficient, bbl/psi
Well I	20.2	0.0665
Well L	19.1	0.215
Well Z	55.1	0.272

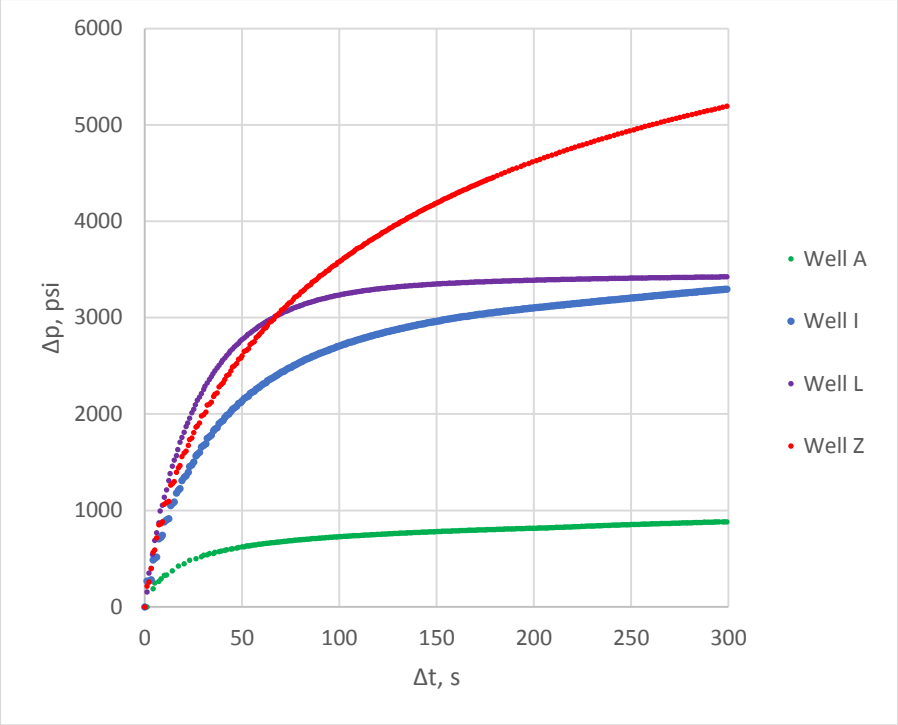

Figure 3-49 Pressure response at early time after shut-in

First, it is clear that Well A has the slowest pressure falloff after shut-in, which is the direct reason for the missing of WBS in its log-log diagnostic plot. As been discussed in Chapter II on early WBS effect, the disappearance of WBS could be the result from slow decline of net pressure, or relatively low pressure loss associated with

friction in the wellbore and near-wellbore vicinity. Several following possible scenarios could be presumed and estimated.

1) Although the leakoff coefficient into matrix is relatively low, high leakoff rate into natural fissures has been presented by the PDL behavior. Therefore, the missing of WBS, or the low decline rate of pressure after shut-in, is probably not the result of slow dissipation rate of net pressure.
2) More likely, the missing of WBS is due to the small pressure loss associated with friction during injection, which probably an indication of good connection between wellbore and fracture.

For those three wells with observed WBS phenomenon, Well I has the smallest WBS coefficient. Correspondingly, compared with other two wells, pressure decline rate of Well I is the lowest, as shown in Figure 3-49. In combination with its interpretation results, we can find that the existing of WBS might be the result of very high leakoff rate at early time after shut-in. While, the impact of pressure loss by friction, is difficult to determine.

Well L has a similar leakoff coefficient with Well Z, but its WBS duration is much shorter than the later. In the pressure difference plot, we can find that their pressure decline curve is close to each other in the early time. Since the injection rate in Well L is much higher than the rest, one possible reason for the rapid decline of recorded pressure at early time is because of the dissipation of friction pressure. According to the interpretation result in Table 3-7, large extension of natural fractures is likely connected,

but they have a lower leakoff coefficient, and probably have little contribution to the rapid pressure decline at beginning.

Well Z has a strong WBS behavior, represented by the longest duration and largest leakoff coefficient. Correspondingly, the rapid pressure decline at early time is relatively steep and lasts for a long duration. Since the early system leakoff coefficient is limited, the strong WBS might be the result of friction dissipation.

3.6 Summary of the Chapter III

In this chapter, four wells drilled in the same pad in Horn River Shale are taken as examples for FCT analysis. As a comparison with tradition Nolte method, which can only be used to determine the closure pressure of main fracture, leakoff coefficient and fluid efficiency, the new-derived PDL model and decoupled fracture model are employed to interpret the pressure falloff data. By adding natural fractures into the fracture system, more parameters are available to describe the leakoff system. These two new model, PDL model and decoupled fracture model, not only can be used to precisely estimate the closure pressure and leakoff coefficient of main fracture, fluid efficiency, but also provide a chance to estimate the extension, leakoff coefficient of connected natural fractures. More parameters therefore are able to be quantified, such as closure pressure, leakoff coefficient and extension of natural fractures. The curve generated by both PDL and decoupled fracture model are able to match the recorded field data, which proves the validation of the new derived models in this dissertation.

Together with geological background, the interpreted result can be used to explain their difference in production performance. Besides, WBS effect is proven to be directly dependent on the pressure decline rate at early time immediately after shut-in. Strong WBS is usually the result of two major mechanisms: rapid decline of net pressure, when the leakoff coefficient is relatively high or PDL/tip-extension occurs; and the dissipation of friction along the wellbore and at the near-wellbore vicinity. Therefore, WBS behavior in some cases might be used to justify the initial leakoff coefficient, or estimate the connection condition between wellbore and fracture.

CHAPTER IV

CONCLUSIONS AND RECOMMENDATIONS

In this chapter, several significant conclusions will be listed as a summary. And, based this dissertation, there are also some other aspects are recommended for the future work.

4.1 Conclusions

This research provides new analytical models for all of the known fracture calibration leakoff behaviors, including wellbore storage (WBS), tip-extension, pressure dependent leakoff (PDL), multiple apparent closure events and transverse storage behavior. The new models provide matches for abnormal leakoff behavior found in field data from Horn River Shale. Several key conclusions are the following.

1. WBS may be an indication of the communication condition between the wellbore and the hydraulic fracture. Dissipation of friction in the wellbore and near-wellbore area looks like classic WBS behavior. Because of fluid expansion, the after-flow effect cannot be neglected for the FCT with small injection volume.
2. The new model for tip-extension shows a composite G-function derivative curve approaching zero at the origin. If the fracture closes shortly after tip-extension, or the recorded data is not long enough for the fracture to close, the extrapolated straight line would have a positive intercept in the pressure axis, which is the commonly accepted indication of tip extension.

3. Poroelastic closure with normal leakoff should always correspond to unit slope if the closure time is less than the injection time or 3/2-slope if the closure time exceeds ten times the injection time on the Bourdet log-log diagnostic derivative plot. Closure process of a natural fracture network can be picked in the same way as that of main fracture.
4. The decoupled fracture model provides a match for PDL and transverse storage behavior. The contribution of fluid leakoff through natural fractures, whether in PDL or transverse storage, can be estimated both by the PDL model and the decoupled fracture model. The decoupled fracture model includes leakoff coefficient and surface area for both the main fracture and the natural fracture network, but the set of parameters for a given behavior is not unique.

4.2 Recommendations

The following works might be done in the future.

1. Since the dissertation has developed the pressure solutions for the most commonly observed leakoff mechanisms before closure, a comprehensive FCT interpretation tool could be constructed. It could include all the flow regimes and before-closure leakoff mechanisms as developed in the dissertation, as well as after-closure analysis.

2. For the FCT in the naturally fracture formation, some other data source, like microseismic map, could be used to calibrate the interpretation result from PDL model or decoupled fracture model.

REFERENCES

Al-Thawad, F.M. and Jamiol Ahmady, M. 2014. A Novel Semi-Analytical Solution for Transient Pressure Data Interpretation of a Fractured Well in an Asymmetric Reservoir. Paper presented at the International Petroleum Technology Conference, Kuala Lumpur, Malaysia International Petroleum Technology Conference. DOI: 10.2523/IPTC-17785-MS.

Bachman, R.C., Anderson, I., Hawkes, R.V. et al. 2013. Interpretation of Closure Stress in the Montney Shale Using Pta Based Techniques. Paper presented at the SPE Hydraulic Fracturing Technology Conference, The Woodlands, Texas, USA. Society of Petroleum Engineers. DOI: 10.2118/163825-MS.

Bachman, R.C., Walters, D.A., Hawkes, R. et al. 2012. Reappraisal of the G Time Concept in Mini-Frac Analysis (Includes Associated Discussion). Paper presented at the SPE Annual Technical Conference and Exhibition, San Antonio, Texas, USA. Society of Petroleum Engineers. DOI: 10.2118/160169-MS.

Bandis, S., Lumsden, A., and Barton, N. 1983. Fundamentals of Rock Joint Deformation. *International Journal of Rock Mechanics and Mining Sciences & Geomechanics Abstracts* **20** (6): 249-268. DOI: 10.1016/0148-9062(83)90595-8

Barree, R.D. 1998. Applications of Pre-Frac Injection/Falloff Tests in Fissured Reservoirs - Field Examples. Paper presented at the SPE Rocky Mountain Regional/Low-Permeability Reservoirs Symposium, Denver, Colorado. Society of Petroleum Engineers 00039932. DOI: 10.2118/39932-ms.

Barree, R.D., Barree, V.L., and Craig, D. 2009. Holistic Fracture Diagnostics: Consistent Interpretation of Prefrac Injection Tests Using Multiple Analysis Methods. *SPE Production & Operations* **24** (3): pp. 396-406. DOI: 10.2118/107877-pa

Barree, R.D., Harris, H.G., Towler, B.F. et al. 2013. Effects of High Pressure-Dependent Leakoff (Pdl) and High Process-Zone Stress (Pzs) on Stimulation Treatments and Production. Paper presented at the SPE Unconventional Resources Conference and Exhibition-Asia Pacific, Brisbane, Australia. Society of Petroleum Engineers. DOI: 10.2118/167038-MS.

Barree, R.D., Miskimins, J.L., and Gilbert, J.V. 2014. Diagnostic Fracture Injection Tests: Common Mistakes, Misfires, and Misdiagnoses. Paper presented at the SPE Western North American and Rocky Mountain Joint Meeting, Denver, Colorado. Society of Petroleum Engineers. DOI: 10.2118/169539-MS.

Barree, R.D. and Mukherjee, H. 1996. Determination of Pressure Dependent Leakoff and Its Effect on Fracture Geometry. Paper presented at the SPE Annual Technical Conference and Exhibition, Denver, Colorado. Society of Petroleum Engineers. DOI: 10.2118/36424-MS.

Barton, N., Bandis, S., and Bakhtar, K. 1985. Strength, Deformation and Conductivity Coupling of Rock Joints. *International Journal of Rock Mechanics and Mining Sciences & Geomechanics Abstracts* **22** (3): 121-140. DOI: http://dx.doi.org/10.1016/0148-9062(85)93227-9

Beaudoin, W.P., Khalid, S., Allison, J. et al. 2011. Horn River Basin: A Study of the Behaviour of Frac Barriers in a Thick Shale Package Using the Integration of

Microseismic, Geomechanics and Log Analysis. Paper presented at the Canadian Unconventional Resources Conference, Calgary, Alberta, Canada. Society of Petroleum Engineers. DOI: 10.2118/147510-MS.

Branagan, P.T., Warpinski, N.R., Engler, B. et al. 1996. Measuring the Hydraulic Fracture-Induced Deformation of Reservoirs and Adjacent Rocks Employing a Deeply Buried Inclinometer Array: Gri/Doe Multi-Site Project. Paper presented at the SPE Annual Technical Conference and Exhibition, Denver, Colorado. Society of Petroleum Engineers. DOI: 10.2118/36451-MS.

Carter, R.D. 1957. Derivation of the General Equation for Estimating the Extent of the Fractured Area. In Appendix of *"Optimum Fluid Characteristics for Fracture Extension"*, ed. Howard, G.C. and Fast, C.R., Drilling and Production Practices, New York: API.

Castillo, J.L. 1987. Modified Fracture Pressure Decline Analysis Including Pressure-Dependent Leakoff. Paper presented at the Low Permeability Reservoirs Symposium, Denver, Colorado. Society of Petroleum Engineers. DOI: 10.2118/16417-MS.

Craig, D.P., Eberhard, M.J., and Barree, R.D. 2000. Adapting High Permeability Leakoff Analysis to Low Permeability Sands for Estimating Reservoir Engineering Parameters. Paper presented at the SPE Rocky Mountain Regional/Low Permeability Reservoirs Symposium, Denver, Colorado. Society of Petroleum Engineers. DOI: 10.2118/60291-MS.

Craig , D.P., Odegard, C.E., Pearson, W.C., Jr. et al. 2000. Case History: Observations from Diagnostic Injection Tests in Multiple Pay Sands of the Mamm Creek Field, Piceance Basin, Colorado. Paper presented at the SPE Rocky Mountain Regional/Low-Permeability Reservoirs Symposium and Exhibition, Denver, Colorado. Society of Petroleum Engineers. DOI: 10.2118/60321-MS.

Ehlig-Economides, C.A., Ahmed, I.A., Apiwathanasorn, S. et al. 2012. Stimulated Shale Volume Characterization: Multiwell Case Study from the Horn River Shale: Ii. Flow Perspective. Paper presented at the SPE Annual Technical Conference and Exhibition, San Antonio, Texas, USA. Society of Petroleum Engineers. DOI: 10.2118/159546-MS.

Ehlig-Economides, C.A. and Economides, M.J. 2011. Water as Proppant. Paper presented at the SPE Annual Technical Conference and Exhibition, Denver, Colorado, USA. Society of Petroleum Engineers. DOI: 10.2118/147603-MS.

Fan, Y. and Chen, Z. 1997. A Rapid Method for Determining Fracturing-Fluid Leakoff Coefficient and Spurt Loss. Paper presented at the SPE Western Regional Meeting, Long Beach, California. Society of Petroleum Engineers. DOI: 10.2118/38308-MS.

Gulrajani, S.N. and Nolte, K.G. 2000. *Fracture Evaluation Using Pressure Diagnostics* Ed Economides, M.J. and Nolte, K.G. Reservoir Stimulation (Third Edition). Chichester, England: John Wiley & Sons Ltd,. Original edition. ISBN 0471491926.

Hagoort, J. 1981. Waterflood-Induced Hydraulic Fracturing. PhD Thesis, Delft University, Delft, Netherlands.

Howard, G.C. and Fast, C.R. 1957. Optimum Fluid Characteristics for Fracture Extension. *Drilling and Prod. Prac. API*: 261-270.

Johnson, M.F., Walsh, W., Budgell, P.A. et al. 2011. The Ultimate Potential for Unconventional Gas in the Horn River Basin: Integrating Geological Mapping with Monte Carlo Simulations. Paper presented at the Canadian Unconventional Resources Conference, Calgary, Alberta, Canada. Society of Petroleum Engineers. DOI: 10.2118/148976-MS.

Koning, E.J.L. and Niko, H. 1985. Fractured Water-Injection Wells: A Pressure Falloff Test for Determining Fracture Dimensions. Paper presented at the Annual Technical Conference and Exhibfiionof the society of Petroleum Engineers, Las Vegas, Nevada. Society of Petroleum Engineers. DOI: 10.2118/14458-MS.

Lee, W.J., Rollins, J.B., and Spivy, J.P. 2003. *Pressure Transient Testing*. Spe Textbook Series. Richardson, Texas: SPE. Original edition.

Mack, M.G. and Warpinski, N.R. 2000. *Mechanics of Hydraulic Fracturing*. Ed Economides, M.J. and Nolte, K.G. Reservoir Stimulation (Third Edition). Chichester, England: John Wiley & Sons. Original edition. ISBN 0471491926.

Marongiu-Porcu, M. 2014. A Global Model for Fracture Falloff Analysis. Ph.D. Thesis, Texas A&M University, College Station, Texas, USA.

Marongiu-Porcu, M., Ehlig-Economides, C.A., and Economides, M.J. 2011. Global Model for Fracture Falloff Analysis. Paper presented at the North American

Unconventional Gas Conference and Exhibition, The Woodlands, Texas, USA. Society of Petroleum Engineers SPE-144028-MS. DOI: 10.2118/144028-ms.

Marongiu-Porcu, M., Retnanto, A., Economides, M.J. et al. 2014. Comprehensive Fracture Calibration Test Design. Paper presented at the Hydraulic Fracturing Technology Conference, The Woodlands, Texas. Society of Petroleum Engineers. DOI: 10.2118/168634-MS.

Mayerhofer, M.J. and Economides, M.J. 1993. Permeability Estimation from Fracture Calibration Treatments. Paper presented at the SPE Western Regional Meeting, Anchorage, Alaska. 1993 Copyright 1993, Society of Petroleum Engineers, Inc. This paper was prepared for presentation at the Western Regional Meeting held in Anchorage, Alaska, U.S.A. 26-28 May 00026039. DOI: 10.2118/26039-ms.

Mayerhofer, M.J. and Economides, M.J. 1997. Fracture-Injection-Test Interpretation: Leakoff Coefficient Vs. Permeability. *SPE Production & Operations* **12** (4): 231-236. DOI: 10.2118/28562-pa

Mayerhofer, M.J., Ehlig-Economides, C.A., and Economides, M.J. 1995. Pressure-Transient Analysis of Fracture Calibration Tests. *SPE Journal of Petroleum Technology* **47** (3): 229-234. DOI: 10.2118/26527-pa

McClure, M.W., Blyton, C.A.J., Sharma, M.M. et al. 2014. The Effect of Changing Fracture Compliance on Pressure Transient Behavior During Diagnostic Fracture Injection Tests. Paper presented at the SPE Annual Technical Conference and Exhibition, Amsterdam, The Netherlands. Society of Petroleum Engineers. DOI: 10.2118/170956-MS.

McGowen, J.M., Gilbert, J.V., and Samari, E. 2007. Hydraulic Fracturing Down Under. Paper presented at the SPE Hydraulic Fracturing Technology Conference, College Station, Texas, U.S.A. Society of Petroleum Engineers. DOI: 10.2118/106051-MS.

Medlin, W.L. and Masse, L. 1984. Laboratory Experiments in Fracture Propagation. *Society of Petroleum Engineers Journal* **24** (03): 258-268. DOI: 10.2118/10377-PA

Meyer, B.R. and Jacot, R.H. 2000. Implementation of Fracture Calibration Equations for Pressure Dependent Leakoff. Paper presented at the SPE/AAPG Western Regional Meeting, Long Beach, California. Society of Petroleum Engineers. DOI: 10.2118/62545-MS.

Mohamed, I.M., Azmy, R.M., Sayed, M.A.I. et al. 2011. Evaluation of after-Closure Analysis Techniques for Tight and Shale Gas Formations. Paper presented at the North American Unconventional Gas Conference and Exhibition, The Woodlands, Texas. Society of Petroleum Engineers. DOI: 10.2118/140136-MS.

Mullen, M. and Enderlin, M. 2010. Is That Frac Job Really Breaking New Rock or Just Pumping Down a Pre-Existing Plane of Weakness?-the Integration of Geomechanics and Hydraulic-Fracture Diagnostics. Paper presented at the 44th U.S. Rock Mechanics Symposium and 5th U.S.-Canada Rock Mechanics Symposium Salt Lake City, Utah. American Rock Mechanics Association.

Nguyen, D.H. and Cramer, D.D. 2013. Diagnostic Fracture Injection Testing Tactics in Unconventional Reservoirs. Paper presented at the SPE Hydraulic Fracturing

Technology Conference, The Woodlands, Texas, USA. Society of Petroleum Engineers. DOI: 10.2118/163863-MS.

Nolte, K.G. 1979. Determination of Fracture Parameters from Fracturing Pressure Decline. Paper presented at the SPE Annual Technical Conference and Exhibition, Las Vegas, Nevada. 1979 Copyright 1979 American Institute of Mining, Metallurgical, and Petroleum Engineers, Inc. 00008341. DOI: 10.2118/8341-ms.

Nolte, K.G. 1990. Fracturing-Pressure Analysis for Nonideal Behavior. Paper presented at the Annual Technical Conference and Exhibition, New Orleans. Society of Petroleum Engineers. DOI: 10.2118/20704-PA.

Nolte, K.G., Mack, M.G., and Lie, W.L. 1993. A Systematic Method for Applying Fracturing Pressure Decline: Part I. Paper presented at the SPE Rocky Mountain RegionaVLow Permeability Reservoirs Symposium, Denver, Colorado. Society of Petroleum Engineers. DOI: 10.2118/25845-MS.

Nolte, K.G., Maniere, J.L., and Owens, K.A. 1997. After-Closure Analysis of Fracture Calibration Tests. Paper presented at the SPE Annual Technical Conference and Exhibition, San Antonio, Texas. 1997 Copyright 1997, Society of Petroleum Engineers, Inc. 00038676. DOI: 10.2118/38676-ms.

Pattay, P.W. 1998. Transient Pressure Behaviour in Fractured Reservoirs. Paper presented at the European Petroleum Conference, The Hague, Netherlands. Society of Petroleum Engineers. DOI: 10.2118/52080-STU.

Reynolds, M.M. and Munn, D.L. 2010. Development Update for an Emerging Shale Gas Giant Field - Horn River Basin, British Columbia, Canada. Paper presented at the SPE Unconventional Gas Conference, Pittsburgh, Pennsylvania, USA. Society of Petroleum Engineers. DOI: 10.2118/130103-MS.

Ribeiro, P.M. and Horne, R.N. 2013. Pressure and Temperature Transient Analysis: Hydraulic Fractured Well Application. Paper presented at the SPE Annual Technical Conference and Exhibition, New Orleans, Louisiana, USA. Society of Petroleum Engineers. DOI: 10.2118/166222-MS.

Rollins, K. and Hyden, R.E. 1998. Pressure-Dependent Leakoff in Fracturing Field Examples from the Haynesville Sand. Paper presented at the SPE Rocky Mountain Regional/Low-Permeability Reservoirs Symposium, Denver, Colorado. Society of Petroleum Engineers. DOI: 10.2118/39953-MS.

Sneddon, I.N. 1946. The Distribution of Stress in the Neighbourhood of a Crack in an Elastic Solid. *Proceedings of the Royal Society of London. Series A, Mathematical and Physical Sciences* **187** (1009): 229-260. DOI: 10.2307/97970

Sneddon, I.N. 1951. *Fourier Transforms*. New York: McGraw-Hill Book Company, Inc. Original edition. ISBN 1124084649.

Sneddon, I.N. and Elliott, H.A. 1946. The Opening of a Griffith Crack under Internal Pressure. *Quarterly of Applied Mathematics* **4** (3): 262-267.

Stegent, N.A., Sorenson, F., Brake, S.C. et al. 2004. Methodology to Implement the Optimum Fracture Design in an Oil-Bearing Reservoir. Paper presented at the

SPE International Petroleum Conference in Mexico, Puebla Pue., Mexico. Society of Petroleum Engineers. DOI: 10.2118/92095-MS.

Valko, P.P. and Economides, M.J. 1997. *Hydraulic Fracture Mechanics*. New York City: John Wiley & Sons. Original edition. ISBN 9780471956648.

Walsh, J.B. 1981. Effect of Pore Pressure and Confining Pressure on Fracture Permeability. *International Journal of Rock Mechanics and Mining Sciences & Geomechanics Abstracts* **18** (5): 429-435. DOI: http://dx.doi.org/10.1016/0148-9062(81)90006-1

Warpinski, N.R. 1985. Measurement of Width and Pressure in a Propagating Hydraulic Fracture. *Society of Petroleum Engineers Journal* **25** (01): 47-54. DOI: 10.2118/11648-PA

Xue, H. and Ehlig-Economides, C. 2013. Permeability Estimation from Fracture Calibration Test Analysis in Shale and Tight Gas. Paper presented at the Unconventional Resources Technology Conference, Denver, Colorado, USA. Society of Petroleum Engineers. DOI: 10.1190/URTEC2013-023.

Yew, C.H. and Liu, G.H. 1993. The Fracture Tip and Critical Stress Intensity Factor of a Hydraulically Induced Fracture. *SPE Production & Facilities* **8** (03). DOI: 10.2118/22875-PA